DOKUZ EYLÜL UNIVERSITY
GRADUATE SCHOOL OF NATURAL AND APPLIED SCIENCES

DEVELOPMENT AND USE OF DIGITAL IMAGE ANALYSIS TECHNIQUES FOR ANALYZING SECTIONAL CHARACTERISTICS OF SOME GEOMATERIALS

by
Okan ÖNAL

March, 2008
İZMİR

DEVELOPMENT AND USE OF DIGITAL IMAGE ANALYSIS TECHNIQUES FOR ANALYZING SECTIONAL CHARACTERISTICS OF SOME GEOMATERIALS

A Thesis Submitted to the
Graduate School of Natural and Applied Sciences of Dokuz Eylül University
In Partial Fulfillment of the Requirements for the Degree of Doctor of Philosophy in
Civil Engineering, Geotechnics Program

by
Okan ÖNAL

March, 2008
İZMİR

Ph.D. THESIS EXAMINATION RESULT FORM

We have read the thesis entitled **"DEVELOPMENT AND USE OF DIGITAL IMAGE ANALYSIS TECHNIQUES FOR ANALYZING SECTIONAL CHARACTERISTICS OF SOME GEOMATERIALS"** completed by **Okan ÖNAL** under supervision of **Assoc. Prof. Dr. Gürkan ÖZDEN** and we certify that in our opinion it is fully adequate, in scope and in quality, as a thesis for the degree of Doctor of Philosophy.

Assoc. Prof. Dr. Gürkan ÖZDEN

Supervisor

Prof. Dr. Arif Şengün KAYALAR	Asst. Prof. Dr. Olcay AKAY
Thesis Committee Member	Thesis Committee Member
Assoc. Prof. Dr. Özgür YAMAN	Assoc. Prof. Dr. A. Bahadır YAVUZ
Examining Committee Member	Examining Committee Member

Prof.Dr. Cahit HELVACI
Director
Graduate School of Natural and Applied Sciences

ACKNOWLEDGMENTS

I would like to thank my supervisor Dr. Gürkan Özden for his valuable guidance throughout my period of thesis. My thanks are due for Dr. Arif Kayalar and Dr. Olcay Akay for their kind discussions.

Additionally, I thank Dr. Ali Hakan Ören, Alper Selver and Burak Felekoğlu for their cooperative works and kind aids. Also, I am indebted to Dr. Adnan Değirmencioğlu for introducing me to the multiple regression analysis used in Chapter 5 of this dissertation and to my father, Dr. İsmet Önal for his valuable comments and suggestions. Research Assistants of the Geotechnics Division of Civil Engineering Department, Rifat Kahyaoğlu and Ender Başari are acknowledged for their help.

I would like to acknowledge the financial support provided by Turkish Scientific & Technological Research Council, TUBITAK, through project grant number MAG 104M358.

Finally, I thank to my wife, Buket. My accomplishment in this dissertation would not have been possible without the tireless support and thoughtful encouragement of my loving wife.

DEVELOPMENT AND USE OF DIGITAL IMAGE ANALYSIS TECHNIQUES FOR ANALYZING SECTIONAL CHARACTERISTICS OF SOME GEOMATERIALS

ABSTRACT

Certain characteristics of geomaterials can be effectively quantified by means of digital image analysis methods. This thesis study targeted development of a suite of digital image processing algorithms directly applicable to geotechnical engineering field. Image processing methods have been applied to the investigation and classification of materials of varying geological origin. The volume measurement technique using digital image processing methods is original to this study. The improvement made to skeleton based segmentation method has been more successful and robust on separating touching soil grains. The digital signature technique was greatly enhanced in order to obtain better results while characterizing grain shapes. Combined application of grayscale and color segmentation techniques was made for the identification of grains and voids adhered together by a cohesive matrix. It was demonstrated that the digital imaging technique and digital data processing algorithms developed herein could be utilized as a powerful nondestructive testing and evaluation method when used with statistical data analysis tools.

Keywords: Digital image processing, volumetric shrinkage, skeleton based segmentation, color segmentation, shape analysis.

BAZI GEOMALZEMELERİN KESİT ÖZELLİKLERİNİN ANALİZİ İÇİN SAYISAL GÖRÜNTÜ İŞLEME TEKNİKLERİNİN GELİŞTİRİLMESİ VE KULLANILMASI

ÖZ

Sayısal görüntü işleme teknikleri kullanılarak geomalzemelerin belirli özellikleri etkin bir şekilde belirlenebilir. Bu tez çalışması geoteknik mühendisliği alanına doğrudan uygulanabilir sayısal görüntü işleme algoritmaları takımı geliştirmeyi hedeflemiştir. Görüntü işleme teknikleri değişik jeolojik orijine sahip materyallerin incelenmesinde ve sınıflandırılmasında kullanılmıştır. Sayısal görüntü işleme kullanarak hacim ölçüm tekniği bu çalışmaya özgüdür. İskelet tabanlı ayrıştırma metodunda yapılan iyileştirmeler birbirine dokunan danelerin bağımsız ayrılmasında başarılı olmuştur. Sayısal imza tekniği, dane şekillerinin nitelendirilmesinde daha iyi sonuçlar elde edilebilmesi için iyileştirilmiştir. Gri ton ve renkli ayrıştırma tekniklerinin birlikte uygulanması, kohezyonlu ortamda bulunan birbirine yapışık dane ve boşlukların belirlenmesinde kullanılmıştır. Bu tez kapsamında geliştirilen sayısal görüntüleme ve sayısal veri işleme algoritmaları, istatistiksel veri analizi araçlarıyla beraber kullanıldığında güçlü bir tahribatsız deney ve değerlendirme metodu olarak kullanılabilir.

Anahtar Sözcükler: Sayısal görüntü işleme, hacimsel büzülme, iskelet tabanlı ayrıştırma, renkli ayrıştırma, şekil analizi.

CONTENTS

Pages

CHAPTER ONE
INTRODUCTION

1.1 A General Overview of Image Processing Methods

Use of nondestructive testing methods (NDT) for investigation and inspection of engineering materials have been accelerated since 1970s. Since then, NDT technologies continue to play a leading role in a number of key industries with growing interest. Nondestructive testing aims the determination of the characteristics of a material or substance without involving its deterioration or destruction. NDT technologies advanced in important ways and have become increasingly user friendly. Applications of these techniques spread out quite rapidly in various engineering fields (Bray & McBride, 1992).

Visual or optical inspection is the oldest known form of the nondestructive tests. In many cases the visual and optical methods may aid in the decision for the application of the most appropriate nondestructive test(s) such as, radiographic, ultrasonic and magnetic field. The naked human eye was the key instrument in the early examples of visual inspection applications. Conventional photographing instruments have made documentation of visual inspection possible.

The processing of images, providing more in depth and detailed data, however, begins with the evolution of the modern digital computer. Since the digital images require tremendous storage and computational power, digital image processing has been dependent on the development of modern digital computers and supporting technologies that include data storage, display, and transmission. Digital image processing is the process of extracting significant information from digitized images by transforming them into other images using various mathematical algorithms. In the last decades, digital imaging and analysis enjoyed wide acceptance in many fields such as material, biomedical and geosciences accompanied by the ever increasing computational power of the computer systems.

Although there are various numbers of digital image processing applications in the literature, the research studies on geomaterials are comparatively limited. This may be attributed to the complexity of the processing systems and algorithms which have resulted in costly imaging and analyses instruments. However, this fact has been altered in favour of the researchers recently, following the development of the cost effective professional imaging equipments and modern technical computing languages that offer toolbox algorithms for image processing operations.

1.2 Objective and Scope of the Research

A comprehensive literature search for image processing applications in geotechnical field has been conducted in this thesis study. In this stage of the dissertation, the research methodologies using the two dimensional photographing technique in the image processing applications has been classified into three main categories: object segmentation, shape characterization (area and void) and volume determination. It is decided that some unique contributions could be made to the literature in all these categories.

The objective of this dissertation was established as the development of digital imaging and image analysis techniques for the estimation of two and three dimensional characteristics of geomaterials using in plane images of test specimens.

The utilization of the color segmentation algorithm has been aimed to employ for the segmentation of the voids in cohesive matrix, where segmentation using the grayscale segmentation algorithms is not applicable. Simultaneously, the conventional grayscale segmentation has been also performed for the determination of grain characteristics bound by the same cohesive matrix. New coefficients for the characterization of the pore shapes with complex geometries have been proposed. On the other hand, a new imaging technique and volume calculation methodology has been suggested for the improvement of the accuracy of the volume calculations of compacted sand and clay mixtures. The new methodology also minimizes the operator based errors and ensures more robust calculation of the volume of the

cylindrical specimens. Surface images of the cubic shaped rock specimens have been used for the estimation of the volumetric characteristics of the rock specimens. The segmentation of the touching grains, at different degrees of angularities has been studied using a segmentation technique based on the skeleton algorithm.

In order to achieve the above mentioned goals of the dissertation, MatLab Technical Computing Language and image processing toolbox have been mastered, so that program codes for the image processing operations and other computational operations could be developed. The neural network toolbox of the MatLab Technical Computing Language and multiple linear regression analysis extension of the Microsoft Excel have been employed while searching correlations between the parameters obtained via image processing and the unconfined compression strength values of the rock specimens.

The techniques that were originally developed during this thesis study have been applied to some selected geomaterials. Ordinary river sand has been used for the determination of the grain size distribution. In order to obtain the grain and void distribution in the cohesive matrix, however, two self compacted concrete specimens were prepared, one of which was intentionally segregated so that different matrix properties and grain distributions could take place. The complex void shapes, occurred in the segregated specimen, have been studied using the proposed shape analysis techniques. The volume determination methodology has been applied to the sand and clay mixtures compacted during laboratory compaction tests. The breccia rock specimens have been employed for the estimation of the unconfined compressive strength values using the surface images along with the results of the nondestructive laboratory tests. It is believed that the methodologies developed for the characterization of composite materials where grains of various sizes are bounded by a cohesive matrix are equally applicable to gravel, sand, clay mixtures.

Finally, grain shapes, originally proposed for the classification of the grain angularity by the Krumbein in 1941 have been digitally rearranged to form touching

groups, of which degrees of angularity are known. These groups have been used in the verification of the skeleton based segmentation algorithm.

Contributions have been made to geotechnical literature by developing new methodologies and improving existing image processing techniques. The applications of these techniques and methods have been made on natural and artificially prepared specimens. Methodologies and analysis methods that were originally developed during this study proved that digital image analyses could be an efficient tool for nondestructive evaluation of geomaterials.

Parameters that were obtained in two dimensional imaging analyses, however, enabled computation and estimation of volumetric specimen characteristics such as shrinkage strain, porosity, pore shape and unconfined compressive strength and grain distribution.

The experimental program for the investigation of the breccia rock specimens carried out in this study was funded by Türkiye Bilimsel ve Teknolojik Araştırma Kurumu, TÜBİTAK (The Scientific & Technological Research Council of Turkey) through project with grant No. MAG 104M358.

1.3 Organization of Dissertation

The dissertation consists of seven chapters. Chapter One outlines the introduction, objectives and scopes of this study and the organization of the dissertation.

Image processing and analysis techniques as well as the general overview of the image processing history and literature, are introduced in the Second Chapter with examples using the grain images to provide appropriate background for evaluating the applications described in this thesis. As a result, a digital sieve analysis application, based on the cross sectional areas of the grains, have been conducted and compared with the conventional sieve analysis results.

In Chapter Three, a new procedure for the determination of volumetric shrinkages of compacted mixtures has been introduced. The comparison of the methods that were based on digital imaging and conventional methods was presented. Chapter Four describes the quantification of grains and voids in cohesive matrix using color and grayscale segmentation techniques.

In Chapter Five, a digital image analysis technique for the study of breccia rock specimens has been presented. Since multiple linear regression and artificial neural networks have been employed for the analysis of the breccia rocks, theories of both concepts have been covered in this section. Automated separation of touching grains using skeleton based segmentation algorithm is presented in Chapter Six along with its applications. Chapter Seven presents the conclusions of this dissertation and recommendations for future studies.

The program codes for all the techniques developed and employed during this thesis have been presented in the appendices.

CHAPTER TWO
IMAGE PROCESSING TECHNIQUES

The background of image processing is introduced in this section. Thereafter, formation, acquisition and processing of digital images will be presented. The digital image processing operations, described as image generation and acquisition, image coding, image enhancement, image segmentation and image analysis, are presented in sequence in this chapter. As a result, a digital sieve analysis application, following the same sequence has been performed.

2.1 Background of Image Processing

The first usage of the digital image processing may be defined as the picture transmission using the submarine cable between London and New York in the early 1920s. The cable picture transmission system reduced the time required to transport a picture across the Atlantic from more than a week to less than couple hours. The system coded pictures using specialized printing equipment for the cable transmission and then reconstructed at the receiving end.

Although the first examples involve digital images, the processing of the images begins with the development of the modern digital computer. Since the digital images require high storage and computational power, digital image processing has been dependent on the development of digital computers and supporting technologies that include data storage, display, and transmission.

The modern digital computer dates back to only the 1940s with the introduction by John von Neumann with the following key concepts;

- A memory to hold a stored program and data
- Conditional branching

These two new concepts forced the development of the central processing unit (CPU). Starting with von Neumann, there were a series of key advances that led to computers powerful enough to be used for digital image processing as summarized below (Gonzales & Woods, 2002);

- The invention of the transistor by Bell Laboratories in 1948
- The development in the 1950s and 1960s of the high-level programming languages COBOL (Common Business-Oriented Language) and FORTRAN (Formula Translator)
- The invention of the integrated circuit (IC) at Texas Instruments in 1958
- The development of operating systems in the early 1960s
- The development of the microprocessor (a single chip consisting of the central processing unit, memory, and input and output controls) by Intel in the early 1970s
- Introduction by IBM of the personal computer in 1981
- Progressive miniaturization of components, starting with large scale integration (LI) in the late 1970s, then very large scale integration (VLSI) in the 1980s, to the present use of ultra large scale integration (ULSI).

In addition to these advances, mass storage devices and display systems, both of which are fundamental requirements for digital image processing, were improved resulting in a convenient environment for the image processing applications.

The above mentioned requirements were met by some pioneer computers in the early 1960s. Although computers, capable of meaningful image processing tasks, are becoming widespread, the advances in digital image processing applications are accelerated by the beginning of the space program. The computer techniques were used for the improvement of the images taken from a space probe at the Jet Propulsion Laboratory in 1964. The pictures of the moon transmitted by Ranger 7 were processed by a computer to correct various types of image distortion inherent in the onboard television camera. The experiences in imaging and enhancement methods are used in further space missions.

Medical imaging, remote earth resources observations and astronomy were other disciplines that use digital image processing techniques in parallel with space applications in the late 1960s and early 1970s. The invention of computerized axial tomography (CAT) in the early 1970s is one of the most important events in the application of image processing in medical diagnosis. Computerized axial tomography is a process in which a ring of detectors encircles an object and an X-ray source, concentric with the detector ring, rotates around the object. The X-rays pass through the object and are collected at the opposite end by the corresponding detectors in the ring. As the source rotates, this procedure is repeated.

Tomography consists of algorithms that use the sensed data to construct an image that represents a “slice” through the object. Motion of the object in a direction perpendicular to the ring of detectors produces a set of such slices, which constitute a three-dimensional (3D) presentation of the inside of the object. After the invention of the computerized axial tomography, the field of image processing has grown vigorously. The developed techniques were also used in the geography, biology, archaeology, physics and many other industrial applications. The given examples deal with the human interpretation of the images. On the other hand, the second major area of application of digital image processing techniques is machine perception, which focuses on procedures for extracting image information in a form suitable for computer processing. Since the machine interpretation of an image differs significantly from the visual features that humans use, new techniques has been used such as statistical moments, Fourier transform coefficients, and multidimensional distance measures.

Automatic character recognition, industrial machine vision for product assembly and inspection, military detection, automatic processing of fingerprints, screening of X-rays and blood samples, and machine processing of aerial and satellite imagery for weather forecasting are typical problems in machine perception that routinely utilize image processing technique.

The availability of the modern computers with cheaper prices and the expansion of networking and communication bandwidth via internet have created unprecedented opportunities for continued growth of digital image processing.

The advances in hardware and software for digital image processing and analysis also provided new opportunities for the civil engineering discipline. However, it is only in the late 1980s that the potential impact in civil engineering has been recognized. A range of topics including engineering document scanning, pavement distress assessment, site evaluation using satellite imaging, studies of crack propagation and micro structure in cement based materials and evaluation of soil fabric are among those that are benefiting from capabilities afforded by the image processing technology. Despite the fact that there are significant numbers of researchers using image processing techniques in a range of civil engineering applications, there had been no meeting among the researchers until 1993. The Engineering Foundation and the National Science Foundation co-sponsored a conference as "Digital Image Processing: Techniques and Applications in Civil Engineering" that was held in Hawaii in March, 1993. The purpose of the conference was to provide an opportunity for researchers and practitioners from academia, government and industry to convene and exchange information and ideas.

The potential usage of the digital image processing techniques was realized with the investigation of the granular materials in geotechnical engineering. After that, optic and electronic microscopes were used for the investigation of the clays in micro scale. Digital image processing techniques were also used in the laboratory tests for the determination of the specimen deformations.

2.2 Basics of the Digital Image Formation

The processing of the digital images begins with transferring the images to the computer memory. This operation is called as acquisition process. The image acquisition can be categorized according to the source of the energy. The principle

energy source for imaging is the electromagnetic energy spectrum (Figure 2.1). Other important sources of energy include acoustic, ultrasonic and electronic waves.

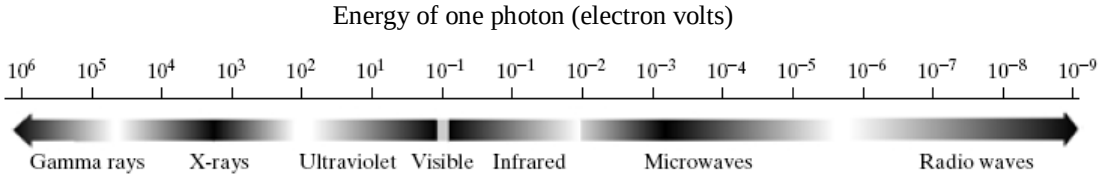

Figure 2.1 The electromagnetic spectrum arranged according to energy per photon (Gonzales & Woods, 2002).

Although the visible part of the electromagnetic spectrum is a very constricted zone, considerable number of the digital image processing applications use visible light in their image acquisition systems. In order to transform the illumination energy into analog data, single imaging sensor (Figure 2.2) or their multiple forms as line or array can be employed. An imaging sensor transforms the incoming energy into voltage by the combination of input electrical power and sensor material that is responsive to the particular type of energy being detected. The output voltage waveform is the response of the sensor, and a digital quantity is obtained from each sensor by digitizing its response.

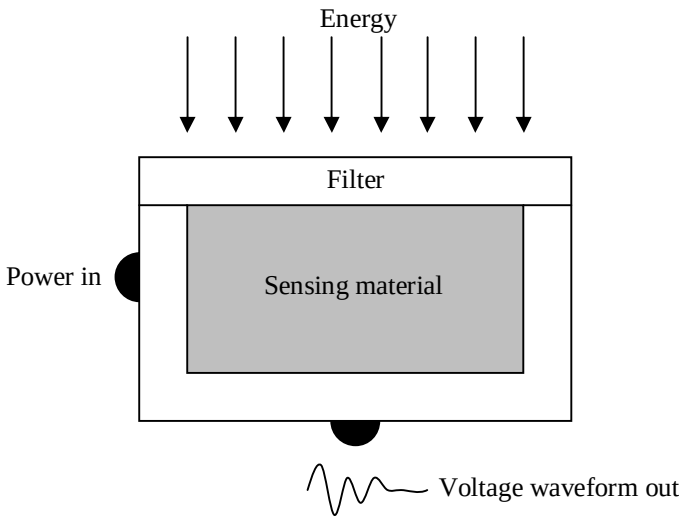

Figure 2.2 Single imaging sensor.

The acquisition can be performed by various types of the sensor formations for the whole electromagnetic spectrum. However, the most encountered acquisition devices for engineering purposes can be mentioned as below.

- **Scanners:** Scanners are functional and cost effective image acquisition devices. They can be used effectively if the objects, which will be scanned, are in two-dimensional (2D) form. Therefore, scanners are mostly preferred for the conventional photographs or 2D slices of the objects. However, scanners work relatively slow owing to their line sensors comparing to other image acquisition devices, so they are not a good solution for massive data input.
- **CCD Cameras:** Charge-coupled device (CCD) is an image sensor, consisting of an integrated circuit containing an array of linked, or coupled, light-sensitive sensors. The CCD cameras offer good sensibility and speed. They are the most frequently used sources of the data for the digital image processing. CCD cameras can be employed in almost every optical imaging device such as telescopes, microscopes or digital cameras. Since only the images obtained by CCD cameras were used in this thesis, the image formation process of the CCD capturing devices will be explained in detail in the next subsection.

- **Electron Microscopes:** The scan electron microscopes (SEM) or transmission electron microscopes (TEM) can be used if there is a need for higher optical magnification compared to the conventional microscopes. A focused electron beam is used in scanning electron microscopy to scan small areas of solid samples. Secondary electrons are emitted from the sample and are collected to create an area map of the secondary emissions. Since the intensity of secondary emission is dependent on local morphology, the area map is a magnified image of the sample. Spatial resolution may reach 1 nanometer for some instruments, but in general 4 nm is a common magnification level. Magnification factors can exceed 500,000. Backscattered electrons and characteristic X-rays are also generated by the

scanning beam and many instruments can utilize these signals for compositional analysis of microscopically small portions of the sample. On the other hand, the transmission electron microscope operates on the same basic principles as the conventional microscope. However, it uses electrons instead of light. Although a light microscope is limited by the wavelength of light, TEM uses electrons as light source. Since the electrons have much lower wavelength, a resolution of thousand times better than conventional microscope can be obtained.

- **Magnetic Resonance Imaging (MRI) and X-Ray Computed Tomography (X-CT):** Both MRI and X-CT systems can generate multiple two dimensional cross sections (slices) of the object. By the processing of the two dimensional sections, a detailed three dimensional reconstruction can be generated for the nondestructive testing purposes. A computed tomography scanner uses X-Rays, a type of ionizing radiation, to acquire its images, making it a good tool for examining materials with a relatively higher atomic number than the matrix surrounding them, such as composite materials or discontinuities on a body. MRI, on the other hand, uses non-ionizing radio frequency signals to acquire its images and is best suited for water containing materials like human tissues or saturated specimens.

2.2.1 Human Vision

The process of human vision has to be studied to some detail in order to understand how vision might be modeled computationally and replicated on computer. The role of the camera in image acquisition systems is analogous to that of the eye in biological systems. The eye is nearly a sphere, with an average diameter of approximately 20 mm, which is free to rotate under the control of extrinsic muscles. Light enters the eye through the transparent cornea, passes through the aqueous humor, the lens, and the vitreous humor, where it finally forms an image on the retina as shown in Figure 2.3.

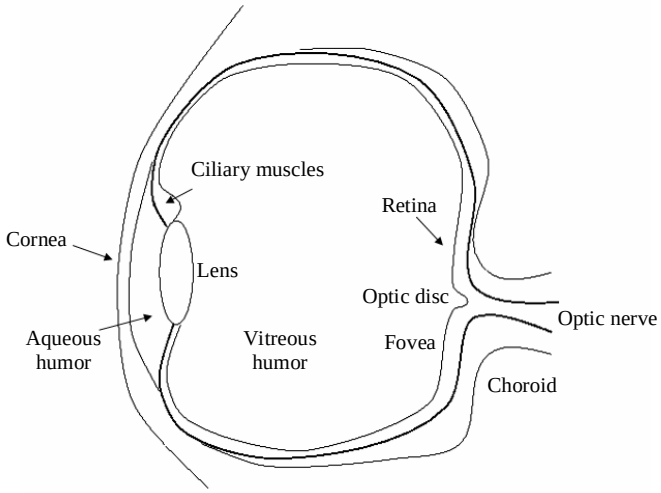

Figure 2.3 Cross-section of the human eye (Adopted from Nalwa, 1993).

When the eye is properly focused by the muscular adjustments of the lens, light from the object outside the eye is imaged on the retina. If this adjustment is not correctly accomplished, the viewer suffers from nearsightedness or farsightedness. Both conditions are easily corrected with optical lenses.

The retina is composed of complex tiling of two classes of light receptors as cones and rods. When these photoreceptors are stimulated by light, they produce electrical signals that are transmitted to the brain via optic nerve. The cones in each eye number between 6 and 7 million and are highly sensitive to color. They are located primarily in the central of the retina called as the fovea. The number of rods is much larger. Some 75 to 150 million are distributed over the retinal surface. They are not involved in color vision and are sensitive to low levels of illumination. The location of the optic nerve on the retina obviously prohibits the existence of light receptors at this point. This point is known as the blind spot and any light that falls upon it is not perceived by the viewer.

The light receptors do not have a continuous physical link to the optic nerve fibers. Rather they communicate through complex system of synapses. Very little is known about what happens to the optic signal once it begins its voyage down the optic nerve. The optic nerve has inputs arriving from both the left and right sides of both eyes, and these inputs split and merge at the optic chiasma (Figure 2.4).

Moreover, what is seen by one eye is slightly different from what is seen by the other, and this difference is used to deduce depth in stereo vision.

From the optic chiasma, the nerve fibers proceed in two groups to the striate cortex, where the visual processing in the brain happens. A large proportion of the striate cortex is devoted to processing information from the fovea (Owens, 1997).

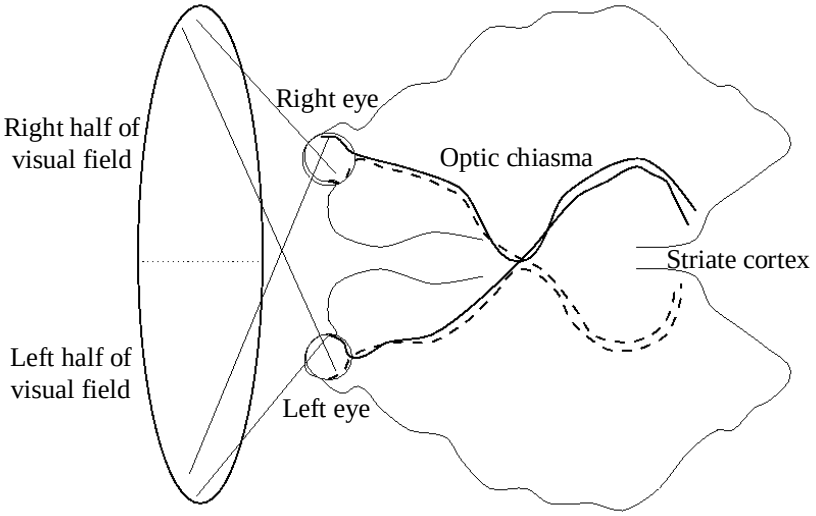

Figure 2.4 The formation of the stereo vision in brain (Adopted from Nalwa, 1993).

2.2.2 Image Formation with a CCD Camera

In order to capture an image with a camera, the scene should be illuminated at least with a single light source. The reflected radiation towards the camera from the surface of the object forms an image by passing through the lenses of the camera and disturbs the CCD sensor or the chemicals on a photograph film (Figure 2.5). The brightness of the surface is a function of illumination and surface properties. The simplest device to form an image of a 3D scene on a 2D plane is a pinhole camera. The pinhole camera model has an infinitely small hole through which light enters before forming an inverted image on the camera surface facing the hole.

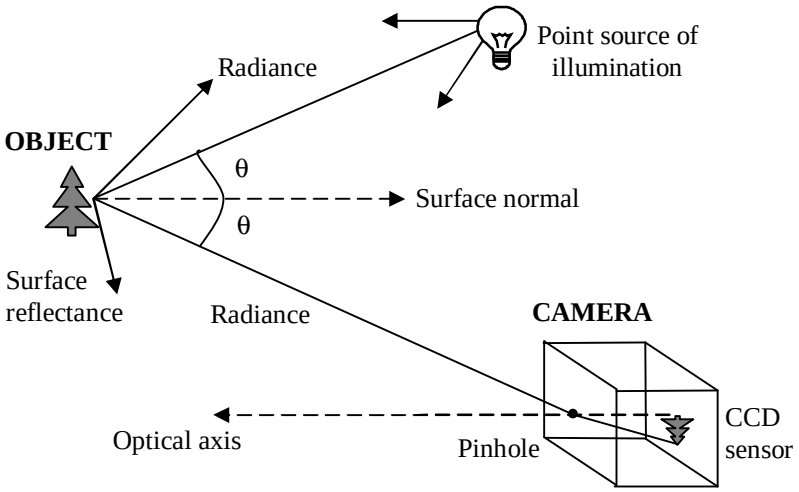

Figure 2.5 Capturing model of the camera.

Lenses are placed in the aperture to focus the bundle of rays from each scene point onto the corresponding point on the image sensors. Assuming the lens is relatively thin and its optical axis is perpendicular to the image plane, it operates according to the following lens law:

$$\frac{1}{u}+\frac{1}{v}=\frac{1}{f^2} \tag{2.1}$$

where, u is the distance of an object point from the plane of the lens, v is the distance of the focused image from this plane, and f is the focal length of the lens as shown in Figure 2.6.

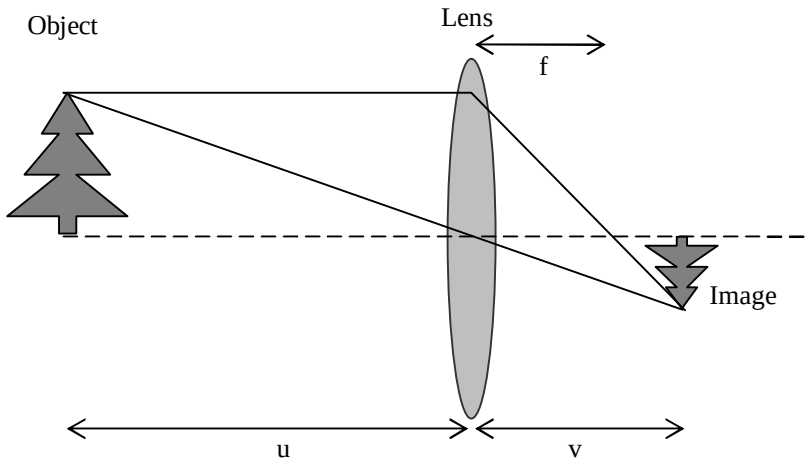

Figure 2.6 Simple lens model.

Once the acquisition device collects the incoming energy and focused on the image plane, an (n×m) array of tiny light sensitive cells converts light energy into electrical charge, which is proportional to the integral of the light received in each sensor (Figure 2.7). The output of the CCD array is a continuous electrical signal (video signal) which is generated by scanning the sensors in a given order and reading out their voltages, which is then digitized by frame grabber. The frame grabber digitizes the signal into a 2D rectangular array (N×M) of integer values. The position of the same point on the image plane will be different if measured in CCD elements (x, y) or image pixels (x_{im}, y_{im}). In general, $n \neq N$ and $m \neq M$, assuming that the origin in both cases is the upper left corner.

$$x_{im} = \frac{N}{n} x, \qquad y_{im} = \frac{M}{m} y \tag{2.2}$$

where, x_{im} and y_{im} are the coordinate of the point in the pixel plane and measured in pixels and x and y are the coordinates of the points in the CCD plane and measured in millimeters. The CCD sensor can be manufactured with a board range of sensing properties and can be packed in rugged arrays of 4000X4000 elements or more. CCD sensors are used widely in digital cameras and other light sensing instruments.

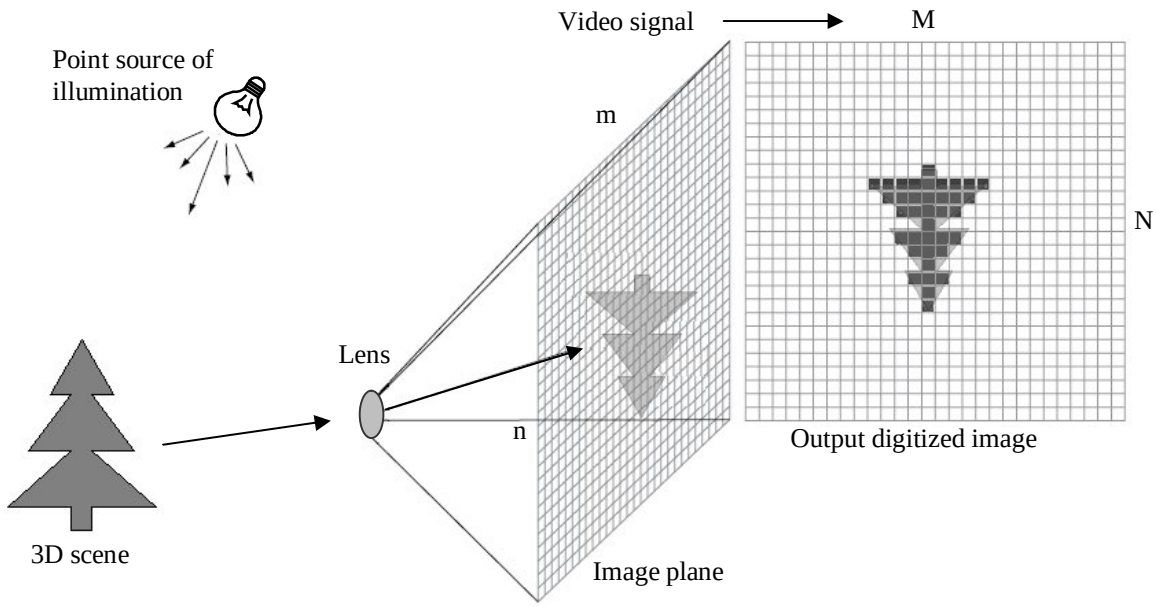

Figure 2.7 Digital image acquisition process.

2.3 Image Coding

Image coding refers to techniques used to store the captured image in the computer memory. Regardless of how the image f(x,y) has been captured, it is arranged in such a manner that the resulting digital image has M rows and N columns and may be presented as the following matrix.

$$f(x,y) = \begin{bmatrix} f(0,0) & f(0,1) & \dots & f(0,N-1) \\ f(1,0) & f(1,1) & \dots & f(1,N-1) \\ \dots & \dots & & \dots \\ f(M-1,0) & f(M-1,1) & \dots & f(M-1,N-1) \end{bmatrix} \quad (2.3)$$

The right side of this equation is by definition a digital image. Each element of this matrix may be called as an image or a picture element. Alternatively the terms pixel or pel are also used. The most commonly used term, however, is pixel. In the case of a grayscale image, the brightness of each pixel (L) is represented by a numeric integer value. Grayscale images typically contain values in the range of 0 to 255, with 0 representing the black, 255 representing the white and values in between representing shades of gray. Although there are no more restrictions on M and N other than being positive integers, the number of gray levels (L) is an integer power of 2 due to the processing, storage and sampling hardware considerations.

A color image can be represented by two-dimensional arrays of Red, Green and Blue layers. Typically, each number in the layers also ranges from 0 to 255, where 0 indicates that none of that primary color is present in that pixel and 255 indicates a maximum amount of that primary color.

2.3.1 Spatial and Gray Level Resolution

The spatial and gray level resolutions are the most important features of any image since they control the data transferred through the image acquisition device to the storage media. Spatial resolution is the minimum distance between two adjacent

pixels or the minimum size of a pixel, which can be detected by an acquisition device. When the spatial resolution decreases, the image shows less detail and fails to pick up smaller features. Figure 2.8 shows an image of size 1024×1024 pixels whose gray levels are represented by 8 bits. The following images shown in this figure are the results of sub sampling the original image. The sub sampling was applied by deleting the appropriate number of rows and columns from the original image, while the number of allowed gray levels was kept constant at 256.

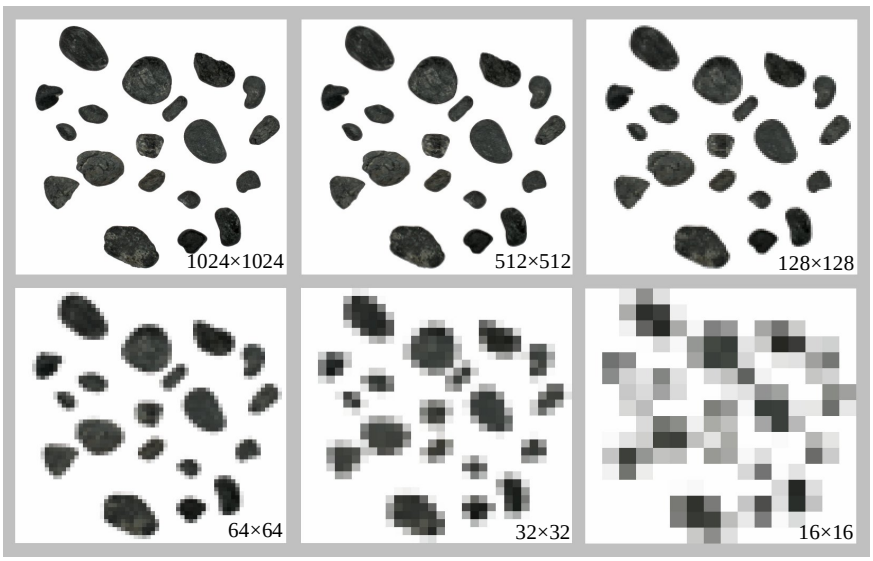

Figure 2.8 The effect of decrease in the spatial resolution in the visual appearance.

Gray level resolution similarly refers to the number of shades of gray in the image. Digital images having higher gray level resolution are composed of a larger number of gray shades and are displayed at a greater bit depth than those of lower gray level resolution. However, measuring discernible changes in the gray level is a highly subjective process. Due to hardware limitations, the number of gray level is an integer power of 2.

While the human eye can discriminate only 20 levels of gray at the same time, a general imaging device can capture 256 gray levels. The visual appearance of decreasing gray level resolution has shown in Figure 2.9, where the spatial resolution was kept constant, while the number of gray levels was gradually decreased from 256 to 2.

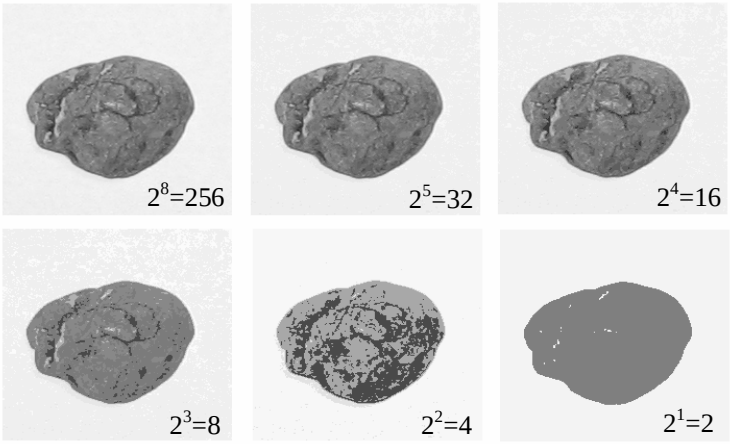

Figure 2.9 The visual appearance of decrease in gray level resolution.

2.4 Image Processing Software

The image processing software packages can be grouped in three main categories. The first group is intended for commercial general purpose usage. For many practical applications commercially available software packages can fulfill the desire of the researchers. The image processing operations can be applied easily without any in depth knowledge of the mathematical computations by selecting desired function in the software menu. ImageJ and ImageTool (Figure 2.10) are successful image processing software packages, both of which are open source and freeware for researchers.

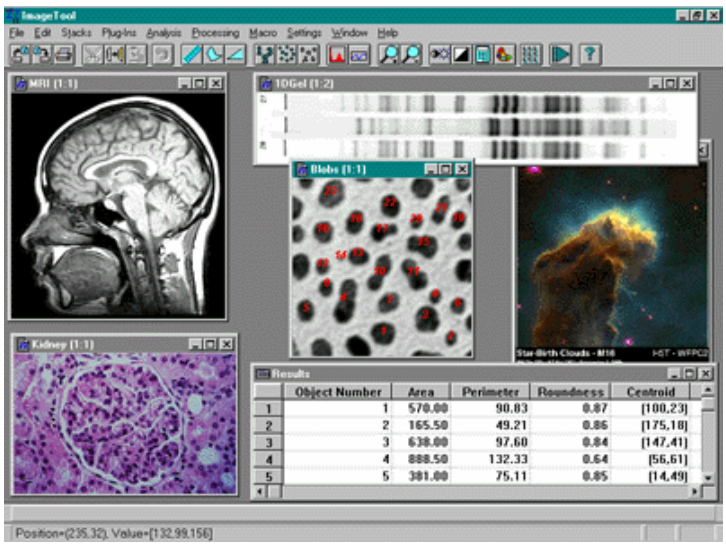

Figure 2.10 Free image processing software package (ImageTool).

The second software group can be mentioned as the software that is bundled with the image acquisition system. Many imaging systems like electron microscopes or X-ray computed tomography devices offer specialized processing and analysis software. Usually, the software packages control the acquisition device as well, and are limited by the set of standard functions. However, for some applications no commercial programs are available.

The third group for the image processing and analysis is the computer coded software via one of the several programming languages. There are several advantages of using a computing language for image analysis. The most significant among these is the ability to have direct access to any portion of the information available in the computing language in terms of ready-to-call image processing functions. These functions present in toolboxes and they are very advantageous for the development of the new image processing functions. By using a computing language, the image processing functions should be coded particularly in that language by the researcher, which enables full control over the image processing functions being applied. Such ability is very useful for the research and the development of new techniques.

In this thesis, the image processing and analysis operations have been coded in MatLab Technical Computing Language. The MatLab and MathCAD offer ideal environments for image processing. In particular, MatLab's matrix oriented language is well suited for image manipulation. Since the images are actually visual renderings of the matrices, all matrix manipulation codes embedded in MatLab results in a very effective way of image processing operations. Moreover, MatLab's Image Processing Toolbox provides a comprehensive set of reference-standard algorithms and graphical tools for image processing, analysis, visualization, and algorithm development. In addition to this, the extracted data from the images can be processed right in the computing language by MatLab commands or the other toolbox functions, which enable one to produce robust solutions for the problem of interest. On the other hand, the MatLab environment is complicated and needs comprehensive knowledge about the computer programming. Nevertheless, MatLab has relatively

slow computational speed compared to high level programming languages such as C or C++.

2.5 Image Enhancement

Image enhancement is the process of improving the quality of a digitally stored image by manipulating the image with a collection of techniques. These techniques aim to improve the visual appearance of an image or convert the image to a form which is better suited for machine interpretation. Unfortunately, there is no general theory for image enhancement when it comes to human perception. However, when image enhancement techniques are used as pre-processing tools for subsequent image processing techniques, quantitative measures can be set so that the most appropriate image enhancement technique is picked. The image enhancement techniques used in this thesis are discussed below.

2.5.1 Histogram Modifications

Histogram modeling techniques provide a sophisticated platform for modifying the dynamic range and contrast of an image. These techniques are very effective in detail enhancement and are used in the correction of nonlinear effects introduced by a digitizer or display system. The gray level histogram of an image is a chart, listing all of the gray levels that are used in the image on the horizontal axis with respect to the number of pixels corresponding to each level. Gray level images usually consist of 256 levels of gray so that the horizontal axis of the histogram extends from 0 to 255. The vertical axis varies in its own scale depending on the number of pixels in the image and the distribution of the gray levels values (Shapiro & Stockman, 2001).

2.5.1.1 Contrast Stretching

Low contrast images occur as a result of poor illumination or wrong settings of lens aperture-shutter speed combination during image capturing. In order to enhance the contrast of the images, a simple linear transformation function, which increase

the dynamic range of the gray levels in the image, can be employed. A low contrast image and histogram presentation of their gray values have been shown in Figure 2.11b and a, respectively. The visual appearance of the image (i.e. of the pixels varying between 0 and 128), on the other hand, can be increased by modifying the gray levels to full fill the entire histogram.

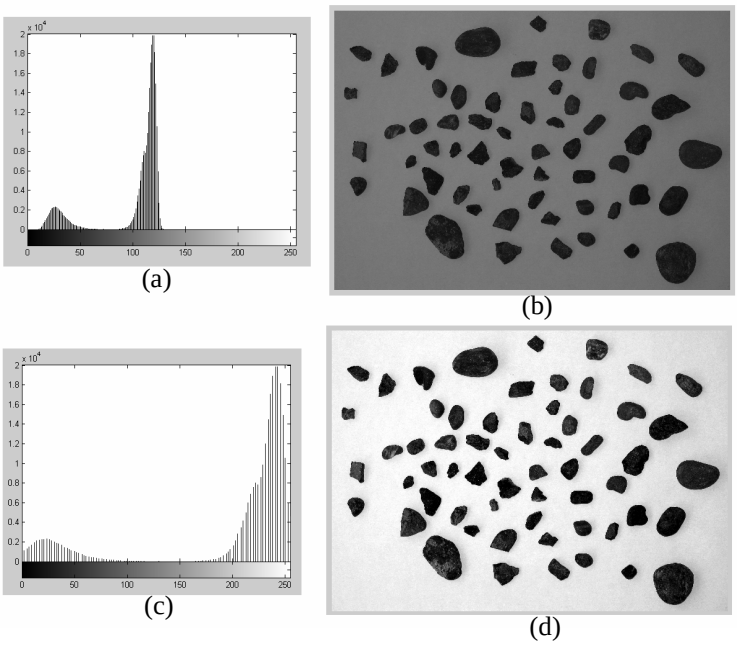

Figure 2.11 Contrast stretching of the grain samples.

The input gray levels of the image were mapped to the target (i.e. output) gray levels using a linear transformation function as shown in Figure 2.12. The enhanced histogram of the image and its resulting appearance are shown in Figure 2.11c and d.

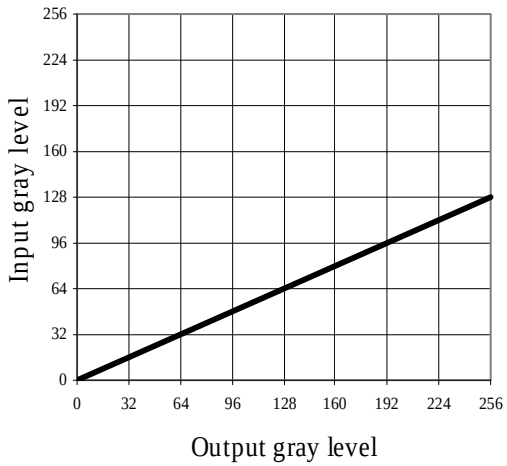

Figure 2.12 The transformations function of the image.

2.5.1.2 Histogram Equalization

Histogram equalization is a methodology which modifies the dynamic range and contrast of an image by altering the intensity histogram of the image. Unlike contrast stretching, histogram modeling operators may employ nonlinear transfer functions to map between pixel intensity values of the input and output images. Histogram equalization employs a monotonic, nonlinear mapping which reassigns the intensity values of pixels in the input image such that the output image contains a uniform distribution of intensities (i.e. a flat histogram). In order to show the nonlinear transformation functions of the histogram equalization technique, four basic image types; dark, light, low contrast, high contrast and their corresponding histograms are presented in Figure 2.13. The histogram equalization technique has been applied to four images. The transformation functions are plotted in the third column. Please note that, in the graphs of the transformation functions, the axes were normalized between 0 and 1. The equalized images and their histograms are given in column four and five, respectively, in the same figure.

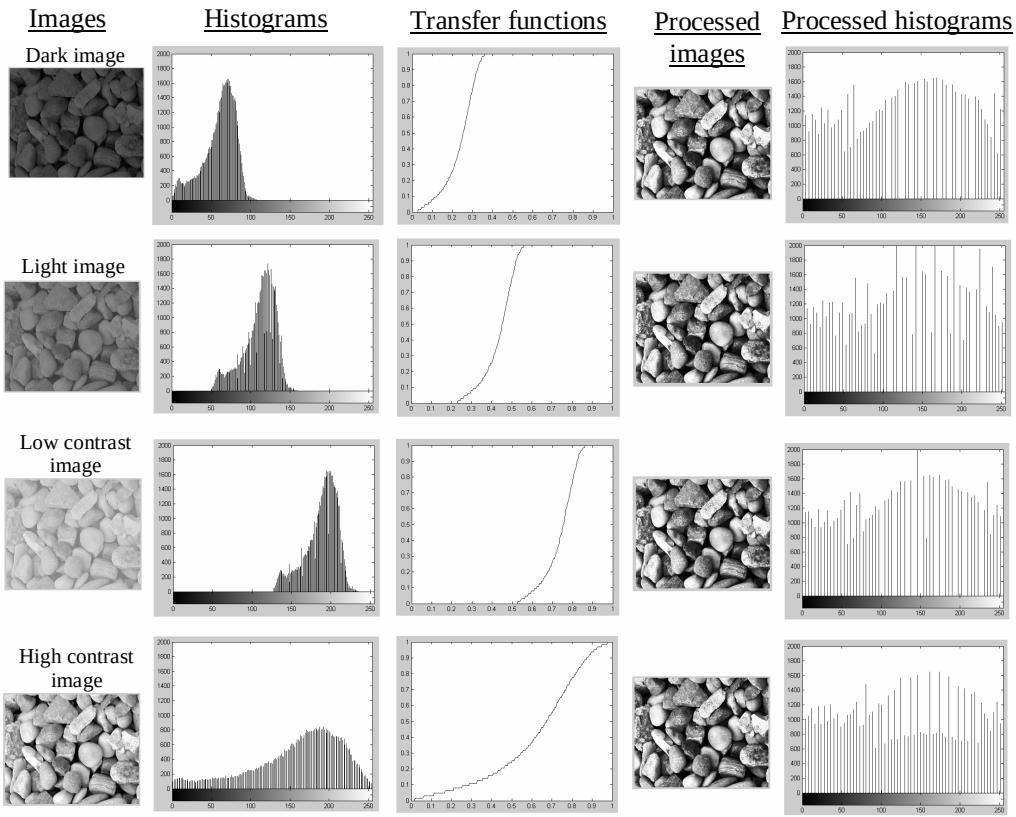

Figure 2.13 The presentation of the histogram equalization technique on four basic image types.

2.5.2 Spatial Filtering

Spatial filtering is the process of applying some neighborhood operations in an image with a filter mask that has the same dimensions as the neighborhood zone. Since it provides a means for removing noise and sharpening blurred images, spatial filtering of images is an important aspect of image processing. The process consists simply of moving the filter mask from pixel to pixel in an image. At each point, the response of the filter at that point is calculated according to the filter coefficients. The mechanics of spatial filtering can be summarized as in Figure 2.14.

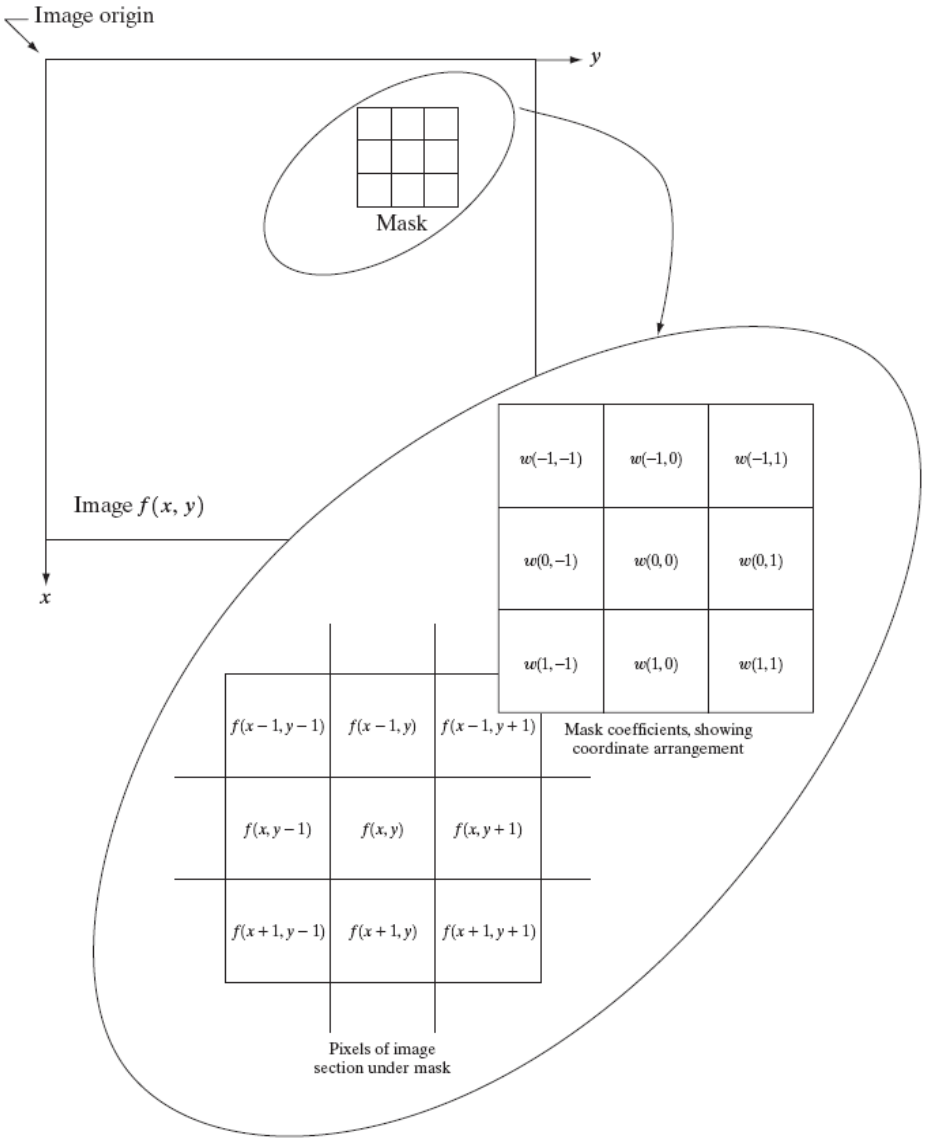

Figure 2.14 The mechanics of spatial filtering (Gonzales and Woods, 2002).

The result of the linear spatial filtering R, for a 3×3 mask at a point (x,y) in the image can be written as;

$$R=\omega(-1,1)\,f(x-1,y-1)+\omega(-1,0)\,f(x-1,y)+\dots + \omega(0,0)\,f(x,y)+\dots+\omega(1,0)\,f(x+1,y)+\omega(1,1)\,f(x+1,y+1) \quad (2.4)$$

Note that the computed value, R, is the value of the central point (x,y) in the filtered image.

2.5.2.1 Smoothing Spatial Filters

The simplest linear spatial filter is the averaging filter. The output of this filter type is the smoothing effect on the image of interest. This is a low-pass filter, which removes high spatial frequencies from an image and also ensures noise reduction in an image. The smoothing process results in an image with reduced sharp transitions in gray levels. Although being a desirable feature of an image, edges are also characterized as sharp transitions and will be smoothed as a side effect. The classic 3×3 masks for smoothing an image for noise removal and their resulting filtered images are shown in Figure 2.15.

Averaging filter $\frac{1}{9}\times\begin{bmatrix}1&1&1\\1&1&1\\1&1&1\end{bmatrix}$ Weighted mean filter $\frac{1}{16}\times\begin{bmatrix}1&2&1\\2&4&2\\1&2&1\end{bmatrix}$

(a) (b) (c)

Figure 2.15. (a) the noisy image, (b) image filtered by the averaging filter, (c) image filtered by the weighted mean filter.

The smoothing filters are also capable of eliminating the local maxima in a matrix, resulting in an efficient way for preprocessing of the image prior to the application of segmentation algorithms, which will be discussed later in the chapter.

2.5.2.2 Sharpening Spatial Filters

Sharpening spatial filters are used to highlight fine details or enhance the details that have been blurred, caused by natural effects or malfunction of an acquisition device. Generally, the sharpening filters are employed for enhancing the image of an improperly focused lens mechanism. The function of a sharpening filter is to emphasize changes in the gray levels. The classic mask for a sharpening filter and the filtered image can be seen in Figure 2.16.

A classic mask for sharpening filter applications: $\frac{1}{9} \times \begin{bmatrix} -1 & -1 & -1 \\ -1 & 8 & -1 \\ -1 & -1 & -1 \end{bmatrix}$

Figure 2.16 Artificially smoothed source image and the filtered image after using the above given mask.

2.5.2.2 Other Spatial Filters for Feature Detection

Spatial filtering can be used to detect a particular feature. For example, a mask to detect isolated points can be constructed by a feature pattern that is large in the center and small in the surrounding pixels as shown in Figure 2.17b. This mask responds

small values in flat regions. However, when the center point differs significantly from its surroundings, the response is exaggerated. Horizontal, vertical and inclined lines can also be detected by spatial filters using the filter masks in Figure 2.17c, d, e, f. The mask in Figure 2.17g is used to detect edges in the image. The combined use of spatial filters is also common. The summation of the filtered images for the edge detector mask in four directions is presented in Figure 2.17h. Note that all possible edges in this figure are detected and exaggerated.

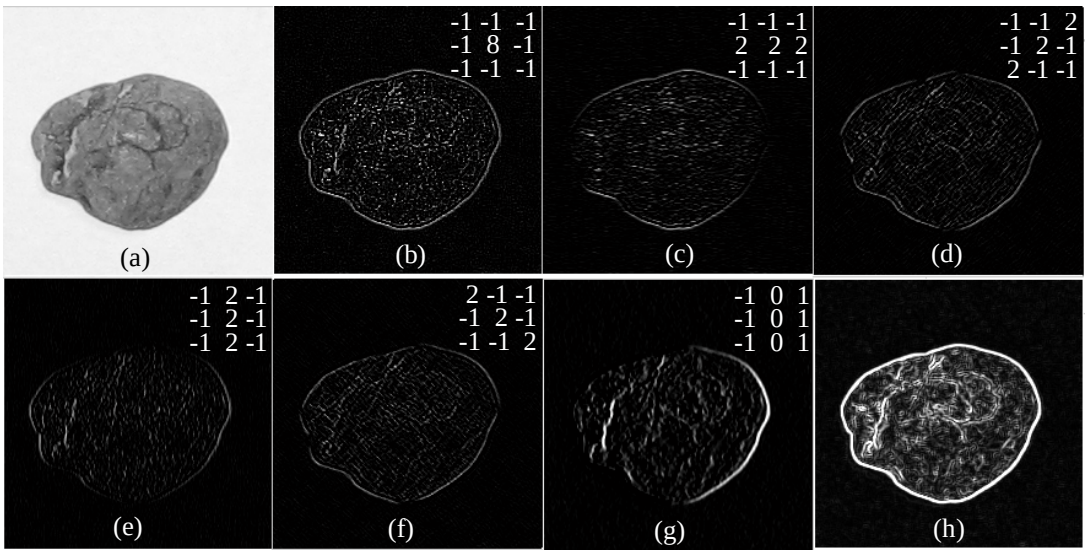

Figure 2.17 The point line and edge detector filters and their resulting images.

2.6 Image Segmentation

Image segmentation refers to the process of partitioning an image into multiple sets of pixels. The goal of segmentation is to simplify and/or change the representation of an image into something that is more meaningful and easier to analyze (Linda & George, 2001). From this point of view, the spatial filters for feature detection can be also included in image segmentation procedures.

2.6.1 Thresholding

The most frequently used methodology for the image segmentation is thresholding. The result of the thresholding procedure is a binary image, whose object pixels have one gray level and all background pixels have another. The process can be summarized as

$$g(x,y)= \begin{cases} 1 \text{ if } f(x, y) > T \\ 0 \text{ if } f(x, y) \leq T \end{cases} \quad (2.5)$$

where, g(x,y) is the value of the segmented image, f(x,y) is the gray level of the pixel (x,y) and T is the threshold value.

The thresholding process of a grain image is presented in Figure 2.18. The histogram of the grain image in this figure is grouped in two dominant zones. The segmentation has been performed by selecting a proper threshold value and applying the procedure given in Equation (2.5). The result of the thresholding operation is given in the same figure.

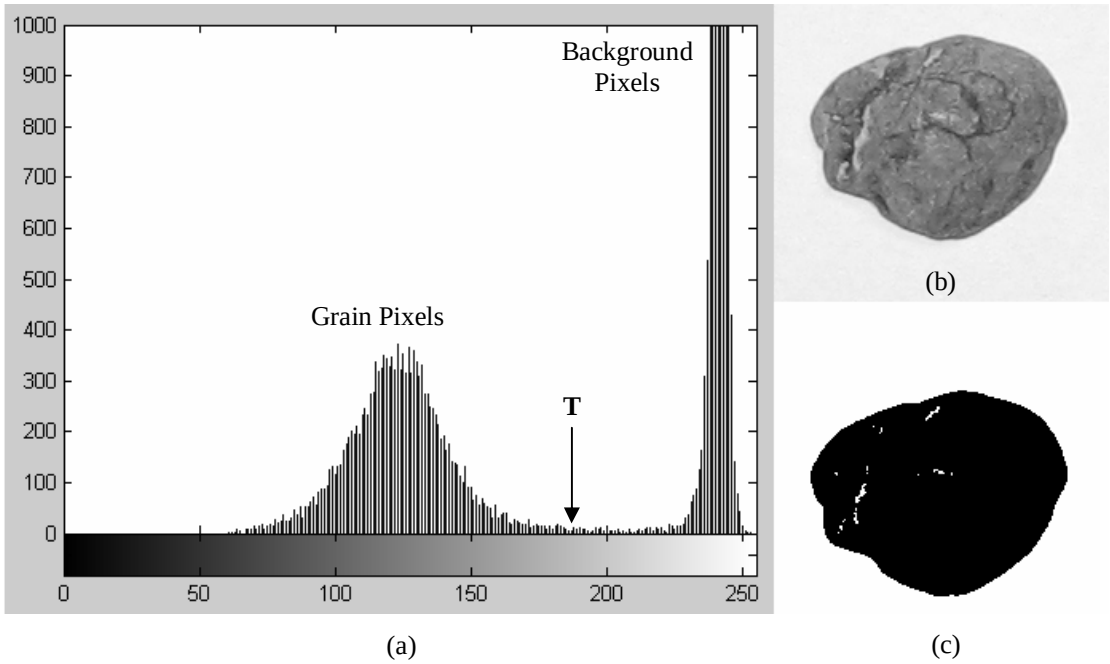

Figure 2.18 Thresholding process, (a) histogram of the grain image, (b) input (c) output images.

2.6.2 Watershed Segmentation

In some cases segmentation of images involves not only discrimination between object and the background pixels, but also separation between the object and object pixels that are in contact in an image (Figure 2.19a). This process is necessary for the individual analysis of the object regions (i.e. area, centroid). Watershed segmentation method is a well-known mathematical morphology for such separation (Vincent & Soille, 1991). This segmentation technique considers an image as a topological surface and defines the catchment basins and the watershed lines in terms of a flooding process. The topological surface is achieved by the distance transform operation, where the distance to the closest background pixel is assigned as altitude value (Figure 2.19b). When the rising water in distinct catchment basins is about to merge, a dam is built to prevent the merging. The flooding will eventually reach a stage when only the tops of the dams are visible above the water line (Figure 2.19d). The union of all dams defines the watershed lines of the image (Figure 2.19e).

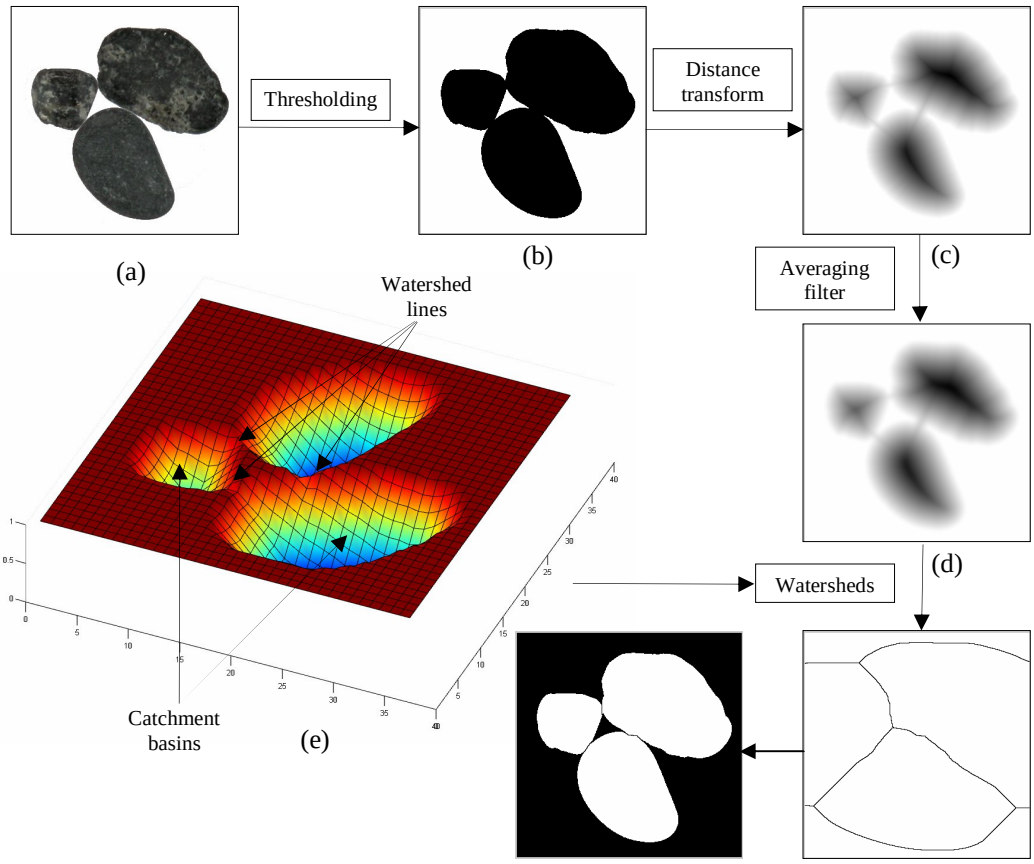

Figure 2.19 Watershed segmentation algorithm tree.

Please note that the smoothing filter was employed in order to eliminate the local minima in the distance map (Figure 2.19c) which prevents the over segmentation of the objects.

2.7 Image Analysis

Image analysis is extracting quantitative information from images. The image processing operations usually results in another image whereas the results of the image analysis algorithms are quantitative information. The image analysis operations are the last stage of the image operations and are usually performed on binary images upon which any necessary segmentation procedures were already completed.

In order to access the information obtained from binary images, a region map, where labels are assigned to pixels has to be generated (Figure 2.20). Quantitative information about the objects could then be obtained examining their regional properties using various algorithms in the region map.

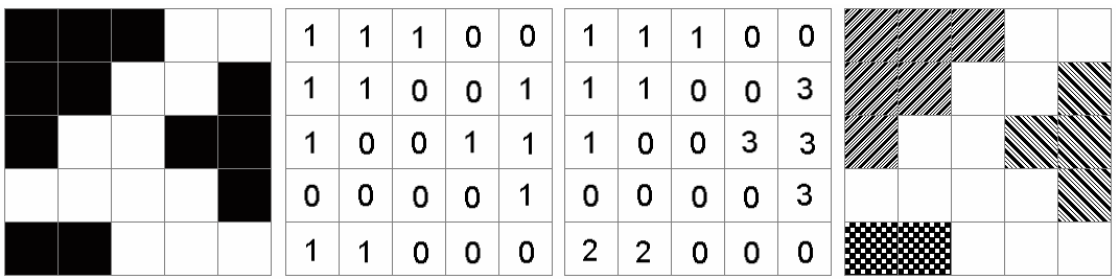

Figure. 2.20 Binary image, binary matrix, label matrix and labeled images.

MatLab image processing toolbox offers the measurement of a set of properties for each labeled region in the labeled matrix. The available properties for each object in the labeled matrix are given in Table 2.1.

Table 2.1 The available region properties of the MatLab's image processing toolbox.

Area	Scalar	The actual number of pixels in the region.
Bounding Box	Vector	The smallest rectangle containing the region.
Centroid	Vector	The center of mass of the region.
Convex Area	Matrix	The number of pixels in convex image.
Convex Hull	Matrix	The smallest convex polygon that can contain the region.
Convex Image	Binary image	The convex hull, with all pixels within the hull filled in.
Eccentricity	Scalar	The eccentricity of the ellipse that has the same second-moments as the region.
Equivalent Diameter	Scalar	The diameter of a circle with the same area as the region.
Euler Number	Scalar	Equal to the number of objects in the region minus the number of holes in those objects.
Extent	Scalar	The proportion of the pixels in the bounding box that are also in the region.
Extrema	Matrix	The extrema points in the region.
Filled Area	Scalar	The number of on pixels in filled image.
Filled Image	Binary image	Binary image of the same size as the bounding box of the region. The on pixels correspond to the region, with all holes filled in.
Image	Binary image	Binary image of the same size as the bounding box of the region.
Major Axis Length	Scalar	The length (in pixels) of the major axis of the ellipse that has the same normalized second central moments as the region.
Minor Axis Length	Scalar	The length (in pixels) of the minor axis of the ellipse that has the same normalized second central moments as the region.
Orientation	Angle	The angle (in degrees) between the x-axis and the major axis of the ellipse that has the same second-moments as the region.
Perimeter	Scalar	The scalar containing the total number of pixels around the boundary of the region.
Pixel Idx List	Vector	Vector containing the linear indices of the pixels in the region.
Pixel List	Matrix	The actual pixels in the region.
Solidity	Scalar	The proportion of the pixels in the convex hull that are also in the region.

2.7.1 A Sample Application of Image Analysis to Geotechnics: Digital Sieve Analysis

The grain size distribution of ordinary river sand has been examined using the image analysis functions of MatLab Technical Computing Language. The digital images of the granular material have been acquired employing a digital camera. Since the view area of the digital camera is limited, the granular material has been imaged in parts (Figure 2.21). The analysis of the whole material has been

established by combining the analysis results of the partially taken images (Önal & Özden, 2006). Similar research studies can be found in the literature for the analysis of the grain size distribution of the granular soils (Raschke & Hryciw, 1997; Mora et al., 1998). Total weight of 494.12 gr granular material has been imaged and the grain size distribution by weight has been determined using mechanical sieving. The acquired images having RGB color definition have been converted to grayscale (Figure 2.22b). Contrast stretching (Figure 2.22c) and thresholding (Figure 2.22d) operations have been applied in order to come up with the binary images.

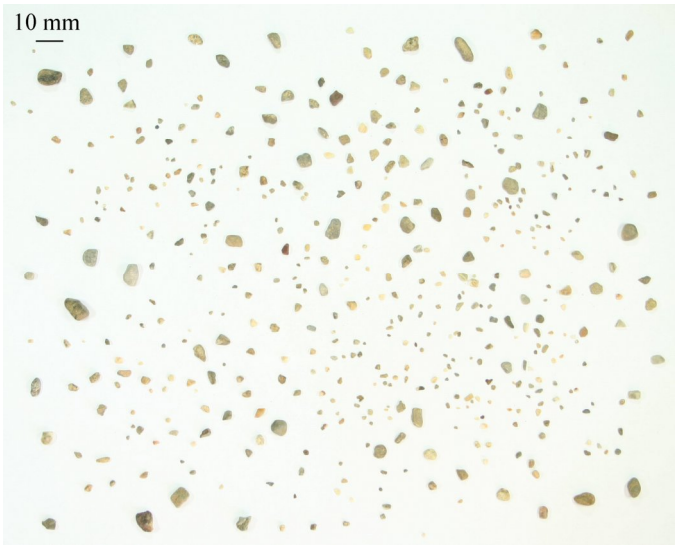

Figure 2.21 The unprocessed image belonging some part of the river sand.

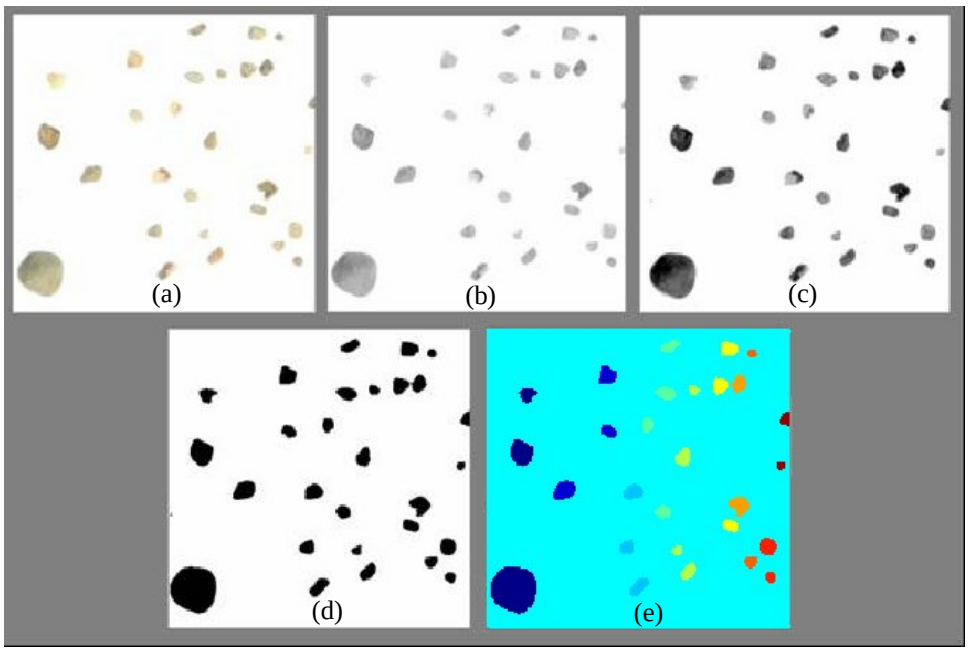

Figure 2.22 Image processing steps of the grain size distribution analysis.

Since the touching grains exist in the acquired images, watershed segmentation has been performed in order to enable the individual analysis of the grain particles. The labeling operation has been processed in the binary images to access the area information for each particle. Since the acquired images are two dimensional matrices, the grain size distribution of the granular material has been calculated using the area information instead of the weights of the grain particles by using Equation 2.6.

$$\%\ \text{Passing}_g = 100 - \left(\frac{Area_1 + Area_2 + \ldots + Area_g}{\sum_{i=1}^{final} Area_i}\right)\times 100 \qquad (2.6)$$

The results of both digital and mechanical evaluation of grain size distribution analysis are shown in Figure 2.23. Please note that the percent passing values are available for each grain particle in the digital analysis, yielding a smooth grain size distribution, which corresponds to an imaginary sieve set containing all possible intermediate sieves.

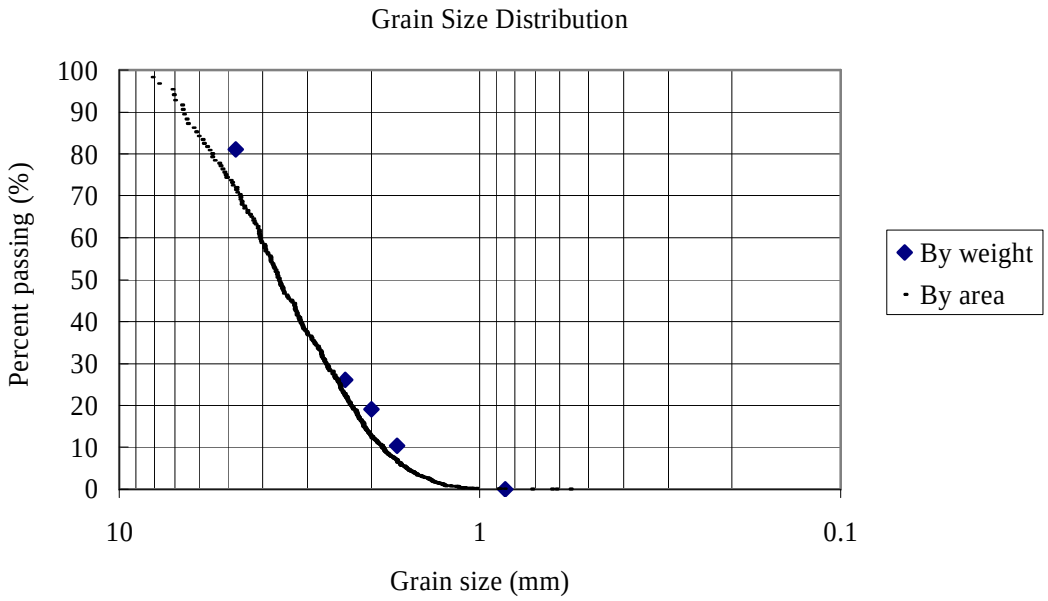

Figure 2.23 The comparison of digital and mechanical grain size distributions of the granular material.

CHAPTER THREE
A NEW METHOD FOR VOLUME MEASUREMENT OF CYLINDRICAL OBJECTS AND ITS APPLICATION TO GEOTECHNICS

3.1 Introduction

Attempts to identify the volume change of soils or compacted specimens have been made since late 1990s. Some of the previous studies were related with the determination of the deformation field during triaxial tests while the rest were directly related with measuring the volumetric shrinkage strains of expansive soils. Unlike with other studies, volumetric shrinkage strain levels in this study were limited to 6%. The strain levels were limited, because it was noted that the maximum allowable volumetric shrinkage strain levels were 5% for evaluating the hydraulic behavior of compacted soils (Kleppe & Olson, 1985). Above this level, cracks induced by drying may increase the hydraulic conductivity of the compacted soils. The principal purpose of this chapter is to present a new digital 2D volume measurement method and its application in geotechnics. The quantification of the volumetric shrinkage of the compacted soils even in the lower strain levels has been chosen as the sample application. Therefore, a special test setup was established and a computer algorithm was developed to identify volume of the specimens from digitized images.

Initially, the final volume changes of compacted bentonite-zeolite mixtures at various bentonite contents were measured by means of Vernier caliper. Consequently, comparison of the digital measurement results with those of the manual readings showed that they were in good agreement.

The same technique has applied in the determination of the volumetric shrinkage of the compacted bentonite-sand mixtures during drying (i.e. real time monitoring of volume measurements). Volumetric shrinkage of compacted bentonite-sand mixtures have been continuously monitored at small strain levels (i.e. <5%) using digital

image processing technique. Volume change of three compacted bentonite-sand mixtures at different initial moisture contents were recorded during drying by means of Vernier caliper and digital measurements. Continuous monitoring of the volumetric shrinkage of bentonite-sand specimens using digital images proved that digital measurement and data reduction methodology developed herein is capable of determining the shrinkage amount with desired accuracy.

It appears that the proposed methodology would provide nondestructive, stable and repeatable volume measurements and is a promising approach for the quantification of volumetric shrinkage strains of compacted mixtures even at small strain levels (Önal et al., 2008).

3.1.1 Literature Review on Digital Based Strain Measurements of Compacted Specimens

Desiccation cracking in soil liners and caps is a serious problem causing the initially impervious liner to act as a permeable barrier. After wetting and drying cycles upon the seasonal changes and fluctuations in the groundwater level, the compacted clay liner tends to either swell or shrink. The swelling/shrinkage process, however, is not reversible. As a result of plastic strains, many fissures and cracks develop during wetting and drying cycles.

The plasticity of soils is one of the key factors that affect both swelling/shrinkage potential and hydraulic conductivity. In general, an increase in the plasticity and molding water content causes an increase in the amount of volumetric shrinkage strain of compacted soils (Kleppe & Olson, 1985; Phifer et al., 1994; Albrecht & Benson, 2001). A soil with high bentonite content is susceptible to high volumetric shrinkage even though these types of soils have very low hydraulic conductivity. For example, Kleppe & Olson (1985) stated that compacted soils having more than 5% volumetric shrinkage strain had a high potential to exhibit major or moderate cracks and cannot be recommended as landfill liner material. Thus, researchers have suggested bentonite-sand mixtures as alternative to clayey soils to reduce the

volumetric shrinkage occurring during drying/wetting cycle (Kleppe & Olson, 1985; Tay et al., 2001). In other words, shrinkage potential of a soil dictates its use as a clay liner. However, determination of shrinkage of soils is often cumbersome.

Digital image analysis methods, on the other hand, enjoy the growing attention of researchers probably because, cost of image capturing equipments and computing power have been greatly reduced in recent years. Determination of grain-size distribution (Raschke & Hryciw, 1997) and local void ratio (Frost & Kuo, 1996), measurement of displacements in laboratory tests (Obaidat & Attom, 1998; Alshibli & Sture, 2000), tracking of displaced particles in direct shear test (Guler et al., 1999), and characterization of soil fabric changes in micro scale during consolidation testing (Adamcewicz et al., 1997) demonstrated applicability of digital image analysis techniques to soil testing.

Generally, the Vernier caliper is used to measure the volumetric shrinkage of compacted specimens. However, it brings some discrepancies; that is, the method only considers the homogenized shrinkage of soils and does not measure whenever the soil had some discontinuity along the sidewall or at the top. The same problem also occurs during triaxial testing. In relation to triaxial tests, volume changes can be measured manually using burettes or linear variable displacement transducers (LVDT) connected to the test cell or the specimen. Thus, the volumetric shrinkage strains directly measured by the conventional methods may be slightly lower or higher than its original shrunk size. For this reason, researchers have been interested to identify the shrinkage amount by means of digital image processing methods.

The efforts were spent mostly for determining the volumetric strain of soils when tested in a triaxial cell. For example, Macari et al. (1997) used video images to compute the rate of volume change of sand during drained conventional triaxial compression test. The experimental results were compared to the volumetric strains obtained by analyzing the front view and side view images. Two video cameras were placed orthogonally to each other to take front and side view images. It was mentioned that the results were in accordance with each other unless irregular shapes

were occurred. In addition to this, Alshibli & Al-Hamdan (2001) estimated the volume change of triaxial soil specimens by locating three cameras at equal distance to capture the entire body of the specimen. The predicted volumetric strain results were in good agreement with the actual volumetric strain measurements.

Utilization of image processing technique to determine the volumetric shrinkage strains were adapted on expansive soils as well (Puppala et al., 2004). Puppala et al. (2004) showed that the manual measurements using the Vernier caliper had similar volumetric shrinkage strain values with those determined by the image processing method. Although the study involves a rather wide range of volume changes on account of expansive soils (i.e. 0-40%), differences between volumetric shrinkage strain values obtained by image processing and conventional methods happened to be in the range of 0.3% to 4.5% and were accepted as negligible in their study.

However, this range of difference in two methods should be reduced when the maximum allowable limit of volumetric shrinkage strain is 5%. Thus, the objectives of this study are to determine the volumetric shrinkage performance of compacted bentonite-zeolite and bentonite-sand mixtures using image-processing technique and to compare obtained digital measurement data with those of the conventional method. Many of the tested compacted specimens had volumetric shrinkage strain values up to 5%, which is the maximum allowable limit for landfill liner applications. Therefore, the study was focused on the limited strain level.

3.2 Materials and Methods

The compacted specimens utilized in this study were obtained from a parallel testing program that was conducted by a fellow researcher (Ören, 2007). Two groups of specimens were used in this study. The first group consists of sixteen compacted bentonite-zeolite mixtures, where bentonite fractions were set as 10, 20, and 30%. Each of the mixtures with 10% and 30% bentonite fractions had three specimens. The remaining ten specimens were compacted at a bentonite ratio of 20%. The target water contents were decided based on the compaction characteristics of the samples.

The mixtures were blended in their air-dry state and then, proper amount of water was added to the mixture with a spray bottle. Then, the wet samples were kept in a sealed plastic bag. After a curing period of one day, the mixtures were compacted at either dry or wet side of the optimum water content. Mixtures were compacted in a mold of 101.6 mm in diameter and 116.4 mm in height. Standard (D 698) and modified Proctor (D 1557) compactive efforts were applied as specified in the ASTM.

The second group of the test specimens consists of three compacted bentonite-sand specimen. The percentages of the sand and the bentonite in the mixture were 80% and 20%, respectively. Cylindrical volumetric shrinkage test specimens were prepared by compacting the bentonite and sand mixture under Standard Proctor compaction effort as specified in the ASTM (D 698).

Figure 3.1 shows the compaction characteristics of the tested specimens. Bold symbols on the curve indicates test specimen on which image analyzing was conducted. Specimens were either at the wet or dry side of the optimum moisture content at the beginning of each volumetric shrinkage test. The compacted specimens were extruded from the compaction mold using a hydraulic jack and left for air-drying.

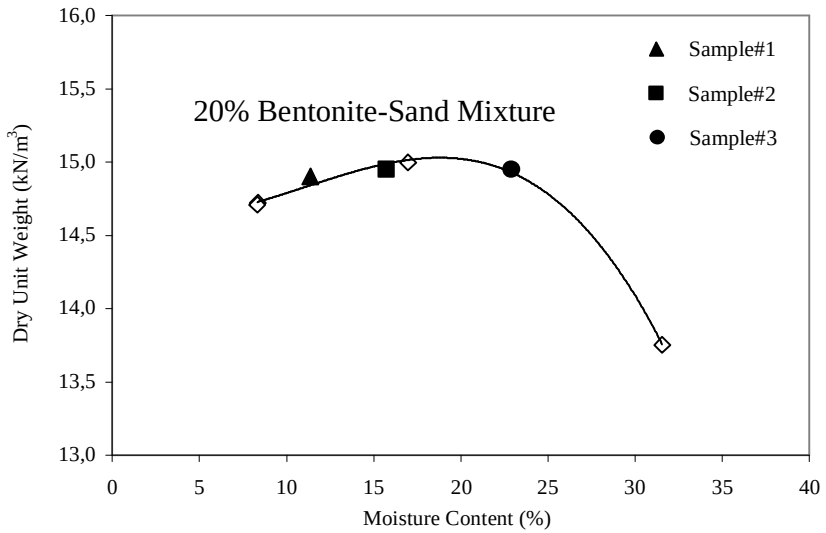

Figure 3.1 The initial moisture contents of the bentonite-sand specimens on the compaction curve.

Both manual and digital volumetric shrinkage measurements were made during the testing program. Manual measurements were performed using a Vernier caliper. The diameter and height of each specimen were measured at several locations on the specimen. The volume of the specimen was then computed with the average height and diameter values. Extreme care was spent while measuring the heights and diameters of the specimens using the Vernier caliper in order not to disturb them since even small spallings and grain decompositions could avoid comparison of the manual measurement data with those of the digital measurements.

Digital measurements, on the other hand, were performed first imaging the samples and then analyzing them using an algorithm specifically developed for this study. The volumetric shrinkage strain for both methods was calculated using the equation:

$$e_v(\%) = \frac{V_i - V_f}{V_i} \times 100 \qquad (3.1)$$

where e_v, V_i and V_f are the volumetric shrinkage strain (%), and the initial and the final volume of the specimen (cm^3), respectively. The initial volume of the specimen has been assumed to be equal to the volume of the compaction mold. Thus, only final volumes of the specimens were computed using measured dimensions of the samples.

3.3 Setup for Image Acquisition

The image acquisition setup has been established in a darkroom where digital measurements were made. The setup consisted of a pedestal, base and specimen plates, a background screen, fluorescence light sources and a digital camera as shown in Figure 3.2a.

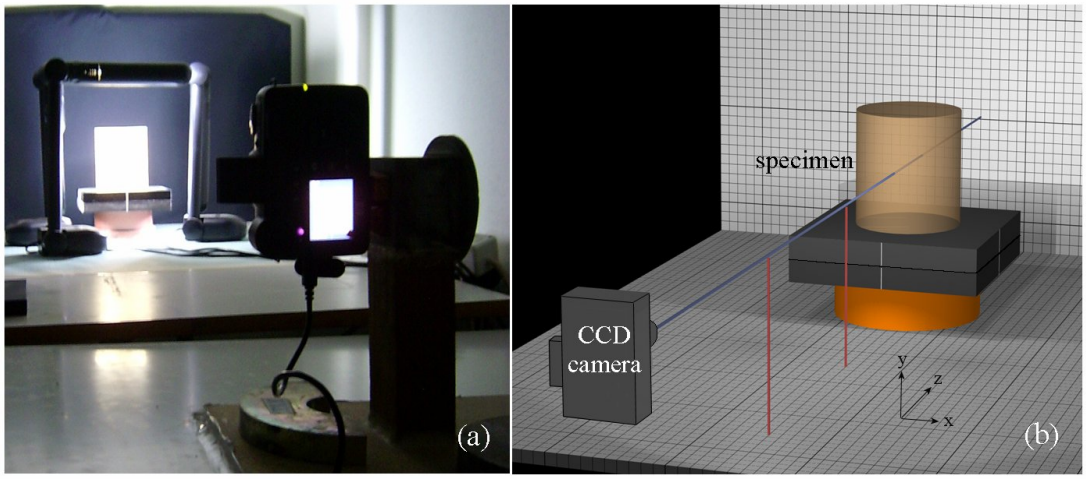

Figure 3.2 Imaging setup (a), specimen illumination during volumetric shrinkage measurements (b) alignment and positioning of the camera and the specimen.

It has been assumed during volume change calculations that the camera and the specimen were perfectly centered. Therefore, a precise alignment and a specimen positioning check mechanism were necessary. A base plate (26 cm x 26 cm) fixed to the pedestal and specimen plates of the same size were used for this purpose. The midpoints of the lateral sides of the pedestal and the specimen plates were marked with white color so that the operator could easily line up the pedestals prior to image acquisition (Figure 3.2b).

Horizontal alignment of a specimen on the plate was checked against a scaled paper placed on the background as shown in the same figure. In order to check the central position of the specimen on the plate, control images at 90˚ rotations were taken with respect to the scaled background paper (Figure 3.3).

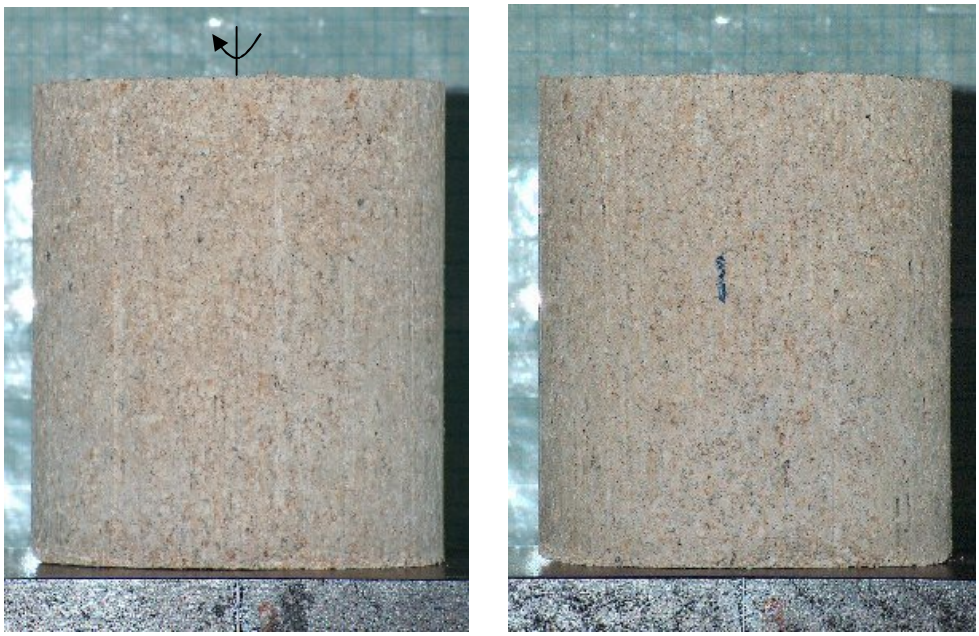

(a) (b)

Figure 3.3 Specimen positioning check before imaging: (a) before rotation, (b) after having rotated by 90°.

A digital camera with a telephoto lens providing a focal length of 37–300 mm was employed throughout the study. The position of the camera was fixed by means of rigid footing. The rotation and the height of the camera were so adjusted that (i) the specimen was centered and (ii) the background plane was perpendicular with respect to the camera. The entire alignment and central positioning process of the camera is illustrated in Figure 3.2b where two vertical lines on the figure illustrate the rods used for the exact central positioning of the camera lens. The rods were removed from the scene once the camera was fully centered.

Transformation of the pixel values of the digital images into millimeters was performed using a polycarbonate calibration object, which was manufactured to be the same size as the compaction mold. Hence, the radius and height of the calibration object were set to 50.85 mm and 116.4 mm, respectively.

A stable and constant lighting condition in the darkroom was maintained by using three fluorescence lamps. The only other light source in addition to the lamps was the internal flashlight of the camera. The light sources were positioned in such a manner

that sides of the specimens were perfectly illuminated to generate a high contrast between the specimen and the background. The black color of the background during the measurements provided additional contrast to the specimen images.

The internal flashlight of the camera was used during the tests in order to increase contrast and to make the borders of the specimen brighter in the images. Since the background was black, the compacted specimen reflected the flashlight. Thus, the contrast of the image was increased increasing the effectiveness of the segmentation algorithm, which was dependent on the difference between the intensity levels of the pixel values.

The flashlight was also used to illuminate shades among the grains, especially along the interface between the compacted specimen and the plate. Figure 3.4 illustrates the influence of the flashlight, where images of the same specimen acquired without the flashlight (left side) and with the flashlight (right side) are given.

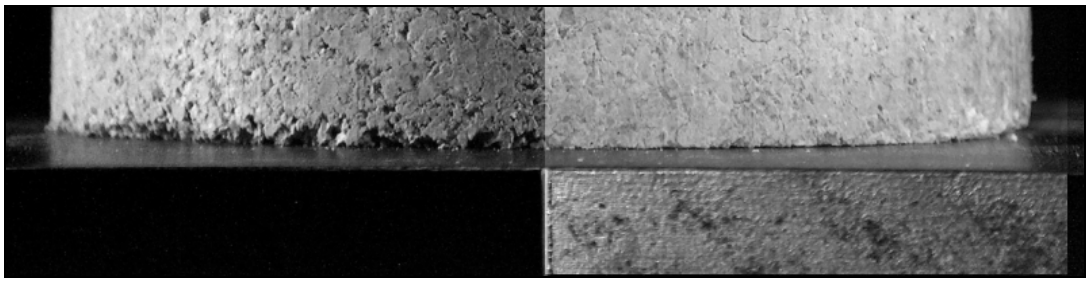

Figure 3.4 Influence of the flashlight in the compacted bentonite-zeolite specimens.

3.4 Camera Adjustments

The telecentricity of the lens was increased utilizing the maximum optical zooming capacity (i.e. a focal length of 300 mm) and increasing the distance between the camera and the compacted specimen so that perspective center lies near infinity. In this manner, the three-dimensional test scene is better pictured into a two-dimensional plane (Figure 3.5). The remaining curved border effects at the top and

the bottom of the specimen images were then filtered out numerically, as defined in the following sub sections.

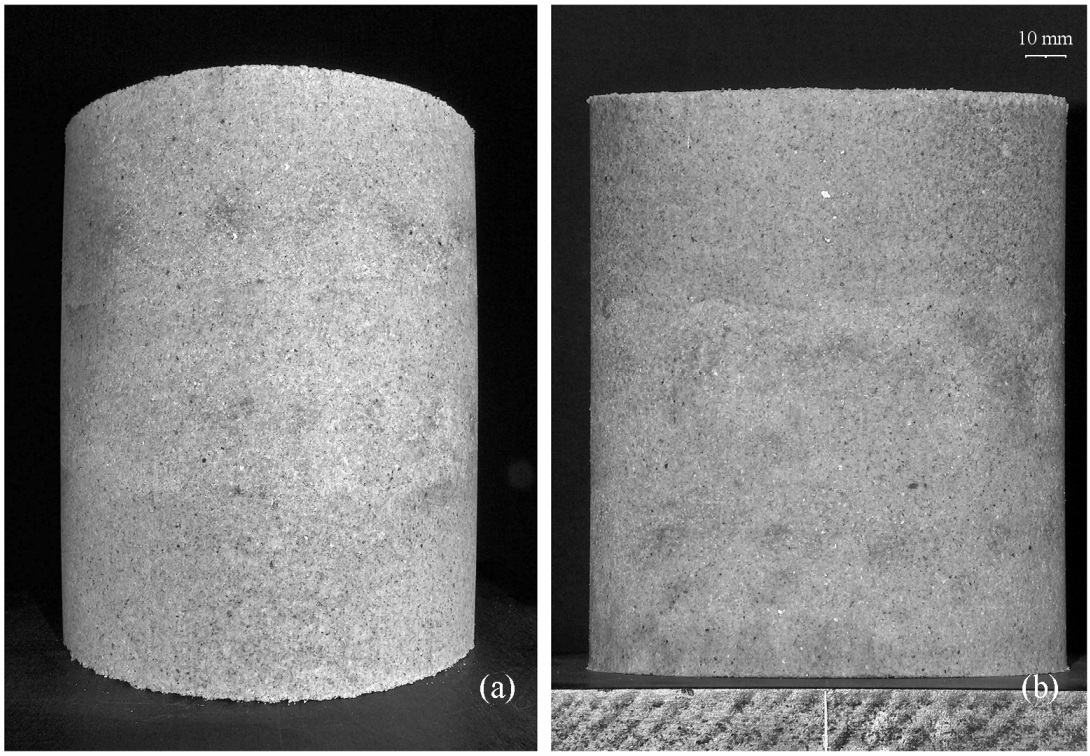

Figure 3.5 (a) imaging with 37 mm focal length, (b) picturing with increased telecentricity.

All images were taken under both fluorescence illumination and camera flashlight. The aperture-shutter speed combination of f.8–1/250 has been the optimal choice for the depth of field and contrast of the image. The camera was manually focused into the central location of the specimen in each image.

Due to the long duration of the test, shutting down and reactivation of the camera was unavoidable. It should be noted that small internal changes in the lens mechanisms of the camera might produce imaging errors, which may be considered as negligible for ordinary imaging purposes, but which should be avoided in precise test measurements.

In order to compensate for imaging errors and misalignments of the specimen with respect to the pedestal, an averaging procedure was followed during each

volumetric strain measurement. Once the specimen was aligned on the pedestal, it was rotated at 90˚ rotations. A total of four images were taken during this process providing one image for each rotation. The camera was shut down and reactivated at least twice for each shrinkage measurement taking eight images minimum in the manner described above.

3.5 Image Processing and Analysis

The Matlab technical computing language and its toolbox functions were used in the computer code that was specifically developed for the image processing and analysis purposes. Other calculation steps, including specimen border detection, polynomial fitting with a least-squares method and geometrical calculations, were also programmed using Matlab's library functions for a rapid and robust evaluation of the test results.

3.5.1 Image Processing

Captured images in true color format were transformed into grayscale images by eliminating the hue and saturation information while retaining the luminance. This resulted in a 2608×1952 intensity image where element values vary between 0 and 255.

In order to increase the dynamic range of the gray levels in the image prior to the segmentation process, a piecewise linear transformation function called contrast stretching was applied to generate a highlighted image of the specimen. Since the specimen and the background pixel values were grouped in two dominant modes, the specimen was extracted from the background by defining appropriate threshold levels. The gray level histogram shown in Figure 3.6a belongs to a contrast stretched image.

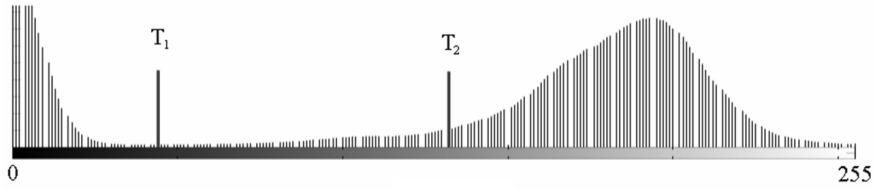

(a)

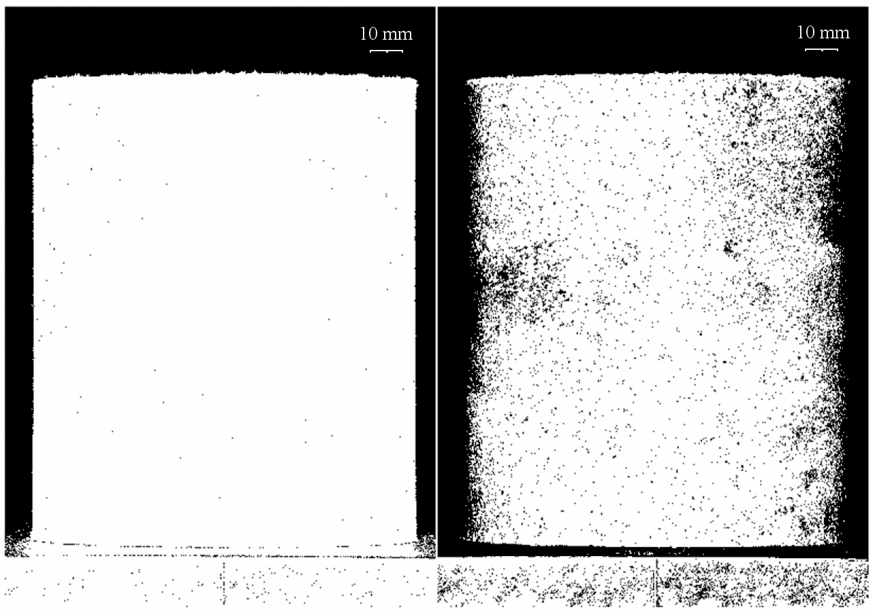

(a) (b)

Figure 3.6 (a) The histogram, (b) - (c) binary images of the specimen thresholded with respect to T_1 and T_2, respectively.

In this procedure, two differing threshold values were used. Pixel values below and above the threshold level are converted to black and white, respectively. The first threshold value, T_1, has been established in an automated manner according to Otsu (1979), where a threshold value to minimize the intraclass variance of the black and white pixels is chosen. The first threshold value (T_1) was applied for the segmentation of the left, right and the top borders of the specimen (Figure 3.6b). Although the plate carrying the specimen was painted matte black, the blazes of the light sources were still able to prevent the use of a single threshold value for the detection of the boundaries of the specimen. Therefore, the use of a second threshold value, T_2, was necessary. Please note that the second threshold value, T_2, was set higher than the T_1 in order to segment the contact line (i.e. bottom border) between the specimen and the plate (Figure 3.6c). This was achieved by adding a constant

value to T_1 so that the zigzagging shape of the bottom border of the specimen is best captured.

The black spots remaining on the binary images (Figures 3.6b and 3.6c) of the specimen were filtered out so that the consequent border detection operation could be made properly. This process resulted in the generation of the images in Figures 3.7a and 3.7b, which were used in the border detection stage. It should be noted that the image processing algorithm was established in such a manner that the border decision was made when the transition from the white pixel to the black pixel first took place while counting the image pixels along the specimen border within a loop in the computer algorithm.

3.5.2 Calculation of the Specimen Dimensions

There were at least eight images for volume calculations in a test session due to the imaging technique, as described above. The average volume of the specimen is obtained by taking the mean value. The radii of the specimens were calculated based on Equation (3.2); whereas, their heights were computed using coordinate data of the specimen borders.

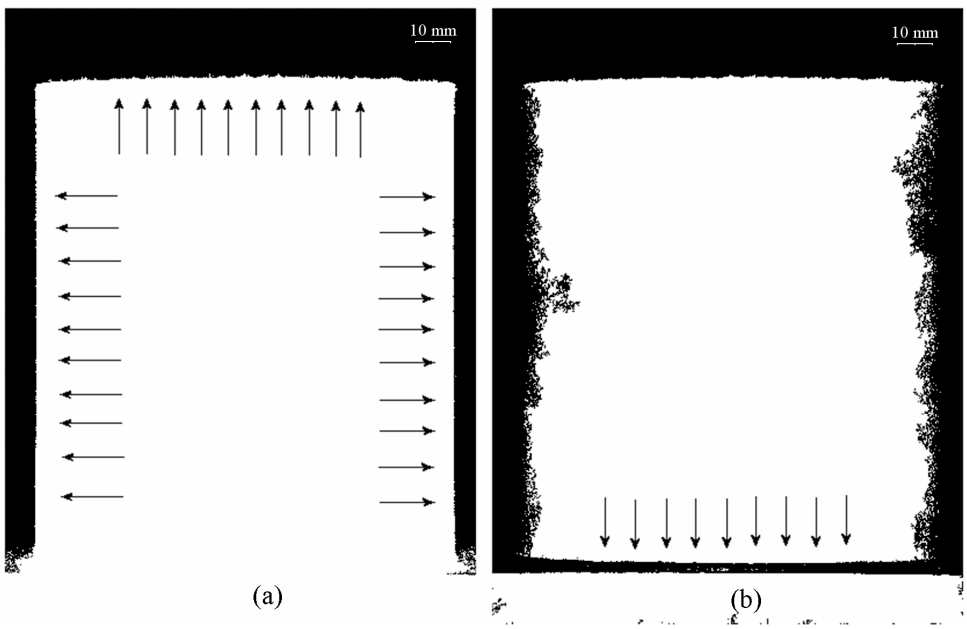

Figure 3.7 Detection of specimen borders: (a) left, right and top borders, (b) bottom border.

The calculation of the average diameter and height of a specimen undergoing volumetric shrinkage can be made by the application of the calibration constant as obtained from the calibration object. The plan geometry of the test setup is shown in Figure 3.8. The geometric parameters of a, α, b, r and x are constant when the calibration object is pictured prior to the volumetric shrinkage tests.

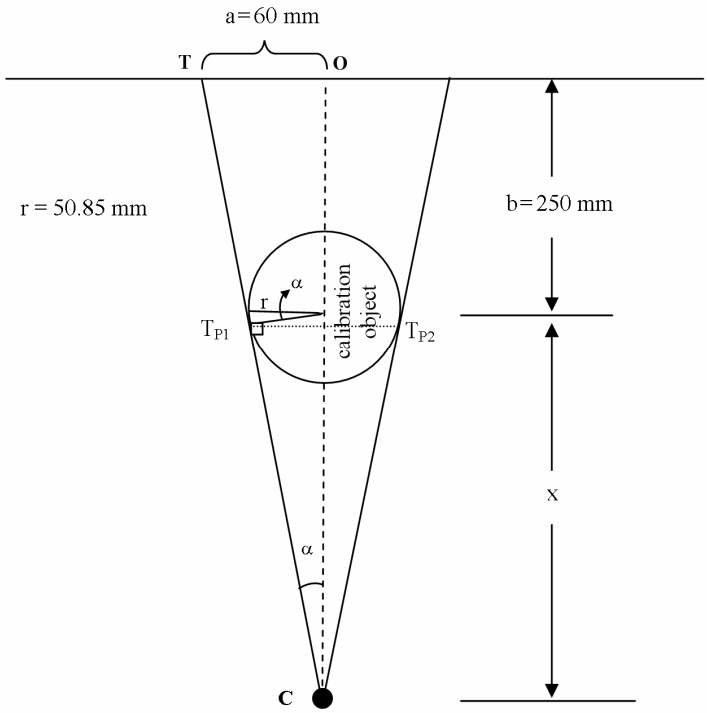

Figure 3.8 Geometry for the calculation of the average diameter.

It can be seen in Figure 3.8 that the camera actually snaps the light rays that are tangent to the specimen borders. Therefore, the line $\overline{T_{P1}T_{P2}}$ can be measured during the test and a geometrical conversion process is necessary in order to come up with the average diameter of the specimen. For this purpose, the left and right vertical border coordinates obtained along the specimen length during the counting process were averaged first, and the length of the line $\overline{T_{P1}T_{P2}}$ is found by taking the difference. The diameter of the test specimen is then calculated from the geometry as in the following:

$$D = \frac{\overline{T_{P1}T_{P2}}}{\cos a} \tag{3.2}$$

In the above calculation, the angle, α, between the central and the tangent lines (i.e. $\overline{CO}$ and $\overline{CT}$) is the key parameter and one may assume it as a constant for the test specimens since the variation of this parameter is quite small throughout the shrinkage tests. Derivation of the equation for the calculation of α of the calibration object is given in Equations 3.3 to 3.6. Once this parameter is computed, it is kept constant in the computer algorithm. The resulting error for the specimen volumes is less than 0.005% when the maximum decrease in specimen diameters is in the order of 2 mm. The maximum measured diameter decrease was 1.2 mm for the test specimens during this study.

The distance between the center of the calibration object and the camera can be calculated using the angle (α) between the line passing through the centerline of the test setup and the line that is tangent to the calibration object side surface:

$$\sin a = \frac{r}{x} \rightarrow x = \frac{r}{\sin a} \tag{3.3}$$

Another equation may be written in order to define x in terms of α:

$$\frac{\frac{a}{r}}{\cos a} = \frac{b+x}{x} \tag{3.4}$$

Equations 3.2 and 3.3 are combined to obtain Equation 3.5 and then Equation 3.6 as in the following:

$$\frac{a \cdot \cos a}{r} = \frac{b + \frac{r}{\sin a}}{\frac{r}{\sin a}} \tag{3.5}$$

$$a = \sin^{-1}\left(\frac{-rb + a\sqrt{a^2 + b^2 - r^2}}{a^2 + b^2}\right) \tag{3.6}$$

where, D is the diameter of the specimen, $\overline{T_{P1}T_{P2}}$ is the distance between tangent points T_{P1} and T_{P2}, and α is as defined above.

Height calculations of the specimens are made using the pixel points lying on the nearest line to the camera along the specimen surface (Figure 3.9). This line ($\overline{H_1H_2}$) may also be defined as the intersection of the central triangular plane ABC and the specimen front surface. The top and bottom pixel points for height calculation on this line are obtained following a series of averaging operations performed along the borders of the image. The sand particles detected on the specimen surface after image acquisition resulted in zigzagging border shapes both at the top and the bottom (Figure 3.10), and imperfect telecentricity generated a curved shape in the same borders of the specimens (Figure 3.11). The averaging procedure, which was basically a least-squares curve fitting smoothing operation, took care of imperfect telecentricity and shape irregularity effects along the borders of the specimen.

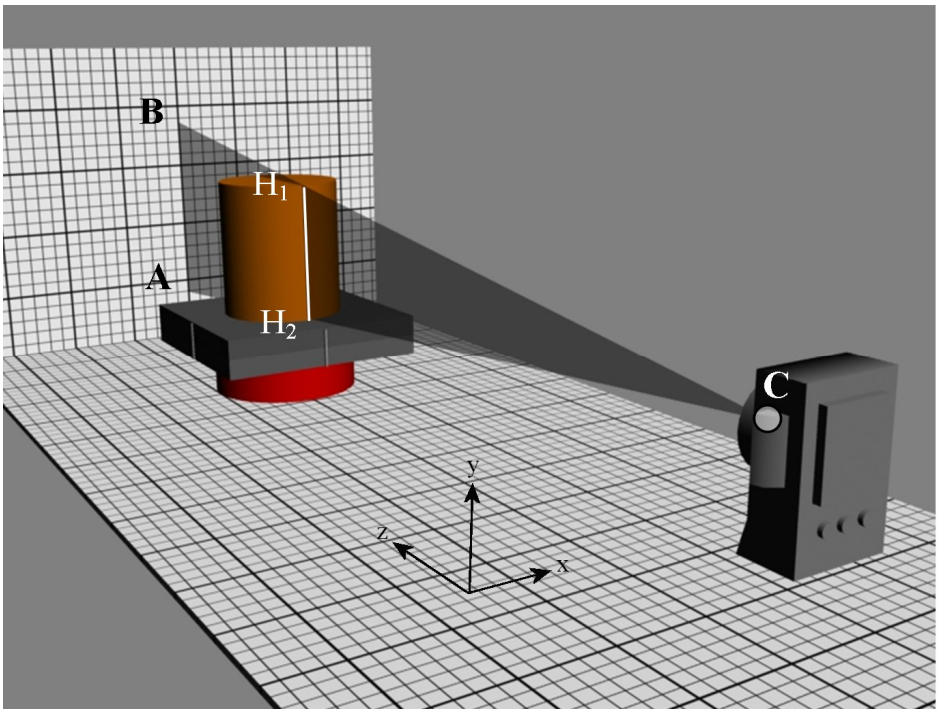

Figure 3.9 Illustration of height detection.

The coordinates of the pixel points on the original shapes of the borders are used as sample points for the least-squares curve fitting application to come up with the second-order polynomials. These polynomials can be regarded as smoothing filters and approximations to the original shape of the borders of compacted specimens.

The intersection points of these polynomials with the line $\overline{H_1H_2}$ yielded the top and the bottom points for height calculation (Figure 3.10a and Figure 3.10b). It should be noted at this point that the generation of the bottom second-order polynomial has been made after avoiding the shadowing effects (see Figure 3.10b), that took place at the contact points of the specimen to the bottom plate since such points may not be illuminated perfectly during image acquisition. Higher illumination levels were not applicable during the test since the interface between the specimen and the specimen plate could not be segmented under bright light.

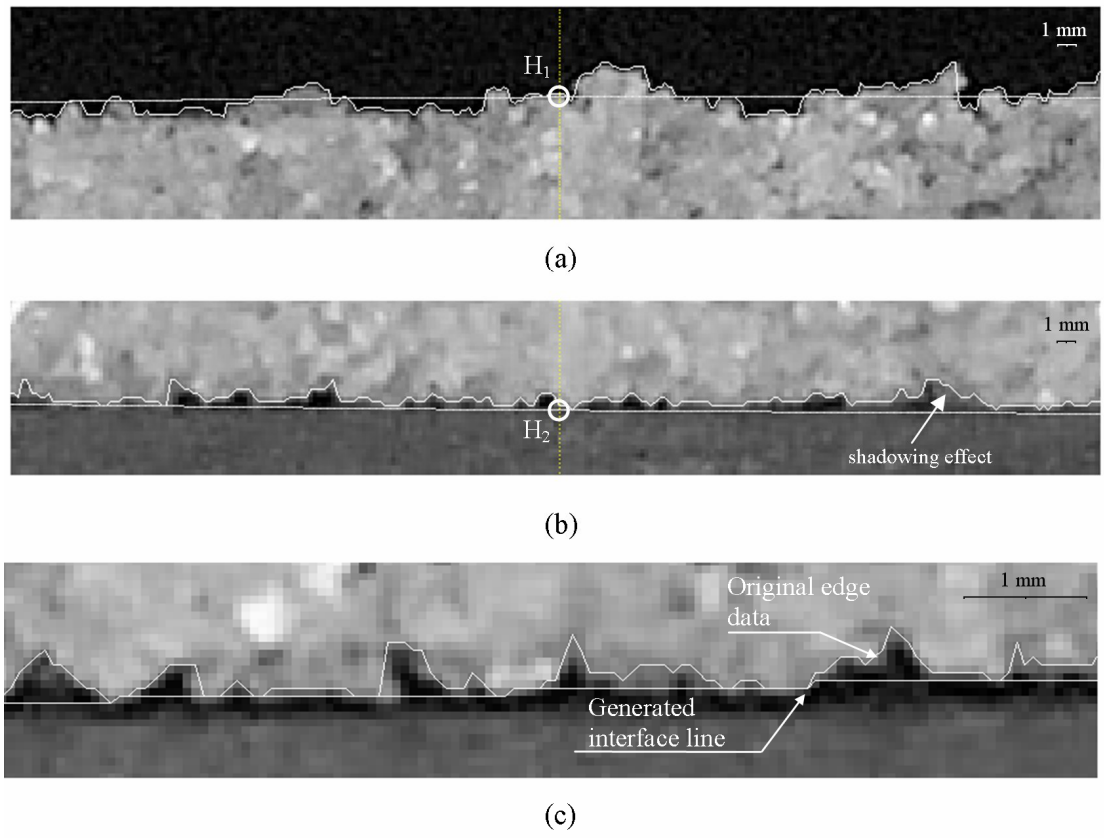

Figure 3.10 (a) the top and (b) the bottom borders, (c) data filtering at the bottom border.

The space left over any two points that is in contact with the specimen plate was considered noisy data due to the shadowing effect. The data pairs are compared with each other as the counting process proceeds towards the centerline from left and right side borders in the algorithm. The contact point with the specimen plates is determined when the coordinate of the forthcoming data is higher than the previous one. In this manner the shadows between the specimen plate and the original edge data are not taken into consideration. As a result of this operation a new data set for edge detection is generated and the interface line between the bottom plate and the specimen is obtained (Figure 3.10c). This generated interface was used as source data in the second order curve fitting algorithm to estimate the bottom border of the specimen. The result of this border detection procedure is shown on the original image of a specimen in Figure 3.11.

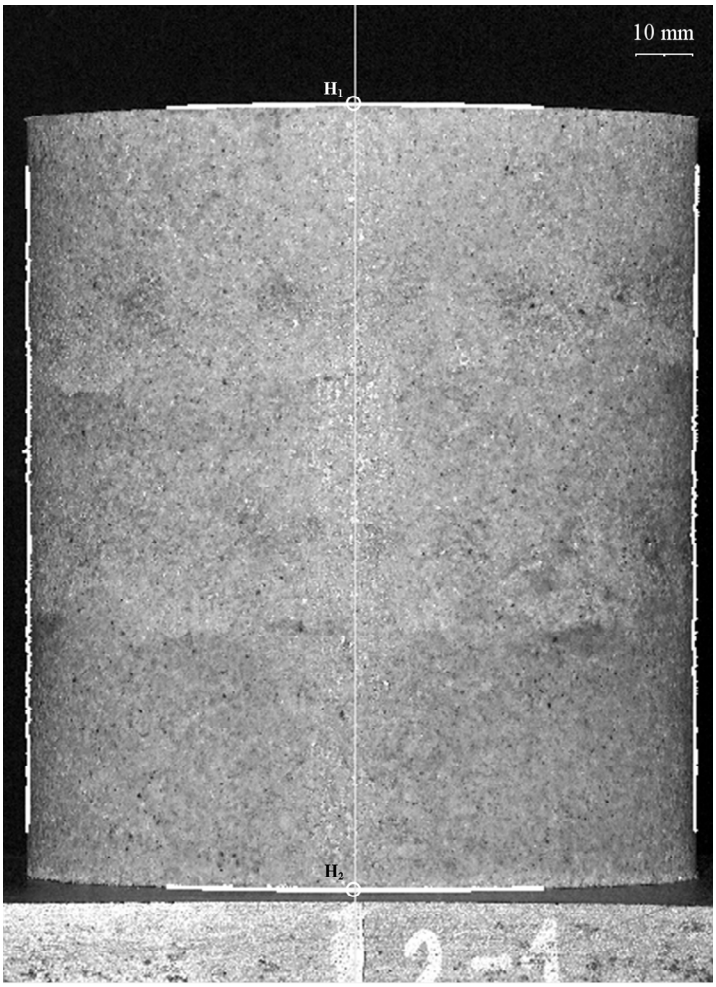

Figure 3.11 Illustration of detected borders of a compacted bentonite-sand specimen.

3.6 Results

The measurement results obtained either by manual or digital measurements for compacted bentonite and zeolite mixtures are given in Figure 3.12. As can be noticed in Figure 3.12, there is a good match between the two measurement techniques for the final volumetric shrinkage strains. It should be noticed that data of each measurement are within the error margin illustrating negligible influence of the error sources defined previously.

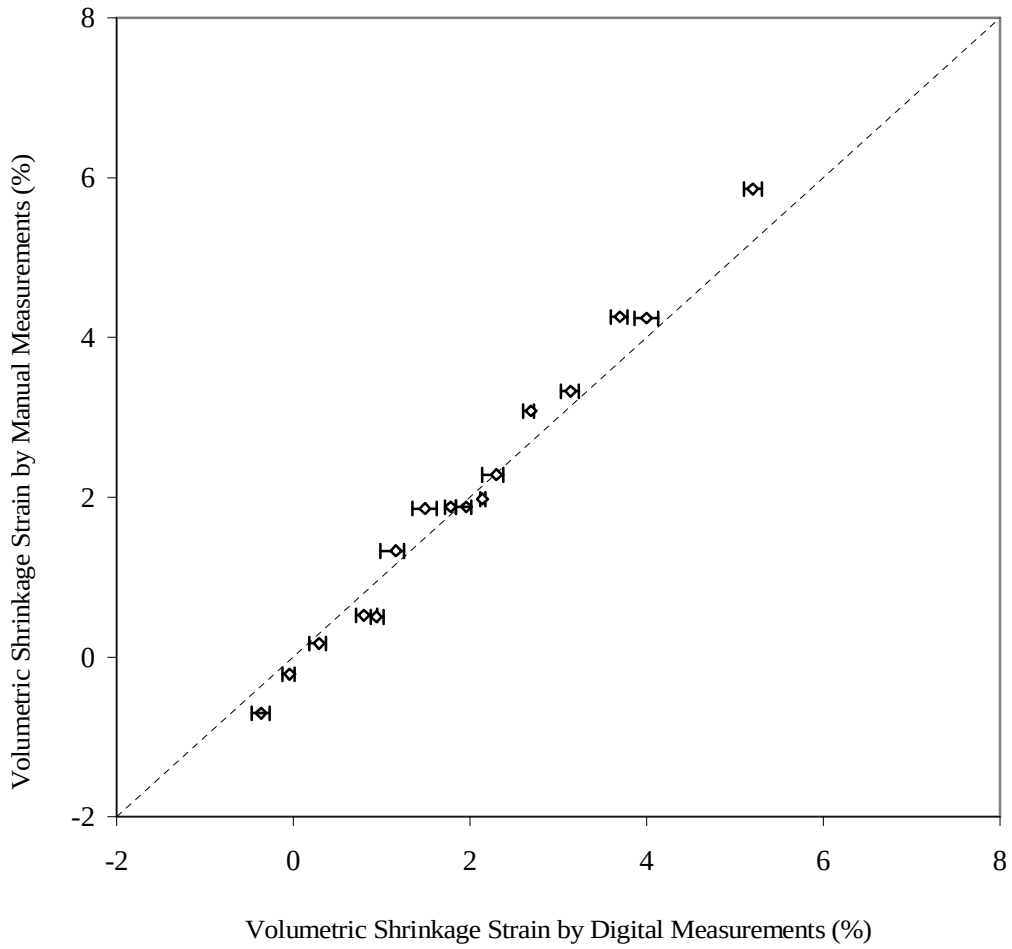

Figure 3.12 Comparison of the results obtained by the two different measuring techniques.

When the specimen is extruded from the mold, it tends to swell. Measurement results showed that negative volumetric strains are sometimes unavoidable indicating that the shrinkage strain of the specimen remained less than the swelling strain taking

place following the extrusion of the specimen from the compaction mold. This type of soil behavior may take place even if the water content of the specimen is low.

The volumetric shrinkage strain values of the digital measurements were slightly higher than those of the manual measurements beyond 3% strain level. Puppala et al. (2004) also reached a similar conclusion although they were focused on larger strain values (i.e. up to 40%). In their study, they stated that digital measurement data exhibited 0.3% to 4.5% higher volumetric shrinkage strains than those of the Vernier caliper measurements.

The volumetric shrinkage behavior of compacted bentonite-sand mixtures with respect to the moisture content variation is given in Figure 3.13. The empty and solid symbols in Figure 3.13 denote the data corresponding to digital and manual measurements, respectively. The negative values at the initial stage of the shrinkage measurements were due to the swelling of the specimens taking place immediately after the extrusion of specimens from the compaction mold. The digital volume measurements were repeated two to four times during any measurement session. The bars in the figure show error ranges of volumetric shrinkage strains for respective moisture contents in digital measurements.

The gradual increase in the volumetric shrinkage strain ceased at a critical moisture content and no volume change has been observed thereafter, although the moisture content was decreasing. Such behavior was similar to those reported by Tay et al. (2001), who mentioned that the volumetric shrinkage of bentonite-sand mixtures ended at a critical moisture content. Figure 3.13 also indicates that the higher the initial moisture content, the higher the volume changes of the specimens. The results of digital and manual volume measurements did not deviate from each other significantly, as one also can notice in Figure 3.13.

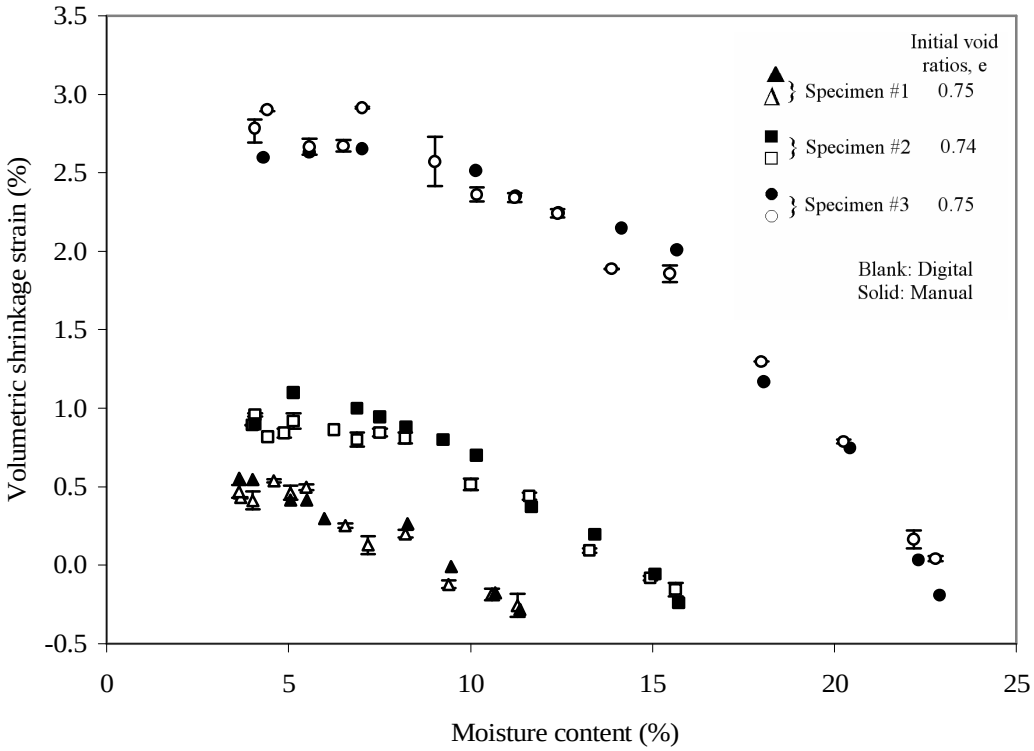

Figure 3.13 Volume change behavior of compacted bentonite-sand specimens and comparison of digital and manual measurement methods.

The digital and manual measurement methods for compacted bentonite-sand mixtures can further be compared in Figure 3.14. The data in this figure correspond to moisture contents where both methods were applied. The figure indicates that there is a good match between the strains obtained through both methods.

In this study, differences between the two measurement techniques can be attributed to the difficulties in measuring the sidewalls of the specimens using the Vernier caliper especially if the specimen sides are not straight. This was more pronounced for cases where higher volumetric shrinkage strains took place. It is believed that the compacted specimen may not be able to shrink in a well-defined shape for such cases. However, the digital measurement technique can take this effect into the consideration during the test since continuous readings along the sidewall can be taken. Therefore, the volumetric shrinkage strain values obtained by

means of digital measurements should be more realistic than those by manual measurements.

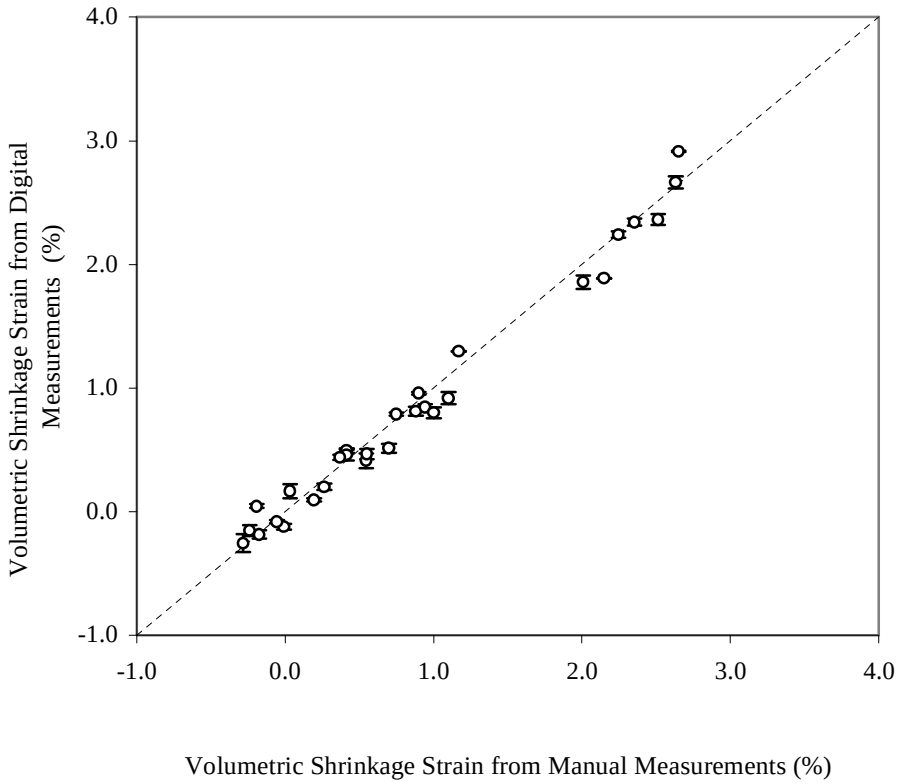

Figure 3.14 Comparison of the manual and digital measurements.

Despite the fact that the digital and manual methods yield close measurement data, utilization of a Vernier caliper in manual measurements may not correctly estimate the real specimen size if irregularities exist on the specimen surface. The potential of irregular shape occurrence or non-uniform shrinkage may arise when the specimen shrinks more than 3% (Ören et al., 2006). The computer algorithm developed in this study, on the other hand, prevents such effects by means of the averaging procedure for specimen borders. Any segmentation errors due to the utilization of the T_2 threshold value are also highly eliminated during the averaging process. Therefore, digital measurements are considered to provide more realistic results.

3.7 Conclusions

The principal purpose of this chapter was that the volumetric shrinkage strain of compacted soil mixtures could be obtained even in the small strain ranges (i.e. 0~5%) by means of the digital image processing technique. The applicability of this technique was tested against manual measurements of compacted bentonite-zeolite and compacted bentonite-sand specimens. It was found that digital and manual measurement data were generally in good agreement within the volumetric shrinkage strain range of interest. The offsets between the results of two techniques increased as the volumetric shrinkage strain get close to 5%. One should note that the manual measurement technique of the Vernier caliper method is not a perfect nondestructive testing since the specimens may be easily disturbed especially along their edges. This type of disturbance effect becomes important if quite low strain values are of interest. The digital measurement technique is especially promising in this respect since it offers steady, repeatable and continuous data. The proposed methodology as defined here is applicable to the volume measurement of any cylindrical objects. It requires utilization of only single camera and is more economic and simpler than other methods, which need multiple cameras. Although the methodology proved to be practical and providing repeatable measurements, it is still somehow operator dependent, which can be easily improved by means of an automatic rotational movement or multiple uses of cameras.

CHAPTER FOUR
QUANTIFICATION OF GRAINS AND VOIDS IN COHESIVE MATRIX

4.1 Introduction

It has been well known that shape, texture and distribution of grains have an influence on the behavior of geomaterials. Literature is rich in research papers regarding influence of these parameters on cohesionless soils. The ratio of voids and their distribution in soils and rocks also affect their behavior in terms of strength and pore fluid flow characteristics. Quantification of both grain and void properties using computational techniques, however, has become only possible in recent years. This was mainly due to the lack of advanced tools for the study of micro fabric of the geomaterials. The imaging techniques was quite costly and computational power simply did not exist for the analyses of digital images of various soil types and rocks.

Research studies regarding determination of grain characteristics such as size, shape, orientation and spatial distribution either in sliced sections of cohesive materials or discrete aggregate samples using digital image analysis methods accelerated since 1980s (Michelland et al., 1989; Yudhbir & Abedinzadeh, 1991; Raschke & Hryciw, 1997; Mora et al., 1998; Kwan et al., 1999). Some pioneering work, however, could be traced back to late 1960s (Saltykov, 1967).

The majority of the above mentioned studies employed grayscale segmentation methods in the analysis of grain characteristics. In order to determine particle properties properly, some researchers have also used watershed segmentation to isolate touching grains (Ghalib & Hryciw, 1999; Kim et al., 2003). One alternative method called as the digital cutting method, which is based on the threshold angle of contact wedge between grains has been proposed by Van den Berg et al. (2002). Digital image analysis data have been employed in the generation of finite element meshes (Yue et al., 2003).

Research studies on void characteristics, however, have been comparatively limited. Void distribution characteristics of soils, bituminous, concrete and rock materials were studied using digital image analysis methods in the past. Crabtree et al. (1984) have successfully segmented the voids in thin sections of blue dyed epoxy impregnated rock material using color segmentation technique. Masad et al. (1999) have studied the structural characterization of asphalt concrete using both X-ray computed tomography and conventional investigation of sliced sections via digital image processing methods. The segmentation of voids has been achieved by grayscale segmentation technique, where a white mortar has been used to provide enough contrast while identifying air voids. Frost & Kuo (1996) have automated the Oda's methodology (1972) to determine the local void ratio of granular material in 2D sections using high level image processing techniques. Similarly, Bhatia & Soliman (1990) have determined the frequency distribution of void ratio for three granular materials having different grain characteristics using image analyzer. Obaidat et al. (1998) used spatial filters and image processing operations of a semi automated computer-vision system to quantify the percentage of voids in mineral aggregates of bituminous mixtures. Soroushian et al. (2003) have developed specimen preparation and image processing techniques focusing on concrete micro cracks and voids for use in automated quantitative micro structural investigation of concrete. He utilized epoxy impregnation so that the grayscale segmentation of the pores and cracks could be made in the scanning electron microscopy images.

The above mentioned studies, however, do not cover the shape characteristics of the voids. Zhang et al. (2005) have investigated the roundness ratio parameters, a basic shape parameter of the air void detected using grayscale segmentation technique. The same shape parameter for voids has been employed for foam concrete by Nambiar and Ramamurthy (2006).

This chapter targets development of image analysis algorithms for the quantification of both grain and void distributions in artificially prepared and segregated samples of granular assemblies in cohesive matrix. It was aimed that

developed algorithms would provide better characterization of grains and voids using digital image analysis techniques.

The computer algorithms as presented here are fast enough and robust avoiding operator dependent errors in the stage of threshold determinations. This aspect of the study is especially reflected in the color segmentation, of which use has been found very beneficial while separating voids from the rest of the image. Trials for segmenting the voids in grayscale segmentation were not proved to be efficient since either void shapes could not be captured satisfactorily or the voids and small objects in the cohesive matrix were not detected during determination of the threshold levels. The color segmentation algorithm as employed in the code avoids such error sources.

Digital image processing algorithms for the analysis and characterization of grains and voids in cohesive matrix were developed using MatLab technical computing language. Utilization of grayscale, color and watershed segmentation algorithms and their performances were demonstrated on artificially prepared self-compacting concrete (SCC) samples. It was considered that SCC samples would be representative for weak rocks and stiff clays with coarser grains. It has been found that color segmentation was more advantageous over the grayscale segmentation for the detection of voids whereas the latter method provided satisfying results for the aggregate grains due to the sharp contrast between their colors and the cohesive matrix. The watershed segmentation method, on the other hand, appeared to be very efficient while separating touching objects in digital images.

For the analysis of complicated void shapes, encountered in the investigated samples, a modified digital signature technique has been developed and coded. The available digital signature method in the literature was found to be inefficient especially for the analyses of complicated void shapes. The digital signature technique as applied in this study is similar to the form index parameter proposed by Masad et al. (2001). However, it has been modified in order to adapt it to the analyses of highly irregular void shapes. The developed digital signature algorithm enabled definition of new shape parameters that were proved to be useful in

characterization of individual voids.

In order to characterize the void shapes in the investigated sample images, two new shape parameters called as coefficients of inclusion and exclusion have been proposed. When compared with the traditional use of the digital signature method, it was found that the methodology followed herein would better characterize complicated void shapes. The developed methodology may also be applied to the analysis of complicated void shapes that are often found in other cementitious materials such as clays and rocks.

The techniques originally developed for the characterization of the void shapes have been applied to the grain shapes in order to quantify the degree of angularity and roughness characteristics.

4.2 Materials and Methods

Experimental work involved casting of artificial test specimens and establishment of the image acquisition system. In order to observe applicability of segmentation algorithms, two specimens were cast using basalt coarse aggregate, river sand and ordinary Portland cement and sliced horizontally into 12 pieces. One of these specimens served as the control sample where proportioning of the mixture has been made in such a manner that minimum segregation is allowed to take place along the specimen length. The other specimen, on the other hand, has been artificially segregated arranging mixture properties. The image acquisition system has been set using a digital camera and a stand, which was used to adjust height of the camera. Details of test specimens and the image acquisition system are given in the following.

4.2.1 Sample Preparation

Two cylindrical specimens, 10 cm in diameter and 60 cm in height, were cast using ordinary Portland cement serving as the cementitious material. Characteristics

of the self-compacting mix proportions for the two specimens are given in Table 4.1. One should note that proportioning of self-compacting mixtures was the same except the admixture of which proportion has been set as 3.3% and 10% of the cement weight in order to produce a non-segregating and an artificially segregated mixture, respectively.

In order to test the grayscale segmentation algorithm, basalt has been selected as the coarse aggregate material due to its dark color so that a sharp contrast between the cohesive matrix and aggregate grains is ensured and a suitable environment for the preferred classification method of single-value thresholding technique for grain detection is formed.

Table 4.1 SCC mix proportions.

Material	Proportion	
	by weight per cubic meter, kg	by volume per cubic meter, l
cement	360	114
water	180	180
inert filler (limestone)	190	74
fly ash	140	62
sand	740	285
coarse aggregate	720	267
air content	-	10
admixture	12 - 36	10.9 - 32.7

Samples were cured in lime-saturated water for 90 days. Following the curing period, samples were horizontally sliced into 12 pieces using a pit saw. In order to highlight voids on slice surfaces, sections have been plastered using jointing mortar and than sandpapered until the section surface reappeared. In this manner, voids have been filled with yellow mortar, which can be detected by means of color segmentation techniques. Finally, sections have been polished to differentiate the coarse aggregate from the cohesive matrix (Figure 4.1).

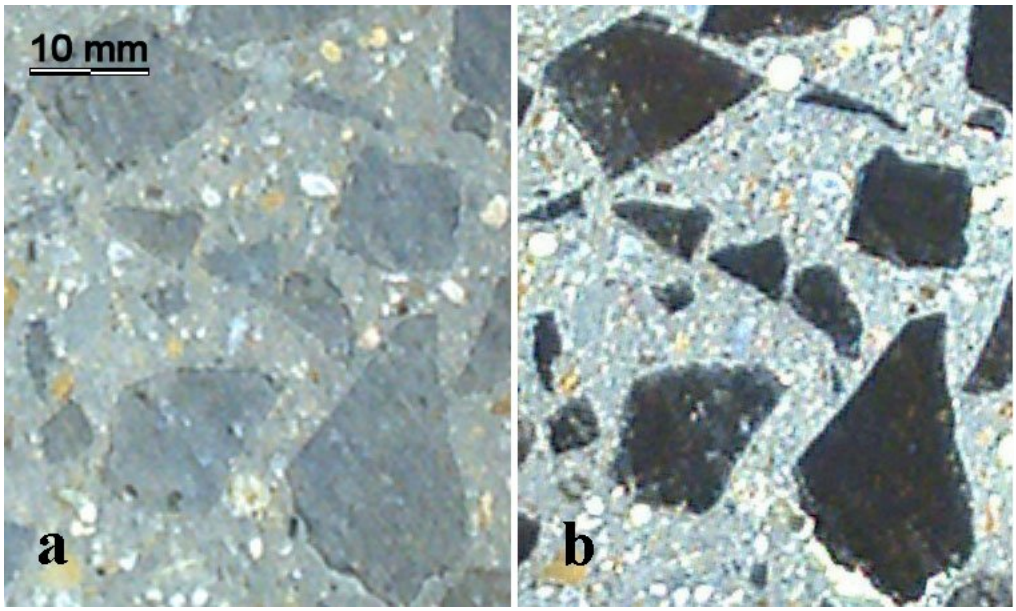

Figure 4.1 Surface preparations of sliced sections prior to image capturing (a) unpolished (b) sand papered and polished.

4.2.2 Image Acquisition System

Since the success of digital image processing operations greatly depends on the quality of the captured images and the illumination conditions, a visual inspection unit housing a high precision digital camera (Canon EOS 350D), EF-S 18-55 mm Lens and three florescence light sources has been build for the acquisition of the specimen images as shown in Figure 4.2. The detailed explanation of the acquisition system can be found in Chapter 5.

The visual inspection unit ensured constant illumination for the image acquisition. Moreover, shutter speed and aperture combination of the camera was kept the same for each captured image. Therefore, contrast, brightness and saturation parameters of the captured images varied in a narrow band, which enhanced the results of the segmentation techniques.

Figure 4.2 Visual inspection unit.

4.3 Image Acquisition

The image acquisition was performed by remote shooting capability of the camera's software. The camera was controlled by the computer via USB cable connection so that a fully insulated area from the ambiance illumination was obtained during image capturing. Since both the grayscale and color segmentation techniques were employed during image processing of an input image in the study, the aperture and shutter speed combination of the camera were set as f5.6 - 1/13 second in order to obtain the best possible contrast and color saturation balance. The images were captured with a resolution of 3456×2304 pixels creating a field view of 182×122 mm and were directly transferred to the computer.

4.4 Image Processing

Image processing involved grayscale, color and watershed segmentation. The grayscale segmentation was employed in the determination of segregation of grains in the soft cohesive matrix of artificial segregated SCC sample whereas the color based segmentation was utilized for the detection of voids within the specimens. The watershed segmentation was used in order to isolate touching grains prior to the determination of their spatial distribution. The MatLab technical computing language was used in image processing operations.

4.4.1 Grayscale Segmentation

Captured images in RGB colors have been processed as multidimensional arrays. A transformation into grayscale images has been made eliminating the hue and saturation information while retaining the luminance, reducing the image into an 8-bit intensity one (Figure 4.3a) with element values ranging 0 to 255. Particle analysis requires conversion of the captured image into a binary image following a contrast stretching transformation step (Figure 4.3b), which is necessary to make grain shapes more visible. The transformation process consists of a piecewise linear function, which increases the dynamic range of the gray levels.

The image is then thresholded in order to filter out the cohesive matrix from the rest of the picture obeying the methodology suggested by Otsu (1979). This method works on the gray levels of the image (Figure 4.3b) by minimizing the intra-class variance of the black and white pixels. Resulting binary image of this step is given in Figure 4.3c.

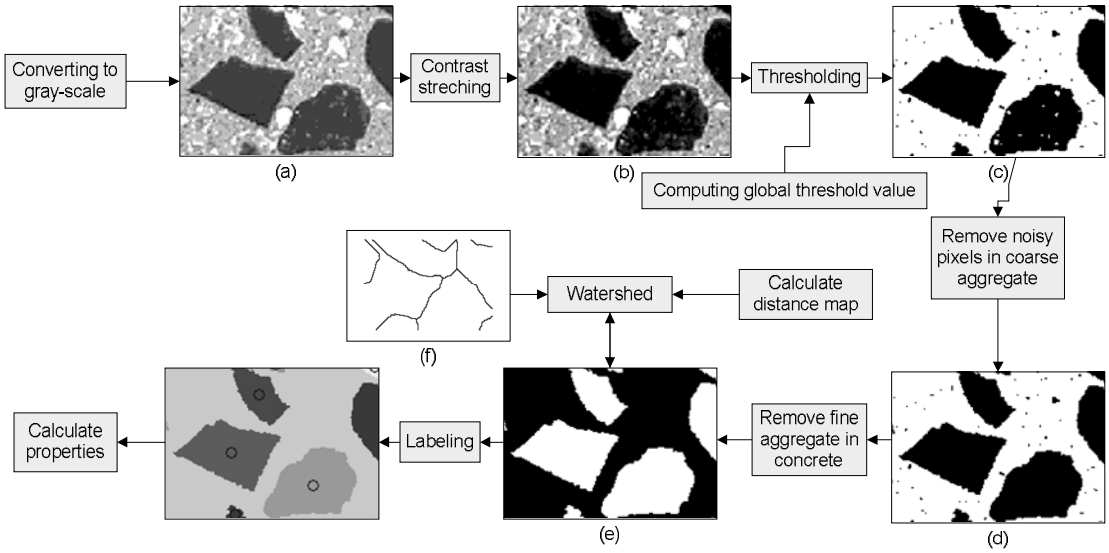

Figure 4.3 Image processing flow chart of coarse grain detection by grayscale segmentation.

The white spots, appearing within the coarse grains probably result from non-uniform illumination or noise of various sources (environmental, transmission, etc). They were eliminated using a morphological operation as shown in Figure 4.3d. This was made by first finding the pixels that were not connected to its neighbors according to the eight adjacency pixel relationship (Gonzalez & Woods, 2002) and then removing them from the image. This process eliminated noisy pixels enclosed in the coarse grains.

The same technique was used for the elimination of finer aggregates in the cohesive matrix using the negative of the image as shown in Figures 4.3e. The touching grains in the final processed image were separated using the watershed segmentation as explained later in the text.

4.4.2 Color Segmentation

Color segmentation has been performed using L*a*b* color space (a coordinate system and a subspace within that system where each color is represented by a single point) for the determination of voids in 2D sections. The L*a*b* color space model (Robertson, 1997) has been introduced as a device independent color model enabling quantification of visual differences in any digitized image since influence of

illumination conditions could be easily normalized in this space by tracing any deviations in lighting conditions in L* layer. The L*a*b color space consists of the luminosity 'L*' or brightness layer, the chromaticity layer 'a*' indicating the location of the color along the red-green axis, and the chromaticity layer 'b*' indicating the location where the color falls along the blue-yellow axis (Figure 4.4). During color segmentation, therefore, captured images were transformed into L*a*b* space firstly.

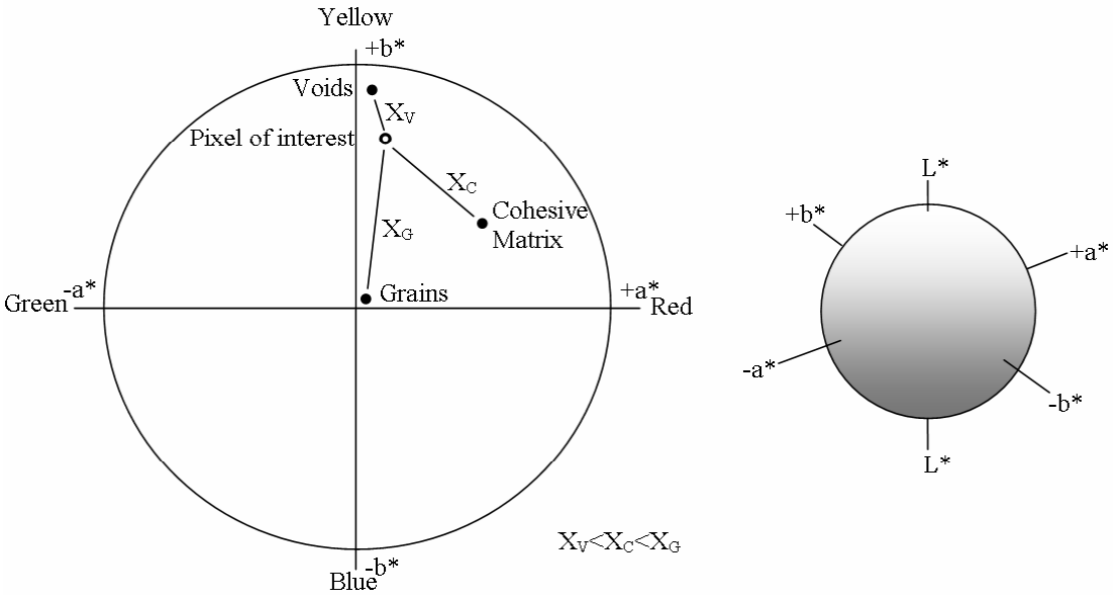

Figure 4.4 The L*a*b* color space model in color segmentation.

It has been necessary to define only specific colors in the original image so that color segmentation could be performed satisfactorily without increasing computational effort and complexity of the algorithm. Four specific colors were selected in the slices of the specimens for this purpose. The selection has been made visually depending on the appearance of the original image. Two tones of yellow colors were selected for the voids, in order to avoid erroneous segmentation, since color transition from the voids to the cohesive matrix in captured images takes place gradually. The grain objects and the cohesive matrix, on the other hand, were related to the black and gray color, respectively. The average a*b* values for each color were calculated in the L*a*b* color space for each selected color. Color

classification is made based on the closest Euclidian distance of each pixel to these average values in color space (Figure 4.4).

The classified pixels have been stored as different layers in a matrix. Following color segmentation, two tones of the yellow layers that were detected in the images have been merged together and transformed to binary form while generating the final image. The flow chart diagram of the color segmentation process for void detection is given in Figure 4.5.

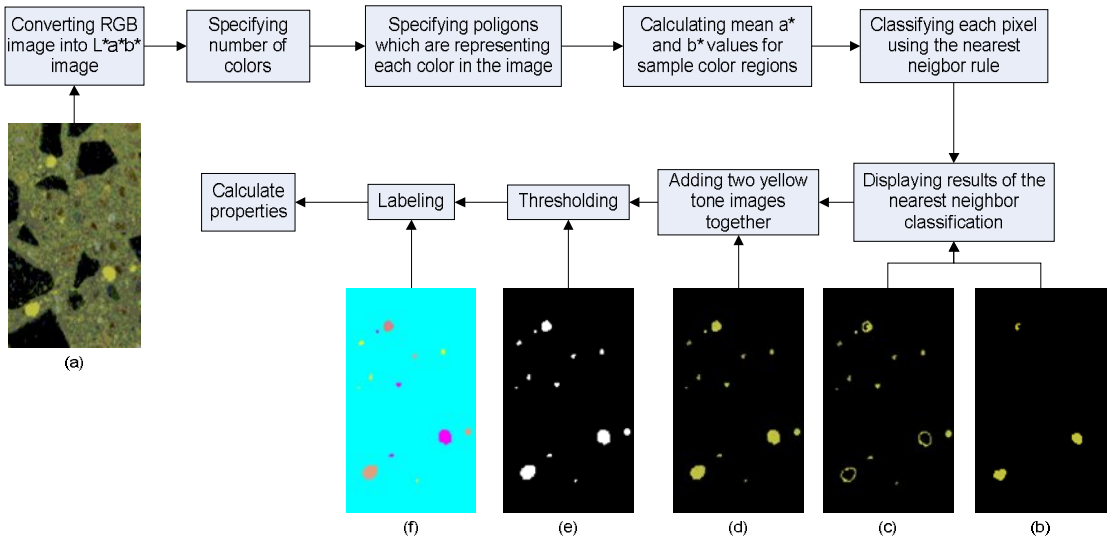

Figure 4.5 Image processing flow chart of void detection by color segmentation.

4.4.3 Watershed Segmentation

A frequent problem encountered in the analysis of digital images is the objects that are in contact. Such contacts avoid one-by-one analysis of individual objects. In order to measure the size and shape of these objects, sections that are in contact should be separated. It appears that the watershed segmentation algorithm originally developed by Beucher & Lantuejoul (1979) and then improved by Vincent & Soille (1991) is the most preferred technique for grain size or grain distribution type problems. Watershed segmentation requires grayscale images as topological surfaces, whose catchment basins are the objects to be identified (Gonzales et al.,

2004). A three-dimensional illustration of topological surface generation is shown in Figure 4.6.

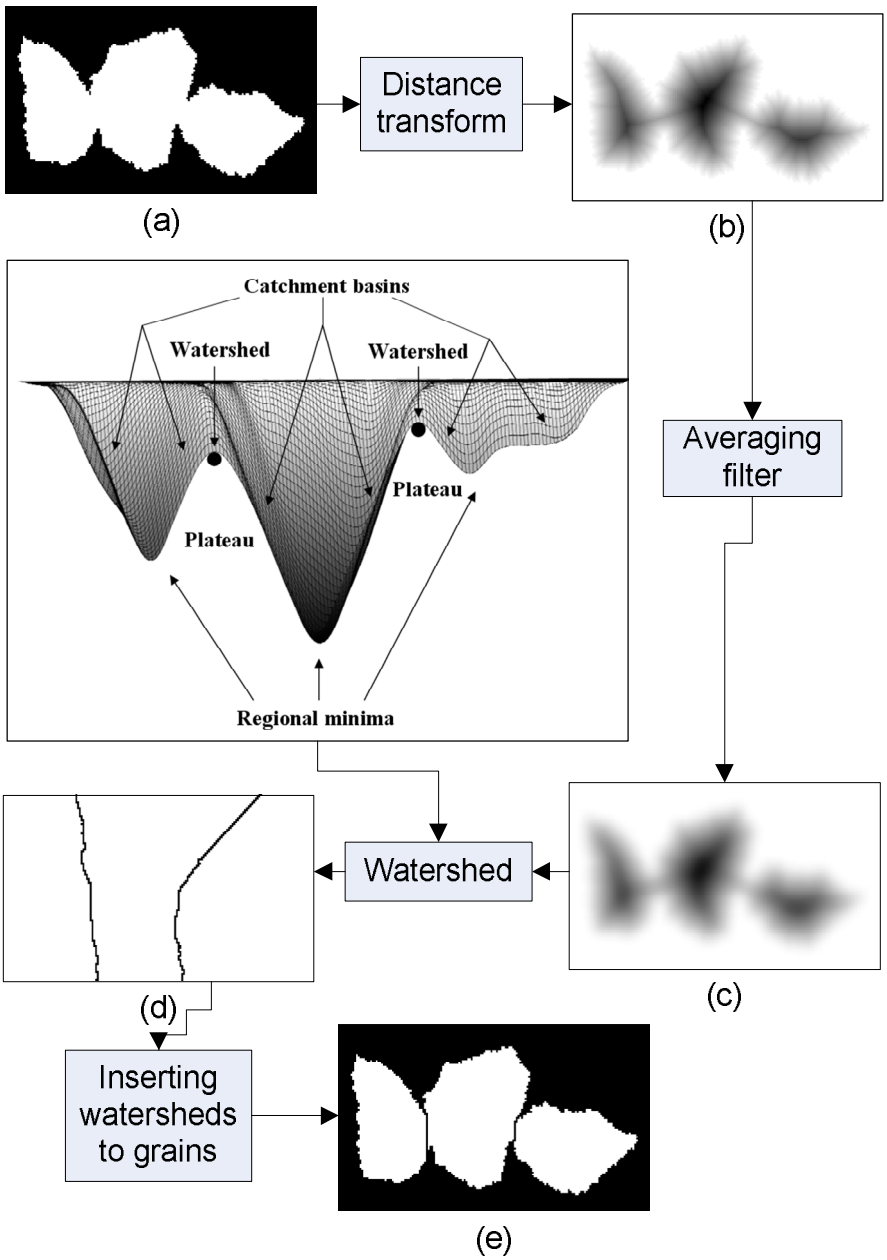

Figure 4.6 Watershed segmentation algorithm tree.

The topological surface can be generated with a process called distance transform, which calculates the Euclidian distances from each pixel to the nearest black pixel (Figure 4.6b). Results of the method, however, may be highly influenced by the presence of irregular boundaries and interior holes. Besides, lack of a minimum in

the ridge of the Euclidian distance map may cause erroneous segmentations of the grains (Russ, 1998). Since the distance map consists of numerous local catchment basins and watershed lines, application of watershed algorithm results in over segmentation of the objects. This effect, however, may be overcome by means of a image filtering algorithm, which eliminates local watershed lines generating a smoothed image as shown in Figure 4.6c. Following the smoothing stage of watershed application, separation lines along the contact points of the grains and voids are obtained as shown in Figure 4.6d, which is superimposed on the original binary image (Figure 4.6a) to come up with the segmented image (Figure 4.6e).

The generation of a separation line may be further explained by the help of the flooded basins analogy where the line passing through the center of the plateau formed by watersheds between two neighboring catchment basins is considered as the dividing border as soon as the gradually increasing water levels in the basins finally form a single water level when they get into contact at the center of the plateau.

4.5 Digital Image Analysis

The image segmentation (i.e. segmented grains or voids in Figure 4.3e and Figure 4.5e) is followed by the characterization of the regions. The sectional area and the centroid for each grain and void were defined for the problem of interest. A region map, where labels are assigned to pixels has been generated using the eight adjacency pixel relationship (Figure 4.7). Quantitative information about the objects could then be obtained examining their regional properties using algorithms in the region map. For instance, grain and void size distribution of the objects in a certain slice of any material can be easily acquired since number of corresponding pixels for each region is already known. Area information can be gathered either in terms of percent of the total pixel area or numerical value of the physical quantity provided that a suitable scale is available in the image. It should be noted that, the broken edges of the segregated specimen due to the low resistance to slicing have been processed as voids during the color segmentation and removed manually before image analysis operations.

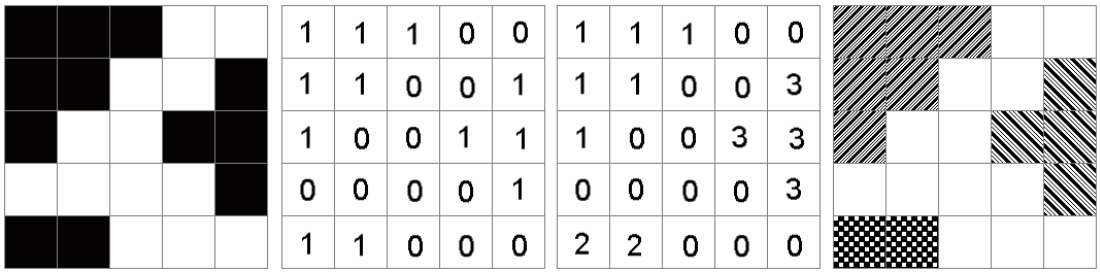

Figure 4.7 Binary Image, binary matrix, label matrix and labeled images.

It has been observed that cohesive matrix characteristics control void shape as well. A closer look to the slice images revealed that voids of the segregated sample are more rounded compared with those of the segregated sample (Figure 4.8).

(a) (b)

Figure 4.8 Void shapes in (a) non-segregated and (b) segregated specimens.

The characteristics of the voids have been numerically expressed using the roundness parameter, R, which is defined as $R = (4 \cdot \pi \cdot \text{area}) / (\text{perimeter})^2$ where area and perimeter are given in pixels for each void. It can be noticed in Table 4.2 that the roundness ratio converges to unity for a perfectly circular void and diverges from unity depending on the distortion of the void shape. The same parameter has been used for void analyses by Lange et al. (1994) and Zhang et al. (2005).

Another widely used parameter for the shape analysis is the eccentricity parameter, which is defined with respect to the axes of an ellipse whose second moment is equal to that of the shape using below equation:

$$e = \sqrt{1 - \frac{b^2}{a^2}} \tag{4.1}$$

where the parameters a and b is the semi major and the semi minor axes of the ellipse, respectively. One can notice in the above given equation that the ellipse parameter varies between 0 and 1. Values of 0 and 1 define two degenerate cases; an ellipse whose eccentricity is 0 being a circle and an ellipse whose eccentricity is 1 being a line.

Table 4.2 Shape characteristics of typical void images.

Shape				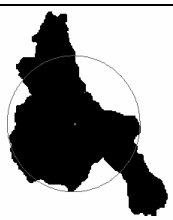	
Roundness Ratio (R_r)	0.81	0.76	0.18	0.33	0.26
Eccentricity (e)	0.35	0.63	0.64	0.82	0.92
Coefficient of inclusion (c_i)	0.046	0.107	0.327	0.184	0.392
Coefficient of exclusion (c_e)	0.045	0.087	0.243	0.366	0.590
c_e-c_i	-0.001	-0.020	-0.084	0.182	0.189
c_e+c_i	0.091	0.107	0.570	0.550	0.982

The eccentricity values of the void shapes in non-segregated and segregated samples are given in Table 4.2. The eccentricities for the void shapes in the segregated sample converge to unity, where the same parameters for the circular voids decrease depending on the degree of elongation.

In the segregated sample, the void shapes are more irregular when compared with those in the non-segregated one, and the roundness ratio parameter is not sufficient to completely characterize a void shape alone as one can notice in Table 4.2. The same is also valid for the eccentricity parameter. In order to provide supplementary tools, additional parameters such as the coefficient of inclusion, c_i, and the coefficient of exclusion, c_e, can be defined.

The coefficients of inclusion and exclusion are defined by evaluating the signature of the void shape with respect to an equivalent circle of which area is equal to that of the void. The circle is positioned at the centroid of the void being analyzed (Figure 4.9a).

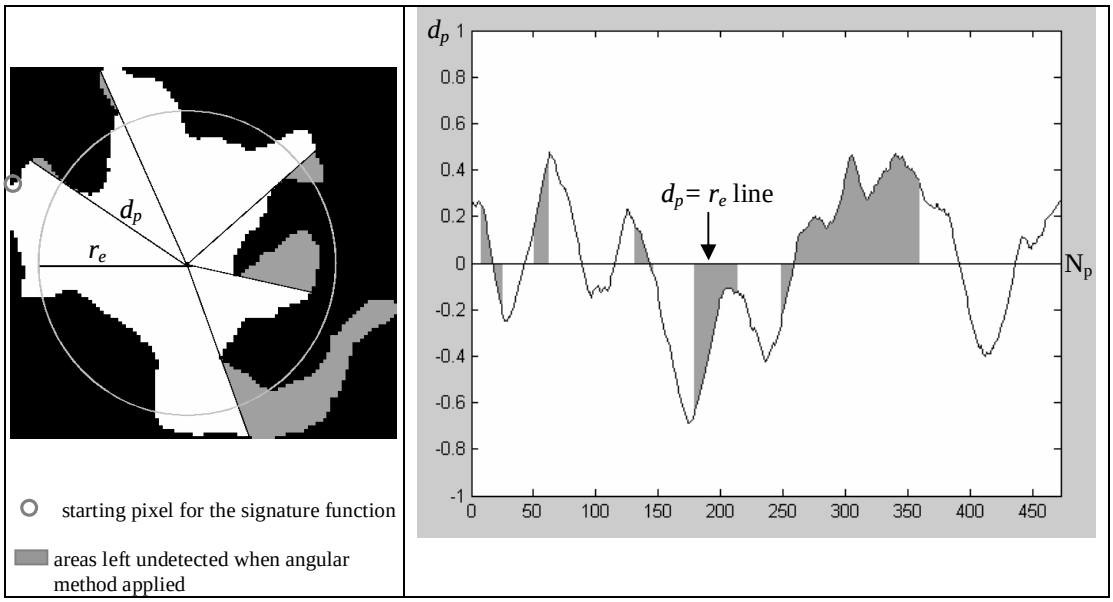

(a) (b)

Figure 4.9 (a) the equivalent circle, (b) digital signature of the void shape using the perimeter method.

The evaluation process starts by assigning a specific value to each border pixel. This is performed by taking the difference between the Euclidean distance of a pixel, d_p, which is defined as the distance from the border of the void shape to the center of the equivalent circle and the radius of the equivalent circle, r_e. This value is later normalized with respect to the radius of the equivalent circle yielding the ordinate of the signature of the void as given in Equation (4.2) and shown in Figure 4.9b. The

abscissa of this figure is set as the number of pixels along the void shape border as explained in the following.

$$d_p = \frac{d_p - r_e}{r_e} \tag{4.2}$$

The coefficient of exclusion is described as the ratio of the sum of the positive values of δ_p to the number of positive valued ordinates of the signature. Namely, this procedure gives the average of the positive side of the signature. The same is also valid for the negative side resulting in the calculation of the coefficient of inclusion. The methodology followed here to obtain the signature of the void shape differs from its predecessors (Masad et al., 2001) by using the number of pixels, N_p, along the perimeter as the abscissa of the signature function instead of angle increments during scanning of the shape. Such a methodology has been found necessary for complete evaluation of the irregularly shaped voids since the angular increment method has failed to detect complicated border shapes.

This fact can be better demonstrated by comparing the coefficients of exclusion and inclusion that were computed using both methods. The angular scanning method yielded 0.203 and 0.249 for exclusion and inclusion coefficients, respectively. The perimeter method, on the other hand, resulted in 0.251 and 0.240 for the same parameters. The difference between these methods is due to the presence of shaded areas left untouched during the angular scanning procedure as illustrated in Figures 4.9a and 4.9b.

4.6 Results and Discussions

An experimental study has been pursued parallel to the development of the image analysis algorithms so that their performances could be assessed using images of the sliced sections of the test samples. Images were analyzed according to the above given methodology. Analysis results pertinent to the quantification of the slice images are presented and discussed as in the following.

Since one of the artificially prepared samples was intentionally segregated by means of additives, image analysis algorithms were expected to capture non-uniform grain and void distribution along sample length. This aspect of the tested materials is shown in Figure 4.10 where digital images of the upper faces of the slices along sample length can be seen. Non-uniform grain and void distributions of the segregated sample are visible in Figures 4.10b and 4.10d, respectively. The other sample, on the other hand, exhibits quite uniform distribution since the cohesive matrix of this sample was able to provide enough resistance to avoid segregation (Figures 4.10a and 4.10c).

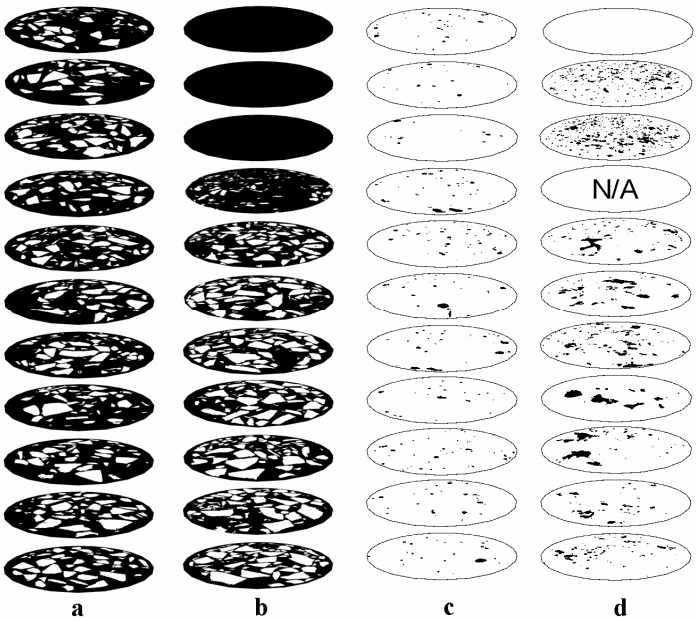

Figure 4.10 (a) grain distribution for the non-segregated specimen, (b) grain distribution for the segregated specimen, (c) void distribution for the non-segregated specimen, (d) void distribution for the segregated specimen.

The non-uniformity of grain and porosity distribution, however, can be best judged using results of digital image analyses. Ratio of the total grain area to the surface area of the slice (area ratio) is plotted with respect to sample length in Figure 4.11a. Area ratios for the segregated and non-segregated samples were computed as 0.23 and 0.24, respectively. These values are quite close to each other and do not yield much information regarding the influence of the cohesive matrix characteristics

on segregation. Instead, standard deviation of the data better demonstrates such an effect. This parameter has been calculated as 0.169 for the segregated sample whereas it has been found as 0.038 for the non-segregated one.

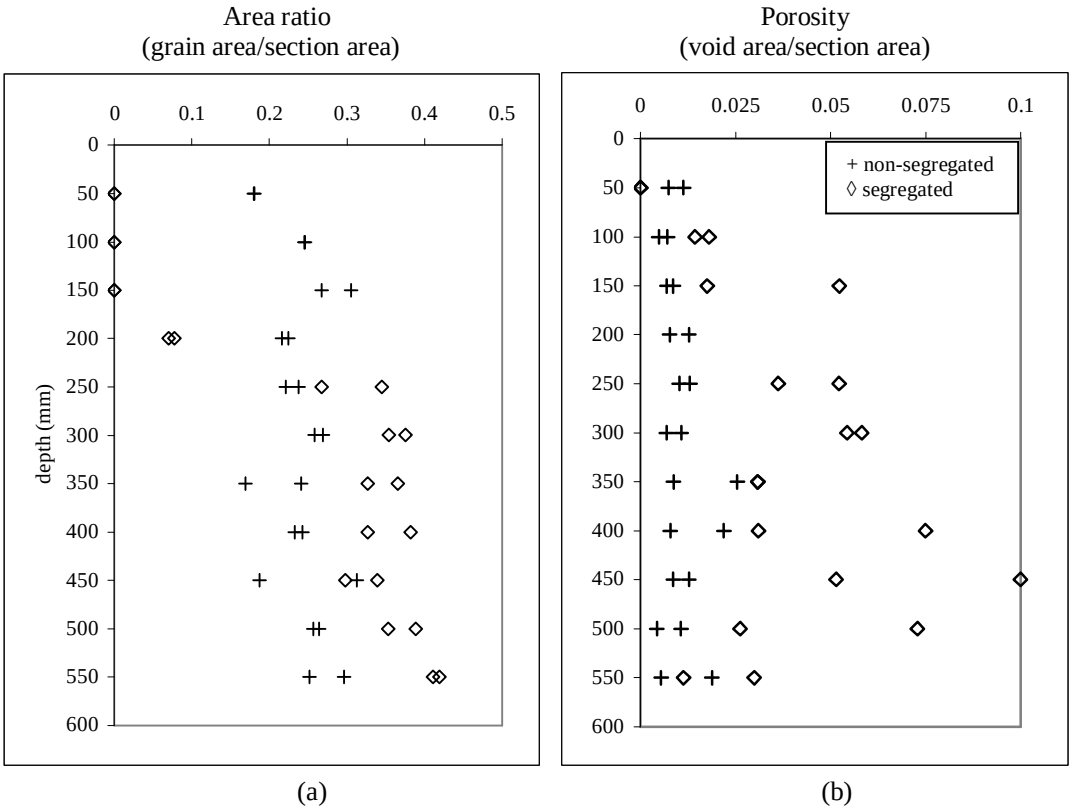

Figure 4.11 (a) grain area ratio variation and (b) porosity variation along specimen length.

Similar evaluations can be made for the porosity distribution along sample length as shown in Figure 4.11b. Porosity is defined as the ratio of the void area to the total section area in this figure. Random distribution of the porosity in the segregated sample is remarkable. The non-segregated sample, however, exhibited more uniform porosity distribution. Respective values of average porosity and its standard deviation have been found as 0.0105 and 0.0053 for the non-segregated sample. Same parameters happened to be 0.0381 and 0.0261 for the segregated sample indicating higher void volume and its non-uniform distribution. Note that it was even not possible to compute porosity for the top fourth image of the segregated sample due to excessive disintegration of the fine river sand under dynamic impact of the blade during slicing operation. Same effect did not exist for coarser basalt grains.

The shape characteristics that are defined in the previous section for void images can effectively describe attributes of a void when they are used in combination. For instance, it can be noticed that the roundness parameter in Table 4.2 may be sufficient while defining a round or nearly round void shape. However, it is not possible to handle complicated void shapes using either the roundness or the eccentricity parameter alone. The eccentricity parameter is a common way of definition of the elongation characteristic of any shape in image processing. It is notable in Table 4.2 that the orientation of the second void shape from left can be captured by the help of the eccentricity parameter, which is considerably larger than that of its left neighbor.

On the other hand, the roundness and eccentricity parameters do not yield enough information about the third and following voids from the left in Table 4.2. The third image, for instance, has the highest perimeter length with respect to its area and there are gaps inclusive with respect to the overall shape of the void. This shape can be quite effectively defined by the help of the coefficient of inclusion, the coefficient of exclusion and the difference of these two parameters. The high inclusion coefficient means that the length of the perimeter remained inside the equivalent circle is a large value. The difference between the coefficient of exclusion and the coefficient of inclusion tells that the shape is an inclusive one with large gaps inside the equivalent circle. The low value of the roundness ratio parameter cannot describe the inclusive feature of this shape since its absolute value describes a highly elongated shape which is not the case. It is not possible to acquire an idea about the actual shape of this void during an automated image analysis operation by only using the roundness ratio and the eccentricity parameters.

The sum of inclusion and exclusion parameters (c_e+c_i) is a measure for the severity of a distorted image with respect to an ideal circle. The value of (c_e-c_i) better describes the actual shape of a void since its negative and positive values tell that the void has either an inclusive or an exclusive shape. A (c_e-c_i) value very close to zero means that the shape is nearly a circle (the first void in Table 4.2). A highly negative value tells that the shape has large gaps inside the equivalent circle (the third void in

Table 4.2). A highly positive value, on the other hand, corresponds to an elongated shape void. A second level differentiation the fourth and fifth voids can be made by considering the value of (c_e+c_i).

The mean values of the difference and sum of the coefficients of inclusion and exclusion have been calculated for each slice image as presented in Figure 4.12. The void shapes, appearing more elongated in the segregated sample, are classified as exclusive shapes. The values of the (c_e-c_i) parameter in the slices of the segregated sample are higher when compared with the non-segregated one (Figure 4.12a). The intensity of the distortion of the voids in the segregated sample is shown in Figure 4.12b. One can notice in both figures that the coefficient of inclusion and exclusion can effectively characterize void shapes in the investigated samples.

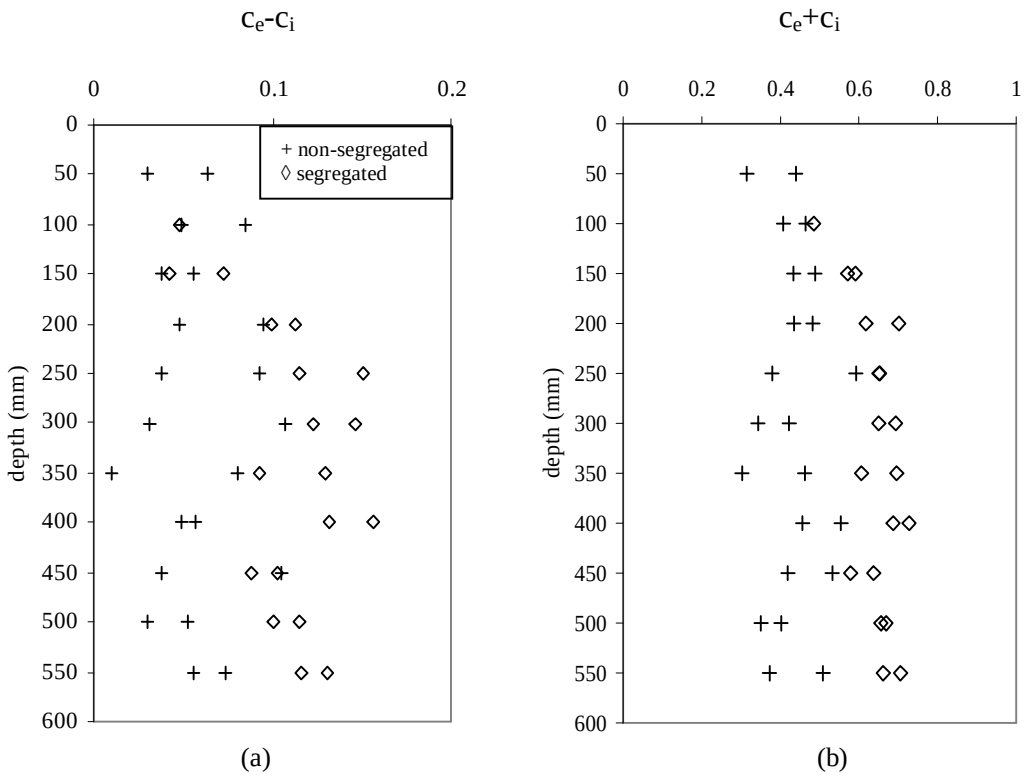

Figure 4.12 (a) the difference and (b) the sum of the coefficients of exclusion and inclusion.

4.6.1 Application of the Shape Coefficients to the Identification of Soil Grains

In order to apply the developed shape coefficients to the problem of determining the degree of angularity of soil grains, the grain images, originally proposed by Lambe & Whitman (1979) as angular, subangular, subrounded, rounded and wellrounded particles, were digitally scanned and used as binary images for the analyses.

The digital signature technique has been applied and coefficients of exclusion and inclusion parameters have been computed. The grain images, their digital signatures and shape coefficients have been presented through the Figures 4.13 to 4.17. The equivalent circles, having the same area with the grains, are also positioned at the centroid of the each grain.

The result of the shape analysis has been presented in Table 4 in terms of the mean values of the shape coefficients for each grain group. The sum of inclusion and exclusion parameters (c_e+c_i), which represents the severity of a distorted image with respect to an ideal circle, showed a good match for the degree of angularity.

It is understood that Lambe and Whitman made their angularity definitions on the basis of existing angels and corners on the plane view of a grain. However, it should be mentioned that, some grains in the groups of Lambe and Whitman may also be positioned in other groups if their digital signatures are comprehensively investigated. The term “angular” represents objects, forming angels or corners, which is measured by c_e+c_i parameter in this study. For instance, the fifth grain, presented as subangular in Figure 4.14, has a large value of c_e+c_i and may be easily classified as more angular than the angular grains presented in Figure 4.13. There are also more angular particles among the rounded grains (the second grain of the rounded grain group) than the grains in the subrounded group.

As mentioned in the above, the visual classification proposed by Lambe & Whitman (1979) may be sometimes open to discussion. This, however, may be

avoided by defining roughness characteristics of the grains as well, which may not be attributed to the angularity characteristics of a grain.

Table 4.3 Mean shape coefficients of the grains.

	Angular	**Subangular**	**Subrounded**	**Rounded**	**Wellrounded**
$\mathbf{c_e}$	0.128	0.129	0.112	0.119	0.097
$\mathbf{c_i}$	0.114	0.104	0.103	0.098	0.100
$\mathbf{c_e+c_i}$	0.242	0.233	0.215	0.217	0.197
$\mathbf{c_e-c_i}$	0.014	0.025	0.009	0.021	-0.003
r	136	172	132	78	47

Since the digital signatures also involve the roughness characteristics, this characteristic of a grain may be expressed as a quantitative value using the digital signature function. A high order polynomial function has been fitted by using the least squares method. The polynomials are presented over the signature graphs as red color function plots in Figures 4.13-4.17. The least squares method estimates best representing value in a series of data for a single point. This characteristic of the method filters out the roughness characteristic of the shape while retaining the general shape of the grain. Since the original signature series still involves the roughness data of the object, the difference the fitted function and the digital signature yields a quantitative value, which reflects a measure for the roughness characteristics.

The sum of differences between signature (blue) and polynomial (red) functions has been divided by the length of the perimeter of the grain, in order to come up with the roughness parameter (r) and the mean value of this parameter for each grain group are presented in Table 4.3. It should be mentioned that, the r parameter is decreasing significantly in the well rounded grains, since the fitted functions is a good approximation of the digital signature series (i.e. there is no remarkable difference between them).

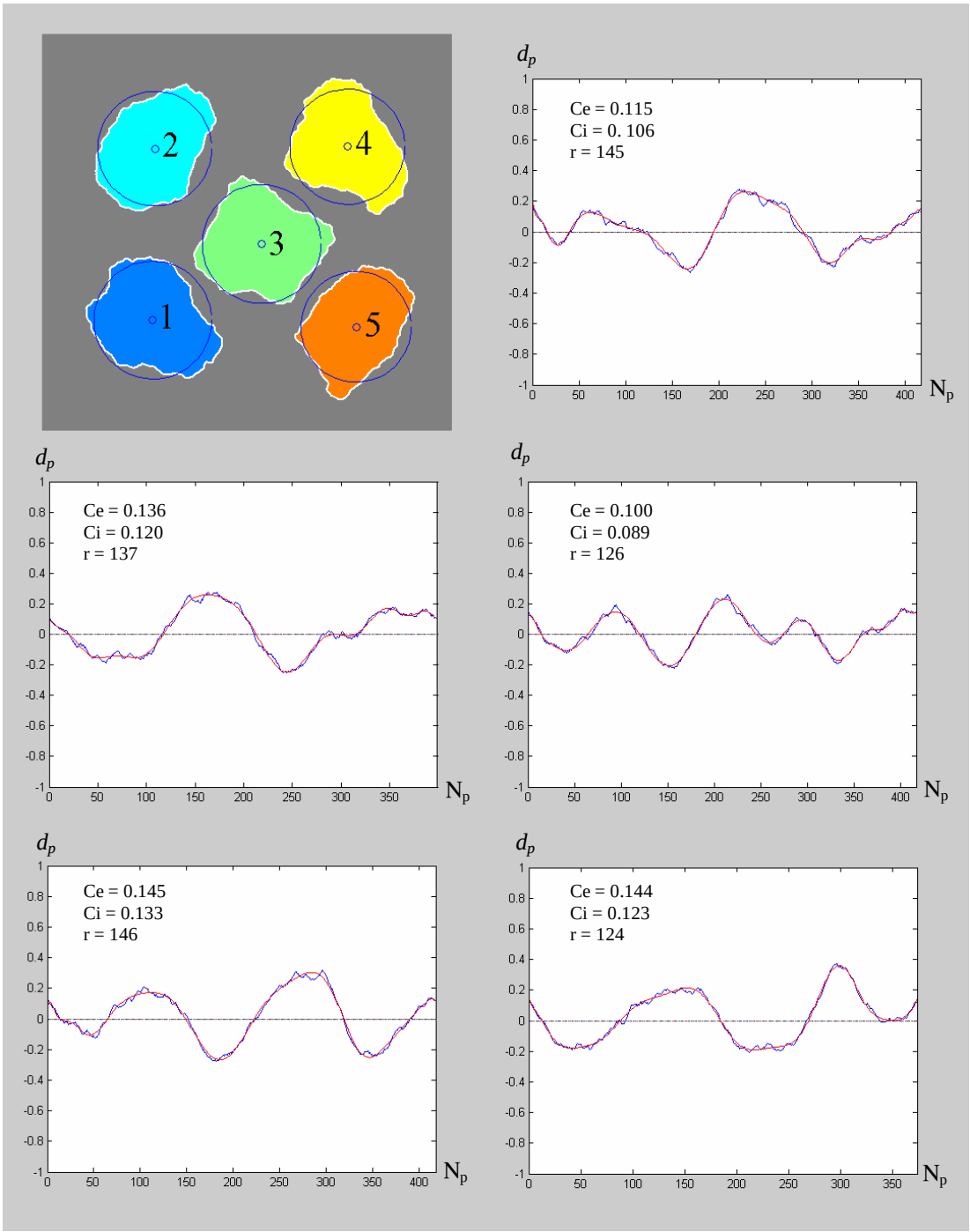

Figure 4.13 Angular particles and their digital signatures.

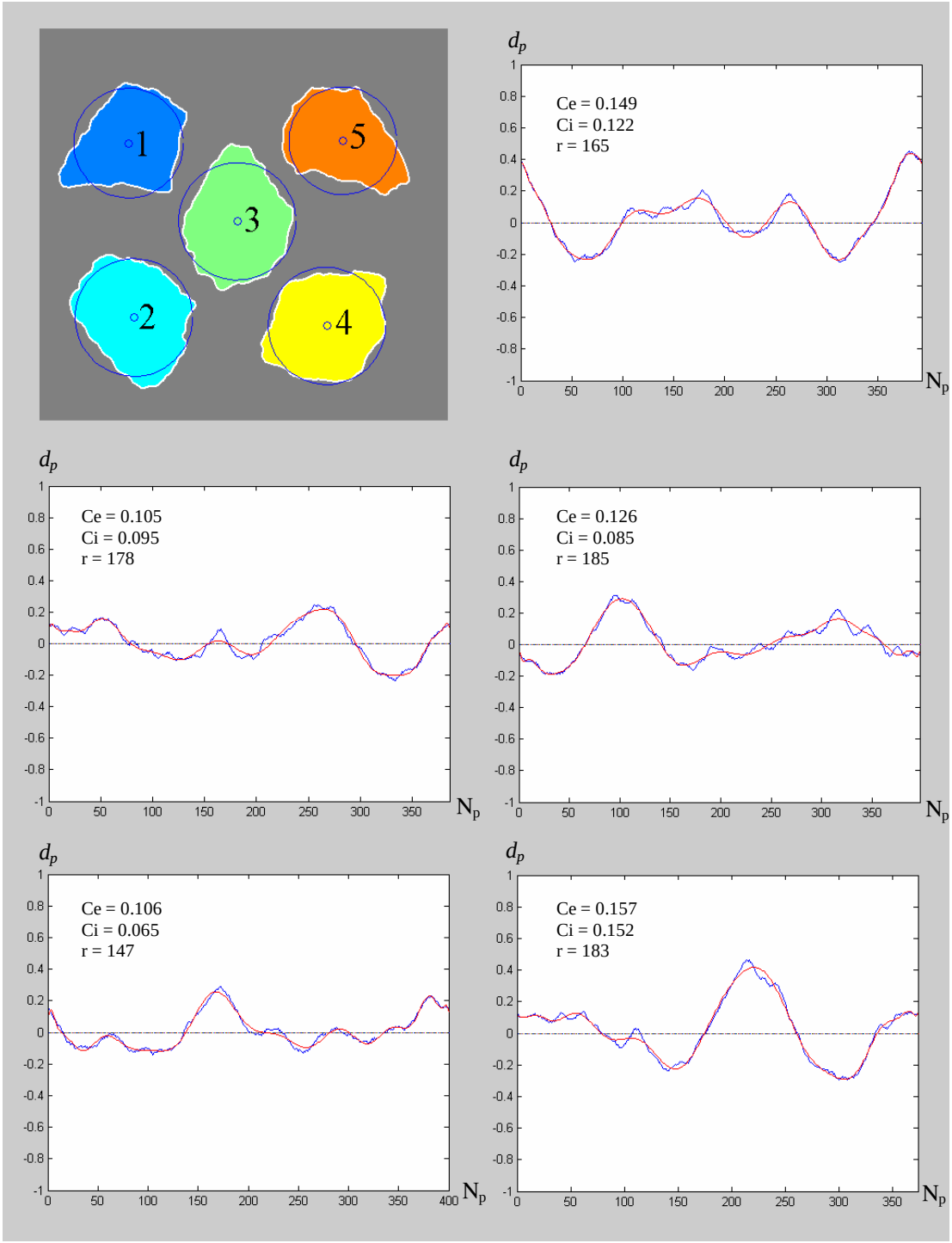

Figure 4.14 Subangular particles and their digital signatures.

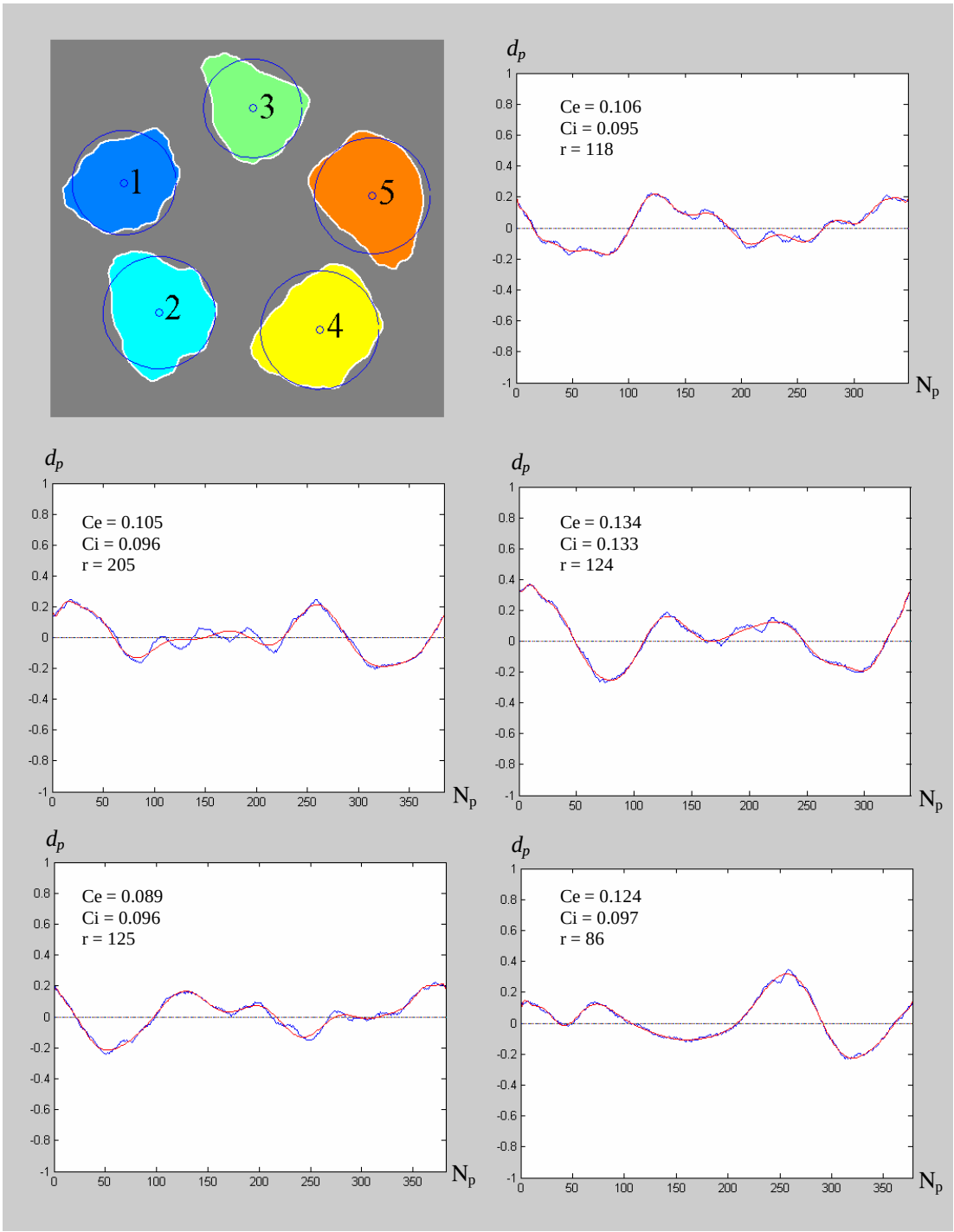

Figure 4.15 Subrounded particles and their digital signatures.

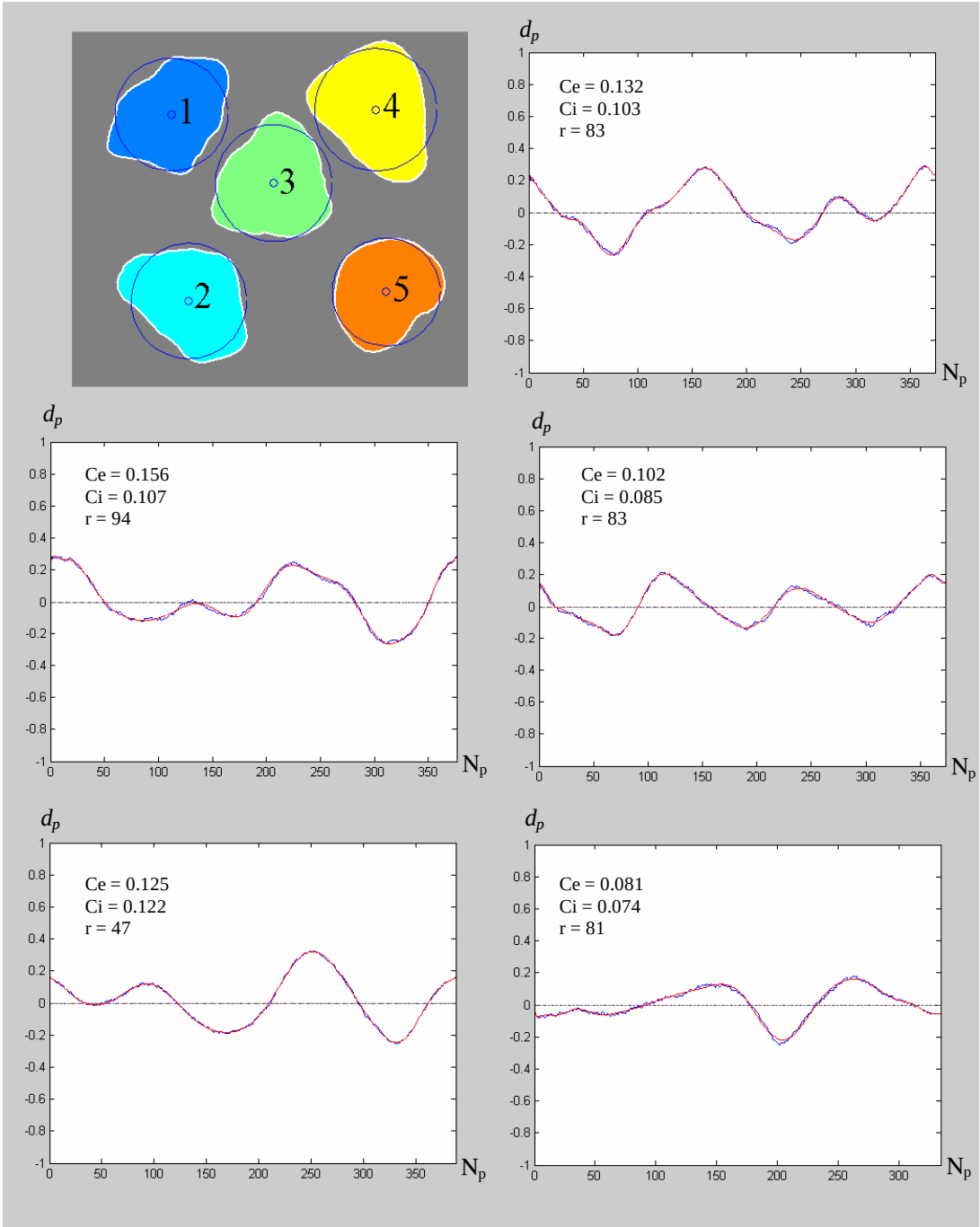

Figure 4.16 Rounded particles and their digital signatures.

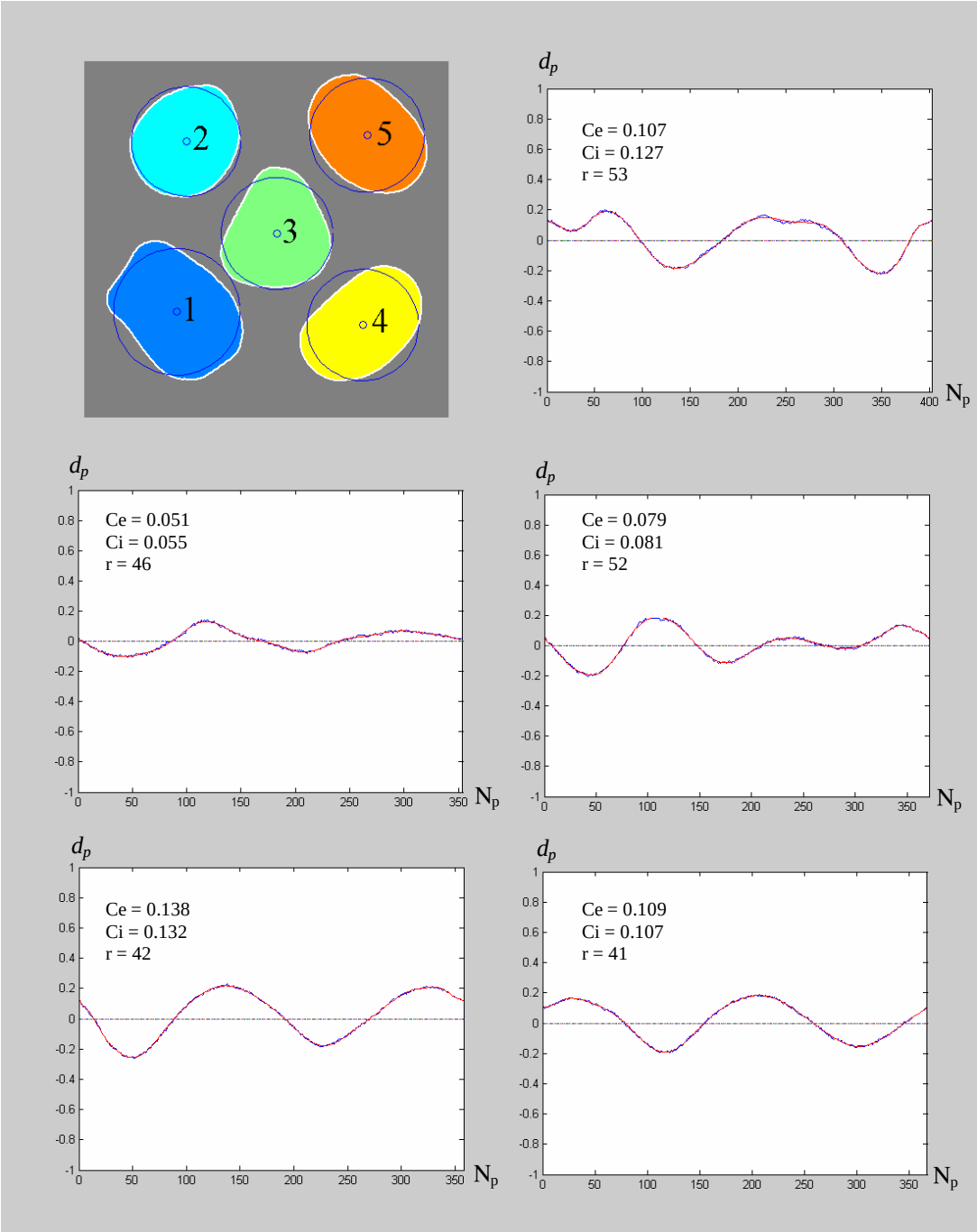

Figure 4.17 Well-rounded particles and their digital signatures.

4.7 Conclusions

The study demonstrated that digital image analysis subroutines readily available in commercial mathematical analyses software packages could be easily organized to form problem specific algorithms. Although the performance of the algorithms developed herein was tested on the images of SCC samples, they are equally applicable to the investigation of geomaterials such as rock with breccias, sandy and gravelly clay samples. Results of the image analyses showed that image analysis methodology as presented here was able to demonstrate that characteristics of the cohesive matrix would have considerable influence on the distribution of coarser grains and voids in SCC samples. The more irregularly shaped voids and random distribution of the porosity in segregated samples may be attributed to the additives used to trigger segregation in concrete samples. It has been noticed that color segmentation would be especially helpful if several different objects with varying colors exist in the original image. The grayscale segmentation, itself, could not fully differentiate the voids from the cohesive matrix. The color segmentation, on the other hand, generates several object layers and can fulfill this task much more effectively.

In order to characterize the void shapes in the investigated sample images, two new shape parameters called as coefficients of inclusion and exclusion have been developed. In addition to the well known roundness ratio and eccentricity shape parameters, these two parameters along with their sum and difference values have been used in the characterization of the highly irregular void shapes. The developed parameters may also have potential use as supplementary features in the neural network applications or object recognition processes in the digital image analysis applications.

The techniques originally developed for the characterization of the void shapes were also applied to grain images. It has been found that the well-known geotechnical way of grain grouping on the basis of grain shapes could be enhanced by considering grain roughness in addition to angularity. A new shape parameter, called as the roughness parameter, has been proposed for this purpose.

CHAPTER FIVE
A DIGITAL IMAGE ANALYSIS METHODOLOGY FOR THE INVESTIGATION OF HETEROGENEOUS PRISMATIC COHESIVE SPECIMENS

5.1 Introduction

Since the size of breccia particles and their shape and distribution might have major effects on the mechanical properties of the breccia rocks, it has been considered that evaluation of the breccia particles on the surface appearances of the cubic test specimens could be a motivating subject for the application of digital image processing techniques to a three-dimensional object. The unconfined compressive strength of the breccia rock specimens have been predicted by using digital image processing and nondestructive laboratory tests in this chapter. While evaluating the destructive and nondestructive test data, multiple linear regression (MLR) and artificial neural network analysis (ANN) have been conducted. The comparison of the success of the two data analysis techniques has been also presented in this section of the dissertation.

Breccia size and distribution are expected to be effective on the mechanical behavior of the breccia rocks. The effect of size distribution in the constituent material property of the volcanic breccia rocks has been investigated by Saotome et al. in 2002. Since the inter particle bonding is relatively low in the investigated volcanic breccias, it was possible to physically separate the particles by freeze and thaw cycles.

The nondestructive investigation of the breccia rocks has been conducted by using digital image analysis techniques (Martinez et al., 2006). A two stage segmentation procedure has been used for the breccia particles and commercial image analysis software was used to determine the geometrical properties of the breccias in order to investigate the relationship with the ultrasonic pulse wave velocities.

Multiple regression analysis, on the other hand, is a common approach to estimate mechanical and physical properties of rock specimens (Shakoor & Brown, 1996; Sonmez et al., 2004; Kahraman & Alber, 2005; Kahraman & Fener, 2007; Tamrakar et al., 2007). Karakuş & Tutmez (2006) have used fuzzy and multiple regression models in order to evaluate the intact rock strength based on point load, Schmidt hammer and sonic velocity. Sonmez et al. (2004) have also used fuzzy algorithms and regression analysis for the estimation of the uniaxial compressive strength and the modulus of elasticity for Ankara Agglomerate.

In this chapter, the engineering properties such as ultrasonic pulse wave velocities, water absorption, effective porosity, and unit weights of the breccia rock specimens have been used in conjunction with the features derived by means of digital image processing methods to predict the unconfined compression strength values. Multiple linear regression analysis and neural networks were used in the prediction models. The comparison of the two data analysis approach has been presented.

5.2 Materials and Methods

5.2.1 Origin of the Specimens

The breccia rock specimens used in this thesis are obtained from the marble quarry of the Enmersan Granit-Mermer ve İnşaat Taahhüt Ticaret A.Ş. (Çakmaktepe location in Çakmaklı village Saruhanli-Manisa).

The limestone capacity of the marble quarry has been examined in the past studies (Yavuz et al., 2003) and it has been deduced that the quarry consists of two main groups of rocks. The first group consists of beige color homogenous limestone, which forms the great proportion of the limestone reservoir (Figure 5.1a). On the other hand, the second group is located in some parts of the quarry and consists of the breccia rock, having a red cohesive matrix (Figure 5.1b). The X-Ray Diffraction (XRD) analyses for both constituent parts of breccia rock have been performed in Centre of Material Research of Izmir Institute of Technology.

The analyses have indicated that, the homogeneous limestone part is consisting of pure calcite. On the other hand, in the red cohesive matrix, calcite is found to be the dominant mineral in addition to quartz, plagioclase, siderite and hematite. There is only smectite type clay mineral present in the sample. The XRD graphs of both materials were given in Appendix J section. The specific gravities for homogeneous limestone part and red cohesive matrix have been determined as 2.70 and 2.72, respectively.

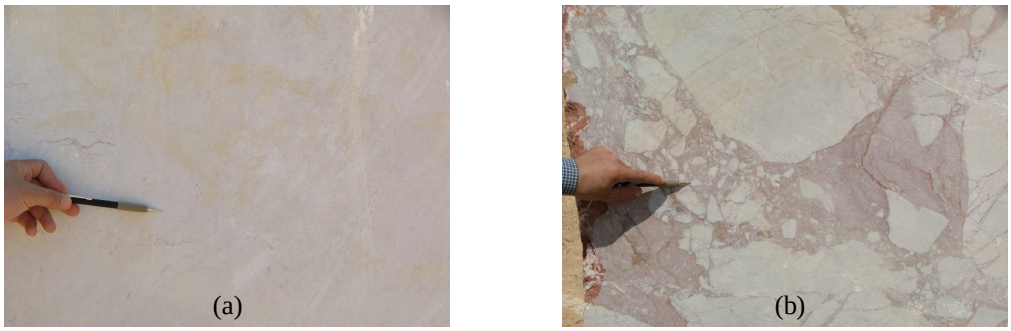

Figure 5.1 The massive (a) and breccia (b) rocks of the marble quarry.

5.2.2 Specimen Preparation

The specimens were cut out from the marble blocks as cubes with a side width of 7 cm. It has been noticed at this stage that the discontinuities formed by the clay and calcium carbonate matrix has enough resistance to the slicing machine. A total number of 193 specimens have been cut out from the marble blocks. The surfaces of the cubes have been processed in order to increase the visual differences between the limestone and the cohesive matrix. This operation was necessary for the success of the digital image processing operations. A series of sandpapers, ranging between #180 and #400, were employed using a vibrating machine, which significantly reduced the roughness of the specimen surfaces (Figure 5.2).

Figure 5.2 The surface preparation of the specimens.

The reduction of the surface roughness resulted in a better visual separation between the limestone and the cohesive matrix. The difference of the processed and unprocessed specimen surface images are shown in Figure 5.3a-b.

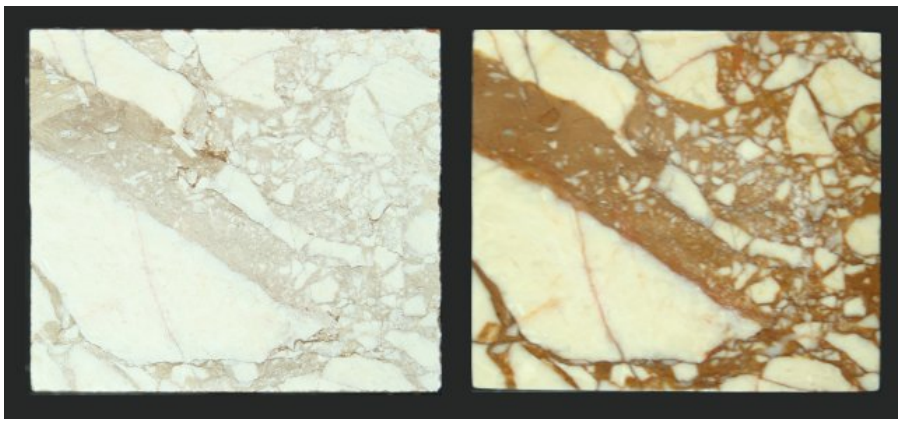

(a) (b)

Figure 5.3 The unprocessed (a) and processed surface (b) of the same specimen.

5.2.3 The Classification of the Specimens According to their Visual Appearances

The specimens have been classified according to their visual appearances. In the classification process, all surfaces of the cube specimens have been taken into consideration and a visual averaging has been performed for the specimens, whose surface appearances show anisotropy. The specimens have been classified into four groups as shown in Figure 5.4a-d. The specimens in the first and last groups are composed of homogeneous limestone and cohesive matrix, respectively. These specimen groups show isotropic visual appearance. On the other hand the second and the third groups are breccia rock specimens where the amount of the cohesive matrix increases with the group number.

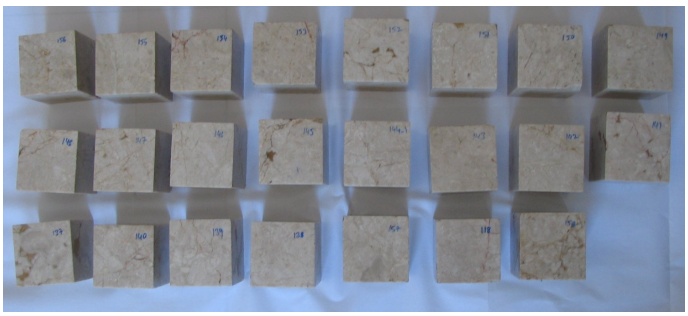

(a) Homogenous isotropic limestone.

Figure 5.4 The visual classification of rocks used in the study.

(b) Breccia rocks, in which the cohesive matrix shows veins in the specimen surfaces.

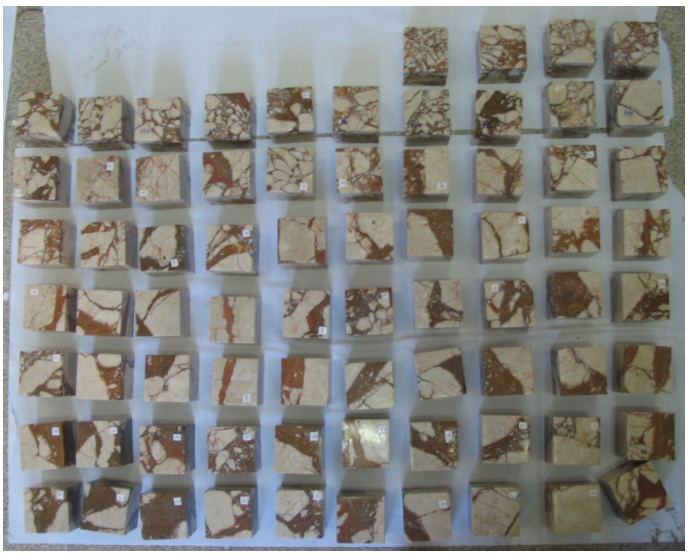

(c) Breccia rocks, in which the limestone parts are separated with thicker matrix and appear as separate grains.

(d) Rocks, whose great proportion show homogeneous isotropic red cohesive matrix.

Figure 5.4 continued.

5.2.3 Image Acquisition System

An image acquisition system has been produced in order to standardize the capturing of the surface images. The system consists of an 8 mega pixel digital camera, connection cables, light sources, a desktop computer, and a cabinet housing all the parts. The cabinet was used to ensure a fully isolated and constantly illuminated area. The size of the cabinet was selected as 50×50×80 cm by considering the sizes of the specimens and the positions of the light sources. A small insert door at the lower half has been provided for the placement of the specimens (Figure 5.5a).

(a) (b)

Figure 5.5 The cabinet (a) and the camera (b) used in the acquisition system.

Canon EOS 350D digital camera with 18-55 mm EF-S zoom lens was employed in the acquisition of the specimen surface images (Figure 5.5b). This type of a camera was selected because of its capability to capture high resolution images by supporting full control over the USB connection. On the other hand, the 18-55 mm EF-S lens ensures manual zoom and focus adjustments, which is necessary for standardizing the image acquisition process.

Special equipment was manufactured by using a rod in order to mount the camera in the cabinet. At one side of the rod, a ball joint has been fixed, enabling free rotation of the digital camera, with a thumbscrew, in order to adjust the camera

position perpendicular to the specimen surfaces (Figure 5.6). The other side of the rod was designed to allow horizontal position adjustment of the camera.

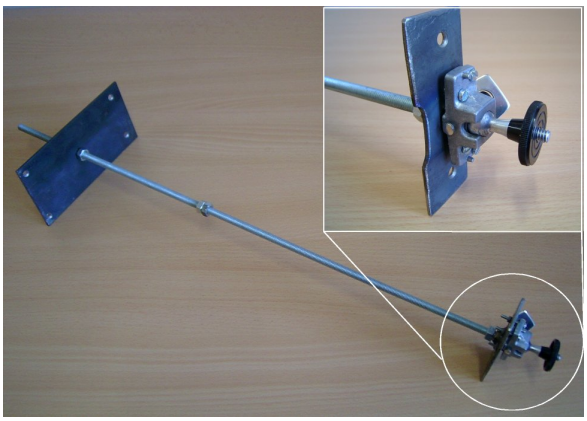

Figure 5.6 The mounting apparatus of the camera.

The cabinet was painted mat black to damp the light in the cabinet. The mounting equipment of the camera was fixed at the top of the cabinet. The camera was also set as to have a perpendicular position to the bottom surface of the cabinet and the USB connections to the desktop personal computer was established via cables. The florescent light sources were positioned to prevent the blazes which may occur at the surfaces of the specimens. The completed image acquisition system is shown in Figure 5.7a and Figure 5.7b.

(a) (b)

Figure 5.7 The image acquisition system while image capturing.

Thin wax layer was applied at the surfaces of the specimens before the image acquisition stage, which increased the visual differences between limestone and cohesive matrices. Please note that the appearance of the specimen at the left side of the Figure 5.8 is duller than the other specimen, whose surface has a thin wax layer.

Figure 5.8 The visual difference between the specimens.

5.2.4 Image Acquisition

Remote shooting capability of the camera was used during the acquisition of the specimen surfaces. The twain interface of the camera's software enabled manual adjustment of the aperture, shutter speed and ISO settings of the camera's objective (Figure 5.9). F5.6 aperture and 1/100 s shutter speed combination with 100 ISO value have resulted in highest quality images for this study.

Figure 5.9 Twain interface
of the camera's software.

The acquired images were transferred directly via the USB connection cable to the desktop computer's hard drive. The Canon®'s ZoomBrowser Ex software was used for the management of the image files in the desktop computer (Figure 5.10).

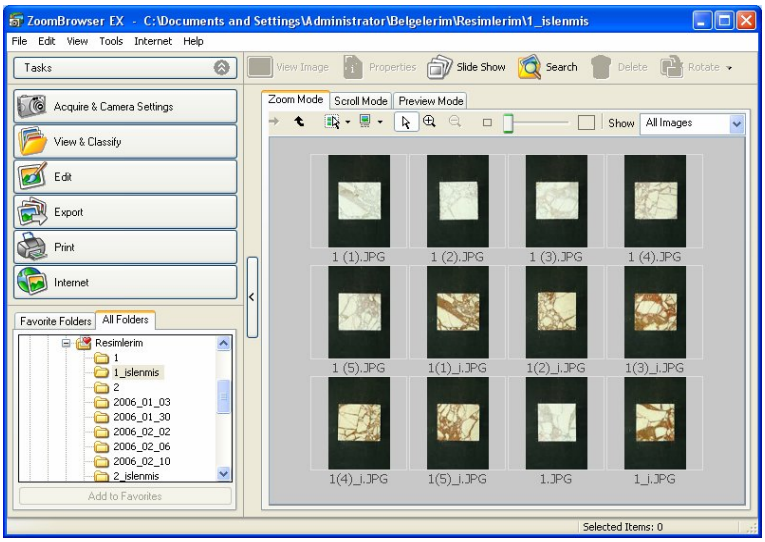

Figure 5.10 File management application used in the desktop computer.

A labeling scheme was planned for the surfaces of the specimens and applied systematically during the image acquisition as shown in Figure 5.11. For example, the fourth surface of the specimen with an ID number of 27 was named and stored as 27_4.jpeg on the computer.

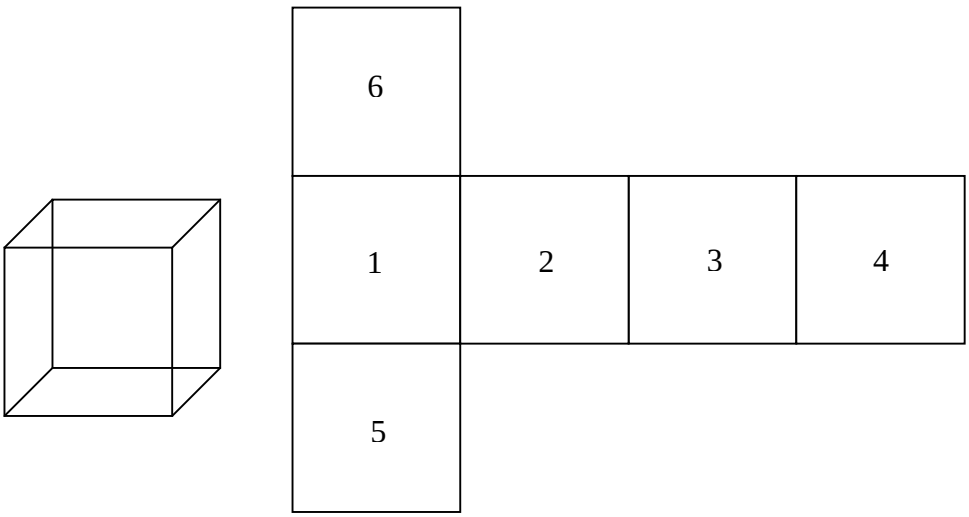

Figure 5.11 The labeling scheme of the specimens.

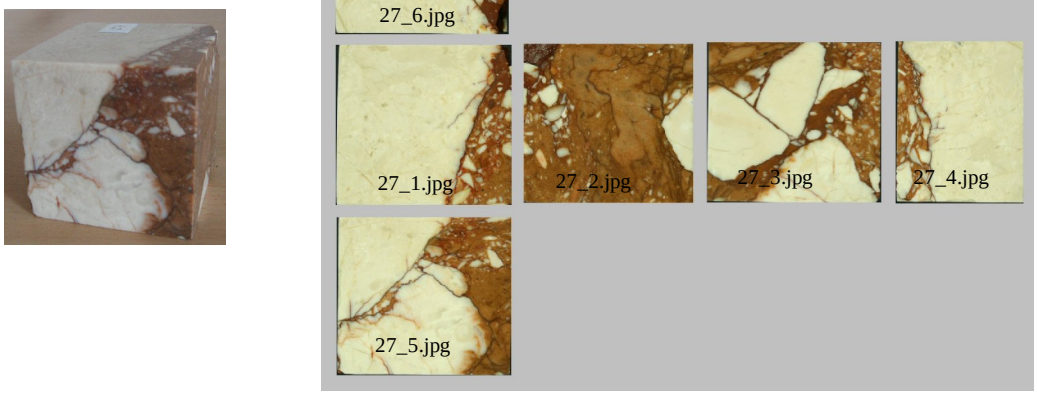

Figure 5.11 continued.

5.2.5 Laboratory Tests and Test Data

The nondestructive laboratory tests on the specimens were conducted at the Geotechnics Laboratory of the Dokuz Eylül University Civil Engineering Department.

5.2.5.1 Ultrasonic Pulse Wave Velocities

Ultrasonic pulse wave velocity measurements of the breccia rock specimens were performed using Pundit Plus® (Figure 5.12) equipment obeying the procedures for laboratory measurements of the pulse velocities of compression and shear waves in rock (ASTM D 2845).

The elastic constants determined by this method are termed ultrasonic since the pulse frequencies used are above the audible range. The test method is valid for wave velocities measurement in both anisotropic and isotropic rocks although the velocities obtained in greatly anisotropic rocks may be influenced by such factors as direction, travel distance and diameter of the transducers.

Figure 5.12 The ultrasound device used in this study.

The dimension limitation for the test specimens is recommended as the ratio of the pulse travel distance to the minimum lateral dimension cannot exceed 5. Also, the two opposite surfaces on which the transducers will be placed shall be parallel to within 0.1 mm / 20 mm of lateral dimensions. Both specimen geometry regulations were verified for all specimens. Energy transmission between the specimen surface and each transducer has been improved using a thin layer of contact jell and pressing the transducer against the specimen surface with a small seating force.

The time, required to pass the compression pulse wave between the transducers, was monitored by the display of the device and the length of the travel direction was measured by a Vernier caliper along the four sides of the specimen. The pulse wave velocities were calculated by the following formulation.

$$PulseWaveVelocity = \frac{DirectionLength}{Time} \tag{5.1}$$

The primary advantage of ultrasonic testing is that it offers good approximations for the prediction of certain mechanical properties. However, the ultrasonic elastic constants, calculated from the measured wave velocities, are only valid for the allowed degree of anisotropy, which is reported in terms of the variation of wave velocities with direction in rock.

In order to estimate the degree of anisotropy in rock, the compression wave velocity in three orthogonal directions was measured. Since a great majority of the compression wave velocities varied more than 2% from their average value, the elastic constants such as Young's modulus of elasticity (E) and modulus of rigidity (G) cannot be calculated according to aforementioned ASTM mentioned. The pulse wave velocity measurements in three orthogonal directions were shown in Figure 5.13 with error bars for each specimen.

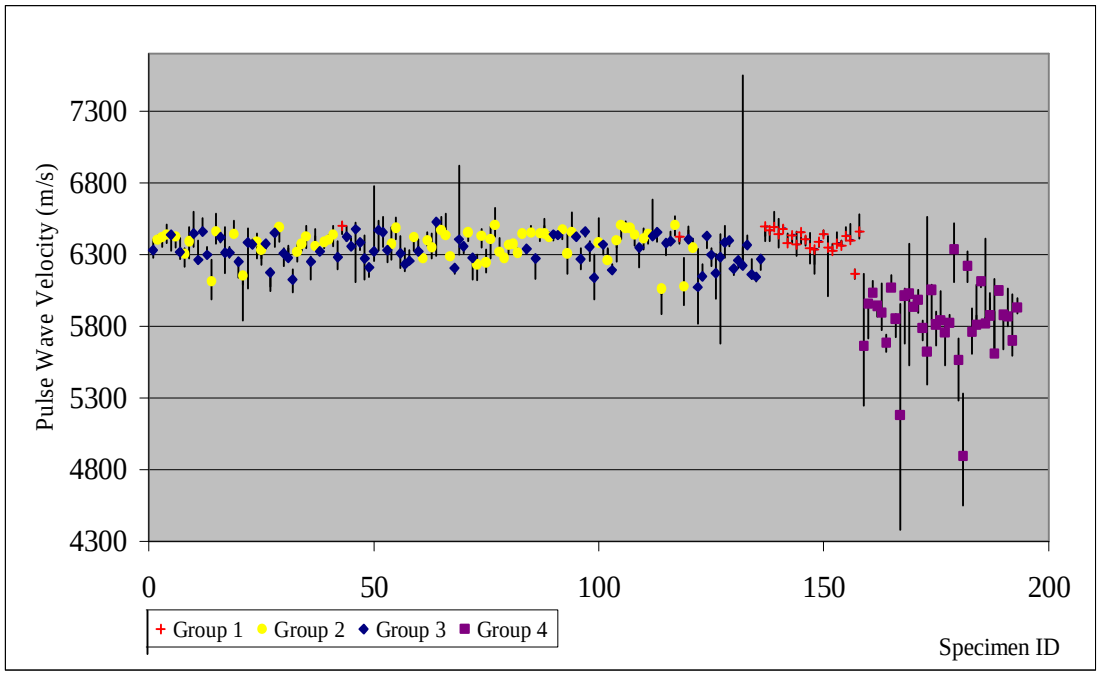

Figure 5.13 The compression pulse wave velocities in three orthogonal directions of the specimens.

Since the first transmitted arrival is that of the compression wave, its detection is relatively easy. The shear wave arrival, however, may be obstructed by vibrations due the ringing of the transducers and reflections of the compression wave. The amplitude of the shear wave relative to the compression wave may be increased and its arrival time could be determined more accurately by means of thickness shear-transducer elements, which is not used in this study. Therefore, only compression wave velocities were measured. Also the characteristics of the compression waves cannot be captured because the pulse wave velocity device does not offer connection port to an oscilloscope.

Since the moisture content of the test specimen can affect the measured pulse wave velocities, the pulse wave velocities have been determined in the oven dry state

(0%) and in a saturated state (100%). It should be noted that the oven temperature did not exceed 50 °C. The specimens were submerged in water until no increment was observed between the weight measurements of the same specimens with time. The pulse wave velocities of the test specimens at dry and saturated conditions are shown in Figure 5.14.

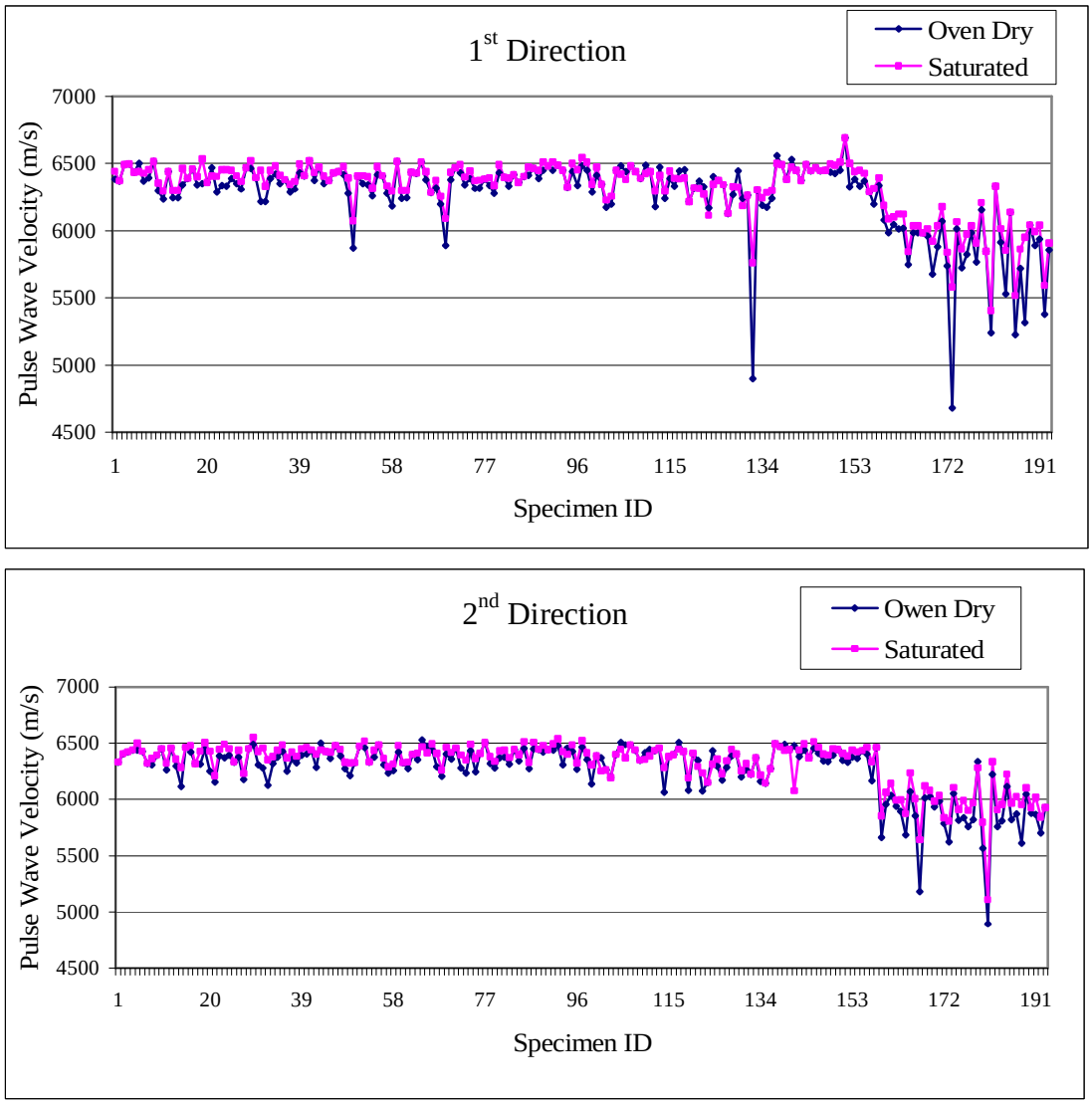

Figure 5.14 Dry and saturated pulse wave velocities of the test specimens in three orthogonal directions.

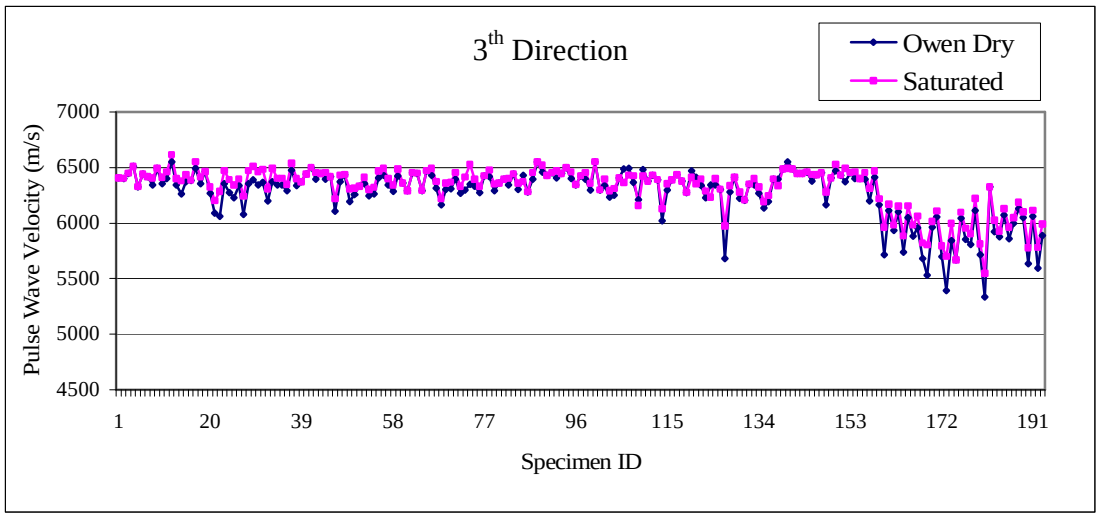

Figure 5.14 continued.

It has been noticed that the pulse wave velocities at the saturated state are slightly higher than those corresponding to the dry condition. This fact took place because of the voids in the dry state was replaced by the water in the saturated state, whose pulse transmission capability is significantly higher.

5.2.5.2 Water Absorption by Weight and Effective Porosity

The specimens are dried for 48 hours in oven at 50 °C. After drying, the specimens are cooled in the room for 30 minutes and weighed. In order to determine the water absorption of the test specimens, they are placed in the water absorption tank (Figure 5.15). At constant time intervals, some specimens were removed from the water tank and dried with damp cloth and weighed. Once no increment at the total weights was monitored, all specimens weighed one at a time following the same procedure.

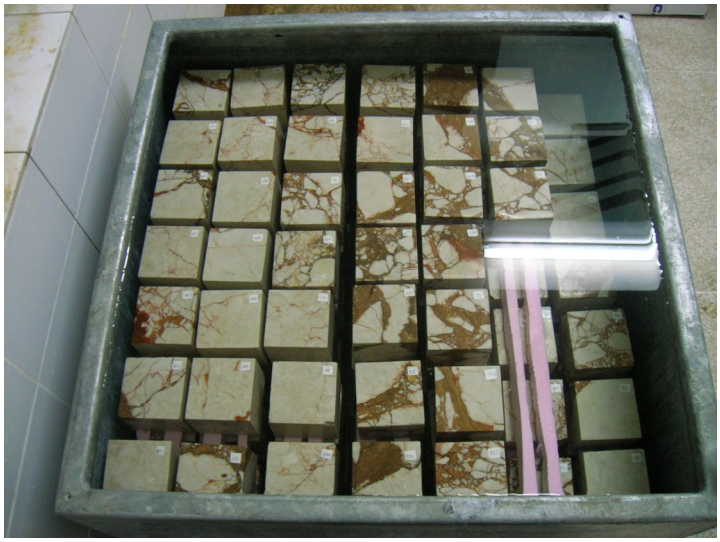

Figure 5.15 The specimens in the water absorption tank.

The water absorptions by weight were calculated as in the following equation;

$$WaterAbsorption = \frac{W_{saturated} - W_{dry}}{W_{dry}} \times 100 \qquad (5.2)$$

The calculated water absorption by weight values for all specimens are shown in Figure 5.16.

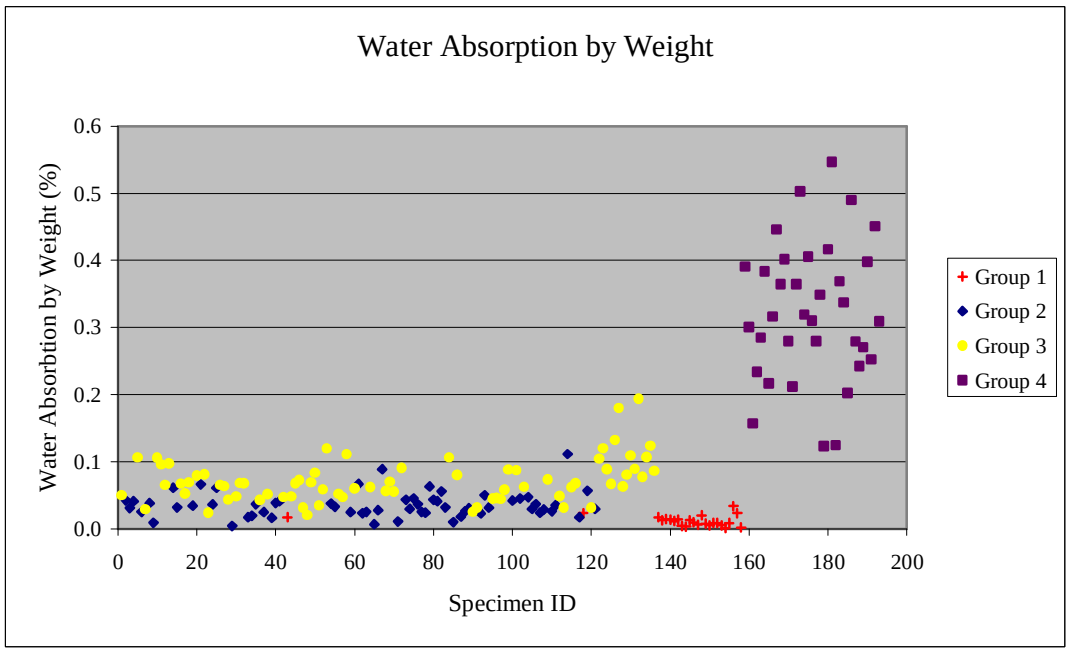

Figure 5.16 Water absorption by weight values for the test specimens.

The effective porosity values of the specimens have been calculated according to the assumption that, all voids in specimens are filled with the absorbed water. Hence, the weight of the absorbed water is equal to the volume of the voids.

The effective porosities of the specimens have been calculated by the following formulation and shown in Figure 5.17.

$$n = \frac{V_{voids}}{V_{specimen}} \times 100 \qquad (5.3)$$

It should be mentioned that the specimens from 137 to 158 are homogeneous limestone samples from Group 1 and specimens from 158 to 193 are specimens consisting of the red cohesive matrix from Group 4.

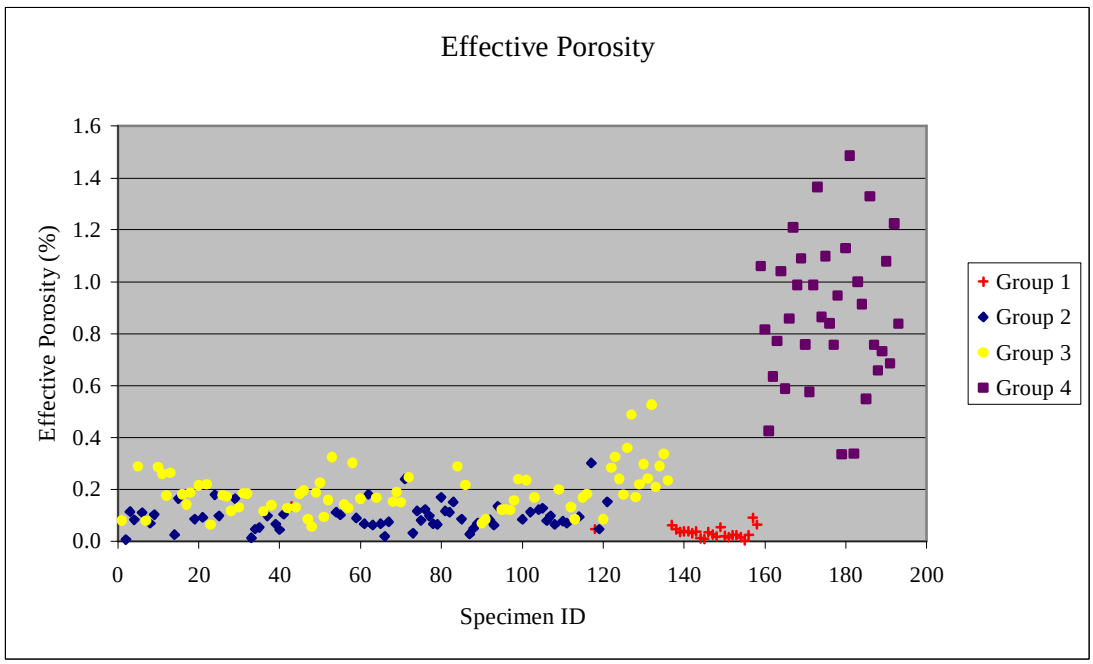

Figure 5.17 Effective porosity of the test specimens.

5.2.5.3 Unit Weight Determination of the Test Specimens

Since some of the specimens have chappy edges on the corners, the volumes of the specimens have been measured by Archimedes method. In order to calculate the exact volume of the test specimens, the weights in air and in water have been determined for each specimen (Figure 5.18).

Figure 5.18 Weighing the specimen in water.

According to the Archimedean principle, the buoyancy force acting on an object ($W_{in\ air}$-$W_{in\ water}$) is equal to the volume of the object times the density of the liquid in which the object has been placed (Equation 5.4).

$$W_{in\ air}-W_{in\ water} = V\times\gamma \qquad (5.4)$$

The weights have been determined in water whose density is assumed as unity in current study. Therefore, the volume is calculated as the difference of the weights of the specimens in air and water, respectively.

After the determination of the precise volumes of the specimens, the unit weights have been computed. The unit weights of the specimens calculated by the volumes determined by Archimedean method are shown in Figure 5.19.

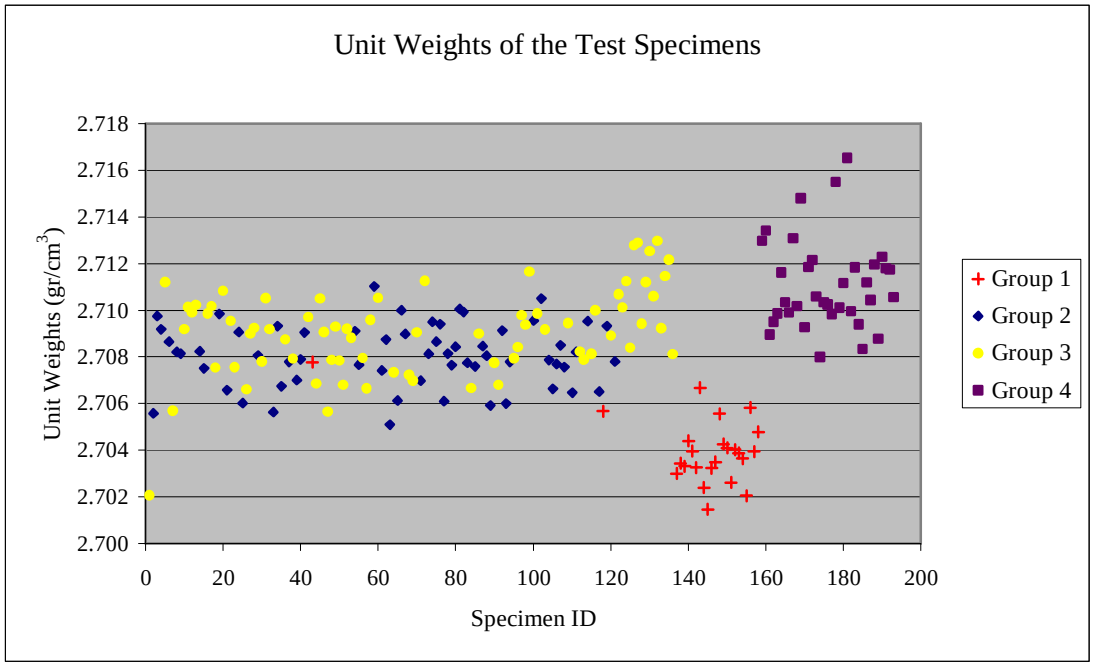

Figure 5.19 The unit weights of the specimens calculated by the volumes determined by Archimedean method.

5.2.5.4 Unconfined Compressive Strength of Test Specimens

Unconfined compressive strength values of the specimens have been determined in the laboratory of the Torbalı Vocational School using a computer controlled test setup with a 300 ton axial load capacity (Figure 5.20). Since 24 specimens have been preserved for future analysis, 169 specimens were subject to destructive tests.

Figure 5.20 The unconfined compressive strength test setup.

The specimens have been placed in the loading frame and axial load is continuously increased on the specimen and applied load is continuously monitored until the specimen failed. The upper platen of the test device was adjusted parallel to the loading surface by means of a spherical seat, which rotates freely in its socket. The axial load was applied along the direction of the fastest ultrasonic pulse wave velocity. The homogeneous isotropic limestone samples exhibited brittle failure mode. The mode of deformation tended to switch towards plastic behavior as the cohesive matrix content increased in the specimens (Figure 5.21).

Figure 5.21 Deformation modes of the tested specimen groups.

The unconfined compressive strength values of the specimens are computed by dividing the ultimate load to the area which lies perpendicular to the loading direction. The variations of unconfined compressive strength values according to the specimen groups are presented in Figure 5.22.

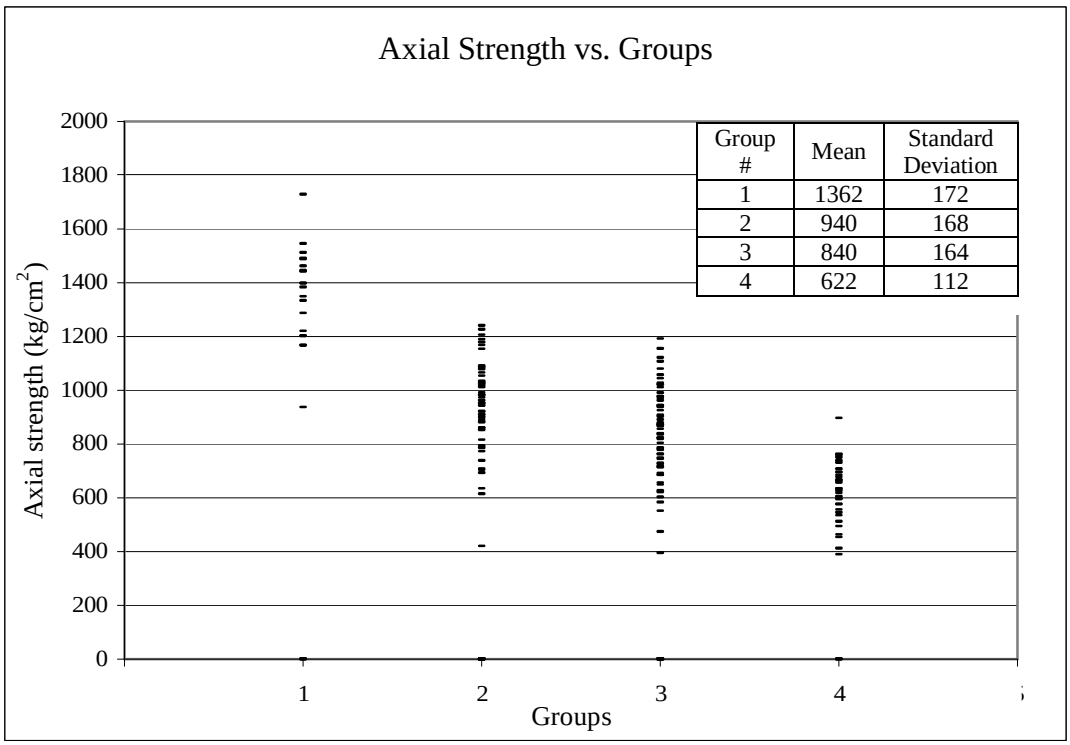

Figure 5.22 Axial strength variations of the specimens in the groups.

5.2.6 Feature Extraction using Image Processing Methods

Since the breccia grain size and orientation are expected to have major effects on the unconfined compressive strength of the test specimens, it was necessary to determine their certain characteristics. This necessity required the segmentation of the breccia grains in the specimen surfaces. This task has been accomplished using digital image processing methods. There after, the area ratio and eccentricity of the breccia grains in the surfaces of the specimens have been computed. The same parameters for each one of the cubic test specimens have been determined on all six surfaces. Therefore, area ratio and eccentricity have been added in the data set so that they could be utilized in the estimation of the unconfined compressive strength of the breccia specimens using these parameters.

5.2.6.1 The Preprocessing of the Specimen Images

Since the acquired images of the specimen surfaces contain the specimen and the background, the quadrilateral surfaces of the specimens have been picked with a selection tool in a commercial drawing software package and resized to 316-by-316 pixel as shown in Figure 5.23.

(a) (b)

Figure 5.23 Unprocessed (a) and preprocessed surface images (b) of the specimens.

The reduction made both in terms of the resolution and the size of the specimen images significantly lowered the computational efforts in the image processing operations. On the other hand, this operation did not affect the breccia grain shape, ratio or other features of the images.

5.2.6.2 Area Ratio of the Breccia Grains

The area ratio of the breccia grains on the surfaces of the specimens have been determined by image processing techniques using MatLab Technical Computing Language. Therefore, an algorithm has been developed to perform grayscale segmentation of the breccia grains in two dimensional surface images of the specimens. Single valued thresholding technique has been applied in order to apply grayscale segmentation to the breccia grains.

The threshold value has been determined by an automatic methodology proposed by Otsu (1979). Instead of the grayscale form of the original image, however, the first layer of the RGB true color images has been used for the prediction of the

threshold value. Namely, the red channel of the RGB true color image has been processed for the determination of the threshold value. This approach has increased the success of the segmentation algorithm as shown in Figure 5.24, where the thresholding were performed by threshold values, determined using red, green and blue channels. Although the red, green and blue channels are color channels, their values are presented as grayscale images in the second column of the same figure.

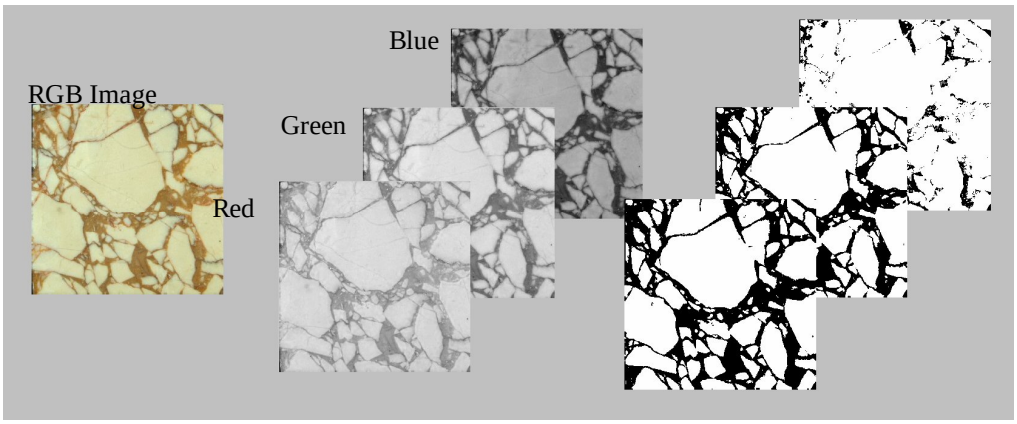

Figure 5.24 Segmentation using the color channels of the specimen images.

On the other hand, the surface images of the homogeneous rock specimens have not been processed by this method. The threshold determination methodology used in this study calculates the threshold value using the histogram of the image. Since the surfaces of the homogeneous limestone (note that breccia grains are of limestone origin) and homogeneous cohesive matrix specimens contain slightly colored veins and slight color variations, the algorithm may have been resulted in erroneous threshold values, causing undesired segmentation results.

The area ratio, described as the ratio of the breccia grains to the cohesive matrix portions, has been calculated as the ratio of pixels that have a value of “1” in the binary matrix to all pixels with values of “1” and “0”. These area ratios were stored in the hard disk for each image as quantitative values.

5.2.6.3 Eccentricity

The eccentricity of the rock specimens has been estimated by using the surface images of the specimens. Therefore, the smallest elements (pixels) of the surface images have been used for the calculation of the centroidal coordinates of each surface by means of the following formulations:

$$c_x = \frac{x_1 + x_2 + \ldots + x_n}{n} \tag{5.5}$$

$$c_y = \frac{y_1 + y_2 + \ldots + y_n}{n} \tag{5.6}$$

where, c is the centroid, x and y are the coordinates of the centroid of each pixel, n is the total number of pixels on the surface. The centroid of the breccia grains of the specimen and the center of the image have been marked with a red cross and a yellow circle in Figure 5.25, respectively. In this manner, the breccia grains are taken into consideration as an equivalent mass generating an eccentricity with respect to the center of the surface image.

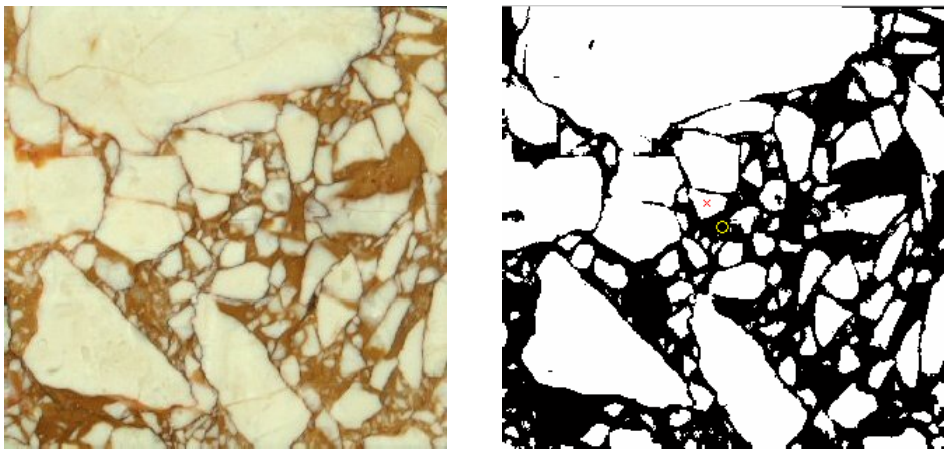

(a) (b)

Figure 5.25 (a) The RGB image and (b) computed eccentricity of the specimen surface.

The three dimensional centroidal coordinates of the breccia grains have been approximated using the centroid and area of the breccia grains on each surface of the

specimens. Therefore, the center of gravity for breccia grains for each axis has been calculated by using the Equations 5.7 to 5.9.

$$\overline{C_x} = \frac{\sum_{i=1}^{6} c_{xi} \times A_i}{\sum_{i=1}^{6} A_i} \tag{5.7}$$

$$\overline{C_y} = \frac{\sum_{i=1}^{6} c_{yi} \times A_i}{\sum_{i=1}^{6} A_i} \tag{5.8}$$

$$\overline{C_z} = \frac{\sum_{i=1}^{6} c_{zi} \times A_i}{\sum_{i=1}^{6} A_i} \tag{5.9}$$

Hence; the total eccentricity of the breccia grains (*e*) of the specimens has been calculated as:

$$e = \sqrt{\overline{C}_x{}^2 + \overline{C}_y{}^2 + \overline{C}_z{}^2} \tag{5.10}$$

The three dimensional centroidal coordinates of the breccia grains in a rock specimen can be best determined with a detailed knowledge about the inner structure. Such a level of knowledge, however, is reached by using powerful X-ray scanning equipment (Garboczi, 2002). Utilization of this kind of equipment was outside the scope of the dissertation. Instead, an approximation was made to define three dimensional eccentricities of the breccia grains with respect to the center of the rock specimen.

5.2.6.4 Three Dimensional Reconstruction of the Specimens

Three dimensional image models of the cubic shaped test specimens have been reconstructed in order to be able to make more in depth examination and keep the 3D

appearances of the samples after they have been subjected to destructive tests. The visual appearances of the cubic samples were virtually obtained in MatLab Technical Computing Language using the surface images of the specimens. The three dimensional models are programmed in OpenGL (Open Graphics Library) environment which enables interactive rotations of the cubic samples. The surface images of the specimens were mirrored and merged together in order to use texture mapping technique as shown in Figure 5.26.

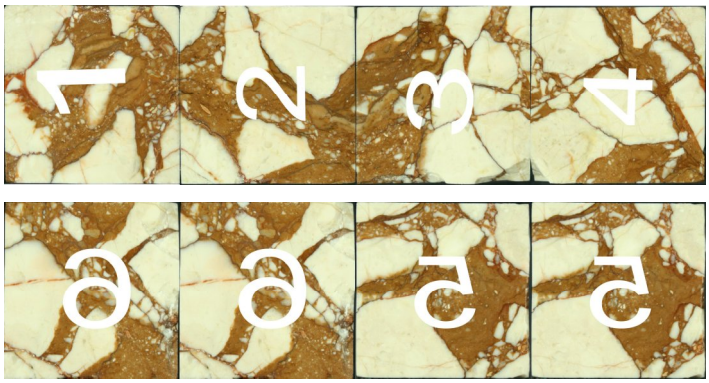

Figure 5.26. Mirrored and merged surface images of the specimen.

The merged images have been warped in a 3D prism and the three dimensional visual appearances of the specimens before the axial strength test were achieved (Figure 5.27).

Figure 5.27 Reconstructed visual appearance of the specimen #131 after destructive test.

5.3 Multiple Linear Regression Analysis of the Test Results

Multiple linear regression analysis is a mathematical technique that aims to learn more about the relationship between several independent variables and a dependent variable by fitting a linear equation to the data. The dependent variable in this study is the unconfined compressive strength of the breccia rock specimens. On the other hand, the laboratory test results such as, effective porosity, unit weight, pulse wave velocity and the features extracted by the image processing operations such as, area ratio, and eccentricity have been used as independent variables. The goal of the multiple linear regression analysis in this study is to predict the result of a destructive laboratory test by using the results of the non-destructive ones. Multiple linear regression analysis can establish that a set of independent variables explains a proportion of the variance in a dependent variable at a significant level through a significance test of R^2, and can establish the relative predictive importance of the independent variables by comparing beta weights.

5.3.1 Multiple Linear Regression Analysis of the Data Set

Multiple linear regression analysis of the data set obtained through the laboratory tests and image processing operations have been performed by using data analysis tools of a commercially available spreadsheet software (Microsoft Corporation, 2003). The methodology behind the spreadsheet multiple linear regression analysis tools is given in the Appendix-A section. Ultrasonic pulse wave velocity, degree of anisotropy, effective porosity, unit weight, area ratio of the breccia grains on the specimen surfaces and their eccentricity values have been used as independent variables to predict the unconfined compressive strength values of the test specimens. Since there exists a strong linear relationship between water absorption and effective porosity values, only the effective porosity parameter has been used in the regression analysis. A total number of 159 specimens have been used in the analysis, following the elimination of 10 out of range results of the unconfined compressive strength test probably caused by the operator dependent errors such as eccentric loading. The relationships between any one independent series and the dependent series, namely unconfined compressive strength values (UCS) are presented in Figure 5.28a-f. The trend lines with respective regression functions and

coefficient of determination values (R^2), which best represent the relationships between each parameter and the unconfined compressive strength have been shown in the same figure.

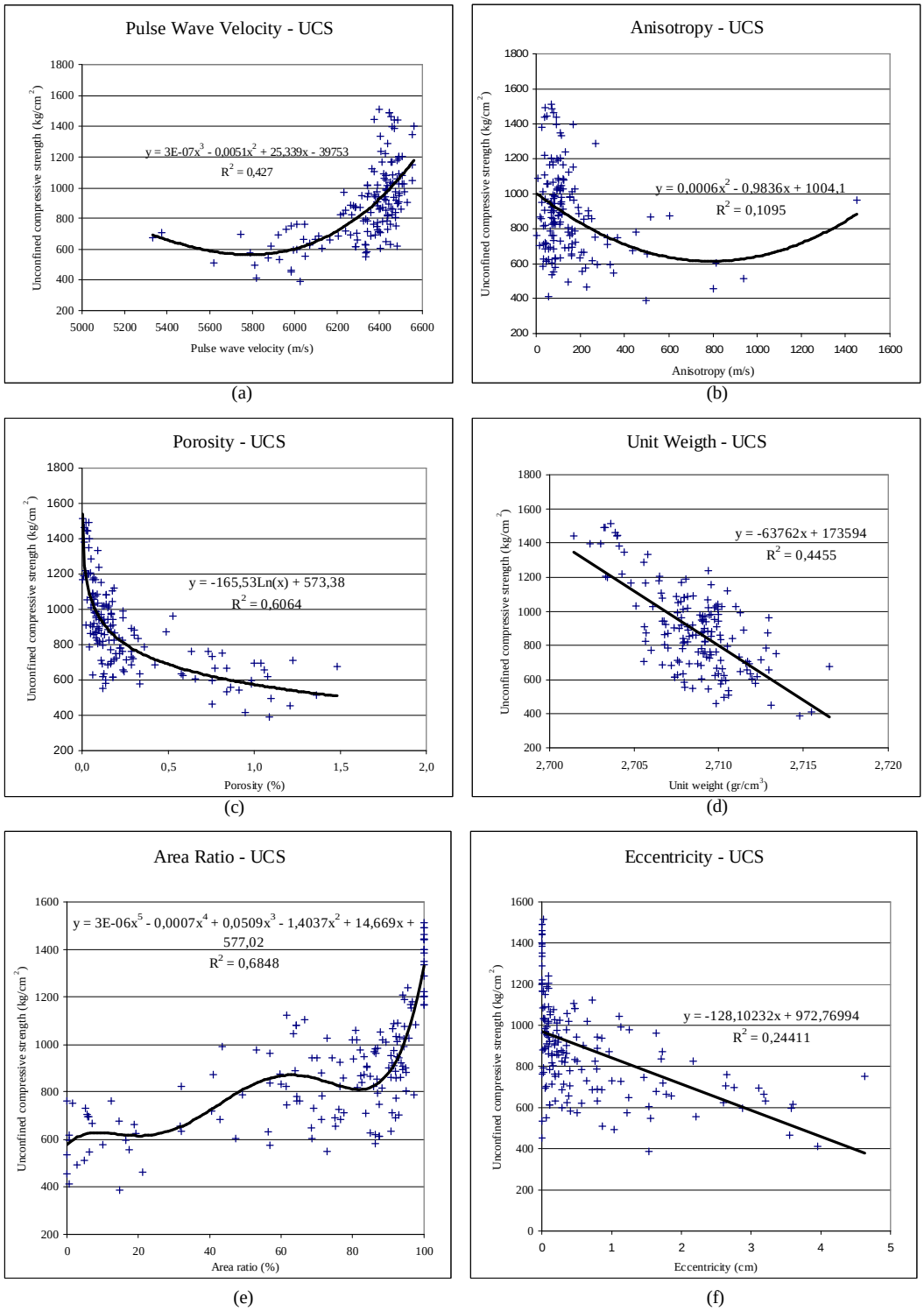

Figure 5.28 The relationship between any one independent series and the dependent series.

The multiple linear regression theory assumes that the relationship between any one independent series and the dependent series must be linear. However, only unit weight and eccentricity values with respect to the unconfined compressive strength can be best captured as linear relationships in Figure 5.28. Therefore, a linearization process has been applied to the other independent variables in order to obey the theory of the multiple regression theory and produce model predictions for the regression analysis.

The regression functions of each independent variable with respect to the dependent variable have been used as the transformation function in the linearization process. In this manner, a new data set has been generated via the regression function (i.e. the independent variable has been input into the function to map the x-axis on the axis of the dependent variable). The results of this process are given in Figure 5.29 where linear relationships between modified independent variables with respect to the dependent variable are shown.

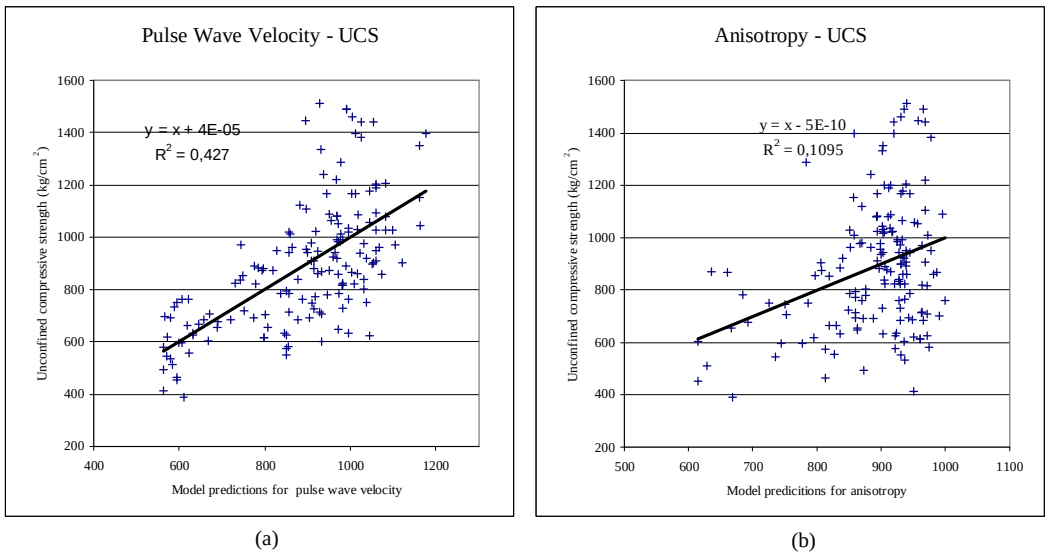

(a) (b)

Figure 5.29 Relationships after linearization process.

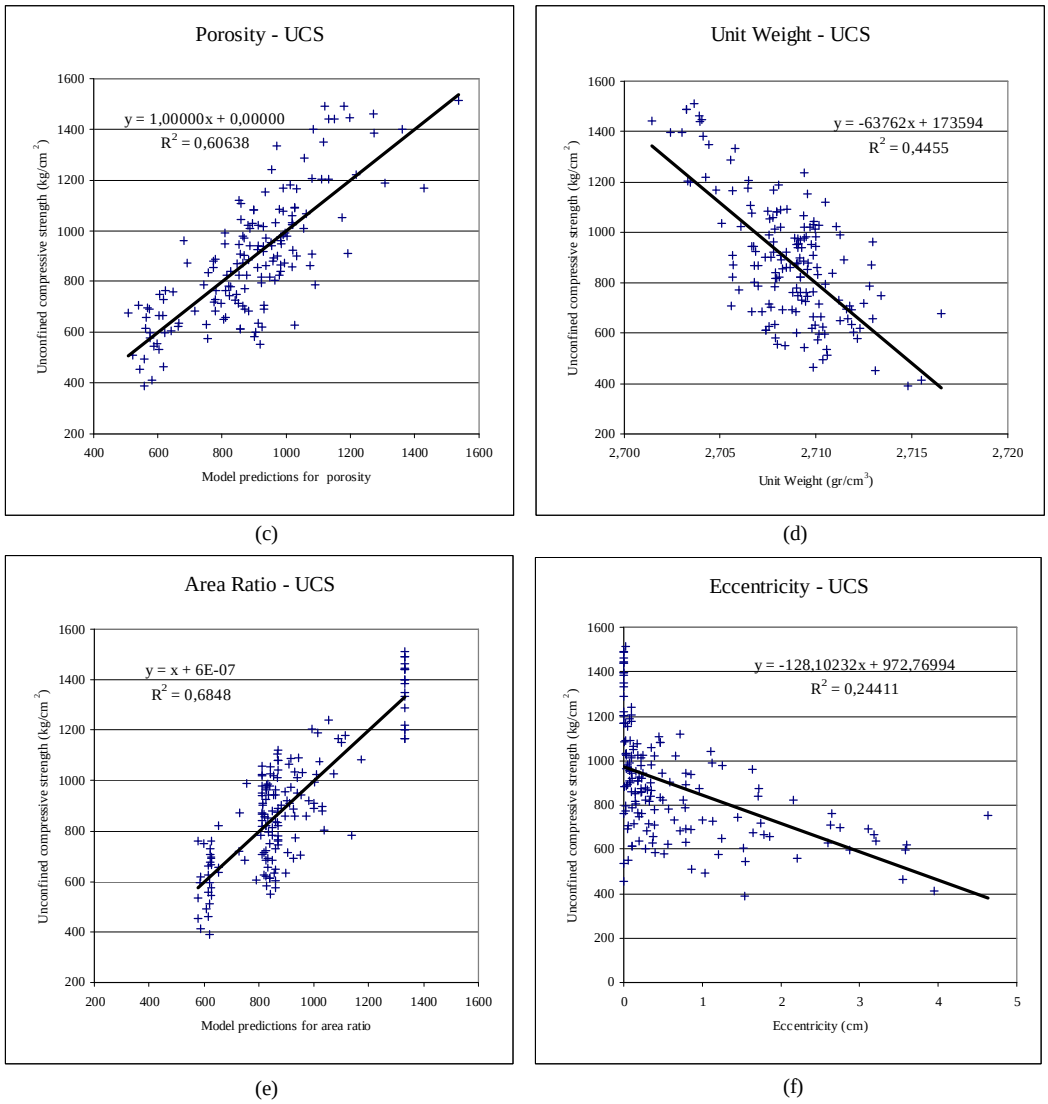

Figure 5.29 Continued.

The multiple linear regression analysis has been performed between the model predictions and the unconfined compressive strength values using data analysis tools of the spreadsheet software. The results table is shown in Table 5.1.

The multiple linear regression function is determined as;

$$Y=5115.4221 + 0.1898\times X_1 + 0.0624\times X_2 + 0.7157\times X_3 - 1987.3277\times X_4 + 0.3095\times X_5 + 31.7877\times X_6 \quad (5.10)$$

where;

Y is the unconfined compressive strength,

X_1 is the model prediction of pulse wave velocity,

X_2 is the model prediction of degree of anisotropy,

X_3 is the model prediction for area ratio,

X_4 is the unit weight,

X_5 is the model prediction for effective porosity,

X_6 is the eccentricity.

Table 5.1 Multiple linear regression results.

SUMMARY OUTPUT

Regression Statistics	
Multiple R	0,85
R Square	0,72
Adjusted R Square	0,71
Standard Error	131,76
Observations	159

ANOVA

	df	*SS*	*MS*	*F*	*Significance F*
Regression	6	6751865,79	1125310,97	64,82	1,98455E-39
Residual	152	2638831,12	17360,73		
Total	158	9390696,91			

	Coefficients	*Standard Error*	*t Stat*	*P-value*	*Lower 95%*	*Upper 95%*
Intercept	5115,4221	19119,5053	0,2675	0,7894	-32658,8678	42889,7120
X Variable 1	0,1898	0,1133	1,6754	0,0959	-0,0340	0,4137
X Variable 2	0,0624	0,1503	0,4151	0,6787	-0,2346	0,3593
X Variable 3	0,7157	0,1043	6,8644	0,0000	0,5097	0,9217
X Variable 4	-1987,3277	7033,6162	-0,2825	0,7779	-15883,6003	11908,9449
X Variable 5	0,3095	0,1351	2,2908	0,0233	0,0426	0,5765
X Variable 6	31,7877	15,8713	2,0028	0,0470	0,4309	63,1445

The unconfined compressive strength values calculated by means of Equation 5.10 for each specimen are presented with respect to the measured unconfined compressive strength values in Figure 5.30.

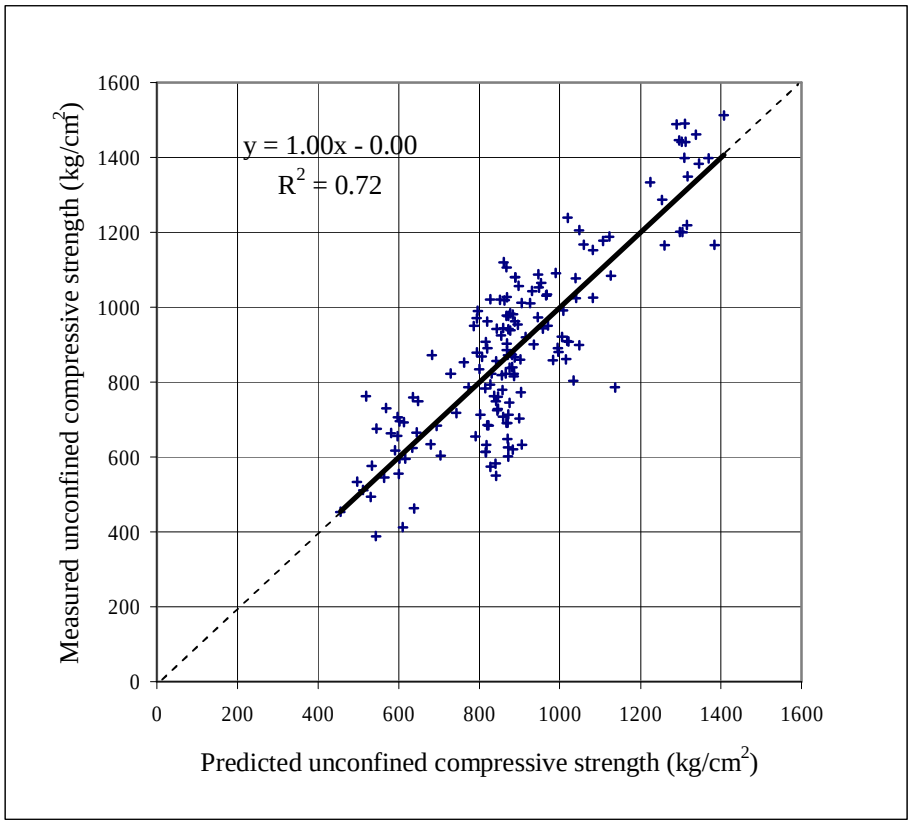

Figure 5.30 The measured and predicted values of the unconfined compressive strength.

The square of the correlation coefficient, called as the coefficient of determination (R-square), is found as 0.72. This means that 72% of the variation in the UCS can be estimated using the independent variables and remaining 28% may be attributed to some other parameters that are not defined yet and testing errors.

$$R^2 = \frac{\text{Sum of squares of regression}}{\text{Sum of squares of (regression + residuals)}} = \frac{\text{Explained variation of Y}}{\text{Total variation of Y}} \quad (5.11)$$

The sum of squares of regression and the sum of squares of total variation can be calculated by the following equations, where the $\overline{X}$ term denotes the mean values. The validity of multiple linear regression model can be judged by performing some standard statistical tests, such as the F-test and the t-test.

$$\text{Sum of squares of regression} = \sum_{k=1}^{6} b_k^2 \sum_{i=1}^{n} (X_{k,i} - \overline{X})^2 \quad (5.12)$$

$$\text{Sum of squares of (regression + residuals)} = \sum_{i=1}^{n} Y_i^2 - n \times \overline{Y}^2 \quad (5.13)$$

5.3.1.1 The F-Test

The F-Test in the Anova table of Table 5.1 is a statistical test, which is used to test the statistical significance of the overall relationship between the dependent variable and the set of independent variables. The F ratio can be calculated by;

$$F=\frac{\text{Mean square of regression}}{\text{Mean square of residuals}} \tag{5.14}$$

Mean square of regression is computed by dividing sum of squares of regression by a number referred to as its degrees of freedom. In a similar manner, the mean square of residuals is computed by dividing sum of squares of residuals by its degrees of freedom.

The test is called F-test, since the calculated value is compared to the F-Table, proposed by Snedecor (1956). The critical F value for the 6 degrees of freedom for the numerator and >120 degrees of freedom for the denominator is 2.19 for the 95% confidence interval. The F-table is in the Appendix-H section of this dissertation.

Since the computed F value is higher than the critical F value (64.82 > 2.19), the null hypothesis of the test can be rejected, which states that the $\beta_1=\beta_2=\ldots=\beta_6=0$ (at least one independent variable affects the variances in the unconfined compressive strength). The presumed model is highly significant.

5.3.1.2 The t-Test

Since the result of the F test from the analysis of variance table is significant, indicating that at least one of the explanatory variables is independently associated with the dependent variable, it is necessary to establish which one of the independent variables is a useful predictor for the dependent variable.

Each of the regression coefficients in the model can be tested using a statistical test (t-test) which follows the t-distribution, proposed by Gosset (1908), with n-k-1 degrees of freedom, where n is the sample size and k is the number of independent variables in the model. The null hypothesis for the t-test states that the coefficient for the independent variable is zero (β=0). In order to reject the null hypothesis, the t values of the independent variables should be greater than the t critical values, derived from the student t distribution table for the desired confidence level. If the null hypothesis is rejected, than there is a strong evidence that a particular independent variable (X_i) has a significant effect on dependent variable (Y) after adjusting for the effects of the other independent variables in the multiple regression models.

The t values for each explanatory variable in Table 5.1 have been calculated by dividing themselves to their standard error. It should be noted that, the critical t value for the >150 degrees of freedom and 95% confidence level is 1.97 in the student t distribution table, which is embedded in the Appendix-I section of this dissertation. Hence, some of the explanatory variables accept the null hypothesis in the Table 5.1. Therefore, a variable selection approach has to be used, in order to determine which variables are significant for the model. This is made in the following.

5.3.1.3 Variable Selection Procedures in Regression

The approaches for variable selection are based on the try and fail procedure because the significance of the variables depends on the variables used in the model. The backward elimination (step-down) method is chosen as the most appropriate variable selection procedure. The multiple regression model is established using all of the available independent variables. The backward elimination technique allows us to search for most meaningful parameters by re-establishing the model after taking out the parameters that failed in the t-test from the data set. Details of this technique are given in Petrie et al. (2002).

5.3.1.4 Backward Elimination

The F and t test results have been used as the criteria for the significance analysis. The explanatory variables X_2 and X_4, representing anisotropy and unit weight values, respectively, in Table 5.1 have been removed from the model. The two variables have been eliminated in the first step, since their significances are relatively low with respect to the other variables in the multiple liner regression model analysis. The multiple linear regression analysis with the remaining explanatory variables is presented in Table 5.2.

Table 5.2 First step analysis in the backward elimination procedure.

SUMMARY OUTPUT

Regression Statistics	
Multiple R	0.85
R Square	0.72
Adjusted R Square	0.71
Standard Error	131.02
Observations	159

ANOVA

	df	*SS*	*MS*	*F*	*Significance F*
Regression	4	6746955.378	1686738.845	98.25	2.31106E-41
Residual	154	2643741.533	17167.15281		
Total	158	9390696.911			

	Coefficients	*Standard Error*	*t Stat*	*P-value*	*Lower 95%*	*Upper 95%*
Intercept	-234.1144	89.4913	-2.6161	0.0098	-410.9033	-57.3254
X Variable 1	0.7203	0.0954	7.5522	0.0000	0.5319	0.9087
X Variable 2	0.3410	0.1201	2.8390	0.0051	0.1037	0.5783
X Variable 3	30.5601	15.5970	1.9594	0.0519	-0.2517	61.3718
X Variable 4	0.1795	0.1104	1.6269	0.1058	-0.0385	0.3976

The variables in Table 5.2 are area ratio of the breccia grains in the specimen surfaces (X_1), effective porosity (X_2), eccentricity (X_3) and pulse wave velocity (X_4). Please note that, removing two explanatory variables did not affected the coefficient of determination (R^2), which means that these variables have no or very minor effect over the variations in the estimates of the unconfined compressive strength values of the specimens.

Since the t test result of the X_4 variable (1.6269) is lower than the critical t value in the student t table (1.97), this variable has not been utilized in further analyses. The result of the second step of the backward elimination procedure has been shown in Table 5.3.

Table 5.3 Second step of the backward elimination process.

SUMMARY OUTPUT

Regression Statistics	
Multiple R	0.84
R Square	0.71
Adjusted R Square	0.71
Standard Error	131.72
Observations	159

ANOVA

	df	*SS*	*MS*	*F*	*Significance F*
Regression	3	6701517.13	2233839.04	128.75	0.00
Residual	155	2689179.79	17349.55		
Total	158	9390696.91			

	Coefficients	*Standard Error*	*t Stat*	*P-value*	*Lower 95%*	*Upper 95%*
Intercept	-152.6725	74.5735	-2.0473	0.0423	-299.9840	-5.3610
X Variable 1	0.7273	0.0958	7.5931	0.0000	0.5381	0.9165
X Variable 2	0.4276	0.1082	3.9499	0.0001	0.2137	0.6414
X Variable 3	22.9251	14.9531	1.5331	0.1273	-6.6130	52.4632

Please note that, the t test result for the eccentricity decreases below the critical value, whereas the same parameter is increases for the effective porosity. A last step for the backward elimination is necessary in order to fulfill the elimination criteria (t > 1.97) by removing the eccentricity variable as shown is Table 5.4.

The predicted unconfined compressive strength values of the specimens after backward elimination are computed by the regression function and shown in Figure 5.31;

$$Y = -69.3343 + 0.7098 \times X_1 + 0.3681 \times X_2 \quad (5.15)$$

where, X_1 and X_2 are the model predictions for the area ratio of the breccia grains and the effective porosity of the specimens and Y is the predicted unconfined compressive strength value.

Table 5.4 Final step of the backward elimination process.

SUMMARY OUTPUT

Regression Statistics	
Multiple R	0.84
R Square	0.71
Adjusted R Square	0.71
Standard Error	132.29
Observations	159

ANOVA

	df	*SS*	*MS*	*F*	*Significance F*
Regression	2	6660736.95	3330368.47	190.31	0.00
Residual	156	2729959.97	17499.74		
Total	158	9390696.91			

	Coefficients	*Standard Error*	*t Stat*	*P-value*	*Lower 95%*	*Upper 95%*
Intercept	-69.3343	51.2736	-1.3522	0.1783	-170.6144	31.9457
X Variable 1	0.7098	0.0955	7.4314	0.0000	0.5211	0.8985
X Variable 2	0.3681	0.1015	3.6267	0.0004	0.1676	0.5686

Please note that, the significance of the regression model (F) has gradually increased in the backward elimination process, while the t values of the variables are computed at each step.

The multiple linear regression function (Equation 5.15) can be presented as a three dimensional surface, where, the explanatory variables (X_1 and X_2) and the response (Y) constitute the orthogonal axes of the graph. Since a linear model was used in the regression, the predicted values constituted a flat surface as shown in Figure 5.32.

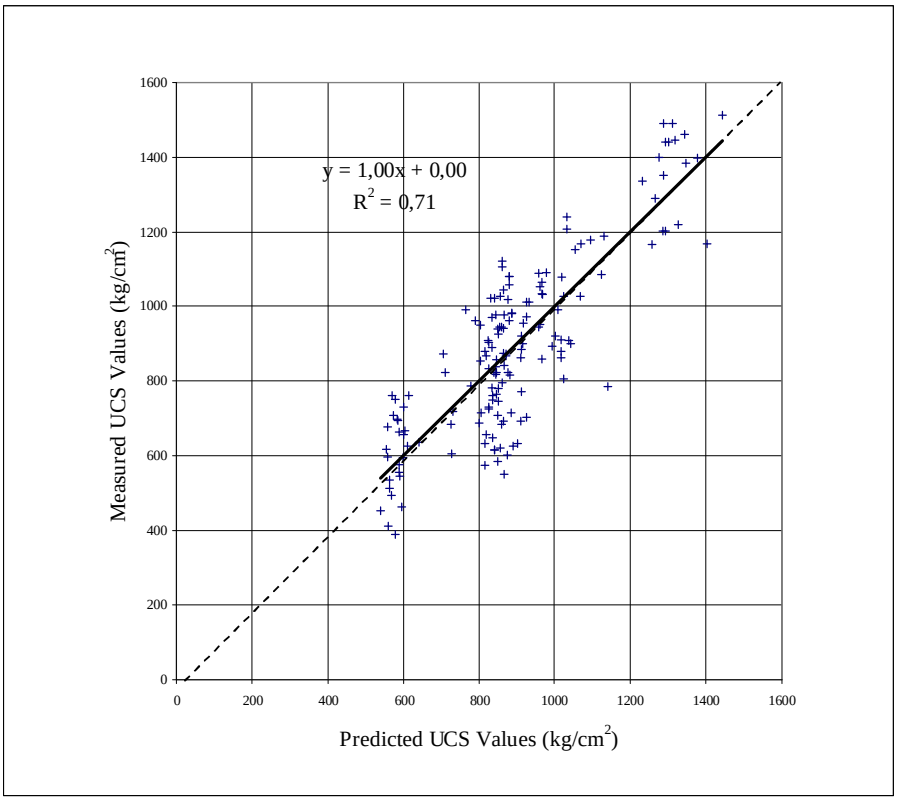

Figure 5.31 The measured and predicted values of the final regression model.

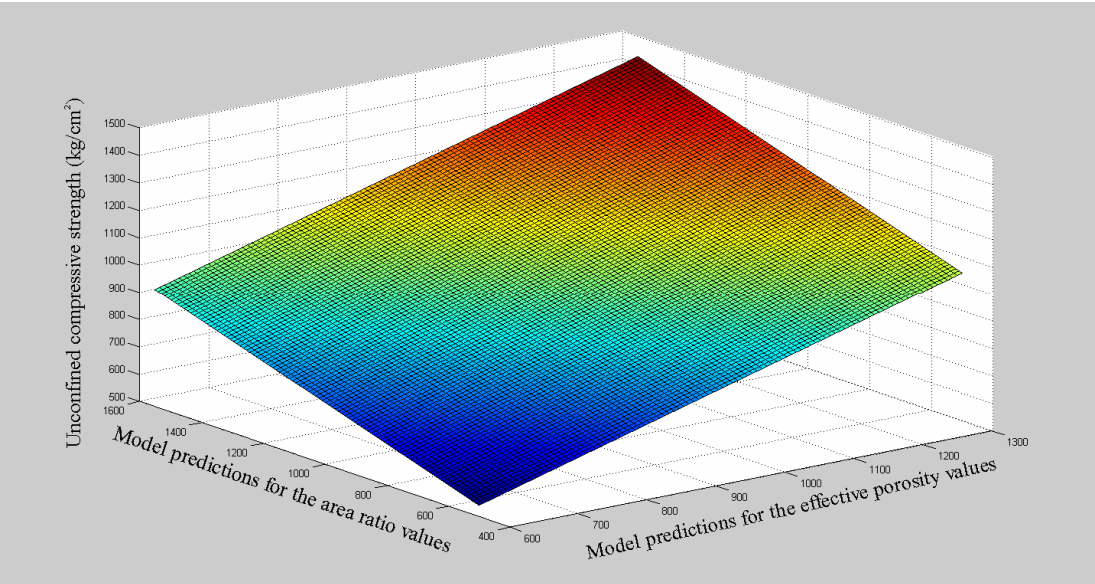

Figure 5.32 The graphical presentation of the predicted values.

It should be mentioned that the x and y axes of the Figure 5.32 are model predictions for the multiple linear regression analysis. The linearization functions can be employed to transform the model predictions to the original input series.

Therefore, the linearization function for the area ratio of the breccia grains of the specimen (Equation 5.16) and the linearization function for the effective porosity values (Equation 5.17) have been used in the Equation 5.15 as presented in Equations 5.18 and 5.19.

$$T_1=0.00000321\times X_1^5 - 0.00069671\times X_1^4 + 0.05092200\times X_1^3 - 1.40367201\times X_1^2 + 14.66937616\times X_1 + 577.02293557 \quad (5.16)$$

$$T_2=-165.52643541*\mathrm{Ln}(X_2) + 573.37706057 \quad (5.17)$$

$$Y_T= -69.3343 + 0.7098 \times T_1 + 0.3681 \times T_2 \quad (5.18)$$

$$Y_T= 2.27665E\text{-}06\times X_1^5-0.00049453\times X_1^4+0.03614444\times X_1^3-0.99632639\times X_1^2 +10.4123232\times X_1-60.93028088\times \log(X_2)+ 551.2967 \quad (5.19)$$

The function derived in Equations 5.16 to 5.19 has been presented in Figure 5.33 as a three dimensional surface. Although the regression function presented in Figure 5.33 looks like a result of a multiple nonlinear regression analysis, the nonlinearity of the regression function is caused from the transformations in the explanatory variables.

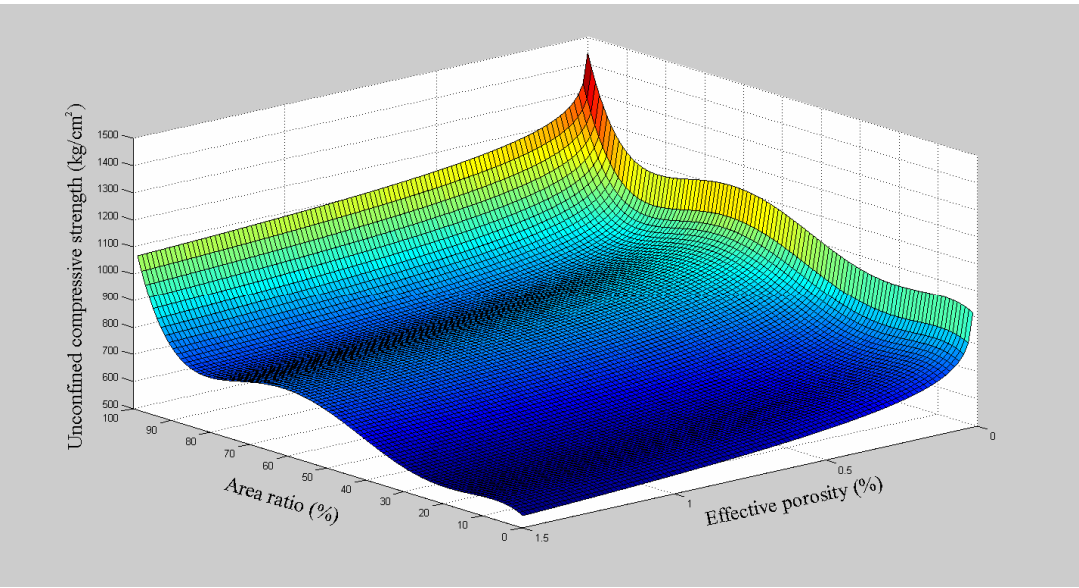

Figure 5.33 The graphical presentation of the final regression function.

It should be mentioned that the proposed regression model is only valid for the allowable intervals of the explanatory variables (i.e. 0 to 100 for the area ratio of the breccia grains and 0.003 to 1.485 for the effective porosity).

The correlation between the area ratio of the breccia grains and the effective porosity of the specimens has been investigated. A trend line with a correlation coefficient of 0.87 can be computed using least squares approximation as a second order polynomial function (Figure 5.34).

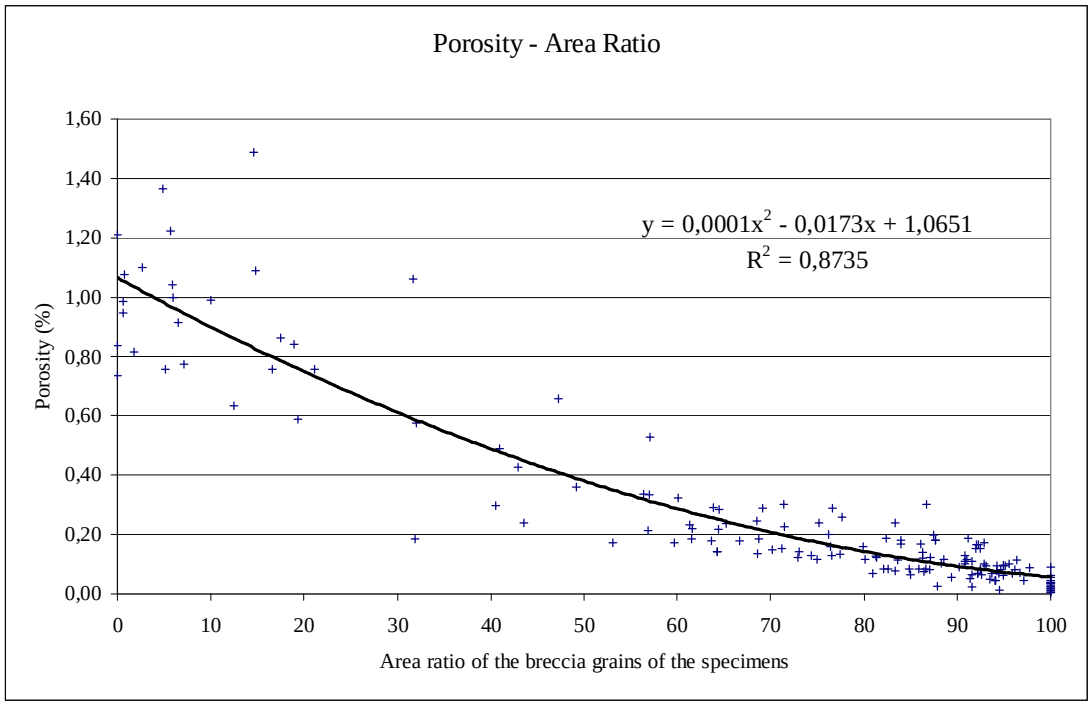

Figure 5.34 Correlation between area ratio of the breccia grains and the effective porosity of the specimens.

Since there is a strong relationship between effective porosity and area ratio of the breccia grains of the specimens, the final regression function of the multiple linear regression model as presented in Equation 5.19 can be further reduced to an equation with a single variable. However, one should note that, such an attempt would reduce the significance of the overall model. On the other hand, this approach has the advantage of rapid evaluation of the unconfined compressive strength values, since the variable used in this approach can be obtained by digital image processing operations.

5.4 Neural Network Analysis of the Test Results

It has been already mentioned in previous sections that the nature of the data and cross correlations between the various elements of the data set are often nonlinear in geomaterials. The multiple linear regression method, however, requires that the data set to be linear. In case of the existence of nonlinearities, the data are linearized by means of transfer functions.

It has been thought in this study that utilization of another data analysis technique, which is capable of searching nonlinear relationships more thoroughly, would be beneficial. Such an attempt would also be useful in cross checking the validity of the outcome of the multiple linear regression analysis. In the current state of the art practice the artificial neural network (ANN) method is acknowledged as one of the contemporary data analysis approaches.

In function approximation problems feed forward back propagation technique is the preferred method (Werbos, 1994). Therefore, algorithm of this neural network approach has been employed in the prediction of the unconfined compressive strength values of the test specimens using the same data set. In the following, results of the neural network analyses are presented. A brief section regarding the theory of the feed forward back propagation neural network method is given in Appendix B.

5.4.1 Neural Network Analysis of the Data Set

The results of the nondestructive laboratory tests and the features derived from the digital image processing operations have been used as the data set in the neural network analysis. The half of the data set (i.e. belonging to 79 test specimens) has been employed as the training set in the supervised learning process. Since the success of the network analysis is evaluated by an iterative procedure, the training set has been kept constant in the setup of the network topology as the odd numbered data rows. The remaining data have been used as the test set for the verification of the neural network. Thus, randomized data selection has been avoided in order to

compare the individual runs of the algorithm. However, since the initial weight factors are assigned in a randomized manner, each individual run of the training algorithm shows slightly varying results.

Since the input data set consists of input values that range between different upper and lower limits, a normalization process has been applied to the data so that its mean and standard deviation are set as 0 and 1, respectively. This preprocessing operation maps the data in a new form, more suitable to train the network.

The success of the neural network analysis has been increased by performing principle component analysis, which captures the variance in a data set in terms of principle components. The goal of the principal component analysis is to find an orthogonal set of vectors that maximize the variance of the projected data. Principal component analysis is a linear transformation of the data into another frame of reference with as little error as possible in order to extract relevant information from high dimensional data sets.

The preprocessed data set has been used in the feed forward back propagation algorithm offered by the neural network toolbox of the MatLab Technical Computing Language. The topology of the network has been organized to consist of one hidden layer with ten neurons, having tangent sigmoid function, and one output layer, having linear function as in the general function approximation applications.

The training has been conducted until maximum epoch, predefined as 250, was reached. The maximum epoch has been determined as 250, because, a decrease in errors over the training data does not mean a decrease over novel data and in fact may lead to less generalization, which is called as over-learning. Over-learning results in an over fitted function, which has good approximation for the training set, but poor approximation for the test set.

After the completion of the network training process, test data set have been normalized using the pre-calculated mean and standard deviation of the training set.

The normalized test data set have been preprocessed by applying the same principal component transformation that was previously computed for the training data. Hence, the test data has been preprocessed in order to use in the trained network.

The simulation of the network has been conducted by using the preprocessed test data. However, the performance of the network can only be evaluated by post processing the output of the network. Therefore, the same transformation matrices used in the preprocessing of the train and test data (i.e. principle component analysis and then normalization), have been used in the post processing operations.

The performance of the network has been evaluated both calculating the percentage errors and presenting the coefficient of determination for the predicted and original values of the data set. Since the initial weight factors are assigned in a random manner, the algorithm has been executed 30 times and the mean of the coefficient of determination and standard deviation of the same value for all runs has been calculated as 0.68 and 0.028, respectively. The same results for the percentage of errors are also calculated as 13.76 and 0.71. Since the training of the network is a trial and error process, the result of the ANN run yielding the highest coefficient of determination value for the data set is presented in Figure 5.35.

A feature elimination procedure similar to the backward elimination of the independent variables in multiple linear regression analysis has been performed. The established network topology has been executed 30 times, while reducing the features in the training set. The maximum, minimum and mean values of the coefficient of determination for the relationship between measured and predicted UCS values have been presented in Table 5.5.

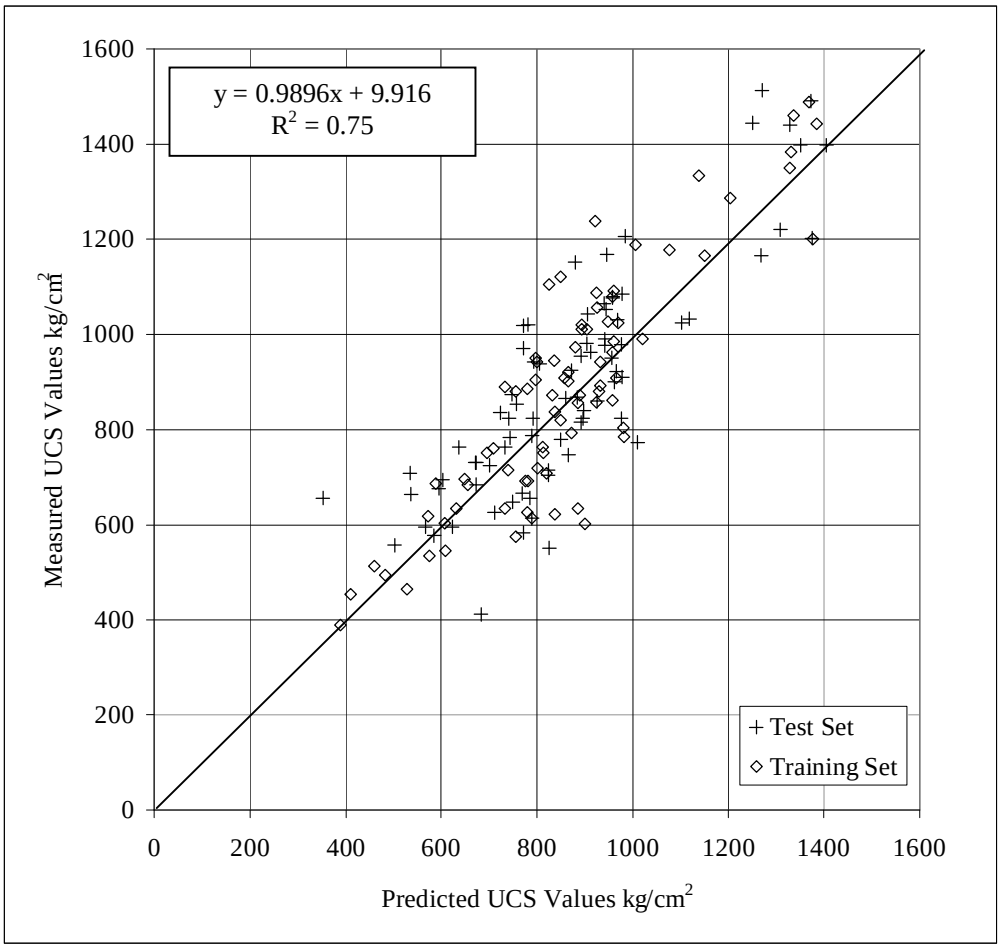

Figure 5.35 The relationship between measured and predicted values of UCS using back propagation neural network algorithm.

Table 5.5 Results of the feature reduction procedure.

Features / **R^2**	Area Ratio E. Porosity Eccentricity Pulse Wave Velocity Anisotropy Unit Weight	Area Ratio E. Porosity Eccentricity Pulse Wave Velocity	Area Ratio E. Porosity Eccentricity	Area Ratio E. Porosity
Max.	0.746	0.698	0.691	0.708
Mean	0.677	0.621	0.650	0.650
Min.	0.628	0.520	0.584	0.540

5.5 Comparison of the Results of MLR and ANN Approaches

The most successful prediction of the UCS values has been obtained by using all of the available features of the cubic breccia rock specimens in both multiple linear regression and artificial neural network analyses. Similar analysis results have been obtained for both data analysis methodologies. The variation in the unconfined compressive strength values of the breccia rock specimens has been explained with a success ratio of 73% using the nondestructive laboratory test and digital image processing operations data. The remaining unexplained part of the variation may be attributed to the existence of an unstudied parameter as well as to the operator and calibration errors inherent in the laboratory tests. Similarly, Sönmez et al. (2004) have obtained similar results in the prediction of the UCS of the 104 Ankara Agglomerate specimens using Fuzzy classification and regression analysis. A relationship, presented by R^2=0.64, has been obtained between the predicted and measured values of the unconfined compressive strength values of the Ankara Agglomerates. On the other hand, Shakoor and Brown (1996) have used Los Angeles abrasion loss, dry density, and absorption parameters in the prediction of the unconfined compressive strength of the 15 carbonate rock specimens using multiple linear regression approach. A coefficient of determination of 0.73 has been found for the homogeneous carbonate rocks.

5.6 Conclusion

Cubic shaped breccia rock specimens have been investigated using laboratory tests and image processing methods, in order to predict the unconfined compressive strength of the test specimens. Specimen and surface preparation operations have been conducted and an image acquisition system has been established.

Nondestructive laboratory tests and features obtained by means of digital image processing operations have been used together to predict the unconfined compressive strength of the breccia rock specimens. Multiple linear regression and feed forward back propagation neural network techniques have been employed in the data

analysis. It has been concluded that, similar results have been achieved using both methods. However, the neural network analysis has been found more advantageous over multiple linear regression analysis, because of the ability of the latter method to take the nonlinearity of the data set into consideration. However, a great proportion of the variation in the unconfined compressive strength values of the cubic test specimens has been explained using both data analysis methods.

It has been determined that the area ratio and effective porosity of the breccia grains have a major influence on the unconfined compressive strength values of the tests specimens. These features can be employed in nondestructive estimation of UCS of the breccia rock specimens. Although the test program may be considered as limited to a certain material source (Saruhanlı-Manisa), the methodology and algorithms followed and developed herein are equally applicable to other types of geomaterials. It should be noted that once the data set and specimen features are established, it is a relatively easy task to derive similar relationships among various data types such as effective porosity versus pulse wave velocity and effective porosity versus area ratio.

CHAPTER SIX
AUTOMATED SEPARATION OF TOUCHING GRAINS USING SKELETON BASED SEGMENTATION

6.1 Introduction

In the last decades, digital image processing has become a very useful tool for the analysis of the granular soils. The size, shape and distribution of the grains have been investigated by various researchers using the digital image processing methods. One of the pioneering applications of the computer vision in geotechnics is the analysis of the grain size distribution of the granular soils (Raschke & Hryciw, 1997; Mora et al., 1998). The particle shape characterization (Brzezicki & Kasperkiewicz, 1999; Bowman, Soga & Drummond, 2001) and its influence on the geotechnical parameters have been also investigated (Sukumaran & Ashmawy, 2001). However, all the above mentioned works use the two-dimensional projection of the grains and give erroneous results when the grains are touching each other.

Since large amount of grains are needed to investigate in order to represent the whole body, intersection of the grain boundaries may occur avoiding individual analyses of grains. The separation of the touching objects has been a very demanding operation in the digital image processing applications. Since the manual separation of the touching grains by an operator is not practical for the engineering purposes, existing autonomous digital separation algorithms were employed by some researchers.

Ghalib & Hryciw used watershed segmentation algorithm for the touching grains in order to investigate the soil particle size distribution in 1999. However, the success of the watershed segmentation algorithm is low when irregular materials like aggregates are the objects to be segmented. The irregularity yields more than one minimum in the distance map for a grain and results in over segmentation of the objects. Therefore, the watershed segmentation algorithm was modified for more

accurate segmentation of the touching grains (Kim et al., 2003; Wang & Paliwal, 2006).

On the other hand, some researchers have developed their own segmentation algorithms for the problem of interest. Berg et al. (2006) have developed a separation algorithm based on the angle of the contact wedges of the grains.

Although some modifications have been made on the watershed segmentation algorithm, the success of the operation still greatly depends on the regularity of the grain shapes generating multiple minima for a single grain. Also the smoothing operation to overcome the multiple local minima problem is an operator dependent operation and may not correctly solve the problem for some grains when the image contains large number of objects.

Therefore, a segmentation procedure has been developed based on the skeleton thinning operation to prevent incorrect separation of the touching grains in this thesis study. The developed algorithm is based on the study of Xu et al. (1999), who used weighted skeletons to separate fiber cross sections for its potential usage in the textile industry. Xu's algorithm (1999) was designed to separate fibers which have regular shapes in general. Many improvements were made to the algorithm and a new procedure has been added in order to separate grain objects when the degree of the regularity of the objects decreased.

In order to prove the efficiency of the separation algorithm, it has been coded in MatLab technical computing language and has been tested on various granular soil samples with varying level of irregularities.

6.2 Skeleton Based Segmentation Algorithm

The segmentation of the touching objects is performed by using the skeleton data of the touching objects. The skeleton based segmentation algorithm consists of six

sub algorithms. The algorithms will be introduced below in the same sequence of the developed MatLab code.

Please note that the skeleton based segmentation algorithm uses the binary image of the grains. Therefore, a proper threshold level needs to be set and a thresholding process needs to be performed in order to achieve binary image of the touching objects.

6.2.1 Generation of Grain Skeletons

Skeleton generation is a morphological process which reduces all objects in a binary image to lines. These simplified caricatures of the objects (skeletons) are very convenient for the shape analysis as they preserve a lot of properties of the initial figure. The first definition of the concept of skeleton was made by Blum (1967). These kinds of techniques have a wide range of applications. For instance, skeleton generation has been applied successfully in solving character recognition problems.

A basic method for skeleton generation is thinning, which is an iterative technique that extracts the skeleton of an object as a result. During iterations, the edge pixels, having at least one adjacent background point, are removed. All those pixels can be eroded, only if its removal doesn't affect the topology of the object. The skeleton represents the shape of the object in a relatively small number of pixels (Parker, 1994). The resulting skeleton line is a central line whose points are in equal distances from two closest points of the object edges (Figure 6.1).

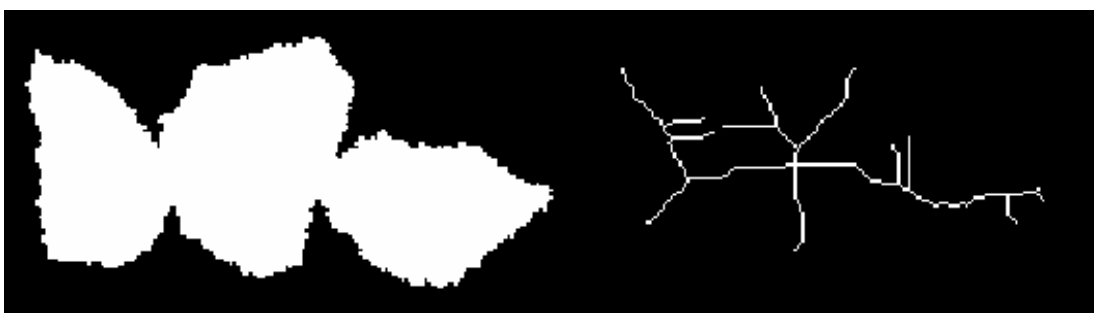

(a) (b)

Figure 6.1 Binary images of the touching grains (a) and their skeleton (b).

6.2.2 Distance Map Matrix

Since the skeletons preserve the structural connectivity of the main components of an object, the distances between a skeleton pixel and the closest boundary pixels yield significant information whether inspected skeleton pixel is on a connection boundary of two components or not.

For such an analysis, the distance transformation is a very convenient approach to generate a distance map. Distance map has the same size with the original binary image whose foreground pixels is replaced with a gray value equal to that pixel's distance from the nearest background pixel.

The distance map can be better visualized as a three-dimensional topological map when the distance values are set as altitude parameters (Figure 6.2).

Figure 6.2 3D presentation of the distance map.

6.2.3 Intersection Matrix

Since the skeleton lines are central, the path these lines follows is always the peak location in the three dimensional topology. On the basis of this circumstance, the intersection of the distance map and the skeletons produce a matrix in which the skeleton contains the connection path data and the distance map contains the distance to the nearest boundary data.

The autonomous separation of the touching grains in this study has been achieved by the analysis of the intersection matrix which has been shown in Figure 6.3.

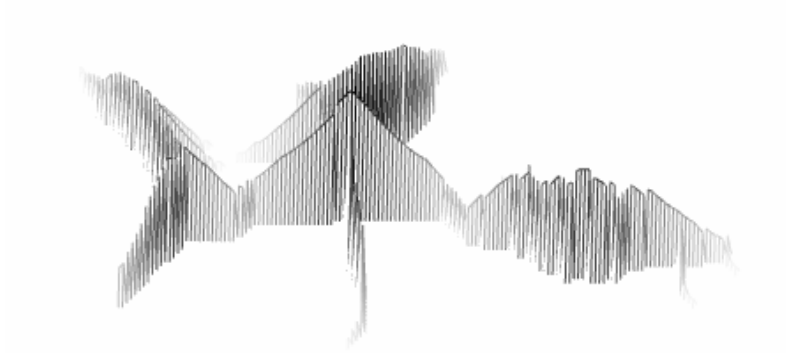

Figure 6.3 The intersection matrix.

As the intersection matrix is visualized as a 3D object, the branches connected to the medial axis always pose upward inclination until they reach an ultimate point.

6.2.4 Removing the Branches

Since the connection of the grains is only possible between two ultimate points, the branches connected to the medial axis needs to be removed from the matrix. This process can be performed by an iterative procedure. In order to remove the branches from the main medial axis, the end points of the skeleton lines need to be detected. The detection process searches the end points of the pixel lines by evaluating the connectivity of every pixel in the skeleton matrix. In skeleton matrix, an edge pixel may be only connected in three different levels of neighborhood condition. The connection map for the edge pixels is presented in Figure 6.4 for possible pixel combinations. Pixels with other connection map conditions in the skeleton matrix may not be an edge pixel.

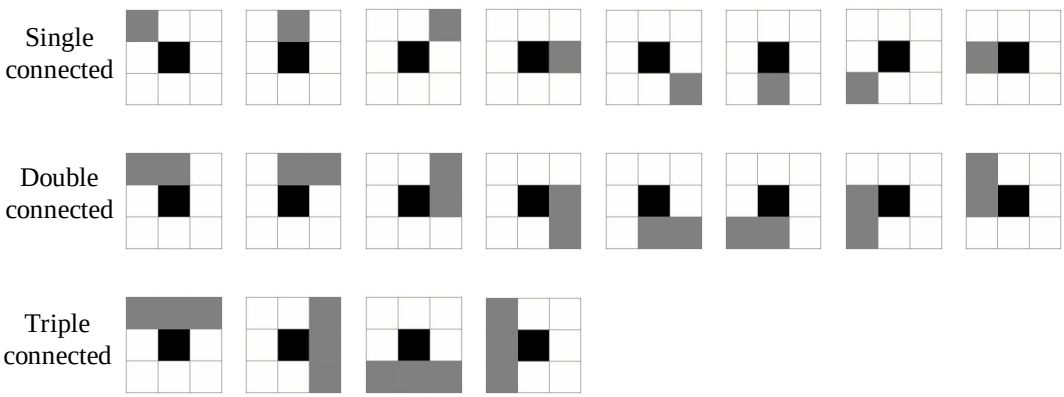

Figure 6.4 The connection maps for single, double and triple connected edge pixels.

The location of the end point pixels and the corresponding value in the intersection matrix are used so that the gradient between the end pixels of consecutive iterations in the intersection matrix could be calculated. Thus, a slope map for each branch has been generated. Due to the local minima on the skeleton paths in the intersection matrix, local downward inclinations have been tolerated by setting two sequent negative gradients as the end criteria for the iteration, which ensured the continuity of the procedure. The above mentioned procedure has been applied until two consequent intersection matrixes are equal during iteration.

6.2.5 Finding the Connection Points

Once the branches have been removed, the medial axis which contains the connection point(s) has been achieved. As shown in Figure 6.5a, it is obvious that the location of the connection between the grain boundaries can be determined by finding the minimum values between two peak points in the intersection matrix. Thus, an averaging operation, which uses a 7×7 smoothing filter, has been applied to the matrix which eliminated local downward inclination and ensured correct locations of the bottom points for the curves (Figure 6.5b).

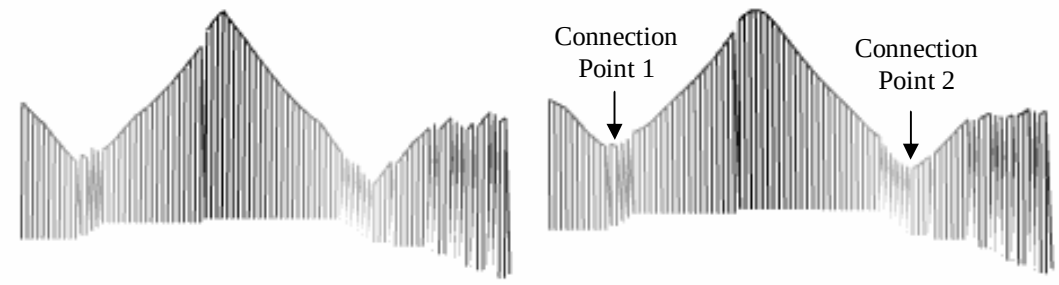

(a) (b)

Figure 6.5 The medial axis which contains the connection points (a), locations of the connection points (b).

The pixels having minimum values (i.e. connection points) in the medial axis have been found iteratively. The pixel having maximum value in the intersection matrix has been found and the neighborhood of this pixel has been examined iteratively. If connectivity with the neighbor pixels has been found, the current pixel has been

removed from the intersection matrix. This procedure continues until no connectivity with the neighboring pixels is left.

6.2.6 Constructing the Separation Lines

In order to construct the separation lines between the grains, the locations of the connection points have been used. The distance map data was employed for the determination of the direction of the separation lines. Therefore, the neighborhoods of the connection points in the distance map matrix have been examined. The pixels, having minimum values, at the two opposite sides of the connection points have been determined and removed from the binary image.

The continuity of the separation lines have been ensured iteratively by finding the minimum value in the neighborhood of the end point of the separation line and removing the pixel which has the same location in the binary image. Thus, the shortest paths to which one can reach with minimum energy through the background have been followed as shown in Figure 6.6a-b. The procedure has ended until no deletion took place.

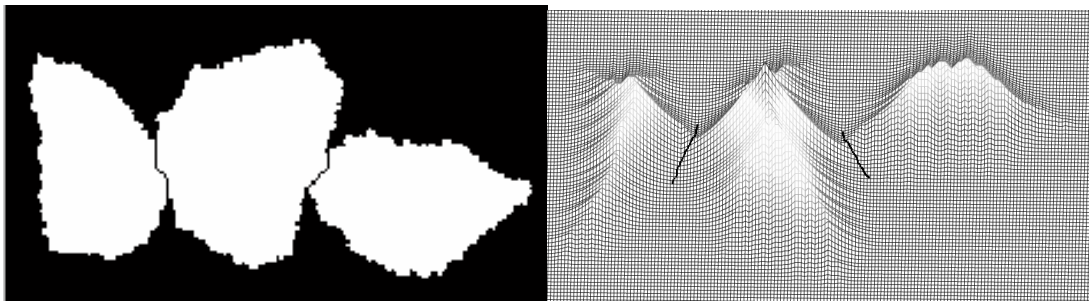

(a) (b)

Figure 6.6 The path of the separation lines (a), the 3D representation of the separation lines over the distance map matrix (b).

6.3 Limitations and Performance

The separation algorithm is sensitive to the internal pixel groups which has the same value as the background pixels and located in the grain objects. This condition may occur due to the reasons listed below:

- An improper threshold level was selected or some grains may have brighter area on their texture.
- When threshold is applied to touching objects, some pixel groups may have the same value as the background pixels at the contact points of the objects (Figure 6.7a).

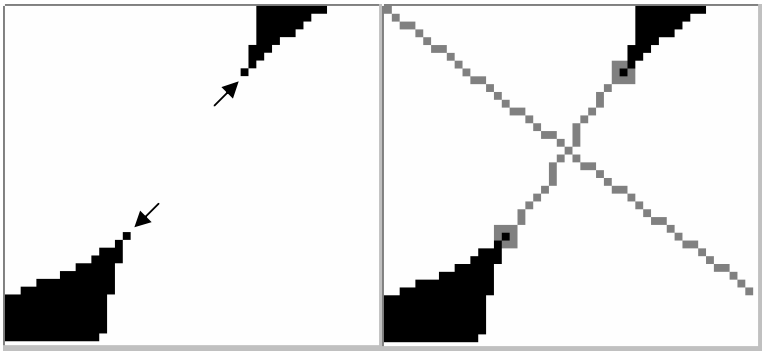

Figure 6.7 Single connected pixels at the contact areas (a), improperly formed skeleton branches (b).

The pixel or pixel groups left over at the contact points of the objects after the thresholding process may result in an over extended skeleton (Figure 6.7b) and a distance map matrix which is deteriorated due to these pixels. Therefore, a subroutine is needed to apply for the grain objects in order to fill the interior gaps with area values less than six pixels. The six pixel limitation was a solution for the pixels that were falsely located at the contact points. One should note that filling of gaps with area values larger than six pixels might generate additional problems since the gaps that are physically exist among the touching grains (Figure 6.8) would not appear otherwise.

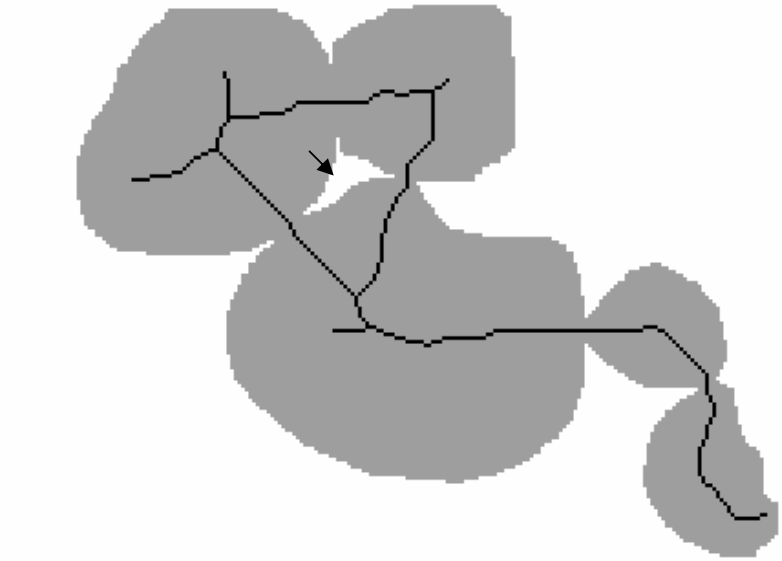

Figure 6.8 The internal gap among the grains and the skeleton of the touching grains.

The developed algorithm is incapable to perform segmentation operations at the pixel groups, whose total areas are less then 49 pixels. This 49 pixel limitation is due to the 7×7 smoothing filter used in the averaging operation during the determination of the minimum points (i.e. connection points) at the intersection matrix.

The algorithm is capable of performing segmentation operation where both touching and non-touching objects are present together in an image. However, the algorithm autonomously performs segmentation operation only at the touching objects. Thus, the speed of the algorithm is dependent on the number of touching objects in an image. The second limitation of the algorithm is the resolution of the image, which both affect the length of the skeletons and the size of the distance map matrix. The flowchart of the skeleton based segmentation algorithm is given in the following.

6.4 Flow Chart of the Segmentation Algorithm

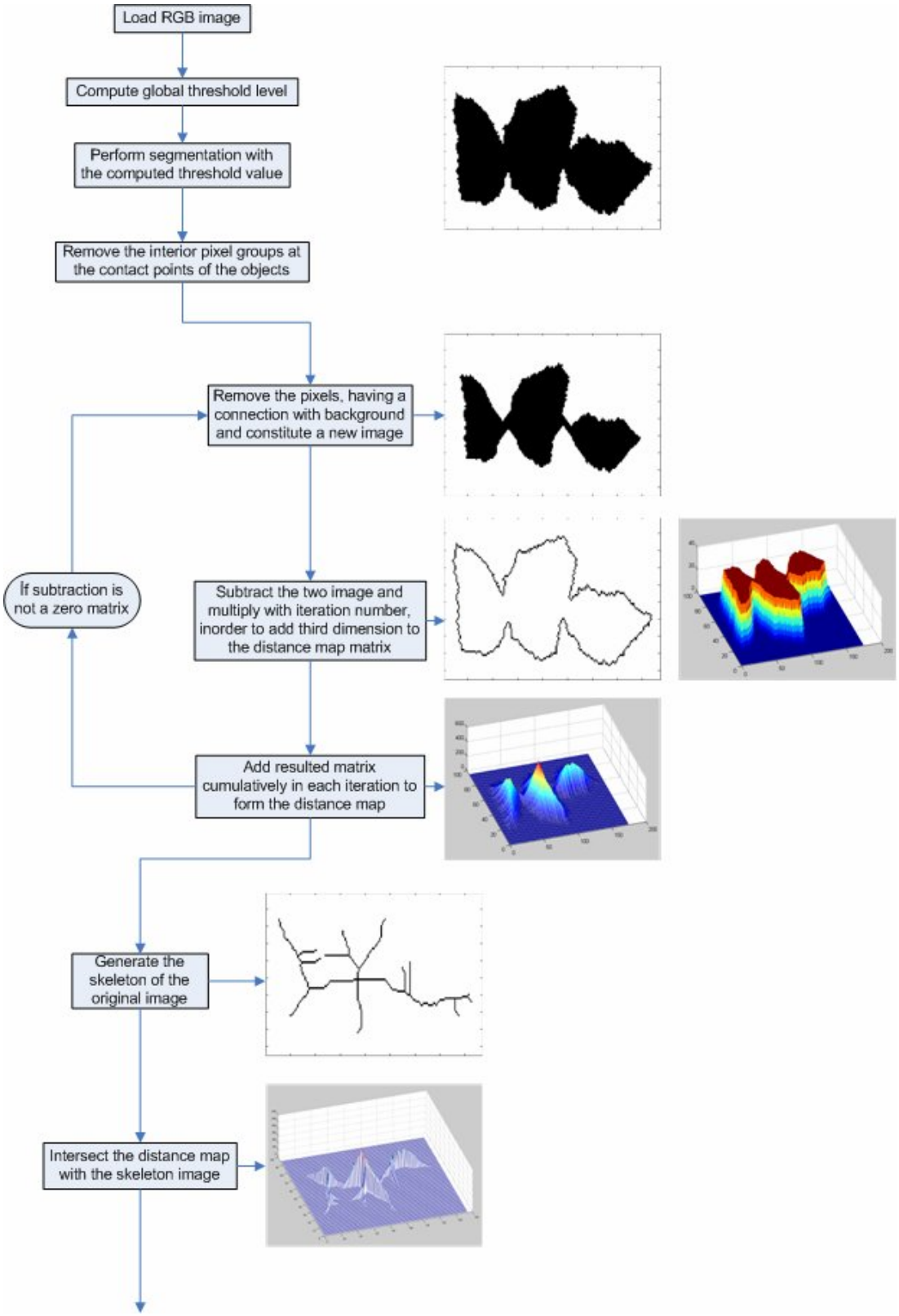

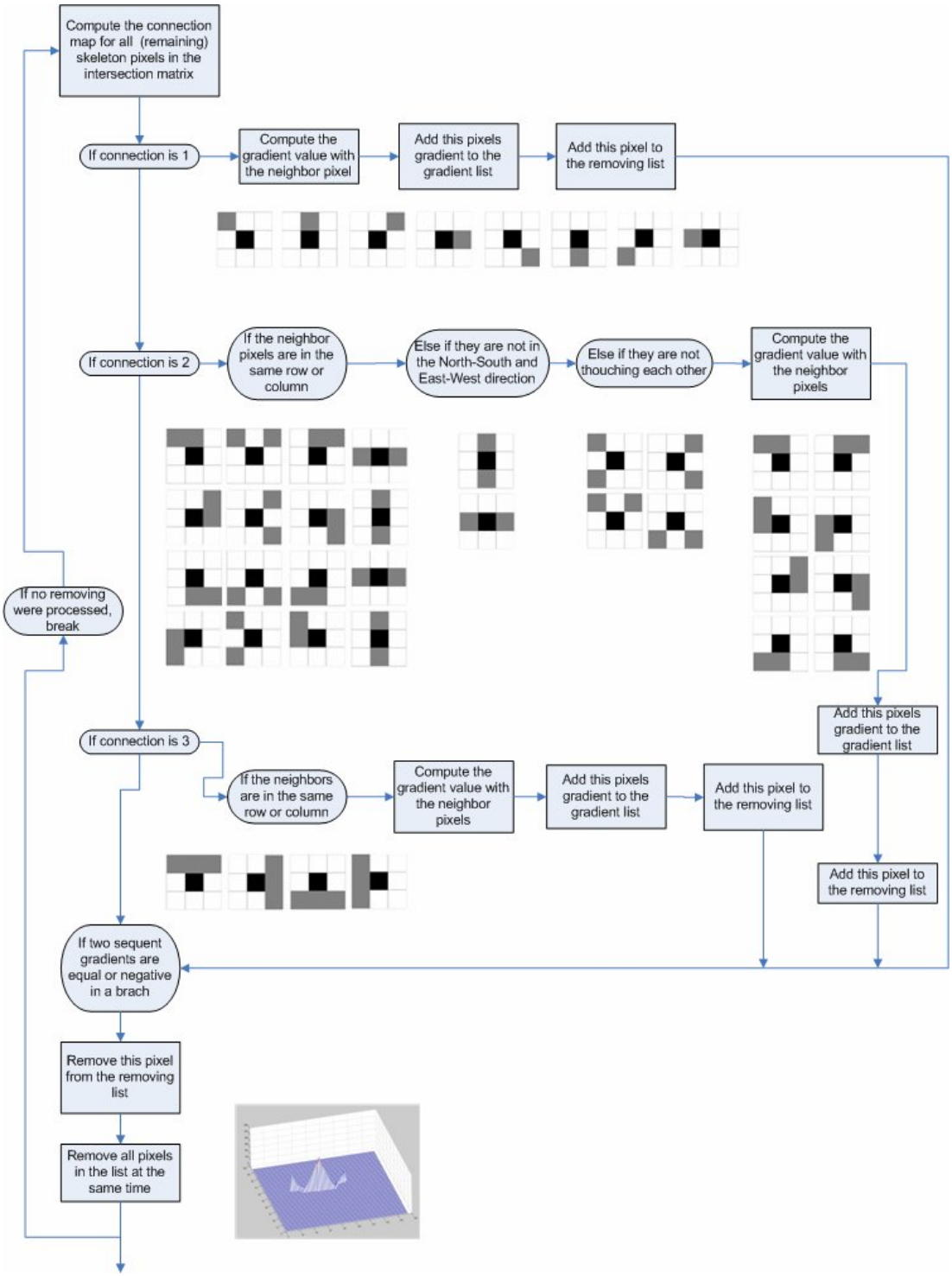
Compute the connection map for all (remaining) skeleton pixels in the intersection matrix
If connection is 1
Compute the gradient value with the neighbor pixel
Add this pixels gradient to the gradient list
Add this pixel to the removing list
If connection is 2
If the neighbor pixels are in the same row or column
Else if they are not in the North-South and East-West direction
Else if they are not thouching each other
Compute the gradient value with the neighbor pixels
Add this pixels gradient to the gradient list
If connection is 3
If the neighbors are in the same row or column
Compute the gradient value with the neighbor pixels
Add this pixels gradient to the gradient list
Add this pixel to the removing list
Add this pixel to the removing list
If two sequent gradients are equal or negative in a brach
Remove this pixel from the removing list
Remove all pixels in the list at the same time
If no removing were processed, break

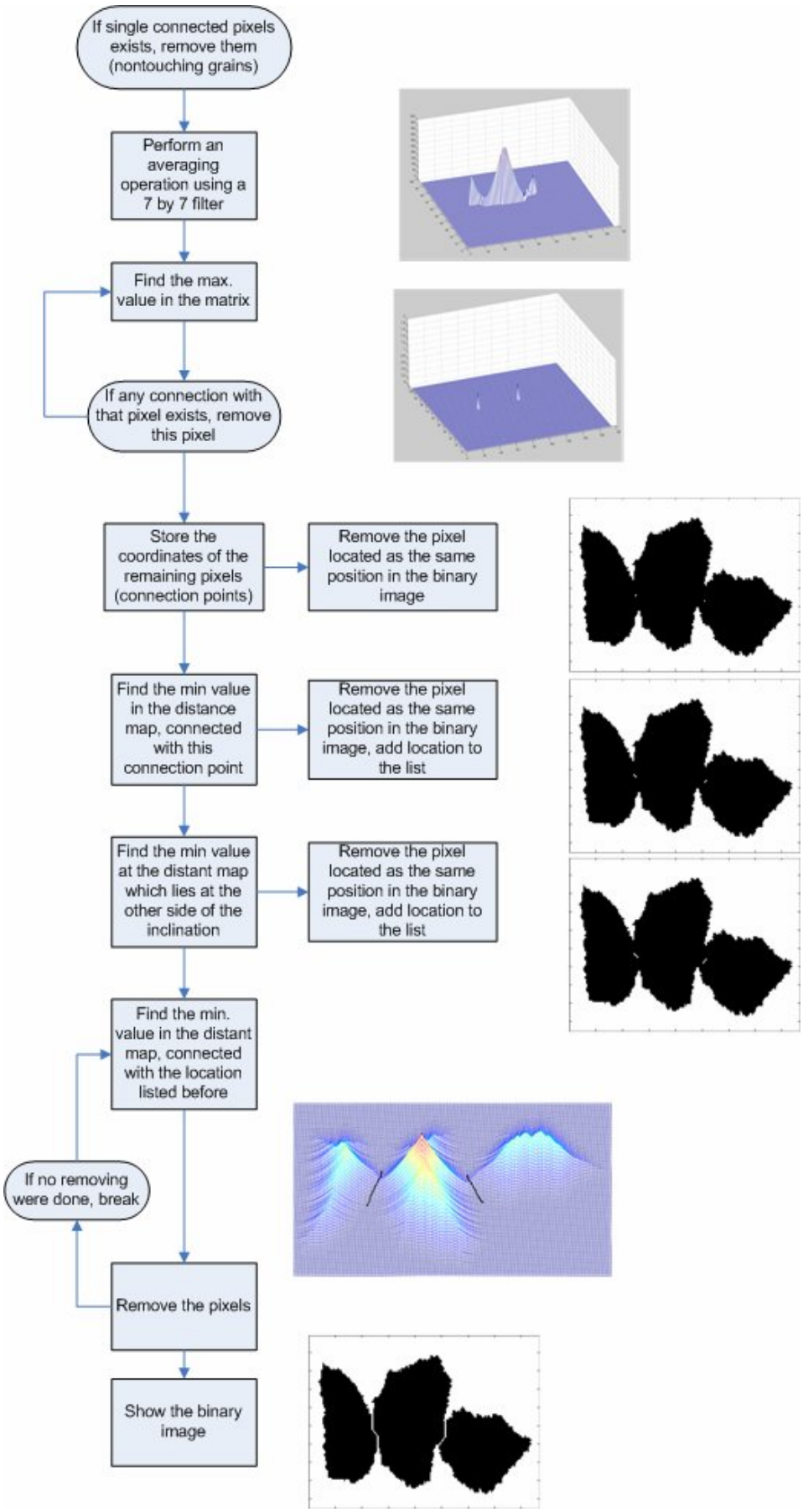
If single connected pixels exists, remove them (nontouching grains)
Perform an averaging operation using a 7 by 7 filter
Find the max. value in the matrix
If any connection with that pixel exists, remove this pixel
Store the coordinates of the remaining pixels (connection points)
Remove the pixel located as the same position in the binary image
Find the min value in the distance map, connected with this connection point
Remove the pixel located as the same position in the binary image, add location to the list
Find the min value at the distant map which lies at the other side of the inclination
Remove the pixel located as the same position in the binary image, add location to the list
Find the min. value in the distant map, connected with the location listed before
If no removing were done, break
Remove the pixels
Show the binary image

6.5 Application of the Skeleton Based Segmentation Algorithm

Visual charts were traditionally used to classify grains based on their shape characteristics. Figure 6.9 shows the classification charts for various levels of grain angularities (Krumbein, 1941). These properties can be measured by several methods. However, using these visual charts is less accurate and more time consuming than many modern methods.

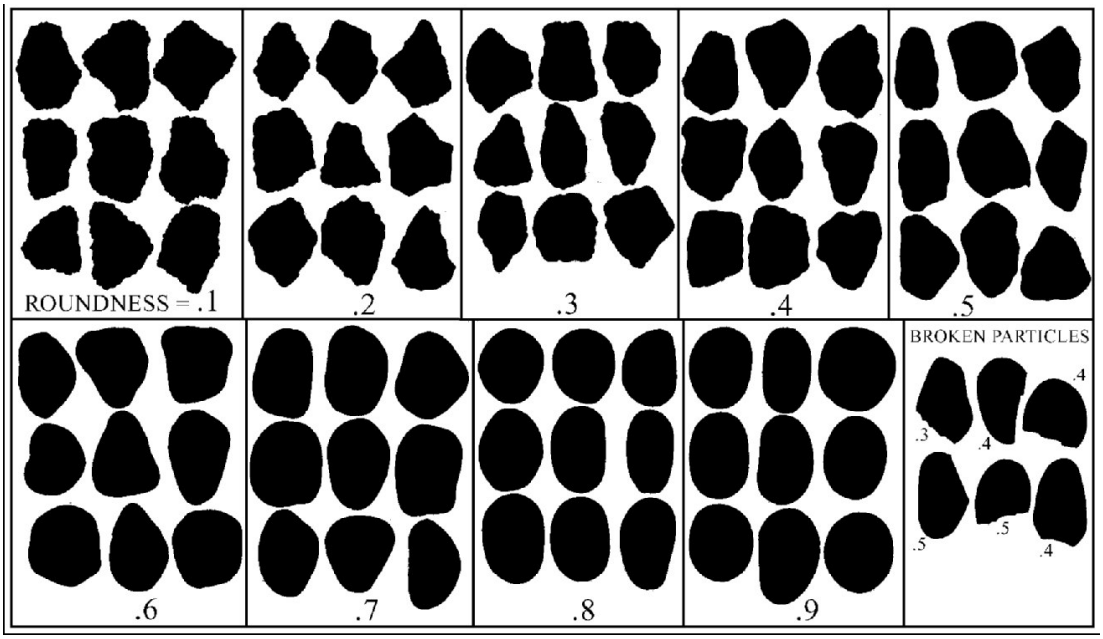

Figure 6.9 Angularity classification chart.

Lambe & Whitman (1979) has entitled the grains by using the angularity classification chart originally proposed by Krumbein. It appears that they somehow arbitrarily selected some grain shapes and called the grains with roundness factors R=0.1, R=0.2, R=0.4, R=0.6, and R=0.7 for angular, sub angular, sub rounded, rounded and well rounded grains, respectively.

In order to test the success of the segmentation algorithm, the above defined five groups of grains corresponding to different level of angularities have been used. The grains in the images have been rotated and relocated in order to form groups, whose grain elements are in contact with each other as shown in the first column of the Figure 6.10. In this column, the skeletons of groups have been also shown on the

unsegmented grain images. The second column in Figure 6.10 shows the processed images of the grain groups. Successful segmentation of the tested grain groups has been achieved as can be seen in the right column of this figure.

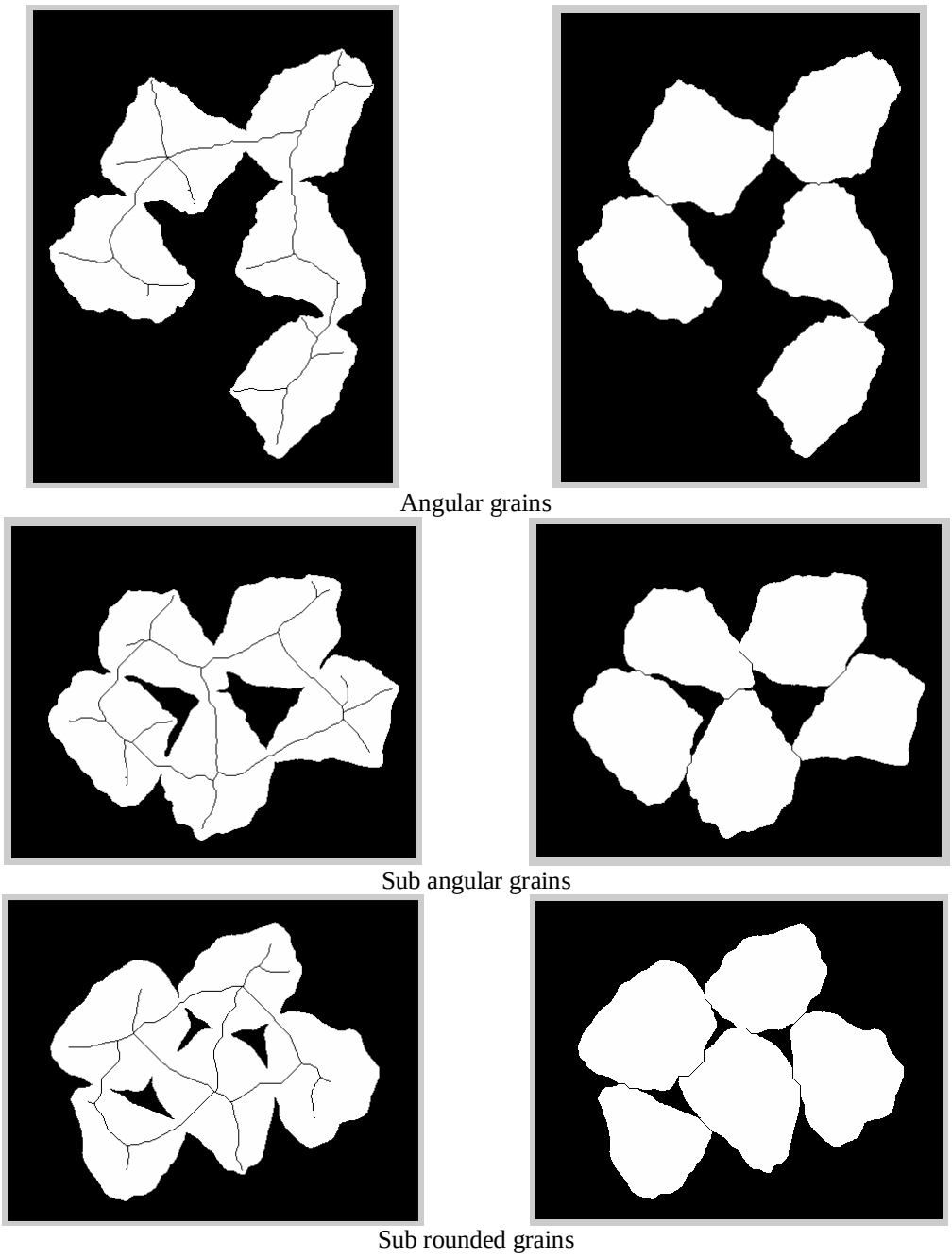

Figure 6.10 The original and segmented images of the grain groups.

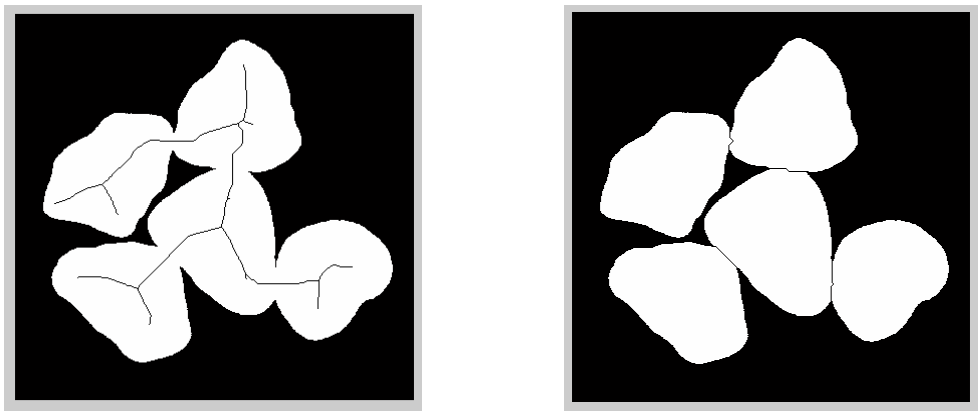

Rounded grains

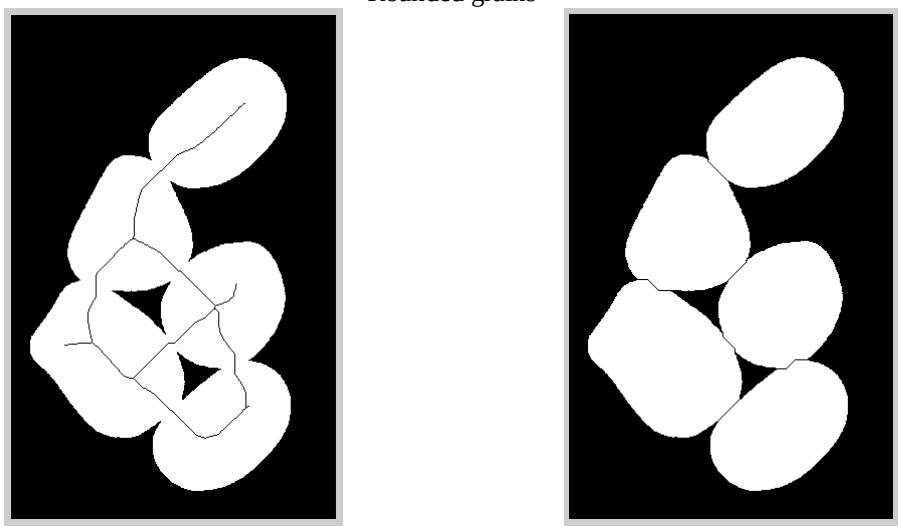

Well rounded grains

Figure 6.10 Continued.

6.6 Conclusion

The purpose of this study was to ensure the correct segmentation of the touching grains so that their individual feature analysis could be made accurately. An improved segmentation algorithm was developed based on the skeleton thinning operation. In order to evaluate the applicability of the algorithm, it was coded using MatLab technical computing language. The image processing toolbox functions of this package was used only for the constitution of the skeletons of the images. The remaining portion of the algorithm was developed by the author. The MatLab code was executed for the grain groups with different level of irregularities. Although the grain positions in the sample images was relocated resulting in excessive number of touching edges, the algorithm worked well in the segmentation of the these grain groups.

CHAPTER SEVEN
CONCLUSIONS

A suite of algorithms has been developed for the investigation of various characteristics of geomaterials using digital image processing methods. Digital image processing (DIP) has been regarded as one of the contemporary nondestructive methods. In this regard a comprehensive literature search has been performed in order to establish the current state-of-the-art of this technique in geotechnical engineering.

During the literature search, it was found that DIP has been in use in three main categories. These categories can be named as object segmentation, shape characterization and volume determination. Following the literature search, it has been decided that contributions could be made to each category. Besides, utilization of various DIP techniques in computer algorithms used for the evaluation of the digital image data of geomaterials was also considered as a major contribution to the field.

Therefore, improvement of skeleton based segmentation, development of a more robust volume measurement technique and utilization of other DIP methodologies such as grayscale and color segmentation in suite of computer algorithms were set as the goals of this dissertation. The overall objective was to grasp and then improve the state-of-the-art of DIP in geotechnics.

The grayscale and color segmentation techniques that were already available in the literature have been applied to the artificially prepared specimens in order to quantify the grains and voids in cohesive matrix. The two segmentation techniques have been combined together to characterize the different constituents of the cohesive matrix at the same time. Especially the utilization of color segmentation was first applied to the segmentation of voids in the image of a cohesive specimen from the background.

The digital signature technique that was traditionally in use for the characterization of the two-dimensional shape of any object has been modified in order to characterize the complex void shapes that would exist in some geomaterials. Development and application of the modified digital signature technique was made on artificially prepared cohesive test specimens. Self compacting concrete technique was used for specimen production purpose.

The developed shape analysis methodology has been also found applicable to the grain shapes while characterizing their angularity and roughness parameters. Therefore, the extent of the new shape analysis technique has been improved by using function approximation methodology for the digital signature functions in order to propose a roughness parameter for the grains. However, future work in this aspect of the dissertation is necessary to investigate relationships between the shape characteristics and mechanical behavior parameters of granular materials by complementary laboratory tests using the proposed digital signature method.

A digital imaging and image processing technique has been developed for the determination of the volumetric shrinkages of the compacted mixtures for small strain levels. The ability to determine the shrinkage strains for less than 5% is a unique contribution to the literature. The new methodology also minimizes the operator based errors and ensured more robust calculation of the volume of the cylindrical specimens. This aspect of the thesis is also open to further enhancement especially in terms of testing equipment development.

A digital image analysis technique for the investigation of heterogeneous prismatic cohesive specimens has been developed and applied to breccia rock specimens. The extracted features and nondestructive laboratory test results are combined together to constitute the data set for the estimation of the unconfined compressive strength values of the breccia rock specimens. Multiple linear regression and artificial neural network analyses have been applied using the data set in order to predict the destructive test parameter of the rock specimens. Similar results have been obtained from both analysis techniques. The 75% of the variations in the

unconfined compressive strength values have been explained by evaluating the data set. The area ratio of the breccia grains and effective porosity of the test specimens have been found as the major explanatory parameters for the variations in the unconfined compressive strength values.

It has been observed both during the literature review and progress of this dissertation that the separation of the touching objects is a complex and demanding process. The existing segmentation techniques are operator dependent and may not be properly applied to the geomaterials with varying degrees of angularity. Therefore, a new segmentation algorithm has been proposed by improving an existing technique, which was proposed for the basic shaped fiber cross sections in the textile industry. The existing technique has been fully refurbished in order to adapt it for the segmentation of the grains with varying degrees of angularities. Finally, the developed algorithm has been coded in MatLab Technical Computing Language and applications for the validation of the algorithm codes have been performed.

REFERENCES

Adamcewicz, A. S., Muhunthan, B., & Masad, E. (1997). Soil fabric changes during consolidation. *Geotechnical Testing Journal, 20* (3), 347-356.

Albrecht, B. A., & Benson, C. H. (2001). Effect of desiccation on compacted natural clays. *ASCE Journal of Geotechnical and Geoenvironmental Engineering,* 127 (1), 67-75.

Alshibli, K. A., & Sture, S. (2000). Shear band formation in plate strain experiments of sand. *ASCE Journal of Geotechnical and Geoenvironmental Engineering, 126* (6), 495-503.

Alshibli, K. A., & Al-Hamdan, M. Z. (2001). Estimating volume change of triaxial soil specimens from planar images. *Computer-Aided Civil and Infrastructure Engineering, 16* (6), 415-421.

ASTM Standard D 698, Standard test methods for laboratory compaction characteristics of soil using standard effort (12400 ft-lbf/ft^3 (600 kN-m/m^3)), ASTM International, West Conshohocken, PA.

ASTM Standard D 2845, Standard Test method for Laboratory Determination of Pulse Velocities and Ultrasonic Elastic Constants of Rock, ASTM International, West Conshohocken, PA.

Bray, D.E., & McBride, D. (1992). *Nondestructive Testing Techniques.* New York: John Wiley & Sons.

Bernacki. M., & Wlodarczyk, P. (2005). *Principles of training multi-layer neural network using backpropagation algorithm.* Retrieved January 02, 2008, from http://galaxy.agh.edu.pl/~vlsi/AI/backp_t_en/backprop.html.

Beucher, S., & Lantuejoul, C. (1979). Use of watersheds in contour detection. In the *Proceedings of the international Workshop on Image Processing, Real-Time Edge and Motion Detection/Estimation*, Rennes, France.

Bhatia, S.K., & Soliman, A.F. (1990). Frequency distribution of void ratio of granular materials determined by an image analyzer. *Soils and Foundations, 30* (1), 1-16.

Blum, H., (1967). A transformation for extracting new descriptors of shape. In *W. Wathen-Dunn, editor, Symposium on Models for the Perception of Speech and Visual Form, pp. 362-380.* MIT Press.

Bowman E. T., Soga K., & Drummond W. (2001). Particle shape characterization using Fourier descriptor analysis. *Géotechnique, 51* (6), 545-554.

Brzezicki J.M., & Kasperkiewicz J. (1999). Automatic image analysis in evaluation of aggregate shape. *ASCE Journal of Computing in Civil Engineering, 13* (2), 123-128.

Crabtree, S.J., Ehrlich, Jr.R., & Prince, C. (1984). Evaluation of strategies for segmentations of reservoir rocks. *Computers Vision, Graphics and Image Processing, 28* (1), 1-18.

Frost, J. D., & Kuo, C. Y. (1996). Automated determination of the distribution of local void ratio from digital images. *Geotechnical Testing Journal, 19* (2), 107-117.

Garboczi, E.J. (2002). Three-dimensional mathematical analysis of particle shape using x-ray tomography and spherical harmonics: Application to aggregates used in concrete. *Cement and Concrete Research, 32* (10), 1621-1638.

Ghalib, A.M., & Hryciw, R.D. (1999). Soil particle size distribution by mosaic imaging and watershed analysis. *Journal of computing in civil engineering, 13* (2), 80-88.

Gonzales, R.C., & Woods, R.E. (2002). *Digital image processing*. New Jersey: Pearson Prentice Hall.

Gonzales, R.C., Woods, R.E., & Eddins, S.L. (2004). *Digital image processing using MATLAB*. New Jersey: Pearson Prentice Hall.

Gosset, W. S. (1908). *The probable error of a mean.* Biometrika, 6 (1), 1-25.

Guler, M., Edil, T. B., & Bosscher, P. J. (1999). Measurement of particle movement in granular soils using image analysis. *ASCE Journal of Computing in Civil Engineering, 13* (2), 116–122.

Gupta, V. (2002). *Statistical analysis with Excel*. Canada: VJ Books Inc.

Haykin, S. (1999). Neural network, a comprehensive foundation. New Jersey: Pearson Prentice Hall.

Kahraman, S. & Alber, M. (2005). Estimating unconfined compressive strength and elastic modulus of a fault breccia mixture of weak blocks and strong matrix. *International Journal of Rock Mechanics & Mining Sciences.* 43, 1277–1287.

Kahraman, S. & Fener, M. (2007). Predicting the Los Angeles abrasion loss of rock aggregates from the uniaxial compressive strength. *Materials Letters.* 61, 4861–4865.

Karakuş, M., & Tutmez, B. (2006). Fuzzy and multiple regression modeling for evaluation of intact rock strength based on point load, Schmidt hammer and sonic velocity. *Rock Mechanics and Rock Engineering.* 39 (1), 45-57.

Kendall, G. (September 21 2001). *Introduction to artificial intelligence*. Retrieved January 03, 2008, from http://www.cs.nott.ac.uk/~gxk/courses/g5aiai/006neural networks /neural -networks.htm.

Kim, H., Haas C.T., Rauch, A., & Browne, C. (2003). 3D Image segmentation of aggregates from laser profiling. *Computer-Aided Civil and Infrastructure Engineering, 18* (4), 254-263.

Kleppe, J. H., & Olson, R. E. (1985). Desiccation cracking of soil barriers. In the *Hydraulic Barriers in Soil and Rock STP 874*, ASTM, West Conshohocken, 263-275.

Krumbein, C.F. (1941). Measurement and geological significance of shape and roundness of sedimentary particles. *Journal of Sedimentary Petrology*, 11 (2), 64-72.

Kwan, A.K.H., Mora, C.F., & Chan, H.C. (1999). Particle shape analysis of coarse aggregate using digital image processing. *Cement and Concrete Research, 29* (9), 1403-1410.

Lambe, T.W., & Whitman R.V. (1979). *Soil Mechnaics.* New York: John Wiley and Sons.

Lange, D.A., Jennings, H.M., & Shah, S.P. (1994). Image analysis techniques for characterization of pore structure of cement based materials. *Cement and Concrete Research, 24* (5), 841-853.

Larsen, P. V. (2008). Multiple linear regression. October 10, 2007. http://statmaster.sdu.dk/courses/st111/module03/index.html.

Linda, G. S., & George, C. S. (2001). *Computer Vision.* New Jersey: Prentice-Hall.

Macari, E. M., Parker, J. K., & Costes, N. C. (1997). Measurement of volume changes in triaxial tests using digital imaging techniques. *Geotechnical Testing Journal, 20* (1), 103-109.

Martinez-Martinez, J., Benavente, D., Garcia del Cura, M.A. (2006). Petrographic quantification of brecciated rocks by image analysis. Application to the interpretation of elastic wave velocities. *Engineering Geology*. 90, 41–54.

Masad, E., Muhunthan, B., Shashisdbar, N., & Harman, T. (1999). Internal structure characterization of asphalt concrete using image analysis. *Journal of Computing in Civil Engineering, 13* (2), 88-95.

Masad, E., Olcott, D., White, T., & Tashman, L. (2001). Correlation of fine aggregate imaging shape indices with asphalt mixture performance. *Transportation research record, Journal of the Transportation Research Board 1757*, 148-156.

MatLab, 2005, The language of technical computing, Version 7.1.0.246 (R14), Service Pack 3. Mathworks Corporation.

Michelland, S., Schiborr, B., Coster, M., Mordike, B.L., & Chermant, J.L. (1989). Size distribution of granular materials from unthresholded images. *Journal of Microscopy, 156* (3), 303-311.

Microsoft Office, 2003. Microsoft Office Professional Edition, Microsoft Coorperation.

Mora, C.F., Kwan, A.K.H., & Chan, H.C. (1998). Particle size distribution analysis of coarse aggregate using digital image processing. *Cement and Concrete Research, 28* (6), 921-932.

Nambiar, E. K. K., & Ramamurthy, K. (2007). Air-void characterization of foam concrete. *Cement and Concrete Research, 37,* 221-230.

Nalwa, V.S. (1993). *A Guided Tour of Computer Vision*. Addison-Wesley Publishing Company.

Obaidat, M. T., & Attom, M. F. (1998). Computer vision based technique to measure displacement in selected soil tests. *Geotechnical Testing Journal, 21* (1), 31-37.

Obaidat, M.T., AI-Masaeid, H.R., Gharaybeh, F., & Khedaywi, T.S. (1998). An innovative digital image analysis approach to quantify the percentage of voids in mineral aggregates of bituminous mixtures. *Canadian Journal of Civil Engineering, 25* (6), 1041-1049.

Oda, M. (1972). Initial fabrics and their relations to mechanical properties of granular materials. *Soils and Foundations, 12* (1), 17-36.

Otsu, N. (1979). A threshold selection method from gray level histograms. *IEEE Transactions on Systems, Man, and Cybernetics, 9* (1), 62-66.

Owens, R. (October 29, 1997). *Computer Vision IT412 Lecture Notes.* Retrieved March 09, 2007, from http://homepages.inf.ed.ac.uk/rbf/CVonline/LOCAL_COPIES/OWENS/LECT1/lect1.html

Önal, O., Ören, A.H., Özden, G., & Kaya, A., (2008). Monitoring shrinkage behavior of compacted bentonite-sand mixtures using digital image processing. *Geotechnical Testing Journal*, 31 (2), 1-8.

Önal, O. & Özden, G. (2006). Sayisal görüntü işleme tekniklerinin geoteknikte uygulama örnekleri. *Zemin Mekaniği ve Temel Mühendisliği Onbirinci Ulusal Kongresi*, 7-8 Eylül 2006, Karadeniz Teknik Üniversitesi, Trabzon.

Ören, A. H., Önal, O., Özden, G., & Kaya, A. (2006). Nondestructive evaluation of volumetric shrinkage of compacted mixtures using digital image analysis. *Engineering Geology*, 85 (3-4), 239-250.

Ören, A. H. (2007). Engineering investigation of zeolite-bentonite mixtures for landfill liner applications. Ph.D. Thesis, Dokuz Eylül University, The Graduate School of Natural and Applied Sciences, İzmir, Türkiye.

Parker, J.,R. (1994). *Practical computer vision using C.* New York: Wiley Computer Publishing.

Petrie, A., Bulman, J. S., & Osburn, J. F. (2002). Further statistics in dentistry Part 6: Multiple linear regression. *British Dental Journal.* 193 (12), 675-682.

Phifer, M.A., Drumm, E.C., & Wilson, G.V. (1994). Effects of Post Compaction Water Content Variation on Saturated Conductivity. In the *Hydraulic Conductivity and Waste Contaminant Transport in Soil STP 1142*, ASTM, West Conshohocken, 318-334.

Puppala, A. J., Balakrishna, K., & Hoyos, L. R. (2004). Volumetric shrinkage strain measurements in expansive soils using digital imaging technology. *Geotechnical Testing Journal, 27* (6), 1-10.

Raschke, S.A., & Hryciw, R.D. (1997). Grain-size distribution of granular soils by computer vision. *Geotechnical Testing Journal, 20* (4), 433-442.

Robertson, A.R. (1997). The CIE 1976 color difference formulae. *Color Research and Application 2*, 7-11.

Russ, J.C. (1998). *The Image Processing Handbook* (3rd ed.). Boca Raton, FL: CRC Press LLC in cooperation with IEEE Press.

Saltykov, S.A. (1967). The determination of the size distribution of particles in an opaque material from a measurement of the size distribution of their sections. In: Elias, H. (Ed.), *Proceedings of the Second International Congress for Stereology*. Springer , New York.

Saotome, A., Yoshinaka, R., Osada, M., & Sugiyama, H. (2002). Constituent material properties and clast-size distribution of volcanic breccia. *Engineering Geology*. 64, 1–17.

Shakoor, A., & Brown, C.L. (1996). Development of a quantitative relationship between unconfined compressive strength and Los Angeles abrasion loss for carbonate rocks. *Bulletin of the International Association of Engineering Geology*. 53, 97-103.

Shapiro, L.G. & Stockman, G.C. (2001). *Computer Vision*. New Jersey, Prentice-Hall.

Snedecor, G. W. (1956). *Statistical Methods*. Iowa, Iowa State U. Press.

Sonmez, H., Tuncay, E., & Gokceoglu, C. (2004). Models to predict the uniaxial compressive strength and the modulus of elasticity for Ankara Agglomerate. *International Journal of Rock Mechanics & Mining Sciences*. 41, 717–729.

Soroushian, P., Elzafraney, M., & Nossoni, A. (2003). Specimen preparation and image processing and analysis techniques for automated quantification of concrete micro cracks and voids. *Cement and Concrete Research, 33* (12), 1949-1962.

Sukumaran, B., & Ashmawy, A. (2001). Quantitative characterization of discrete particles. *Géotechnique, 51* (7), 619-627.

Tamrakar, N. K., Yokota, S. & Shrestha, S. D. (2007). Relationships among mechanical, physical and petrographic properties of Siwalik sandstones, Central Nepal Sub-Himalayas. *Engineering Geology*. 90, 105–123.

Tay, Y. Y., Stewart, D. I., & Cousens, T. W. (2001). Shrinkage and desiccation cracking in bentonite-sand landfill liners. *Engineering Geology, 60* (1-4), 263-274.

Van den Berg, E.H., Meesters, A.G.C.A., Kenter, J.A.M., & Schlager, W. (2002). Automated separation of touching grains in digital images of thin sections. *Computers and Geosciences, 28* (2), 179-190.

Vincent, L., & Soille, P. (1991). Watersheds in digital spaces: an efficient algorithm based on immersion simulations. *IEEE Transactions of Pattern Analysis and Machine Intelligence, 13* (6), 583-598.

Wonnacott, T.H., & Wonnacott, R.J. (1984). Introductory statistics for business and economics. New York: John Wiley & Sons.

Wang, G., & Paliwal J. (2006). Separation and identification of touching kernels and dockage components in digital images. *Canadian Biosystems Engineering, 48* (7), 1-7.

Werbos, P.J. (1994). *The Roots of Backpropagation: From Ordered Derivatives to Neural Networks and Political Forecasting*, New York: John Wiley & Sons.

Xu, B., Wang, S., & Su, J. (1999). Fiber Image Analysis, Part III: Autonomous Separation of Fiber Cross Sections. *Journal of Textile Institute*. 90, 288-297.

Yavuz, A.B., Türk, N. & Koca, M.Y. (2003). The use of micritic limestone as building stone. A case study of Akhisar Beiege marble in Western Turkey. In the

Proceedings of the *Industrial Minerals and Building Stones,* 277-281, İstanbul, Turkey, 2003.

Yue, Z.Q., Chen, S., & Tham, L.G. (2003). Finite element modeling of geomaterials using digital image processing. *Computers and Geotechnics, 30* (5), 375-397.

Yudhbir, J., & Abedinzadeh, R. (1991). Quantification of particle shape and angularity using the image analyzer. *Geotechnical Testing Journal, 14* (3), 296-308.

Zhang Z., Ansari, F., & Vitillo, N. (2005). Automated determination of entrained air-void parameters in hardened concrete. *ACI Materials Journal, 102* (1), 42-48.

APPENDICES

APPENDIX A- The Multiple Linear Regression Analysis Methodology

The multiple regression analysis is a useful tool to predict a dependent variable; however, there are some assumptions that have to be made, in order to perform a linear regression analysis (Gupta, 2002).

- The relationship between any one independent series and the dependent series should be linear.
- The sample size must be greater than the number of independent variables.
- There are no strong linear relationships among the independent variables.
- The residual terms follow several rules;
  - i. The mean or expected value of the residuals equals zero.
  - ii. The residual terms have the same variance
  - iii. A residual term for one observation should have no relation with the residual terms for other observations or with any of the independent variables.
  - iv. The residual terms have a normal density function.

Multiple linear regression is an extension of the simple regression with more than one independent variable and can be expressed as in Equation A-1.

$$Y_i = b_0 + b_1 x_{i,1} + b_2 x_{i,2} + ... + b_k x_{i,k} + e_i \qquad \text{(A-1)}$$

where, Y_i are the response variable, ε_i, are independent normally distributed random variables with zero mean and constant variance (σ^2) and, x are independent variables. The definition of a multiple linear regression model is that the predicted values of the dependent variable,

$$\hat{Y}_i = b_0 + b_1 x_{i,1} + b_2 x_{i,2} + ... + b_k x_{i,k} \qquad \text{(A-2)}$$

is a linear function of the regression parameters. Since there are several explanatory variables, matrix notations has been preferred in order to simplify complex notations. n equations can be derived from Equation A-1.

$$Y_1 = b_0 + b_1 x_{1,1} + b_2 x_{1,2} + \ldots + b_k x_{1,k} + e_1 \quad \text{(A-3)}$$

$$Y_2 = b_0 + b_1 x_{2,1} + b_2 x_{2,2} + \ldots + b_k x_{2,k} + e_2 \quad \text{(A-4)}$$

$$Y_n = b_0 + b_1 x_{n,1} + b_2 x_{n,2} + \ldots + b_k x_{n,k} + e_n \quad \text{(A-5)}$$

From the above equations, n dimensional vector ***Y***, containing the response variables, and n×(k+1) dimensional model matrix ***x*** can be constructed. The first column in ***x*** is a vector of unity (corresponding to the intercept β_0) while the remaining k columns correspond to the k explanatory variables. In particular, the ith row $x_{(i)}$ of ***x*** is given by $x_{(i)} = (1, x_{(i,1)}, x_{(i,2)}, \ldots, x_{(i,k)})$. Thus, ***Y*** and ***x*** are given by:

$$\mathbf{Y} = \begin{bmatrix} Y_1 \\ Y_2 \\ . \\ Y_n \end{bmatrix} \quad \text{(A-6)}$$

And,

$$\mathbf{x} = \begin{bmatrix} 1 & x_{1,1} & x_{1,2} & \ldots & x_{1,k} \\ 1 & x_{2,1} & x_{2,2} & \ldots & x_{2,k} \\ & & & & \\ 1 & x_{n,1} & x_{n,2} & \ldots & x_{n,k} \end{bmatrix} \quad \text{(A-7)}$$

Furthermore, $\boldsymbol{\beta}$ and $\boldsymbol{\varepsilon}$ denote the vector of regression parameters and vector of random errors, respectively:

$$\boldsymbol{\beta} = \begin{bmatrix} b_0 \\ b_1 \\ \cdot \\ b_k \end{bmatrix} \tag{A-8}$$

$$\boldsymbol{\varepsilon} = \begin{bmatrix} e_1 \\ e_2 \\ \cdot \\ e_n \end{bmatrix} \tag{A-9}$$

Recall that $\boldsymbol{x}$ has a dimension of n×(k+1), and observe that dimension of $\boldsymbol{\beta}$ is (k+1)×1. The matrix product $\boldsymbol{x\beta}$ results in the below equation:

$$\boldsymbol{Y}_{n\times 1} = \boldsymbol{x}_{n\times k}\boldsymbol{\beta}_{k\times 1} + \boldsymbol{\varepsilon}_{n\times 1} \tag{A-10}$$

where, the random errors ε_i, (i=1,2,…,n) are independent normally distributed random variables with zero mean and constant variance (σ^2). The vector of fitted or predicted values is given by:

$$\hat{\boldsymbol{Y}} = \boldsymbol{x\beta} \tag{A-11}$$

The fitted values are estimates of the expected response for given values of the explanatory variables $x_{i,1}$, $x_{i,2}$,…,$x_{i,k}$.

The principle of least squares has been applied to the Equation (A-1), in order to obtain the best regression function. According to this principle, the best fitting model is the one that minimizes the sum of squared residuals, where residuals are the deviations between the observed response variables and the values predicted by the fitted model. Note that the residuals ε_i are given by;

$$e_i = Y_i - b_0 - b_1 x_{i,1} - b_2 x_{i,2} - \ldots - b_k x_{i,k} \tag{A-12}$$

It follows that the residual sum of squares, RSS, is given by;

$$\text{RSS}=\sum_{i=1}^{n} e_i^{\,2} = \sum_{i=1}^{n} (Y_i - b_0 - b_1 x_{i,1} - b_2 x_{i,2} - \ldots - b_k x_{i,k})^2 \qquad \text{(A-13)}$$

In order to minimize the RSS with respect to β_0, β_1,…, β_k, the k+1 partial derivatives of the RSS can be used;

$$\frac{\partial RSS}{\partial b_0}, \frac{\partial RSS}{\partial b_1}, \ldots, \frac{\partial RSS}{\partial b_k} \qquad \text{(A-14)}$$

Equating the derivatives to zero and rearranging the terms yields the following system of k+1 equation with k+1 unknowns (Larsen, 2008).

$$b_0 n + b_1 \sum_{i=1}^{n} x_{i,1} + b_2 \sum_{i=1}^{n} x_{i,2} + \ldots + b_k \sum_{i=1}^{n} x_{i,k} = \sum_{i=1}^{n} y_i \qquad \text{(A-15)}$$

$$b_0 \sum_{i=1}^{n} x_{i,1} + b_1 \sum_{i=1}^{n} x_{i,1}^2 + b_2 \sum_{i=1}^{n} x_{i,1} x_{i,2} + \ldots + b_k \sum_{i=1}^{n} x_{i,1} x_{i,k} = \sum_{i=1}^{n} x_{i,1} y_i \qquad \text{(A-16)}$$

$$b_0 \sum_{i=1}^{n} x_{i,2} + b_1 \sum_{i=1}^{n} x_{i,1} x_{i,2} + b_2 \sum_{i=1}^{n} x_{i,2}^2 + \ldots + b_k \sum_{i=1}^{n} x_{i,2} x_{i,k} = \sum_{i=1}^{n} x_{i,2} y_i \qquad \text{(A-17)}$$

…

$$b_0 \sum_{i=1}^{n} x_{i,k} + b_1 \sum_{i=1}^{n} x_{i,1} x_{i,k} + b_2 \sum_{i=1}^{n} x_{i,2} x_{i,k} + \ldots + b_k \sum_{i=1}^{n} x_{i,k}^2 = \sum_{i=1}^{n} x_{i,k} y_i \qquad \text{(A-18)}$$

These equations must be solved simultaneously for β_0, β_1,… β_k in order to achieve the least squares estimates $b_0', b_1', \ldots, b_k'$ of β_0, β_1,… β_k, respectively. In order to give explicit formula for the least squares estimates of the regression parameters, it is convenient to express as matrix notation. Without matrix notation, the formula very quickly becomes unmanageable when the number of independent variables increases.

The residuals in Equation (A-12) may be written in matrix form as;

$$\boldsymbol{\varepsilon} = \boldsymbol{Y} - \boldsymbol{x\beta} \tag{A-19}$$

The sum of the squared residuals should be minimized, in order to perform least squares estimation.

$$\sum e_i^2 = [e_1 e_2 \ldots e_n] \times \begin{bmatrix} e_1 \\ e_2 \\ \cdot \\ e_n \end{bmatrix} = \boldsymbol{\varepsilon}' \, \boldsymbol{\varepsilon} \tag{A-20}$$

The term $\boldsymbol{\varepsilon}' \, \boldsymbol{\varepsilon}=\boldsymbol{(Y-x\beta)'(Y-x\beta)}$ has to be minimized, where the prime denotes the transpose of the matrix.

If the derivative with respect to the β is obtained:

$$\frac{d}{db}\boldsymbol{((Y - x\beta)'(Y - x\beta)} = -2 \, \mathbf{x}'(\mathbf{Y}-\mathbf{x}\,\boldsymbol{\beta}) \tag{A-21}$$

Than made equal to zero:

$$-2 \, \boldsymbol{x}'(\boldsymbol{Y}-\boldsymbol{x}\,\boldsymbol{\beta}) = 0 \tag{A-22}$$

Or,

$$\boldsymbol{x}' \, \boldsymbol{Y} = (\boldsymbol{x}' \, \boldsymbol{x}) \, \boldsymbol{\beta} \tag{A-23}$$

The solution of $\boldsymbol{\beta}$ matrix gives the least square solution for $\boldsymbol{\beta}$. By multiplying the inverse of the $\boldsymbol{x}' \, \boldsymbol{x}$ to the left of the equation (A-23);

$$\boldsymbol{\beta} = (\boldsymbol{x}'\boldsymbol{x})^{-1}\boldsymbol{x}'\boldsymbol{Y} \qquad \text{(A-24)}$$

where, $\boldsymbol{Y}$ is the vector of observed response variables and the superscripts prime and -1 denote transposed and inverse matrices, respectively.

APPENDIX B- The Feed Forward Back Propagation Algorithm

The human brain computes in an entirely different way from the conventional digital computer. The development of the artificial neural networks is inspired by the complex, nonlinear and parallel computing capability of the human brain. Human brain has the capability to organize its structural constituents, known as neurons, so as to perform certain computations many times faster than the fastest digital computer in existence today (Haykin, 1999). Computation occurs in parallel across large numbers of neurons, rather than in the serial fashion of traditional computer architectures. The analogy between human and artificial neurons in the learning procedure has to be mentioned, in order to introduce feed forward back propagation artificial neural networks briefly.

Human Neurons

The mystery about how the brain trains itself to process information is still unclear. However, from a computational point of view, it is known that the fundamental processing unit of the brain is a neuron. In the human brain, there are approximately 10 billion neurons, each of which is connected to about 10,000 other neurons.

A single neuron (Figure B-1) consists of a cell body called the soma, a number of spine like extensions called dendrites, and a single nerve fibre called an axon which branches out from the soma and connects to other neurons. Neurons combine input signals from these connections or synapses to determine if and when it will transmit a signal to other neurons through the connecting dendrites and synapses. The synapses modulate the input signals before they are combined, and the system learns by changing the modulation at each synapse. Neurons, interconnected by axons and dendrites, form the basic neural network.

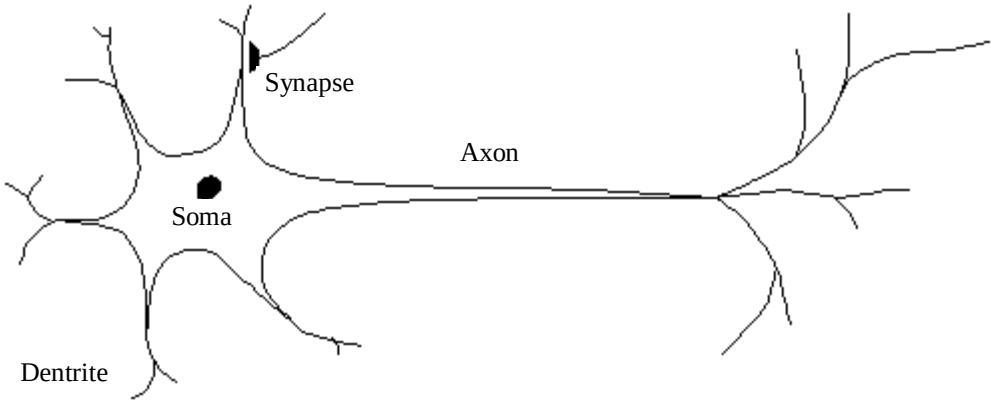

Figure B-1 A simple neuron.

Signals move from neuron to neuron via electrochemical reactions. The synapses release a chemical transmitter which enters the dendrite. This raises or lowers the electrical potential of the cell body. The soma sums the inputs it receives and once a threshold level is reached an electrical impulse is send down the axon, which is also called as “firing”. These impulses eventually reach synapses and the cycle continues. It has been found that synapses exhibit plasticity. This means that long term changes in the strengths of the connections can be formed depending on the firing patterns of other neurons. This is thought to be the basis for learning in our brains (Kendal, 2001).

Artificial Neurons

An artificial neuron is an information processing unit and performs a simple computation. It receives signals from its input links and uses these values to compute the activation level for the neuron. This value is passed to other neurons via its output links. The model of a simple artificial neuron is shown in Figure B-2.

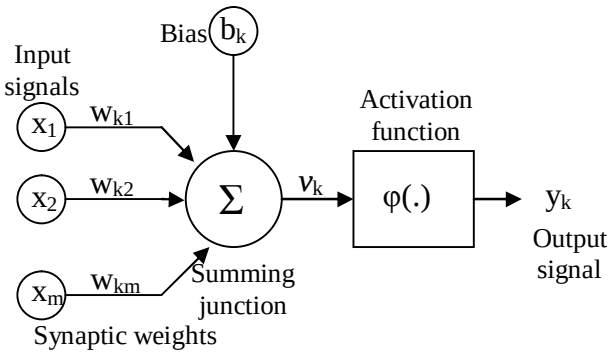

Figure B-2 A simple artificial neuron.

In Figure B-2, three elements of a neuron can be identified as the synaptic weights, the summing junction and the activation function. The neural model also includes an externally applied bias, which has the effect of increasing or decreasing the net input of the activation function.

In mathematical terms, a neuron (k) can be described by writing the Equations B-1 and B-2.

$$u_k = \sum_{j=1}^{m} w_{kj} x_j \qquad \text{(B-1)}$$

$$y_k = j\,(u_k + b_k) \qquad \text{(B-2)}$$

where, x_1, x_2, …,x_m are input signals; w_{k1},w_{k2},…, w_{km} are synaptic weights of neuron; u_k is the linear combiner output due to the input signals; b_k, is the bias; $\varphi(.)$ is the activation function; and y_k is the output signal of the neuron.

The activation function, denoted by $\varphi(v)$, defines the output of a neuron in terms of the induced local field v. Some common activation functions are shown in Figure B-3.

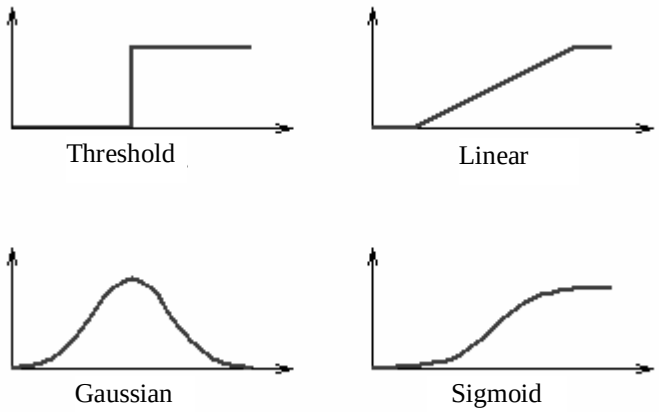

Figure B-3 Activation functions for the neurons.

Feed Forward Back Propagation Networks

The network consists of source nodes that constitute the input layer, one or more hidden layers of computation nodes, and an output layer of computation nodes as presented in Figure B-4. The input signal propagates though the network in a forward direction, on a layer by layer basis. Multilayer perceptions have been applied successfully to solve some difficult and diverse problems by training them in a supervised manner with a highly popular algorithm known as the error back propagation algorithm.

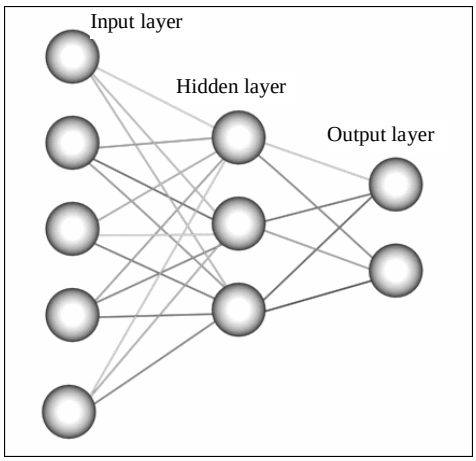

Figure B-4 A sample multilayer network.

Error back propagation learning consists of two passes through the different layers of the network as the forward pass and the backward pass. In the forward pass, an input vector is applied to the sensory nodes of the network, and its effect propagates through the network layer by layer. Finally, a set of outputs is produced as the actual response of the network. During the forward pass the synaptic weights of the networks are all fixed. During the backward pass, on the other hand, the synaptic weights are all adjusted in accordance with an error correction rule. Specifically, the actual response of the network is subtracted from a target response to produce an error signal. This error signal is than propagated backward through the network against the direction of synaptic connections (Haykin, 1999).

The topology of the feed forward back propagation network and the error propagation mechanism (Bernacki & Wlodarczyk, 2005) used in this study have been presented in the following. Although the neurons in the input layer, hidden layer and output layer in the presentation have been kept minimal, the same topology has been used in the study except the number of neurons in the layers. The network propagates from the input layer to the hidden layer using the Equations B-3 to B-5 and than to the output layer using the Equations B-6 and B-7.

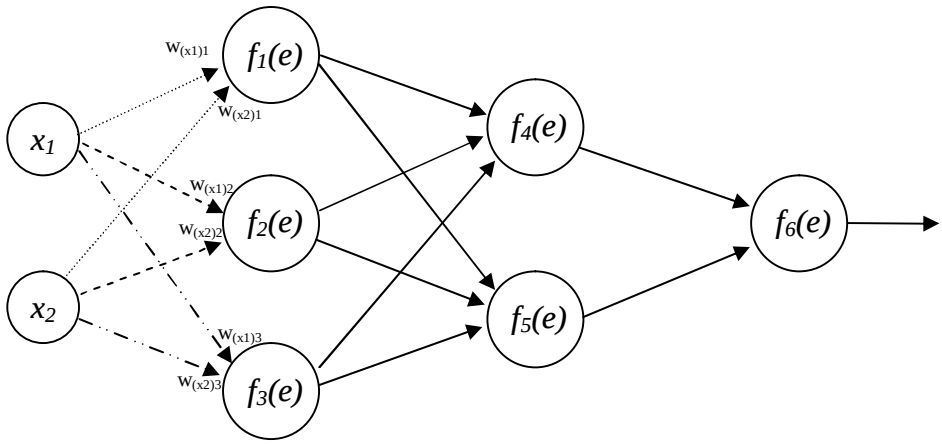

$$y_1 = f_1(w_{(x1)1}x_1 + w_{(x2)1}x_2) \quad \text{(B-3)}$$

$$y_2 = f_2(w_{(x1)2}x_1 + w_{(x2)2}x_2) \quad \text{(B-4)}$$

$$y_3 = f_3(w_{(x1)3}x_1 + w_{(x2)3}x_2) \quad \text{(B-5)}$$

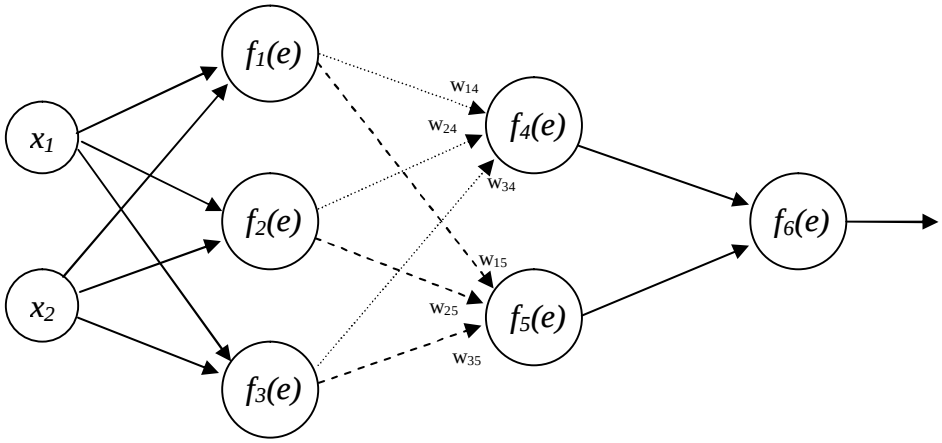

$$y_4 = f_4(w_{14}y_1 + w_{24}y_2 + w_{34}y_3) \quad \text{(B-6)}$$

$$y_5 = f_5(w_{15}y_1 + w_{25}y_2 + w_{35}y_3) \quad \text{(B-7)}$$

The output signal can be calculated by the Equation B-8.

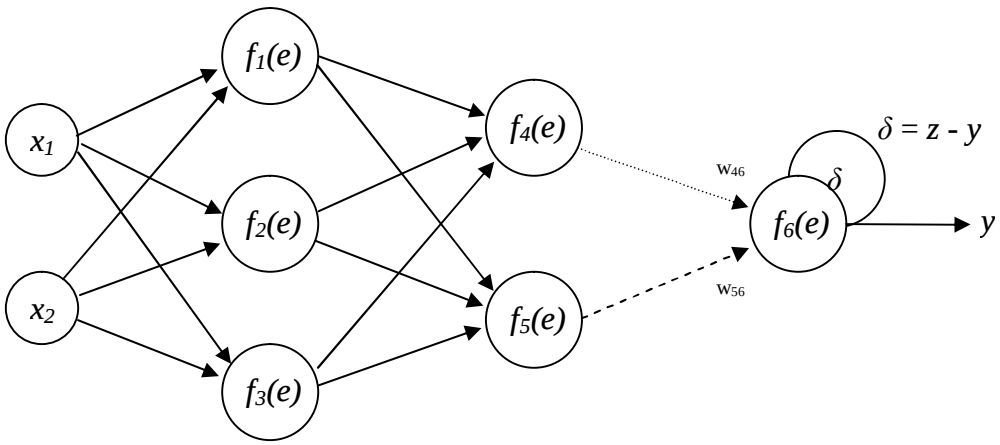

$$y = f_6(w_{46}y_4 + w_{56}y_5) \quad \text{(B-8)}$$

The output signal of the network y is compared with the desired output value (z), which is found in training data set. The difference is called error signal δ of output layer neuron. Since it is impossible to compute the error signal of the neurons directly, the error signal δ has been propagated back to all neurons. The weight coefficients used to propagate errors back are equal to this used during computing output value. Only the direction of data flow is changed.

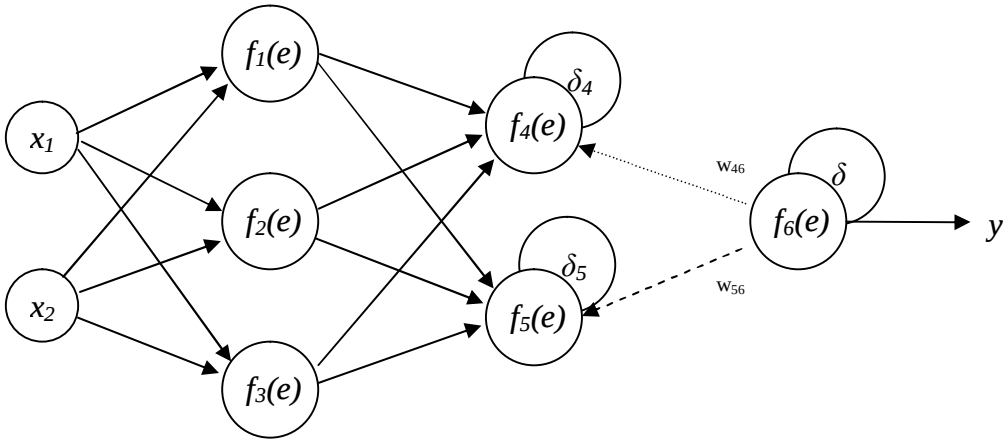

$$d_4 = w_{46} d \tag{B-9}$$

$$d_5 = w_{56} d \tag{B-10}$$

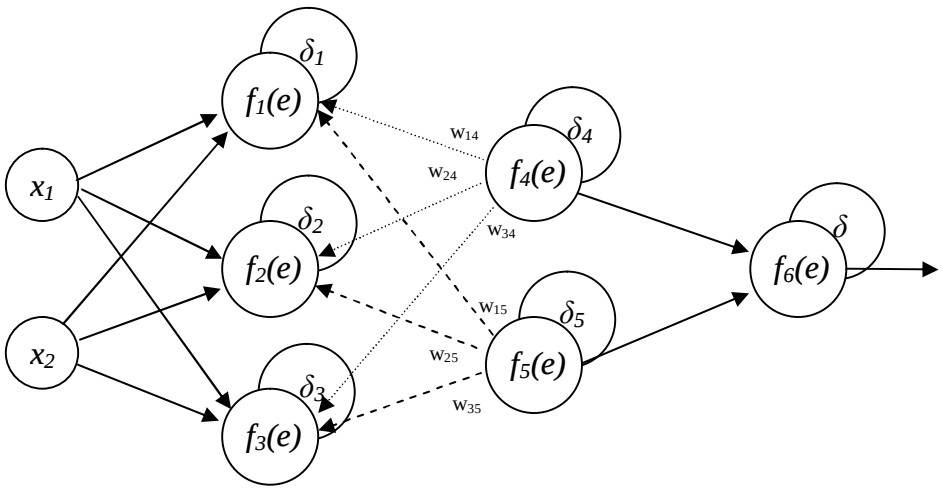

$$d_1 = w_{14} d_4 + w_{15} d_5 \tag{B-11}$$

$$d_2 = w_{24} d_4 + w_{25} d_5 \tag{B-12}$$

$$d_3 = w_{34} d_4 + w_{35} d_5 \tag{B-13}$$

When the error signal for each neuron is computed, the weight coefficients of each neuron input node may be modified.

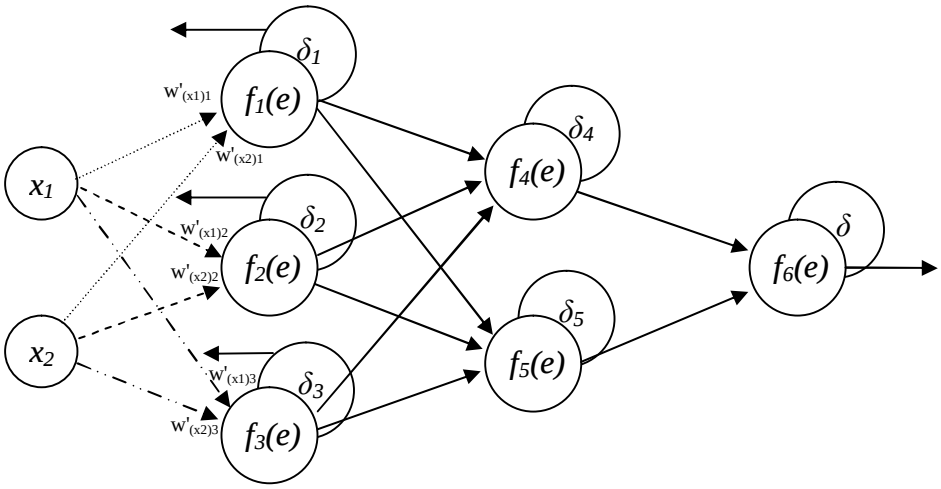

$$w'_{(x1)1} = w_{(x1)1} + hd_1 \frac{df_1(e)}{de} x_1 \quad \text{(B-14)}$$

$$w'_{(x2)1} = w_{(x2)1} + hd_1 \frac{df_1(e)}{de} x_2 \quad \text{(B-15)}$$

$$w'_{(x1)2} = w_{(x1)2} + hd_2 \frac{df_2(e)}{de} x_1 \quad \text{(B-16)}$$

$$w'_{(x2)2} = w_{(x2)2} + hd_2 \frac{df_2(e)}{de} x_2 \quad \text{(B-17)}$$

$$w'_{(x1)3} = w_{(x1)3} + hd_3 \frac{df_3(e)}{de} x_1 \quad \text{(B-18)}$$

$$w'_{(x2)3} = w_{(x2)3} + hd_3 \frac{df_3(e)}{de} x_2 \quad \text{(B-19)}$$

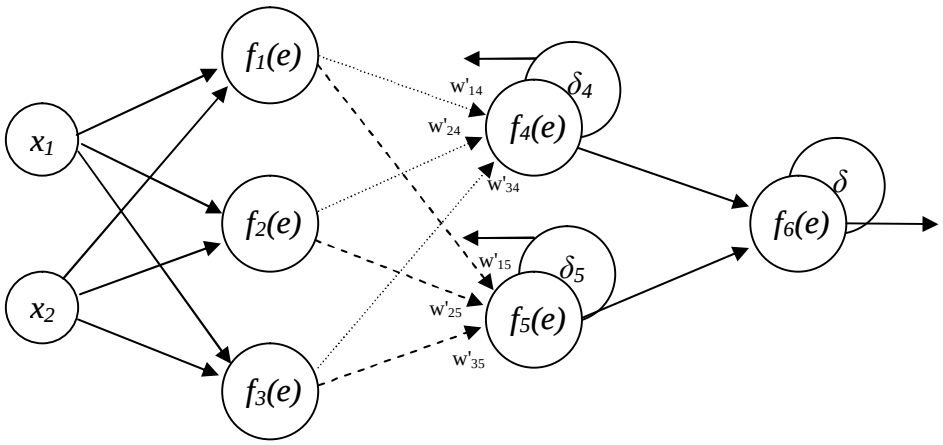

$$w'_{14} = w_{14} + hd_4 \frac{df_4(e)}{de} y_1 \quad \text{(B-20)}$$

$$w'_{24} = w_{24} + hd_4 \frac{df_4(e)}{de} y_2 \quad \text{(B-21)}$$

$$w'_{34} = w_{34} + hd_4 \frac{df_4(e)}{de} y_3 \quad \text{(B-22)}$$

$$w'_{15} = w_{15} + hd_5 \frac{df_5(e)}{de} y_1 \quad \text{(B-23)}$$

$$w'_{25} = w_{25} + hd_5 \frac{df_5(e)}{de} y_2 \quad \text{(B-24)}$$

$$w'_{35} = w_{35} + hd_5 \frac{df_5(e)}{de} y_3 \quad \text{(B-25)}$$

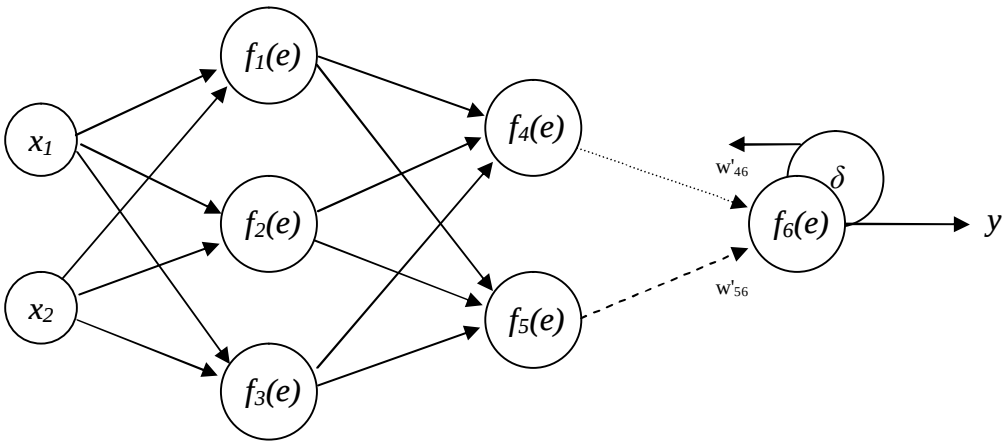

$$w'_{46} = w_{46} + hd \frac{df_6(e)}{de} y_4 \quad \text{(B-26)}$$

$$w'_{56} = w_{56} + hd \frac{df_6(e)}{de} y_5 \quad \text{(B-27)}$$

where, η is the learning rate parameter of the back propagation algorithm. The smaller is the learning rate parameter, the smaller changes to the synaptic weights in the network will be the trajectory in weight space. On the other hand, a large learning rate parameter yields large changes in the synaptic weights, which may result an unstable network. The iteration process goes on until certain stopping criterion is reached. The stopping criterion is typically determined by measuring the mean square error of the training data while training with the data. When this mean square error reaches a certain limit, the training is stopped.

APPENDIX C1

```
%% THIS MATLAB CODE WAS WRITTEN FOR DETERMINATION OF THE VOLUME OF
%% COMPACTED SOIL MIXTURES


clear, close all, clc                          %Clear all
variables, close all figures and clear the screen
OriginalImage=imread('HPIM4.jpg');             %Load the picture.
In this sample, files are HPIM1.jpg, HPIM2.jpg, HPIM3.jpg, HPIM4.jpg
imshow(OriginalImage),title('OriginalImage');  %Display the
original image on the screen
GrayToneImage = rgb2gray(OriginalImage);               %Convert the
RGB picture to grayscale image
figure, imshow(GrayToneImage),title('GrayToneImage');  %Display the
grayscale image on the screen
AdjustedGrayToneImage =
imadjust(GrayToneImage,stretchlim(GrayToneImage) , [0 1]); %Apply
contrast enhancement to grayscale image
figure,
imshow(AdjustedGrayToneImage),title('AdjustedGrayToneImage');
%Display the adjusted grayscale image on the screen
T1= graythresh(AdjustedGrayToneImage)-0.25;    %Compute the
threshold value(T1) by OTSU method
T2= graythresh(AdjustedGrayToneImage)+0.09;     %Compute the
threshold value(T2) by OTSU method
AdjustedAndThresholdedGrayToneImage1 =
im2bw(AdjustedGrayToneImage,T1);       %Threshold the adjusted
grayscale image with T1
AdjustedAndThresholdedGrayToneImage2 =
im2bw(AdjustedGrayToneImage,T2);       %Threshold the adjusted
grayscale image with T2
figure,
imshow(AdjustedAndThresholdedGrayToneImage1),title('AdjustedAndThres
holdedGrayToneImage1'); %Display the thresholded image on the screen
figure,
imshow(AdjustedAndThresholdedGrayToneImage2),title('AdjustedAndThres
holdedGrayToneImage2'); %Display the thresholded image on the screen
FiledAdjustedAndThresholdedGrayToneImage1=
imfill(AdjustedAndThresholdedGrayToneImage1,'holes');    %Fill the
internal gaps of the thresholded image
```

```
FiledAdjustedAndThresholdedGrayToneImage2=
imfill(AdjustedAndThresholdedGrayToneImage2,'holes');    %Fill the
internal gaps of the thresholded image
figure,
imshow(FiledAdjustedAndThresholdedGrayToneImage1),title('FilledImage
1');      %Display the filled image on the screen
figure,
imshow(FiledAdjustedAndThresholdedGrayToneImage2),title('FilledImage
2');      %Display the filled image on the screen
%%Clear variables for more free memory
clear GrayToneImage
clear AdjustedGrayToneImage
clear AdjustedAndThresholdedGrayToneImage1
clear AdjustedAndThresholdedGrayToneImage2
Final=FiledAdjustedAndThresholdedGrayToneImage1;
Final2=FiledAdjustedAndThresholdedGrayToneImage2;
clear FiledAdjustedAndThresholdedGrayToneImage1
clear FiledAdjustedAndThresholdedGrayToneImage2
%% Compute the mean pixel coordinate value for the left side of the
%% specimen (1750 pixel were processed)
imshow(OriginalImage),title('OriginalImage');   %Display the
original image on the screen
hold on
for i=450:2200
    for j=976:-1:0
        if Final(i,j)~=Final(i,j-1)
            x1(i-449)=j-0.5;
            break
        end
    end
end
y1=1:size(x1,2);
y1=y1+449;
plot(x1,y1,'b')
StartingPixel=mean(x1);
hold on
v=1:2608;
%% Compute the mean pixel coordinate value for the right side of the
%% specimen (1750 pixel were processed)
```

```
for i=450:2200;
    for j=976:1952
        if Final(i,j)~=Final(i,j-1)
            x2(i-449)=j-0.5;
            break
        end
    end
end
y2=1:size(x2,2);
y2=y2+449;
plot(x2,y2,'b')
StopingPixel=mean(x2);
hold on
v=1:2608;
l=1:1952;
%plot(l,1304,'y')
%% Calculate the distance between left and right borders of the
specimen
Tangent_pix=StopingPixel-StartingPixel;
%% Process the upper border of the specimen (975 pixels were
processed)
order=2;
y=zeros(1,976);
for j=488:1464;
    for i=1304:-1:0
        if Final(i,j)~=Final(i-1,j)
            y(j-487)=i-0.5;
            break
        end
    end
end
x=488:1464;
plot(x,y,'b')
pp=polyfit(x, y, order); %Fit a second degree polynomial
pval=polyval(pp,x);
hold on
plot(x,pval, 'w','LineWidth',1)
l=250:2367;
plot(976,l,'y')
```

```
intersection_top=polyval(pp,976); % Calculate the intersection of
the curve and axis line
plot(976,intersection_top,'o')
clear x
clear y
clear pval
%% Process the bottom border of the specimen (975 pixels were
processed)
y=zeros(1,976);
for j=488:1464;
    for i=1304:2608;
        if Final2(i,j)~=Final2(i-1,j)% Second image was used
(Final2)
            y(j-487)=i-0.5;
            break
        end
    end
end
x=488:1464;
plot(x,y,'r')
%% Apply a correction for the bottom border of the specimen
sbt=y(1);
for i=1:fix(size(y,2)/2)
    if y(i)>sbt
        Yy(i)=y(i);
        Xx(i)=x(i);
        sbt=y(i);
    else
        Yy(i)=sbt;
        Xx(i)=x(i);
    end
end
sbt2=y(size(y,2));
for i=fix((size(y,2))):-1:fix((size(y,2)))/2
    if y(i)>sbt2
        Yy(i)=y(i);
        Xx(i)=x(i);
        sbt2=y(i);
    else
```

```
        Yy(i)=sbt2;
        Xx(i)=x(i);
    end
end
plot(Xx,Yy,'b')
pp=polyfit(Xx,Yy,order);
pval=polyval(pp,Xx);
hold on
plot(Xx,pval, 'w','LineWidth',1)
l=0:2607;
intersection_bottom=polyval(pp,976);
plot(976,intersection_bottom,'o')
format long g
Tangent_pix; %The distance between tangent points
K_for_Height=0.056566617394207;      %This cooefficient was obtained
from the calibration code. Code can be found at
http://www.geocities.com/matlabcode/imageprocessing/volumetricshrink
age/index.htm/
K_for_Diameter=0.0586220840358314;   %This cooefficient was obtained
from the calibration code
Height=(intersection_bottom-intersection_top)*K_for_Height/10
%Calculate the height (cm)
Diameter=(Tangent_pix*K_for_Diameter/cos(2.054*pi/180))/10
%Calculate the diameter (cm)
Volume=pi*Diameter^2/4*Height   %Calculate the volume of specimen
(cm^3)
```

APPENDIX C2

```
%% THIS CODE COMPUTES THE CALIBRATION COEFFICIENTS FOR DIAMETER
%% AND HEIGHT USING THE CALIBRATION OBJECTS
%% CALIBRATION CODE
%% For Diameter-------------------------------------------------------
---
clear, close all, clc
A=imread('DiameterCalibration.jpg');
OriginalImage=A;
GrayToneImage = rgb2gray(OriginalImage);
AdjustedGrayToneImage =
imadjust(GrayToneImage,stretchlim(GrayToneImage) , [0 1]);
level = graythresh(AdjustedGrayToneImage)-0.2;
AdjustedAndThresholdedGrayToneImage1 =
im2bw(AdjustedGrayToneImage,level);
FiledAdjustedAndThresholdedGrayToneImage1=
imfill(AdjustedAndThresholdedGrayToneImage1,'holes');
clear A
clear OriginalImage
clear GrayToneImage
clear AdjustedGrayToneImage
clear AdjustedAndThresholdedGrayToneImage1
Final=FiledAdjustedAndThresholdedGrayToneImage1;
clear FiledAdjustedAndThresholdedGrayToneImage1
%% For the left border of the specimen
for i=450:2200
    for j=976:-1:0
        if Final(i,j)~=Final(i,j-1)
            x1(i-449)=j-0.5;
            break
        end
    end
end
y1=1:size(x1,2);
y1=y1+449;
StartingPixel=mean(x1);
%% For the right border of the specimen
for i=450:2200;
    for j=976:1952
```

```
        if Final(i,j)~=Final(i,j-1)
            x2(i-449)=j-0.5;
            break
        end
    end
end
y2=1:size(x2,2);
y2=y2+449;
StopingPixel=mean(x2);
Tangent_pix=StopingPixel-StartingPixel;
format long g
k_Diameter=101.8*cos(2.054*pi/180)/Tangent_pix
%%For Height-------------------------------------------------------------
---
clear all, close all
A=imread('HeightCalibration.jpg');
OriginalImage=A;
GrayToneImage = rgb2gray(OriginalImage);
AdjustedGrayToneImage =
imadjust(GrayToneImage,stretchlim(GrayToneImage) , [0 1]);
level = graythresh(AdjustedGrayToneImage)-0.2;
level2 = graythresh(AdjustedGrayToneImage)+0.15;
AdjustedAndThresholdedGrayToneImage1 =
im2bw(AdjustedGrayToneImage,level);
AdjustedAndThresholdedGrayToneImage2 =
im2bw(AdjustedGrayToneImage,level2);
FiledAdjustedAndThresholdedGrayToneImage1=
imfill(AdjustedAndThresholdedGrayToneImage1,'holes');
FiledAdjustedAndThresholdedGrayToneImage2=
imfill(AdjustedAndThresholdedGrayToneImage2,'holes');
clear A
clear OriginalImage
clear GrayToneImage
clear AdjustedGrayToneImage
clear AdjustedAndThresholdedGrayToneImage1
clear AdjustedAndThresholdedGrayToneImage2
Final=FiledAdjustedAndThresholdedGrayToneImage1;
Final2=FiledAdjustedAndThresholdedGrayToneImage2;
clear FiledAdjustedAndThresholdedGrayToneImage1
```

```
clear FiledAdjustedAndThresholdedGrayToneImage2
%% For the top border of the specimen
order=2;
y=zeros(1,976);
for j=488:1464;
    for i=1304:-1:0
        if Final(i,j)~=Final(i-1,j)
            y(j-487)=i-0.5;
            break
        end
    end
end
x=488:1464;
pp=polyfit(x, y, order);
pval=polyval(pp,x);
intersection_top=polyval(pp,976);
clear x
clear y
clear pval
%% For the bottom border border of the specimen
y=zeros(1,976);
for j=488:1464;
    for i=1304:2608;
        if Final2(i,j)~=Final2(i-1,j)
            y(j-487)=i-0.5;
            break
        end
    end
end
x=488:1464;
sbt=y(1);
for i=1:fix(size(y,2)/2)
    if y(i)>sbt
        Yy(i)=y(i);
        Xx(i)=x(i);
        sbt=y(i);
    else
        Yy(i)=sbt;
        Xx(i)=x(i);
```

```
    end
end
sbt2=y(size(y,2));
for i=fix((size(y,2))):-1:fix((size(y,2)))/2
    if y(i)>sbt2
        Yy(i)=y(i);
        Xx(i)=x(i);
        sbt2=y(i);
    else
        Yy(i)=sbt2;
        Xx(i)=x(i);
    end
end
pp=polyfit(Xx,Yy,order);
pval=polyval(pp,Xx);
intersection_bottom=polyval(pp,976);
format long g
k_Height=  (116.7)/(intersection_bottom-intersection_top)
```

APPENDIX D1

```
%% THIS MATLAB CODE WAS WRITTEN FOR THE QUANTIFICATION OF THE GRAINS
%% AND VOIDS IN COHESIVE MATRIX
%%
%% QUANTIFICATION OF GRAINS
%% Clearing Variables and loading image
clear, close all, clc                                  %Clears all
variables, figures and texts
OriginalImage=imread('sample image for grain detection.bmp');
%Read image from file
    imshow(OriginalImage),title('Original Image');  %Show original
image on screen
%% Converting an RGB image to grayscale
GrayScaleImage = rgb2gray(OriginalImage);           %Converting RBG
to grayscale
    figure, imshow(GrayScaleImage),title('GrayScale Image');   %Show
grayscale image as a new figure
    clear OriginalImage                             %Clear original
image from memory
%% Adjusting image intensity values
AdjustedGrayScaleImage =
imadjust(GrayScaleImage,stretchlim(GrayScaleImage) , [0 1]);
%Adjusting image intensity values by finding limits to contrast
stretch the grayscale image.
    figure, imshow(AdjustedGrayScaleImage),title('Adjusted GrayScale
Image');             %Show adjusted grayscale image
    clear GrayScaleImage                            %Clear grayscale
image
%% Thresholding Image
level = graythresh(AdjustedGrayScaleImage);             %Compute
global image threshold using Otsu's method
BinaryImage = im2bw(AdjustedGrayScaleImage,level);      %Converting
adjusted grayscale image to a binary image, based on threshold
    figure, imshow(BinaryImage),title('Binary Image');   %Show
binary image
    clear AdjustedGrayScaleImage                        %Clear
adjusted grayscale image
%% Removing small objects inside the grains from binary image
```

```
BinaryImage = bwareaopen(BinaryImage,200);
%Removing connected components smaller than 200 pixel
    figure, imshow(BinaryImage) ,title('Binary Image >200');  %Show
binary image
%% Reversing the binary image
BinaryImage=1-BinaryImage;                              %Subtracting
binary image from a same size unity matrix
    figure, imshow(BinaryImage) ,title('Reverse Binary Image');
%Show reverse binary image
%% Removing small objects outside the grains from binary image
BinaryImage = bwareaopen(BinaryImage,200);              %Removing
connected components smaller than 200 pixel
    figure, imshow(BinaryImage),title('Binary Image >200');  %Show
eliminated reverse binary image
%% Watershed segmentation
%% Distance transformation
D=-bwdist(~BinaryImage,'euclidean'); % Applying distance transform
Distances= mat2gray(D); %Converting distance map to a matrix
    figure, imshow(Distances)
%% Softening image for a proper result
h=ones(27,27)/729 ; %Correlation matrix
Soften = imfilter(Distances,h,1); %Filtering image
    figure, imshow(Soften);
%% Watershed segmentation
L=watershed(Soften,8); %Applying watershed segmentation
    figure, imshow(L)
BinaryImage(L==0)=0;%Inserting watersheds to grains
    figure,imshow(BinaryImage)
BinaryImage = bwareaopen(BinaryImage,40); %Removing watershed
defects
%% Labeling connected components in binary image
[labeled, numObjects] = bwlabel(BinaryImage,8);         %Labeling 8-
connected components in binary image
RGB_Label= label2rgb(labeled, @spring, 'c', 'shuffle'); %Converting
label matrix into an RGB image
    figure, imshow(RGB_Label),title('RGB Labeled Image with
Centroids');    %Show RGB label
    clear BinaryImage                                   %Clear
binary image
```

```
%% Determining areas and centroids of grains
graindata = regionprops(labeled,'basic');               %Accessing
basic properties of regions
for i=1:numObjects                                      %Plotting
centroids of grains in RGB label image
    hold on
    plot(graindata(i).Centroid(1),graindata(i).Centroid(2),'bo');
end
%% Calculating total area
BazaltArea=0;                           %Variable set to zero
for i=1:numObjects                     %Adding areas of all objects
    BazaltArea=BazaltArea+graindata(i).Area;
end
BazaltArea                              %Display results in pixels
GrainRatio=BazaltArea/622565            %Calculation grain
ratio(BazaltArea/TotalArea)
%% Calculating lateral stability of grains
StaticMx=0;StaticMy=0;X=0;Y=0;          %Variables set to zero
for i=1:numObjects                      %For all grains
    StaticMx=StaticMx+graindata(i).Centroid(1)*graindata(i).Area;
%Multiplying areas with x-coordinates
end
X=StaticMx/BazaltArea;                  %X-coordinate of grains
total centroid
for i=1:numObjects                      %For all grains
    StaticMy=StaticMy+graindata(i).Centroid(2)*graindata(i).Area;
%Multiplying areas with y-coordinates
end
Y=StaticMy/BazaltArea;                  %Y-coordinate of grains
total centroid
plot(X,Y,'bx')                          %Plotting coordinates in
same figure as a black 'x' sign
%% Plotting 3-D view of grain data
figure,                                 %In a new figure
grid on                                 %Grid on
for i=1:numObjects                      %For all objects
    plot3 (graindata(i).Centroid(1), graindata(i).Centroid(2),
graindata(i).Area, 'o'); %Putting a 'o' sign in every objects
coordinate with the hight of their areas
```

```
    hold on                                 %Keep the figure on screen
end
%% Inserting a plane in 3-D view, which represents the average area
of the grains
for k=1:80:1280                             %Adjusting the grid aperture
            for l=1:60:960                  %Adjusting the grid aperture
                plot3(k,l,(BazaltArea/numObjects),'r')  %Putting
average grain area to grid coordinates
            end
end
```

APPENDIX D2

```
%% QUANTIFICATION OF VOIDS
%% Image Processing Toolbox                    Version 4.2
(R14)
%% Clearing variables and loading image
clear all,clc      %Clears all variables, figures and texts
pic=imread('sample image for void detection.bmp'); %Read image from
file
figure(1),imshow(pic),title('OriginalImage'); %Show original image
on screen


%% Specifying number of colors
nColors=5; %Specifying number of colors which will be segmented in
image
sample_regions=false([size(pic,1) size(pic,2) nColors]);%Building
empty sample regions


%% Specifying poligons which are representing each color in the
image
region_coordinates=[ 760 441; 752 452; 766 454];
count=1;
sample_regions(:,:,count)=roipoly(pic,region_coordinates(:,1,count),
region_coordinates(:,2,count));
% Selecting a polygonal region of interest in the image
region_coordinates2=[ 295 225; 291 252; 270 235];
count=2;
sample_regions(:,:,count)=roipoly(pic,region_coordinates2(:,1,1),reg
ion_coordinates2(:,2,1));

region_coordinates3=[ 425 188; 453 198; 446 162];
count=3;
sample_regions(:,:,count)=roipoly(pic,region_coordinates3(:,1,1),reg
ion_coordinates3(:,2,1));

region_coordinates4=[ 783 306; 801 322; 797 310];
count=4;
sample_regions(:,:,count)=roipoly(pic,region_coordinates4(:,1,1),reg
ion_coordinates4(:,2,1));
```

```
region_coordinates5=[ 860 179; 852 198; 872 196];
count=5;
sample_regions(:,:,count)=roipoly(pic,region_coordinates5(:,1,1),reg
ion_coordinates5(:,2,1));

%% Dispalying sample regions for each color
figure,
imshow(sample_regions(:,:,1)),title('sample region for first
color');
figure,
imshow(sample_regions(:,:,2)),title('sample region for second
color');
figure,
imshow(sample_regions(:,:,3)),title('sample region for third
color');
figure,
imshow(sample_regions(:,:,4)),title('sample region for fourth
color');
figure,
imshow(sample_regions(:,:,5)),title('sample region for fifth
color');

%% Converting RGB image into an L*a*b* image
cform=makecform('srgb2lab');
lab_fabric=applycform(pic,cform);

%% Calculating the mean 'a*' and 'b*' value for sample color regions
a=lab_fabric(:,:,2);
b=lab_fabric(:,:,3);
color_markers = repmat(0,[nColors,2]);
for count= 1:nColors
    color_markers(count,1)=mean2(a(sample_regions(:,:,count)));
    color_markers(count,2)=mean2(b(sample_regions(:,:,count)));
end

%disp(sprintf('[%0.3f,%0.3f]',color_markers(1,1),color_markers(1,2))
);
```

```
%% Classifying each pixel using the nearest neighbor rule
color_labels=0:nColors-1;
a=double(a);
b=double(b);
distance=repmat(0,[size(a),nColors]);
for count=1:nColors
    distance(:,:,count)=((a-color_markers(count,1)).^2+(b-
color_markers(count,2)).^2).^0.5;
end
[value, label]=min(distance,[],3);
label=color_labels(label);
clear value distance;

%% Displaying results of the nearest neigbor classification
rgb_label=repmat(label,[1 1 3]);
segmented_images=repmat(uint8(0),[size(pic),nColors]);
for count=1:nColors
    color=pic;
    color(rgb_label~=color_labels(count))=0;
    segmented_images(:,:,:,count)=color;
end
%% Adding two yellow tone images together
figure, imshow(segmented_images(:,:,:,1)), figure,
imshow(segmented_images(:,:,:,2))
Voids=imadd(segmented_images(:,:,:,1),segmented_images(:,:,:,2));
figure,
imshow(Voids);
%% Thresholding Image
level = graythresh(Voids);              %Compute global image
threshold using Otsu's method
BinaryImage = im2bw(Voids,level);       %Converting adjusted
grayscale image to a binary image, based on threshold
    figure, imshow(BinaryImage),title('Binary Image');   %Show
binary image
BinaryImage = imfill(BinaryImage,'holes'); % Fill internal holes
%% Watershed segmentation
%% Distance transformation
D=-bwdist(~BinaryImage,'euclidean'); % Applying distance transform
```

```
Distances= mat2gray(D); %Converting distance map to a matrix
    figure, imshow(Distances)
%% Softening image for a proper result
h=ones(3,3)/9 ; %Correlation matrix
Soften = imfilter(Distances,h,1); %Filtering image
    figure, imshow(Soften);
%% Watershed segmentation
L=watershed(Soften,8); %Applying watershed segmentation
    figure, imshow(L)
BinaryImage(L==0)=0;%Inserting watersheds to grains
    figure,imshow(BinaryImage)
BinaryImage = bwareaopen(BinaryImage,3);  %Removing watershed
defects
%% Labeling connected components in binary image
[labeled, numObjects] = bwlabel(BinaryImage,8);         %Labeling 8-
connected components in binary image
RGB_Label= label2rgb(labeled, @spring, 'c', 'shuffle'); %Converting
label matrix into an RGB image
    figure, imshow(RGB_Label),title('RGB Labeled Image with
Centroids');    %Show RGB label
%% Determining areas and centroids of voids
voiddata = regionprops(labeled,'basic');               %Accessing
basic properties of regions
for i=1:numObjects                                    %Plotting
centroids of grains in RGB label image
    hold on
    plot(voiddata(i).Centroid(1),voiddata(i).Centroid(2),'bo');
end
%% Calculating total void area
VoidArea=0;                            %Variable set to zero
for i=1:numObjects                     %Adding areas of all objects
    VoidArea=VoidArea+voiddata(i).Area;
end
VoidArea                               %Display results in pixels
Porosity=VoidArea/622565            %Calculation grain
ratio(VoidArea/TotalArea)
```

```
%% EXAMPLE CODE FOR WATERSHED SEGMENTAION FOR TOUCHING GRAINS
%% Clearing variables and loading image
clear all,close all,clc %Clears all variables, figures and texts
grains=imread('grains.bmp'); %Read image from file
    figure,imshow(grains),title('Image to be segmented'); %Show
original image on screen

%% Distance transformation
D=-bwdist(~grains,'euclidean'); % Applying distance transform
Distances= mat2gray(D); %Converting distance map to a matrix
    figure, imshow(Distances)
%% Softening image for a proper result
h=ones(8,8)/64 ; %Correlation matrix
Soften = imfilter(Distances,h,1); %Filtering image
    figure, imshow(Soften);
%% Watershed segmentation
L=watershed(Soften,8); %Applying watershed segmentation
    figure, imshow(L)
grains(L==0)=0;%Inserting watersheds to grains
    figure,imshow(grains)
```

APPENDIX D3

```
%% THIS MATLAB CODE WAS WRITTEN FOR THE GENERATION OF THE
%% DIGITAL SIGNATURE USING THE PERIMETER ALGORITHM
%% APPLICATION TO GRAIN IMAGES WITH SEVERAL DEGREES OF
%% ANGULARITIES
%%
%% Digital signature
clc, clear all, close all;
%% Accessing Boundary coordinates
I = imread('wellrounded.tif');% angular.tif subangular.tif
subrounded.tif rounden.tif wellrounded.tif
BW = im2bw(I, graythresh(I));
%BW=abs(1-BW); %Negative
[B,L] = bwboundaries(BW,'noholes');
imshow(label2rgb(L, @jet, [.5 .5 .5]))
hold on
for k = 1:length(B)
   boundary = B{k};
   plot(boundary(:,2), boundary(:,1), 'w', 'LineWidth', 2)
   clear boundary
end
%% Labeling connected components in binary image
[labeled, numObjects] = bwlabel(BW,8);
%Labeling 8-connected components in binary image
RGB_Label= label2rgb(labeled, @spring, 'c', 'shuffle');
%Converting label matrix into an RGB image
%% Determining areas and centroids of these shapes
graindata = regionprops(labeled,'all');
%Accessing basic properties of regions
for i=1:numObjects
%Plotting centroids of grains in RGB label image
    hold on
    plot(graindata(i).Centroid(1),graindata(i).Centroid(2),'bo');
    t=0:0.1:2*pi;
    xr=graindata(i).EquivDiameter/2*cos(t);
    yr=graindata(i).EquivDiameter/2*sin(t);

plot(xr+graindata(i).Centroid(1),yr+graindata(i).Centroid(2),'b');
end
```

```
%hold on
for k=1:length(B);
    boundary = B{k};
    for i=1:length(boundary);
        %plot(boundary(i,2),boundary(i,1),'x')
        %plot(graindata(k).Centroid(1),graindata(k).Centroid(2),'x')
        Distance(i)=((sqrt((boundary(i,2)-
graindata(k).Centroid(1)+0.5)^2+(boundary(i,1)-
graindata(k).Centroid(2)+0.5)^2))/(sqrt((4*graindata(k).Area)/pi)/2-
0.5)-1);
%                           x              x
y
%                           y
    end

    D(k)={Distance};

    %hold on ,
    figure, plot(D{k})
    axis([0 length(Distance) -1
1])%2*(sqrt((4*graindata(k).Area)/pi)/2)])
    hold on, plot(1:length(Distance),0)

    Polynom=polyfit(1:length(Distance),Distance,20);
    Polynom=polyval(Polynom,1:length(Distance));
    %%
    counts=0;
    for s=1:length(Polynom)-1
        if Polynom(s)>0 %
            if Polynom (s+1)<0
                counts=counts+1;
                ZeroPoint(counts)=s;
            end
        end
        if Polynom(s)<0 %
            if Polynom (s+1)>0
                counts=counts+1;
                ZeroPoint(counts)=s;
            end
```

```
        end
    end
    ZeroPoint
    %%%
    Positive=0;
    Negative=0;
    countP=0;
    countN=0;
    for p=1:length(Distance)
        if Distance(p)>0
            countP=countP+1;
            Positive=Positive+Distance(p);
        end
        if Distance(p)<0
            countN=countN+1;
            Negative=Negative+Distance(p);
        end
    end
    PositiveAverage=Positive/countP
    NegativeAverage=Negative/countN
    %%%
    plot(Polynom,'r')
    roughness=sum(abs(Distance-Polynom))/length(Distance)
    clear ZeroPoint
    clear Polynom
    clear boundary
    clear Distance
    hold off
end
```

APPENDIX E1

```
%% THIS MATLAB CODE WAS WRITTEN FOR THE AUTOMATED SEPARATION OF
%% BRECCIAS
%% IN THE SURFACE IMAGES OF THE TEST SPECIMENS

close all;
clear all;
clc;

% name format of images
name_format='_';
read_format='rszt';
write_format1='RgrayThresh';
write_format2='Threshed';
name=name_format;

% 256 for 8 bit images
Ng=256;

Features=[];
Comat=[];


for iter=1:201;

    temp1=int2str(iter);
    name1=[read_format temp1 name_format];

    for iter2=1:6

        name2=[name1   int2str(iter2)]

        I = imread(name2,'jpg');



        thresh=graythresh(I(:,:,1));
        c=im2bw(I(:,:,:),thresh);
```

```
        %thresh2=graythresh(rgb2gray(I));
        %d=im2bw(I(:,:,:),thresh2);

        %%figure, imshow (I)
        figure,imshow(c)%,figure,imshow(d);

        name2=[write_format2 temp1 name_format int2str(iter2)
'.png']
        %name3=[write_format1 temp1 name_format int2str(iter2)
'.png']
        imwrite(c,name2,'png');
        %imwrite(d,name3,'png');
        r=0;
        x=0;
        y=0;
        for i=1:316
            for j=1:316
                if c(j,i)==1
                    r=r+1;
                    x=x+i;
                    y=y+j;
                end
            end
        end

        if r==0
            R(iter,iter2)=0;
            X=0;
            Y=0;
        else
            R(iter,iter2)=r/(316*316)*100;
            X=(x/r-158.5)*7/316; %transformed to cm
            Y=-(y/r-158.5)*7/316; %transformed to cm
        end

        SM(iter,iter2,1)=X;
        SM(iter,iter2,2)=Y;
```

```
            X,Y,R(iter,iter2)

            hold on, plot((x/r),(y/r),'rx'), plot(316/2,316/2,'yo')
        end

    end
```

APPENDIX E2

```
%% THIS MATLAB CODE WAS WRITTEN FOR THE DETERMINATION
%% OF THE ECCENTRICITIES OF THE LIMESTONE PARTS OF THE SPECIMENS
%%

load StMo;
load VR;
for iter=1:201;
    TMX(iter)=0;
    TMY(iter)=0;
    TMZ(iter)=0;

    for iter2=1:6
        if iter2==1

            TMX(iter)=TMX(iter)+StM(iter,iter2,1)*VR(iter,iter2)*49/
            100;
            TMY(iter)=TMY(iter)+StM(iter,iter2,2)*VR(iter,iter2)*49/
            100
            TMZ(iter)=TMZ(iter)+3.5*VR(iter,iter2)*49/100;
        end
        if iter2==2

TMX(iter)=TMX(iter)+StM(iter,iter2,1)*VR(iter,iter2)*49/100 ;
            TMY(iter)=TMY(iter)-3.5*VR(iter,iter2)*49/100 ;

TMZ(iter)=TMZ(iter)+StM(iter,iter2,2)*VR(iter,iter2)*49/100;
        end
        if iter2==3

TMX(iter)=TMX(iter)+StM(iter,iter2,1)*VR(iter,iter2)*49/100;
            TMY(iter)=TMY(iter)-
StM(iter,iter2,2)*VR(iter,iter2)*49/100;
            TMZ(iter)=TMZ(iter)-3.5*VR(iter,iter2)*49/100;
        end
        if iter2==4

TMX(iter)=TMX(iter)+StM(iter,iter2,1)*VR(iter,iter2)*49/100;
            TMY(iter)=TMY(iter)+3.5*VR(iter,iter2)*49/100;
```

```
            TMZ(iter)=TMZ(iter)-
StM(iter,iter2,2)*VR(iter,iter2)*49/100;
        end
        if iter2==5
            TMX(iter)=TMX(iter)+3.5*VR(iter,iter2)*49/100;

TMY(iter)=TMY(iter)+StM(iter,iter2,2)*VR(iter,iter2)*49/100;
            TMZ(iter)=TMZ(iter)-
StM(iter,iter2,1)*VR(iter,iter2)*49/100;
        end
        if iter2==6
            TMX(iter)=TMX(iter)-3.5*VR(iter,iter2)*49/100;

TMY(iter)=TMY(iter)+StM(iter,iter2,2)*VR(iter,iter2)*49/100;

TMZ(iter)=TMZ(iter)+StM(iter,iter2,1)*VR(iter,iter2)*49/100;
        end
    end
    TMX(iter)=TMX(iter)/sum (VR(iter,:)*49/100);
    TMY(iter)=TMY(iter)/sum (VR(iter,:)*49/100);
    TMZ(iter)=TMZ(iter)/sum (VR(iter,:)*49/100);
end
```

APPENDIX E3

```
%% THIS MATLAB CODE WAS WRITTEN FOR THE 3D RECONSTRUCTION OF THE
%% MARBLE SPECIMENS
%%

set(gcf,'renderer','openGL')

hold on
axis equal
axis  off vis3d
title('3D Reconstraction of the specimen')
%figure('Name','Simulation Plot Window','NumberTitle','off')

yuzey2=imread('6655mirror.jpg');
X=[1 0 0 1 1;0 -1 -1 0 0];
Y=[0 -1 -1 0 0;1 0 0 1 1];
Z=[1.4 1.4 0 0 1.4;1.4 1.4 0 0 1.4];
warp(X,Y,Z,yuzey2)

yuzey=imread('1234s.jpg');
x=[1 0 -1 0 1; 1 0 -1 0 1];
y=[0 1 0 -1 0;0 1 0 -1 0];
z=[0 0 0 0 0 ;1.4 1.4 1.4 1.4 1.4];
warp(x,y,z,yuzey)
```

APPENDIX E4

```
%% THIS MATLAB CODE WAS WRITTEN FOR THE NEURAL NETWORK ANALYSIS
%% OF THE DATASET OBTAINED BOTH LABORATORY TESTS AND IMAGE
%% PROCESSING OPERATIONS
%%
%% FEED FORWARD BACK PROPAGATION NEURAL NETWORK ANALYSIS OF THE
%% DATASET OBTAINED BOTH LABORATORY TESTS AND IMAGE PROCESSING
%% OPERATIONS

clear all
close all
clc
load Data.mat;
F1=Data(:,2);
F2=Data(:,3);
F3=Data(:,4);
F4=Data(:,5);
F5=Data(:,6);
F6=Data(:,7);

dataAll=[F1 F2 F3 F4 F5 F6]';
targetsAll=Data(:,8)';
train_data=dataAll(:,1:2:159);
train_targets=targetsAll(:,1:2:159);
test_data=dataAll(:,2:2:158);
test_targets=targetsAll(:,2:2:158);

min_frac=0.001;

[norm_input,input_mean,input_std,norm_train_targets,train_targets_me
an,train_targets_std]=prestd(train_data,train_targets);
[dim_reduced_train_data,trans_mat]=prepca(norm_input,min_frac);
[m,n]=size(dim_reduced_train_data);

net=newff(minmax(dim_reduced_train_data),[10 1],{'tansig'
'purelin'});
net.trainfcn='traingda';
net.trainparam.show=1000;
net.trainparam.goal=0.001;
```

```
net.trainparam.epochs=250;
net=train(net,dim_reduced_train_data,norm_train_targets);

[norm_test_data]=trastd(test_data,input_mean,input_std);
[dim_reduced_test_data]=trapca(norm_test_data,trans_mat);
test_results=sim(net,dim_reduced_test_data);
postpro_test_results=poststd(test_results,train_targets_mean,train_t
argets_std);

%percentageErrors=abs(test_targets-
postpro_test_results)./test_targets*100;
%mean(percentageErrors)
%figure;plot(percentageErrors,'b*');
figure,
plot(test_targets,postpro_test_results,'x');

training_set=sim(net,dim_reduced_train_data);
postpro_train_set_results=poststd(training_set,train_targets_mean,tr
ain_targets_std);
hold on
plot(train_targets,postpro_train_set_results,'or');

Measured_Values=[test_targets train_targets]';
Predicted_Values=[postpro_test_results postpro_train_set_results]';
[fresult,gof] = fit(Measured_Values,Predicted_Values,'poly1')
percentageErrors=abs(Measured_Values-
Predicted_Values)./Measured_Values*100;
mean(percentageErrors)
%figure, plot(Measured_Values,Predicted_Values,'x')
```

APPENDIX F

```
%% THIS MATLAB CODE WAS WRITTEN FOR THE AUTOMATED SEPERATION
%% OF THE TOUCHING GRAINS
%%

clear all,close all,clc             %Clears all variables, figures
and texts
grains=imread('tsubrounded.tif');      %Read image from file

%% Thresholding Image
level = graythresh(grains);         %Compute global image threshold
using Otsu's method
grains = im2bw(grains,level);       %Converting adjusted grayscale
image to a binary image, based on threshold
%%Removing noise
grains=1-grains;                    % The negative of the matrix for
finding the unconnected pixel in 4 neighborhood.
grains=bwareaopen(grains,6,4);
grains=1-grains;
figure,imshow(grains)

%%Calculation of Weighted skeletons (Distances matrix)
A=grains;%zeros(size(grains));
grains1=grains;
Control=zeros(size(grains));
z=1;
while isequal(grains1, Control)==0%
    z=z+1;
    grains2 = bwmorph(grains1,'remove'); %For each z value the outer
pixel chain will be removed
   A=A+(grains1-grains2)*z;        %Two resulting image are
subtracted, and the result was assigned as altitude value.
    grains1=grains1-grains2;        %maintaining loop
end
D=A;                                %will e used in Deleting
procedure
BWSkeleton= bwmorph(grains,'thin', Inf);    %Intersecting the
distances and result of the thining operation matrixes
A(BWSkeleton==0)=0;
```

```
Distances=A;
clear A;

%% Removing the single connected pixels (end points of the branches)
in the intersection matrix.
%% In order to reach the medial axis of the object, which is the
result of the
%branch removing operation, single connected pixels has been
scanned. However,
%the scanning operation should be completed, and all single
connected pixels
%should be considered together by the deleting procedure. Therefore,
a list of
%the single connected pixels and a gradient map has been computed.
If gradient
%condition is appropriate for deletion, the pixels will be removed.
And the
%loop continues…
gradient=1;                          % considering a positive
gradient
Control=zeros(size(Distances));
t=0;                                 % t is the count
while isequal(Distances, Control)==0
    %figure, imshow(Distances)
    t=t+1;
    count=0;
    for i=2:(size(Distances,2)-1)       % From left to right
        for j=2:(size(Distances,1)-1)   % From top to bottom
            if Distances(j,i)~=0        % if not equal to zero,
there is a pixel in medial axis
                connect=0;a=0;b=0;

                        for k=-1:1
                           for l=-1:1
                               % connection value
                               if k==0 & l==0

                               else
```

```
                                    if Distances(j+l,i+k)~=0
                                        connect=connect+1;
                                        a(connect)=k;b(connect)=l;
                                    end
                                end
                            end
                        end
                        % if single connected
                        if connect==1
                            count=count+1;
                            %plot(i,j,'xr')
                            del(count,1)=i; %
                            del(count,2)=j; %

gradient(t,count)=Distances(j+max(b),i+max(a))-Distances(j,i); %
considering max values.
                            if gradient(t,count)==0
                                gradient(t,count)=0.0001; %default
gradient
                            end

                        end
                        % if dual connected
                        if connect==2
                            if a(1)==a(2) | b(1)==b(2) % if they are
in the same row and column
                                if (a(1)==0 & a(2)==0) % if they are
in +
                                elseif(b(1)==0 & b(2)==0) % if they
are in +
                                elseif a(1)+a(2)==0 | b(1)+b(2)==0 %
subtracting the discrete position
                                else
                                        count=count+1;
                                    del(count,1)=i;     %add to
delete list
                                    del(count,2)=j;     %add to
delete list
                                    %plot(i,j,'xy')
```

```
gradient(t,count)=Distances(j+max(b),i+max(a))-Distances(j,i) %
control the max values.
                                        if gradient(t,count)==0

gradient(t,count)=0.0001; %default gradient
                                        end
                                    end
                                end
                            end
                            % if triple connected
                            if connect==3 %
                                if (a(1)==a(2) & a(1)==a(3) &
a(2)==a(3)) | (b(1)==b(2) & b(1)==b(3) & b(2)==b(3))
                                        count=count+1;
                                    del(count,1)=i;
                                    del(count,2)=j;

gradient(t,count)=Distances(j+max(b),i+max(a))-Distances(j,i) %
control the max values.
                                        if gradient(t,count)==0

gradient(t,count)=0.0001; %default gradient
                                        end
                                end
                            end
                end
            end
        end
    end
    % if no del there is nothing to delete.
    if count==0
        break
    end
    %% Deleting pixels
    Control=Distances;
    for v=1:size(del,1)                    %length(del)
        if t<3
            Distances(del(v,2),del(v,1))=0; % the first pixel will
be deleted directly
```

```
        else % Deleting criteria
%xxxxxxxxxxxxxxxxxxxxxxxxxxxxxxxxxxxxxxxxxxxxxxxxxxxxxxxxxxxxxxxxxxxxxxxxxxxxxxxxxx
xxxxxx
                if gradient(t,v)==0 % if a gradient value is zero in
the gradient table (means that the branch is come to an end), the
gradient will be used from the nearest value in the gradient table.
                    for i=v:size(del)-1
                        if gradient(t,i+1)~=0
                            gradient(t,v)=gradient(t,i+1);
                        end
                    end
                end
                   if  gradient(t,v) <= 0 & gradient(t-1,v) <= 0 %&
gradient(t-2,v) < 0 %& gradient(t-3,v) < 0& gradient(t-4,v) < 0%
else
                        Distances(del(v,2),del(v,1))=0;
                       %plot(del(v,1),del(v,2),'oy')
                        gradient;
                    end
%xxxxxxxxxxxxxxxxxxxxxxxxxxxxxxxxxxxxxxxxxxxxxxxxxxxxxxxxxxxxxxxxxxxxxxxxxxxxxxxxx
xxxxxx
        end
    end
    size(del)
    del
    clear del           % clear
end

%% Remove the single pixels (max points for the non touching
objects)
for i=1:(size(Distances,2)-1)
    for j=1:(size(Distances,1)-1)
       if Distances(j,i)~=0
           connect=0;
           for k=-1:1
                  for l=-1:1
                      if Distances(j+l,i+k)~=0
                            connect=connect+1;
                      end
```

```
                    end
                end
                if connect==1,
                   Distances(j,i)=0;
                end
            end
        end
end
%% An averaging has been done because the values may be the same for
a series.
avDistances=zeros(size(Distances));
for i=1:(size(Distances,2)-1)
   for j=1:(size(Distances,1)-1)
       av=0;count=0;
       Total=zeros(1,20);
       Values=zeros(1,20);%
        if Distances(j,i)~=0
                    for k=-3:3 % 7*7 is the limitations
                        for l=-3:3

                                    if Distances(j+l,i+k)~=0
                                        count=count+1;

Values(count)=Distances(j+l,i+k);
                                    end
                        end
                    end
                    for f=1:count
                       Total(f)=Values(f)^2/sum(Values); %
Calculating an weighted average.
                    end

                    avDistances(j,i)=sum(Total);
        end
   end
end
Distances=avDistances;
avDistances=round(avDistances);%% the local minimums has been
eliminated.
```

```
Control=zeros(size(Distances));

while isequal(Distances, Control)==0
    Control=Distances;

%hold on
pass=0; alone=0;
    m=max(max(Distances));
    for i=1:(size(Distances,2)-1)
            for j=1:(size(Distances,1)-1)
                if Distances(j,i)~=0
                    if Distances(j,i)==m
                                % deleting criteria

                                for k=-3:3
                                   for l=-3:3
                                       if
Distances(j+l,i+k)==0,alone=alone+1;end
                                       if Distances(j+l,i+k)~=0

                                                if k~=0 | l~=0 %

Distances(j,i)=0;
                                                end

                                                if
Distances(j+l,i+k)==0,alone=alone+1;end
                                           end
                                   end
                                end
                                if alone==48,
                                     Distances(j,i)=0.5; %
                                end
                        pass=1; % at each time only one pixel should
be processed
                        break,
```

```
                    end
                end
            end
            if pass==1, break, end
    end
    %imshow(Distances);
end

count=0,
for i=1:(size(Distances,2)-1)
    for j=1:(size(Distances,1)-1)
       if Distances(j,i)~=0
            count=count+1;
            dellist(count,1)=i;
            dellist(count,2)=j;
       end
    end
end
if count==0,break,end% if there is nothing to seperate

dellist %

%xxxxxxxxxxxxxxxxxxxxxxxxxxxxxxxxxxxxxxxxxxxxxxxxxxxxxxxxxxxxxxxxxxxxxxxxx
xxxxxx

for u=1:size(dellist,1)
    tek=0
    ortj=0
    orti=0
    for i=-10:10
        for j=-10:10

                if
avDistances(j+dellist(u,2),i+dellist(u,1))==avDistances(dellist(u,2)
,dellist(u,1))
                    tek=tek+1;
                    ortj=ortj+j
```

```
                    orti=orti+i
                end


            end
        end

        orti=round(orti/tek)
        ortj=round(ortj/tek)

          %

        if avDistances(dellist(u,2)+orti,dellist(u,1)+ortj)==
avDistances(dellist(u,2),dellist(u,1))
            dellist(u,1)=dellist(u,1)+ortj;
            dellist(u,2)=dellist(u,2)+orti;
        else
            dellist(u,1)=dellist(u,1)-ortj;
            dellist(u,2)=dellist(u,2)-orti;
        end
end
%xxxxxxxxxxxxxxxxxxxxxxxxxxxxxxxxxxxxxxxxxxxxxxxxxxxxxxxxxxxxxxxxxxxxxxxxx
xxxxxx

for y=1:size(dellist,1)
    count=0;
                        for k=-1:1
                           for l=-1:1
                               %
                               if k==0 & l==0


                               else
                                    count=count+1;

list(y,count)=D(dellist(y,2)+l,dellist(y,1)+k) ; %

                               end
                           end
```

```
                        end
list
end

% removing the listed pixels from the image
for y=1:size(list,1)
    grains(dellist(y,2),dellist(y,1))=0;
end
%clear dellist
count=0;

for y=1:size(list,1)% for each pixels in the del list a new list was
created in order to find the min value.

    [C,I(y)]=min(list(y,:))
    % for eight connection
        if I(y)==1, count=count+1; ok(count,1)=dellist(count,1)-1
;ok(count,2)=dellist(count,2)-1;end
        if I(y)==2,count=count+1; ok(count,1)=dellist(count,1)-1
;ok(count,2)=dellist(count,2);end
        if I(y)==3,count=count+1; ok(count,1)=dellist(count,1)-1
;ok(count,2)=dellist(count,2)+1;end
        if I(y)==4,count=count+1; ok(count,1)=dellist(count,1)
;ok(count,2)=dellist(count,2)-1;end
        if I(y)==5,count=count+1; ok(count,1)=dellist(count,1)
;ok(count,2)=dellist(count,2)+1;end
        if I(y)==6,count=count+1; ok(count,1)=dellist(count,1)+1
;ok(count,2)=dellist(count,2)-1;end
        if I(y)==7,count=count+1; ok(count,1)=dellist(count,1)+1
;ok(count,2)=dellist(count,2);end
        if I(y)==8,count=count+1; ok(count,1)=dellist(count,1)+1
;ok(count,2)=dellist(count,2)+1;end



end
% removing the new list from the grains matrix
for y=1:size(list,1)% first neighbor
    grains(ok(y,2),ok(y,1))=0;
end
```

```
ok2=dellist+(dellist-ok);% the second neighbor

for y=1:size(list,1)%bulunan ilk noktanın ikinci bitişiği
    grains(ok2(y,2),ok2(y,1))=0;
end

for p=1:size(ok2,1) % adding the lists together
   ok(size(ok,1)+1,1)=ok2(p,1);
   ok(size(ok,1),2)=ok2(p,2);
end
% adding the dellist together
for p=1:size(dellist,1)
   dellist(size(dellist,1)+1,1)=dellist(p,1);
   dellist(size(dellist,1),2)=dellist(p,2);
end

ok;
% find the min in the ok list
rep=1;
g=length(ok);

GControl=zeros(size(grains));
u=1;
while isequal(grains, GControl)==0 %
u=u+1;
GControl=grains;
    for i=rep:length(ok)
        if u==2
            minu=100000000;

                                    for k=-1:1
                                       for l=-1:1
                                           %
                                           if ok(i,1)<=dellist(i,1)
& ok(i,2)<=dellist(i,2)
                                               if k==0 & l==0
                                               elseif k==1
```

```
                                        elseif l==1
                                        else

                                                if
D(ok(i,2)+l,ok(i,1)+k)<minu

minu=D(ok(i,2)+l,ok(i,1)+k);al=k;bl=l;
                                                end


                                        end
                                    end
                                    if ok(i,1)>=dellist(i,1)
& ok(i,2)>=dellist(i,2)
                                        if k==0 & l==0
                                        elseif k==-1%
                                        elseif l==-1
                                        else

                                                if
D(ok(i,2)+l,ok(i,1)+k)<minu

minu=D(ok(i,2)+l,ok(i,1)+k);al=k;bl=l; %

                                                end


                                        end
                                    end

                                    if ok(i,1)<=dellist(i,1)
& ok(i,2)>=dellist(i,2)
                                        if k==0 & l==0
                                        elseif k==1%
                                        elseif l==-1
                                        else
```

```
                                                    if
D(ok(i,2)+l,ok(i,1)+k)<minu

minu=D(ok(i,2)+l,ok(i,1)+k);al=k;bl=l;

                                                    end


                                                end
                                            end
                                            %
                                            if ok(i,1)>=dellist(i,1)
& ok(i,2)<=dellist(i,2)
                                                if k==0 & l==0
                                                elseif k==-1
                                                elseif l==1
                                                else

                                                    if
D(ok(i,2)+l,ok(i,1)+k)<minu

minu=D(ok(i,2)+l,ok(i,1)+k);al=k;bl=l;

                                                    end
                                                 end
                                            end
                                        end
                                    end

                                    ok(length(ok)+1,1)=ok(i,1)+al;%
                                    ok(length(ok),2)=ok(i,2)+bl;

grains(ok(i,2)+bl,ok(i,1)+al)=0;%
                                    %figure, hold on,imshow(grains)



        else %
```

```
                minu=100000000;%

                                        for k=-1:1
                                           for l=-1:1
                                               %
                                               if k==0 & l==0

                                               else

                                                        if
D(ok(i,2)+l,ok(i,1)+k)<minu

minu=D(ok(i,2)+l,ok(i,1)+k);al=k;bl=l; %

                                                        end
                                                  end
                                           end
                                        end

                                        ok(length(ok)+1,1)=ok(i,1)+al;
                                        ok(length(ok),2)=ok(i,2)+bl;

grains(ok(i,2)+bl,ok(i,1)+al)=0;%
                                        %figure, hold on,imshow(grains)
        end
    end
    rep=rep+g;%
end
figure,imshow(grains)
```

APPENDIX G

Results of the Laboratory Tests and Image Processing Operations

Specimen #	Specimen Length (mm) Directions						Weight (gr)	Pulse Wave Velocities (m/s) Directions			Pulse Wave Velocities (m/s) Saturated Directions			Max Dry Pulse Wave Velocities (m/s)	Anisotropy (For Dry Wave Velocities)
	1		2		3			1	2	3	1	2	3		
1	7.09	7.08	6.90	6.90	6.98	6.98	918.97	6382.9	6330.3	6403.7	6440.9	6330.3	6403.7	6404	73.39
2	7.14	7.13	6.98	6.98	6.91	6.92	923.44	6370.5	6403.7	6402.8	6370.5	6403.7	6402.8	6404	33.13
3	6.82	6.81	6.93	6.94	6.91	6.89	876.25	6490.5	6421.3	6448.6	6490.5	6421.3	6448.6	6490	69.18
4*	6.95	6.95	6.83	6.82	6.91	6.89	878.78	6495.3	6438.7	6509.4	6495.3	6438.7	6509.4	6509	70.75
5	6.95	6.95	6.83	6.82	6.95	6.97	886.7	6435.2	6438.7	6327.3	6435.2	6500.0	6327.3	6439	111.41
6	6.83	6.82	6.88	6.87	6.89	6.89	870.83	6500.0	6425.2	6439.3	6438.7	6425.2	6439.3	6500	74.77
7	7.01	7.00	7.14	7.14	6.88	6.85	923.72	6368.2	6318.6	6415.9	6426.6	6318.6	6415.9	6416	97.30
8	6.83	6.85	6.93	6.94	6.98	6.98	888.43	6392.5	6304.5	6345.5	6452.8	6362.4	6403.7	6393	87.98
9	6.88	6.93	6.84	6.84	7.07	7.08	896.56	6514.2	6392.5	6490.8	6514.2	6392.5	6490.8	6491	121.63
10	6.99	6.99	6.90	6.90	7.05	7.05	909.88	6297.3	6448.6	6351.4	6354.5	6448.6	6409.1	6449	151.30
11	6.86	6.86	6.95	6.95	7.05	7.03	898.41	6236.4	6261.3	6400.0	6293.6	6318.2	6458.7	6400	163.64
12	6.96	6.95	7.04	7.04	6.88	6.88	891.18	6439.8	6458.7	6552.4	6439.8	6458.7	6615.4	6552	112.57
13*	6.93	6.93	6.96	7.02	6.99	6.96	906.22	6243.2	6297.3	6340.9	6300.0	6354.5	6399.1	6341	97.67
14	6.93	6.93	6.90	6.92	6.89	6.89	872.46	6243.2	6115.0	6263.6	6300.0	6281.8	6379.6	6264	148.59
15	6.85	6.85	6.98	6.98	6.81	6.83	877.99	6342.6	6463.0	6373.8	6462.3	6463.0	6434.0	6463	120.37
16	6.96	6.97	6.98	7.02	6.96	6.96	911.19	6389.9	6422.0	6385.3	6389.9	6481.5	6385.3	6385	36.70
17	7.03	7.05	7.01	7.01	6.87	6.89	897.12	6458.7	6315.3	6490.6	6458.7	6315.3	6552.4	6491	175.25
18	6.85	6.85	7.01	7.00	7.00	6.98	899.58	6342.6	6310.8	6354.5	6401.9	6426.6	6412.8	6343	43.73
19	6.86	6.86	6.90	6.89	6.91	6.92	879.37	6351.9	6443.9	6462.6	6533.3	6504.7	6462.6	6463	110.76
20	6.99	7.00	6.88	6.87	7.02	7.02	908.29	6359.1	6250.0	6267.9	6359.1	6425.2	6324.3	6359	109.09
21*	6.86	6.85	7.02	7.01	7.01	7.00	906.54	6467.0	6153.5	6091.3	6406.5	6208.0	6199.1	6467	375.68
22	6.98	6.98	7.03	7.02	6.85	6.85	901.71	6288.3	6386.4	6061.9	6403.7	6445.0	6284.4	6386	324.42
23	6.97	6.97	6.88	6.88	6.86	6.86	883.07	6336.4	6370.4	6351.9	6453.7	6490.6	6471.7	6336	34.01
24	6.84	6.84	6.98	6.95	6.89	6.91	884.89	6333.3	6389.9	6272.7	6452.8	6449.1	6388.9	6390	117.18
25	7.03	7.03	6.95	6.98	6.85	6.85	902.08	6390.9	6331.8	6227.3	6449.5	6331.8	6342.6	6391	163.64

Appendix G Continued.

26	7.04	7.06	6.89	6.88	7.04	7.03	916.7	6351.4	6375.0	6337.8	6409.1	6434.6	6395.5	6375	37.16
27	6.95	6.93	7.06	7.02	6.87	6.86	898.98	6309.1	6175.4	6075.2	6367.0	6230.1	6240.9	6309	233.87
28	6.85	6.86	6.89	6.92	6.91	6.94	878.69	6467.0	6453.3	6353.2	6467.0	6453.3	6472.0	6467	113.77
29	7.04	7.05	6.88	6.88	6.96	6.97	907.12	6463.3	6490.6	6389.9	6523.1	6552.4	6509.3	6491	100.66
30*	6.91	6.90	7.08	7.05	6.98	6.98	912.61	6393.5	6308.0	6345.5	6393.5	6422.7	6463.0	6394	85.48
31	6.83	6.84	6.97	6.97	7.00	7.00	896.23	6213.6	6279.3	6363.6	6448.1	6453.7	6481.5	6364	150.00
32	6.91	6.89	6.98	6.99	7.07	7.06	913.89	6216.2	6127.2	6197.4	6330.3	6350.0	6308.0	6216	89.02
33	6.90	6.90	6.82	6.83	6.88	6.88	869.86	6388.9	6319.4	6370.4	6448.6	6378.5	6490.6	6389	69.44
34	6.86	6.88	6.88	6.89	6.91	6.92	879.8	6420.6	6375.0	6344.0	6481.1	6434.6	6402.8	6421	76.52
35	6.80	6.79	6.94	6.94	6.90	6.93	875.66	6350.5	6425.9	6344.0	6410.4	6486.0	6402.8	6426	81.89
36	6.95	6.96	6.95	6.93	6.85	6.86	890.99	6380.7	6252.3	6289.0	6380.7	6367.0	6347.2	6381	128.48
37	6.98	6.98	7.00	6.99	6.99	7.00	891.35	6288.3	6359.1	6476.9	6345.5	6417.4	6537.4	6477	188.56
38	6.95	6.93	6.77	6.76	6.91	6.91	876.77	6309.1	6322.4	6339.4	6367.0	6382.1	6398.1	6339	30.36
39	6.75	6.76	6.90	6.90	6.89	6.87	863.75	6433.3	6388.9	6370.4	6495.2	6448.6	6370.4	6433	62.96
40	7.00	6.97	6.98	6.98	6.75	6.77	884.86	6408.3	6403.7	6438.1	6408.3	6463.0	6438.1	6438	34.43
41	6.90	6.92	6.89	6.89	6.82	6.83	874.94	6518.9	6439.3	6500.0	6518.9	6439.3	6500.0	6519	79.62
42	7.07	7.08	6.85	6.85	6.84	6.84	893.04	6373.9	6284.4	6392.5	6431.8	6401.9	6452.8	6393	108.12
43*	6.79	6.80	6.89	6.89	6.90	6.89	866.3	6471.4	6500.0	6443.9	6471.4	6439.3	6443.9	6500	56.07
44	6.92	6.92	7.06	7.07	6.97	6.97	914.97	6348.6	6422.7	6394.5	6407.4	6422.7	6453.7	6423	74.10
45	7.08	7.07	7.06	7.06	6.86	6.87	916.61	6373.9	6360.4	6415.9	6373.9	6418.2	6415.9	6416	55.53
46	6.94	6.95	6.86	6.87	6.90	6.90	872.32	6430.6	6476.4	6106.2	6430.6	6476.4	6216.2	6476	370.22
47	6.95	6.96	6.97	6.95	6.80	6.83	886.45	6439.8	6385.3	6369.2	6439.8	6444.4	6429.2	6440	70.66
48	6.80	6.80	6.96	6.96	6.95	6.95	887.37	6415.1	6270.3	6435.2	6476.2	6327.3	6435.2	6435	164.91
49	6.84	6.84	7.08	7.08	7.00	7.00	912.41	6275.2	6210.5	6194.7	6392.5	6321.4	6306.3	6275	80.54
50	7.05	7.04	6.83	6.83	6.94	6.95	901.33	5870.8	6324.1	6256.8	6073.3	6324.1	6313.6	6324	453.24
51	6.79	6.79	7.00	6.98	7.02	7.03	895.11	6405.7	6472.2	6328.8	6405.7	6472.2	6328.8	6472	143.39
52	6.98	6.99	6.85	6.84	7.05	7.05	907.69	6350.0	6457.5	6351.4	6408.3	6519.0	6409.1	6458	107.55
53	6.85	6.85	6.97	6.96	6.99	7.00	894.56	6342.6	6331.8	6245.5	6401.9	6331.8	6301.8	6343	97.06
54	6.89	6.88	6.89	6.88	6.89	6.89	879.13	6259.1	6375.0	6263.6	6316.5	6434.6	6321.1	6375	115.91
55	6.87	6.86	7.06	7.08	6.98	6.99	909.37	6415.9	6486.2	6408.3	6476.4	6486.2	6467.6	6486	77.98
56	6.99	6.98	7.00	7.00	6.86	6.90	902.83	6408.3	6306.3	6429.9	6408.3	6363.6	6490.6	6430	123.60

Appendix G Continued.

57	7.02	7.04	6.85	6.86	7.05	7.03	908.84	6276.8	6231.8	6342.3	6333.3	6289.0	6400.0	6342	110.52
58	6.90	6.95	6.82	6.82	7.22	7.24	917.98	6183.0	6256.9	6287.0	6295.5	6314.8	6342.1	6287	103.92
59	6.97	6.97	6.88	6.86	6.87	6.88	889	6514.0	6420.6	6425.2	6514.0	6481.1	6485.8	6514	93.46
60	6.86	6.87	7.02	7.02	6.93	6.93	896.86	6240.9	6324.3	6357.8	6298.2	6324.3	6357.8	6358	116.89
61	7.18	7.18	6.90	6.90	6.86	6.85	912.94	6243.5	6272.7	6289.0	6298.2	6330.3	6289.0	6289	45.51
62	6.82	6.82	6.98	6.97	7.04	7.03	900.44	6434.0	6399.1	6454.1	6434.0	6399.1	6454.1	6454	55.05
63	7.14	7.13	6.98	6.99	6.84	6.83	914.73	6427.9	6350.0	6448.1	6427.9	6408.3	6448.1	6448	98.11
64	7.03	7.04	6.86	6.85	6.99	6.98	906.12	6513.9	6528.6	6292.8	6513.9	6467.0	6292.8	6529	235.78
65*	6.94	6.97	7.06	7.05	6.86	6.86	906.01	6380.7	6472.5	6471.7	6439.8	6413.6	6471.7	6472	91.74
66	6.97	6.98	6.89	6.88	7.00	7.02	907.85	6283.8	6434.6	6431.2	6283.8	6495.3	6490.7	6435	150.80
67	6.88	6.89	6.85	6.86	6.95	6.94	882.56	6316.5	6289.0	6313.6	6375.0	6406.5	6371.6	6317	27.52
68	6.89	6.87	7.13	7.14	6.96	6.97	922.16	6198.2	6204.3	6163.7	6254.5	6258.8	6218.8	6204	40.63
69	7.06	7.07	6.98	6.98	6.80	6.81	902.21	5887.5	6403.7	6300.9	6090.5	6463.0	6359.8	6404	516.17
70	7.01	7.02	6.88	6.85	6.93	6.95	903.55	6377.3	6356.5	6309.1	6435.8	6415.9	6367.0	6377	68.18
71	6.86	6.85	6.97	6.97	6.97	6.97	895.9	6467.0	6453.7	6394.5	6467.0	6453.7	6453.7	6467	72.49
72	6.95	6.94	6.90	6.91	6.84	6.83	883.03	6430.6	6277.3	6270.6	6490.7	6393.5	6328.7	6431	159.91
73	7.05	7.03	6.86	6.85	6.98	7.00	901.78	6342.3	6231.8	6297.3	6400.0	6347.2	6412.8	6342	110.52
74	7.02	7.03	7.00	7.02	6.86	6.85	907.44	6386.4	6431.2	6347.2	6445.0	6490.7	6528.6	6431	83.97
75	6.96	6.93	6.87	6.87	6.84	6.84	880.99	6313.6	6245.5	6333.3	6371.6	6361.1	6392.5	6333	87.88
76	6.89	6.88	6.86	6.85	6.90	6.90	877.52	6316.5	6406.5	6272.7	6375.0	6406.5	6330.3	6407	133.81
77	6.89	6.90	6.83	6.83	6.88	6.87	872.12	6384.3	6504.8	6425.2	6384.3	6504.8	6425.2	6505	120.50
78	6.90	6.91	6.82	6.83	6.93	6.93	879.82	6334.9	6319.4	6416.7	6393.5	6378.5	6476.6	6417	97.22
79	6.96	6.98	6.90	6.91	6.93	6.91	893.2	6279.3	6277.3	6290.9	6336.4	6334.9	6348.6	6291	13.64
80	6.89	6.87	6.81	6.82	6.94	6.92	878.75	6429.9	6369.2	6357.8	6490.6	6429.2	6357.8	6430	72.11
81	6.84	6.85	6.89	6.88	6.91	6.90	875.32	6397.2	6375.0	6393.5	6397.2	6434.6	6393.5	6397	22.20
82	6.84	6.84	6.88	6.88	6.91	6.92	877.53	6333.3	6311.9	6344.0	6392.5	6370.4	6402.8	6344	32.11
83	6.92	6.94	6.95	6.97	6.77	6.76	880.99	6416.7	6444.4	6442.9	6416.7	6444.4	6442.9	6444	27.78
84	6.81	6.80	7.10	7.10	7.00	6.99	911.74	6359.8	6339.3	6301.8	6359.8	6396.4	6359.1	6360	58.01
85	6.98	6.98	6.93	6.88	6.94	6.95	906.34	6403.7	6453.3	6430.6	6403.7	6514.2	6371.6	6431	49.60
86	7.07	7.04	6.84	6.83	6.91	6.91	898.33	6413.6	6270.6	6281.8	6472.5	6328.7	6281.8	6414	142.99
87	6.85	6.85	6.90	6.90	6.97	6.97	890.08	6462.3	6448.6	6394.5	6462.3	6509.4	6453.7	6462	67.77

Appendix G Continued.

88	6.98	6.95	6.95	6.97	6.87	6.88	885.37	6389.9	6444.4	6547.6	6449.1	6444.4	6547.6	6548	157.71
89	6.84	6.83	6.94	6.93	6.90	6.92	881.51	6448.1	6421.3	6457.9	6509.5	6481.3	6518.9	6458	36.65
90	6.88	6.86	7.03	7.01	6.99	7.02	909.91	6481.1	6440.4	6426.6	6481.1	6440.4	6426.6	6481	54.53
91	6.83	6.84	6.95	6.95	6.97	6.97	891.89	6448.1	6435.2	6453.7	6509.5	6495.3	6453.7	6454	18.52
92	6.87	6.88	6.80	6.80	6.93	6.91	871.15	6485.8	6476.2	6407.4	6485.8	6538.5	6467.3	6486	78.44
93	6.98	6.95	7.00	7.00	6.89	6.90	902.67	6449.1	6306.3	6443.9	6449.1	6422.0	6443.9	6449	142.77
94	6.96	6.95	6.97	6.98	6.82	6.82	891.62	6322.7	6458.3	6495.2	6322.7	6399.1	6495.2	6495	172.51
95	6.96	6.95	6.87	6.88	6.92	6.90	888.96	6439.8	6425.2	6398.1	6500.0	6485.8	6457.9	6440	41.67
96	6.99	6.95	7.08	7.08	6.91	6.92	921.24	6336.4	6265.5	6344.0	6453.7	6321.4	6344.0	6336	78.55
97	6.86	6.88	6.92	6.91	6.87	6.88	879.65	6481.1	6462.6	6425.2	6542.9	6523.6	6425.2	6481	55.90
98	6.84	6.83	6.95	6.90	6.92	6.89	878.49	6448.1	6353.2	6393.5	6509.5	6412.0	6453.3	6448	94.90
99	6.93	6.90	6.93	6.94	7.00	6.98	898.56	6286.4	6137.2	6297.3	6344.0	6304.5	6354.5	6297	160.13
100	6.92	6.93	6.90	6.89	6.94	6.95	882.5	6412.0	6384.3	6551.9	6472.0	6384.3	6551.9	6552	167.63
101	6.92	6.91	6.81	6.82	6.97	7.01	885.85	6344.0	6369.2	6297.3	6344.0	6252.3	6297.3	6369	71.86
102	6.98	6.97	6.76	6.76	6.98	6.96	887.42	6172.6	6259.3	6336.4	6227.7	6259.3	6394.5	6336	163.80
103	6.89	6.87	6.81	6.81	6.85	6.86	865.23	6198.2	6190.9	6231.8	6254.5	6190.9	6289.0	6232	40.91
104	6.84	6.83	6.97	6.98	6.94	6.94	886.72	6448.1	6399.1	6252.3	6448.1	6399.1	6309.1	6448	195.86
105	6.86	6.88	7.02	7.03	6.98	6.98	909.89	6481.1	6504.6	6403.7	6420.6	6445.0	6403.7	6505	100.96
106	6.90	6.88	6.94	6.94	6.81	6.81	878.32	6439.3	6486.0	6485.7	6379.6	6367.0	6364.5	6486	46.73
107	6.92	6.95	6.87	6.88	6.81	6.82	876.85	6481.3	6485.8	6490.5	6481.3	6485.8	6429.2	6490	9.17
108	6.95	6.96	6.89	6.89	6.81	6.81	879.47	6439.8	6439.3	6364.5	6439.8	6439.3	6424.5	6440	75.33
109	6.97	6.96	6.85	6.86	6.93	6.86	883.85	6389.9	6347.2	6211.7	6389.9	6347.2	6156.3	6390	178.20
110	6.94	6.94	6.85	6.87	6.87	6.87	881.74	6486.0	6411.2	6481.1	6425.9	6351.9	6420.6	6481	74.77
111	6.88	6.90	6.89	6.90	6.89	6.88	881.36	6439.3	6443.9	6375.0	6439.3	6384.3	6375.0	6444	68.93
112	6.86	6.86	7.01	7.01	7.00	7.02	907.04	6180.2	6431.2	6431.2	6293.6	6431.2	6431.2	6431	251.01
113	6.87	6.85	6.97	6.98	6.97	6.96	895.58	6471.7	6458.3	6389.9	6411.2	6458.3	6389.9	6472	81.79
114	6.80	6.80	6.97	6.97	6.93	6.92	880.57	6238.5	6060.9	6021.7	6296.3	6279.3	6128.3	6239	216.79
115*	7.02	7.03	6.89	6.89	7.05	7.05	918.11	6386.4	6379.6	6294.6	6445.0	6379.6	6351.4	6386	91.72
116	7.02	7.04	7.10	7.10	6.84	6.83	919.34	6333.3	6396.4	6387.9	6390.9	6396.4	6387.9	6396	63.06
117	6.90	6.89	6.77	6.76	6.89	6.88	867.22	6443.9	6504.8	6434.6	6384.3	6442.9	6434.6	6505	70.23
118	6.84	6.84	6.81	6.81	6.89	6.88	864.76	6452.8	6424.5	6375.0	6392.5	6424.5	6375.0	6453	77.83

Appendix G Continued.

119	6.84	6.83	6.85	6.89	6.84	6.84	866.47	6213.6	6079.6	6275.2	6213.6	6189.2	6275.2	6275	195.58
120	6.97	6.93	6.99	6.98	6.85	6.87	893.75	6318.2	6408.3	6471.7	6318.2	6408.3	6411.2	6472	153.52
121	6.88	6.88	6.90	6.94	6.86	6.86	881.55	6370.4	6348.6	6411.2	6311.9	6290.9	6351.9	6411	62.59
122	6.84	6.83	7.05	7.04	7.03	7.04	911.14	6328.7	6073.3	6337.8	6270.6	6234.5	6395.5	6338	264.56
123	6.96	6.98	6.84	6.81	7.04	7.04	901.25	6168.1	6148.6	6230.1	6114.0	6148.6	6285.7	6230	81.44
124	6.93	6.90	6.87	6.89	6.99	6.97	892.57	6402.8	6429.9	6345.5	6344.0	6311.9	6232.1	6430	84.45
125	6.83	6.81	6.98	7.00	7.05	7.03	902.95	6373.8	6297.3	6342.3	6373.8	6354.5	6400.0	6374	76.53
126	6.85	6.85	6.97	6.97	6.94	6.93	890.53	6342.6	6168.1	6304.5	6342.6	6223.2	6304.5	6343	174.45
127	6.98	6.99	6.84	6.86	6.91	6.95	889.48	6127.2	6284.4	5680.3	6127.2	6342.6	5974.1	6284	604.08
128	6.96	6.96	6.97	6.95	6.97	6.97	909.47	6270.3	6385.3	6279.3	6327.3	6444.4	6336.4	6385	115.05
129	6.83	6.83	7.02	7.06	7.10	7.13	918.15	6443.4	6400.0	6409.9	6324.1	6400.0	6409.9	6443	43.40
130	6.87	6.86	7.01	7.00	6.95	6.99	906.58	6240.9	6199.1	6223.2	6184.7	6254.5	6279.3	6241	41.79
131*	6.83	6.82	6.99	7.03	6.90	6.88	888.86	6261.5	6258.9	6207.2	6261.5	6315.3	6207.2	6261	54.26
132	6.85	6.86	6.98	6.96	6.90	6.94	887.63	4896.4	6223.2	6348.6	5760.5	6223.2	6348.6	6349	1452.20
133	7.01	6.98	6.94	6.94	7.03	7.05	921.84	6301.8	6367.0	6342.3	6301.8	6367.0	6400.0	6367	65.17
134	6.93	6.93	6.96	6.96	6.83	6.83	889.33	6187.5	6159.3	6266.1	6243.2	6214.3	6324.1	6266	106.76
135	7.05	7.03	6.81	6.83	6.94	6.93	895.42	6175.4	6144.1	6137.2	6285.7	6144.1	6192.0	6175	38.27
136	6.86	6.87	7.07	7.10	6.99	7.00	917.13	6240.9	6269.9	6190.3	6298.2	6269.9	6245.5	6270	79.65
137	7.09	7.08	7.08	7.08	6.96	6.98	939.7	6560.2	6495.4	6394.5	6500.0	6495.4	6394.5	6560	165.69
138	7.08	7.07	7.05	7.05	6.92	7.02	937.04	6490.8	6467.9	6394.5	6490.8	6467.9	6336.4	6491	96.33
139	7.02	7.02	7.33	7.34	7.08	7.06	977.14	6381.8	6491.2	6486.2	6381.8	6434.2	6486.2	6491	109.33
140	7.07	7.04	7.01	7.03	7.08	7.07	940.7	6532.4	6440.4	6550.9	6472.5	6440.4	6490.8	6551	110.56
141	6.98	6.95	7.31	7.33	7.06	7.08	969.21	6449.1	6477.9	6486.2	6449.1	6076.9	6486.2	6486	37.16
142	7.02	7.00	7.13	7.16	7.08	7.10	950.33	6372.7	6379.5	6445.5	6372.7	6436.9	6445.5	6445	72.73
143*	7.06	7.09	7.00	7.03	7.03	7.02	937.16	6490.8	6435.8	6445.0	6490.8	6495.4	6445.0	6491	55.05
144	7.10	7.08	6.99	7.02	7.05	7.03	939.16	6445.5	6368.2	6458.7	6445.5	6368.2	6458.7	6459	90.53
145	7.04	7.06	7.10	7.10	7.00	7.03	939.97	6467.9	6454.5	6377.3	6467.9	6513.8	6435.8	6468	90.62
146	7.09	7.09	7.11	7.11	7.08	7.07	942.43	6445.5	6405.4	6431.8	6445.5	6463.6	6431.8	6445	40.05
147	7.08	7.11	7.05	7.03	7.09	7.10	950.25	6450.0	6342.3	6450.0	6450.0	6400.0	6450.0	6450	107.66
148	7.08	7.08	7.09	7.10	7.03	7.03	949.41	6436.4	6334.8	6166.7	6495.4	6391.9	6276.8	6436	269.70
149	7.07	7.07	7.03	7.03	6.98	6.98	932.97	6427.3	6390.9	6403.7	6486.2	6449.5	6403.7	6427	36.36

Appendix G Continued.

150	7.03	7.03	7.03	7.01	7.05	7.05	932.7	6449.5	6440.4	6467.9	6509.3	6440.4	6527.8	6468	27.52
151	7.40	7.05	7.10	7.12	6.95	6.94	935.29	6689.8	6348.2	6430.6	6689.8	6405.4	6430.6	6690	341.60
152	7.09	7.08	6.96	6.96	7.07	7.08	938.27	6325.9	6327.3	6373.9	6500.0	6385.3	6490.8	6374	47.98
153	7.03	7.01	6.94	6.96	7.04	7.03	924.16	6381.8	6376.1	6454.1	6440.4	6435.2	6454.1	6454	77.98
154	6.95	6.98	6.93	6.94	7.05	7.03	915.59	6331.8	6362.4	6400.0	6449.1	6421.3	6458.7	6400	68.18
155	7.06	7.08	7.00	7.02	7.04	7.04	938.88	6369.4	6431.2	6400.0	6427.3	6431.2	6400.0	6431	61.82
156	6.99	6.97	7.09	7.12	7.09	7.11	944.63	6288.3	6400.9	6396.4	6288.3	6459.1	6454.5	6401	112.61
157*	7.00	7.01	7.09	7.09	6.95	6.93	938.16	6199.1	6165.2	6196.4	6310.8	6330.4	6309.1	6199	33.90
158	7.03	7.04	7.11	7.10	7.10	7.13	954.25	6337.8	6459.1	6409.9	6395.5	6459.1	6468.2	6459	121.25
159	6.99	6.99	6.97	6.96	6.95	6.98	903.58	6078.3	5662.6	6163.7	6185.8	5852.9	6218.8	6164	501.12
160	7.01	6.99	6.99	6.95	6.97	6.98	911.6	5982.9	5957.3	5717.2	6087.0	6060.9	5961.5	5983	265.69
161	6.95	6.96	6.99	7.01	6.98	6.96	911.13	6047.8	6034.5	6114.0	6100.9	6140.4	6168.1	6114	79.55
162	6.81	6.78	6.95	6.95	7.00	7.00	888.77	6013.3	5940.2	5932.2	6121.6	5991.4	5982.9	6013	81.07
163	6.97	6.99	6.96	6.95	7.15	7.12	926.5	6017.2	5894.1	6098.3	6122.8	5995.7	6150.9	6098	204.22
164	6.95	6.96	7.00	6.98	7.07	7.05	915.14	5747.9	5682.9	5739.8	5844.5	5873.9	5883.3	5748	65.01
165	6.90	6.86	6.93	6.91	7.02	7.01	896.12	5982.6	6070.2	6047.4	6035.1	6234.2	6153.5	6070	87.57
166*	7.00	7.00	6.96	6.97	7.00	7.00	913.37	5982.9	5852.9	5882.4	6034.5	6004.3	5982.9	5983	129.96
167	7.00	7.00	6.99	7.00	6.98	6.96	913.39	5982.9	5181.5	5957.3	5982.9	5641.1	6060.9	5983	801.42
168	7.04	7.03	6.97	6.98	6.99	6.98	914.06	5961.9	6012.9	5678.9	6012.8	6118.4	5820.8	6013	334.07
169	7.00	6.97	6.99	6.99	6.98	6.95	909.38	5678.9	6025.9	5527.8	5919.5	6078.3	5804.2	6026	498.08
170	7.00	7.00	7.00	7.00	6.98	6.97	911.83	5882.4	5932.2	5961.5	6034.5	5982.9	6012.9	5962	79.19
171	6.98	6.98	6.98	7.02	6.80	6.76	887.07	6069.6	5982.9	6053.6	6177.0	6034.5	6108.1	6070	86.66
172	6.70	6.73	7.00	7.01	6.95	6.96	876.05	5739.3	5789.3	5700.8	5839.1	5837.5	5795.8	5789	88.44
173	6.98	6.97	6.97	6.97	7.02	7.00	916.53	4681.2	5621.0	5392.3	5580.0	5808.3	5699.2	5621	939.76
174	6.98	6.97	7.01	7.03	6.96	6.95	909.29	6012.9	6051.7	5844.5	6065.2	6104.3	5995.7	6052	207.19
175	7.10	7.09	6.97	6.98	6.96	6.98	918.1	5721.8	5812.5	5666.7	5863.6	5911.0	5666.7	5813	145.83
176	7.00	6.98	6.94	6.96	7.02	7.00	910.07	5825.0	5840.3	6043.1	5974.4	5991.4	6095.7	6043	218.10
177	7.00	7.00	6.95	6.98	7.02	7.03	912.48	5982.9	5756.2	5854.2	6034.5	5902.5	5953.4	5983	226.71
178	7.09	7.09	6.99	6.98	7.02	7.03	929.3	5764.2	5820.8	5805.8	5908.3	5970.1	5903.4	5821	56.61
179	7.01	7.02	6.96	6.98	6.91	6.90	908.13	6153.5	6336.4	6110.6	6208.0	6279.3	6220.7	6336	225.74
180	7.01	7.02	6.95	6.96	6.97	6.98	910.65	5845.8	5564.0	5717.2	5845.8	5795.8	5812.5	5846	281.83

Appendix G Continued.

181	6.93	6.91	7.00	7.00	6.98	6.99	901.67	5242.4	4895.1	5332.1	5406.3	5109.5	5543.7	5332	436.96
182	6.97	6.96	7.03	7.03	6.96	6.95	915.26	6331.8	6221.2	6322.7	6331.8	6333.3	6322.7	6332	110.58
183	6.98	6.97	6.96	6.98	6.98	7.00	908.49	5911.0	5760.3	5923.7	6012.9	5906.8	6025.9	5924	163.40
184	6.96	6.97	7.15	7.14	6.93	6.94	922.36	5527.8	5808.9	5877.1	5852.9	5954.2	5927.4	5877	349.34
185	6.99	7.00	6.97	6.97	6.98	6.99	915.01	6136.0	6114.0	6073.9	6136.0	6223.2	6127.2	6136	62.05
186	6.95	6.95	7.03	7.05	6.97	6.98	904.37	5225.6	5818.2	5861.3	5515.9	5966.1	5961.5	5861	635.78
187	7.00	6.95	7.00	6.98	7.01	7.02	913.58	5717.2	5873.9	5995.7	5861.3	6025.9	6047.4	5996	278.51
188	7.03	7.01	6.86	6.83	7.00	6.98	895.57	5318.2	5610.7	6131.6	5949.2	5952.2	6185.8	6132	813.40
189	7.02	7.00	6.96	6.95	7.00	7.03	913.86	6043.1	6047.8	6047.4	6043.1	6100.9	6100.0	6048	4.72
190	6.95	6.95	7.00	6.99	6.98	7.00	908.37	5889.8	5878.2	5637.1	5991.4	5928.0	5776.9	5890	252.73
191*	7.02	6.99	7.05	7.03	6.97	6.97	915.58	5936.4	5866.7	6060.9	6038.8	6017.1	6114.0	6061	194.20
192	6.99	6.99	7.00	7.02	6.93	6.94	904.58	5376.9	5699.2	5592.7	5592.0	5841.7	5779.2	5377	322.26
193	6.96	6.98	7.00	6.99	7.00	7.02	911.94	5857.1	5928.0	5890.8	5906.8	5928.0	5991.5	5928	70.82

Appendix G Continued.

Specimen #	Area Ratios (%)	Unit Weights (gr/cm3)	E. Porosity (%)	Water Absorption by weight (%)	Eccentricity as Vector (cm)	Operator Classification	Axial Strengths (kg/cm2)
1	68.59	2.702	0.135	0.050	0.29	3	601.9
2	83.67	2.706	0.114	0.042	0.39	2	708.1
3	92.46	2.710	0.083	0.031	0.09	2	950.8
4*	89.98	2.709	0.111	0.041	0.14	2	1225.5
5	69.15	2.711	0.287	0.106	0.64	3	729.7
6	92.16	2.709	0.068	0.025	0.24	2	858.5
7	83.33	2.706	0.079	0.029	0.22	3	872.3
8	86.58	2.708	0.104	0.038	0.07	2	Reserved
9	91.52	2.708	0.024	0.009	0.18	2	909.9
10	64.53	2.709	0.286	0.106	0.24	3	762.2
11	77.65	2.710	0.259	0.096	0.31	3	714.2
12	63.64	2.710	0.176	0.065	1.11	3	1043.8
13*	59.53	2.710	0.263	0.097	0.66	3	473.4
14	92.05	2.708	0.165	0.061	0.05	2	691.9
15	97.70	2.708	0.086	0.032	0.01	2	1084.9
16	83.96	2.710	0.181	0.067	0.19	3	907.7
17	73.03	2.710	0.142	0.052	0.18	3	1027.0
18	91.17	2.708	0.187	0.069	0.14	3	714.2
19	93.08	2.710	0.092	0.034	0.02	2	1031.3
20	56.94	2.711	0.215	0.079	1.71	3	838.1
21*	89.68	2.707	0.179	0.066	0.17	2	420.6
22	61.58	2.710	0.219	0.081	1.45	3	745.8
23	85.03	2.708	0.064	0.024	0.36	3	626.2
24	94.99	2.709	0.098	0.036	0.01	2	880.6
25	92.24	2.706	0.165	0.061	0.02	2	772.8

Appendix G Continued.

26	66.68	2.707	0.177	0.065	0.45	3	1106.6
27	59.72	2.709	0.172	0.063	1.72	3	873.6
28	80.13	2.709	0.117	0.043	0.85	3	938.2
29	94.51	2.708	0.012	0.004	0.07	2	1189.3
30*	71.34	2.708	0.131	0.048	0.59	3	1154.8
31	61.56	2.711	0.184	0.068	0.72	3	1121.0
32	31.94	2.709	0.184	0.068	2.16	3	822.9
33	94.16	2.706	0.047	0.017	0.08	2	908.2
34	91.38	2.709	0.052	0.019	0.12	2	1065.2
35	92.90	2.707	0.099	0.037	0.10	2	943.2
36	74.98	2.709	0.116	0.043	0.79	3	691.6
37	93.70	2.708	0.067	0.025	0.11	2	921.1
38	86.35	2.708	0.139	0.051	0.41	3	582.7
39	97.14	2.707	0.044	0.016	0.10	2	785.7
40	88.28	2.708	0.104	0.038	0.14	2	816.1
41	91.57	2.709	0.111	0.041	0.05	2	973.2
42	81.26	2.710	0.127	0.047	0.10	3	1021.4
43*	100.00	2.708	0.047	0.017	0.00	1	937.5
44	76.50	2.707	0.130	0.048	0.20	3	925.0
45	63.16	2.711	0.183	0.068	0.58	3	Reserved
46	87.46	2.709	0.196	0.072	0.20	3	749.6
47	85.94	2.706	0.085	0.032	0.28	3	823.0
48	89.43	2.708	0.055	0.020	0.22	3	1011.3
49	64.99	2.709	0.187	0.069	0.21	3	Reserved
50	71.54	2.708	0.225	0.083	0.57	3	783.1
51	95.14	2.707	0.094	0.035	0.15	3	803.9
52	76.42	2.709	0.158	0.058	0.76	3	822.7
53	59.37	2.709	0.324	0.120	1.65	3	Reserved
54	90.81	2.709	0.102	0.038	0.08	2	953.6
55	90.18	2.708	0.089	0.033	0.35	2	901.0
56	64.33	2.708	0.141	0.052	0.47	3	1080.2

Appendix G Continued.

57	74.35	2.707	0.128	0.047	0.25	3	942.8
58	71.38	2.710	0.301	0.111	0.28	3	879.3
59	94.47	2.711	0.067	0.025	0.25	2	1025.1
60	64.81	2.711	0.163	0.060	0.10	3	Reserved
61	87.61	2.707	0.181	0.067	0.11	2	613.8
62	91.76	2.709	0.063	0.023	0.09	2	Reserved
63	92.18	2.705	0.068	0.025	0.03	2	1034.0
64	83.98	2.707	0.167	0.062	0.59	3	903.1
65*	96.54	2.706	0.018	0.007	0.02	2	738.4
66	86.42	2.710	0.075	0.028	0.35	2	980.9
67	83.29	2.709	0.239	0.088	0.15	2	950.2
68	71.24	2.707	0.153	0.056	0.29	3	684.6
69	82.37	2.707	0.189	0.070	0.30	3	867.9
70	70.16	2.709	0.150	0.055	0.80	3	941.9
71	92.58	2.707	0.030	0.011	0.08	2	Reserved
72	68.57	2.711	0.246	0.091	1.24	3	648.5
73	88.58	2.708	0.117	0.043	0.39	2	1018.7
74	87.01	2.710	0.081	0.030	0.05	2	983.7
75	89.99	2.709	0.123	0.045	0.01	2	Reserved
76	95.53	2.709	0.099	0.036	0.10	2	1239.4
77	95.86	2.706	0.068	0.025	0.04	2	1025.6
78	91.61	2.708	0.065	0.024	0.09	2	1088.0
79	92.86	2.708	0.170	0.063	0.06	2	703.4
80	91.08	2.708	0.117	0.043	0.23	2	920.3
81	90.80	2.710	0.111	0.041	0.15	2	860.5
82	92.54	2.710	0.151	0.056	0.10	2	1011.5
83	89.83	2.708	0.086	0.032	0.07	2	Reserved
84	76.61	2.707	0.288	0.106	0.85	3	685.6
85	87.85	2.708	0.027	0.010	0.12	2	1052.9
86	64.45	2.709	0.217	0.080	0.39	3	779.3
87	93.47	2.708	0.049	0.018	0.10	2	860.8

Appendix G Continued.

88	90.54	2.708	0.070	0.026	0.06	2	Reserved
89	90.32	2.706	0.083	0.031	0.19	2	Reserved
90	80.98	2.708	0.068	0.025	0.36	3	1057.3
91	84.86	2.707	0.085	0.031	0.35	3	866.0
92	94.92	2.709	0.062	0.023	0.09	2	899.3
93	93.16	2.706	0.135	0.050	0.08	2	Reserved
94	86.62	2.708	0.085	0.031	0.04	2	962.3
95	81.33	2.708	0.122	0.045	0.32	3	818.6
96	72.99	2.708	0.123	0.046	0.07	3	550.8
97	86.27	2.710	0.120	0.044	0.56	3	621.0
98	79.95	2.709	0.157	0.058	0.66	3	1020.8
99	75.23	2.712	0.238	0.088	0.38	3	656.0
100	96.42	2.710	0.114	0.042	0.05	2	1152.8
101	65.22	2.710	0.236	0.087	0.19	3	763.5
102	87.14	2.711	0.122	0.045	0.03	2	793.8
103	86.07	2.709	0.169	0.062	0.05	3	970.4
104	90.88	2.708	0.128	0.047	0.19	2	633.6
105	94.67	2.707	0.080	0.030	0.17	2	1078.1
106	89.45	2.708	0.099	0.036	0.11	2	Reserved
107	92.63	2.709	0.065	0.024	0.03	2	1091.2
108	94.28	2.708	0.077	0.028	0.07	2	991.4
109	76.24	2.709	0.199	0.074	1.13	3	725.3
110	96.70	2.706	0.071	0.026	0.10	2	1178.3
111	94.20	2.708	0.095	0.035	0.05	2	891.4
112	77.51	2.708	0.131	0.049	0.21	3	856.1
113	82.63	2.708	0.085	0.031	0.34	3	840.0
114	86.73	2.710	0.302	0.111	0.14	2	852.9
115*	67.83	2.708	0.168	0.062	0.18	3	1191.3
116	68.76	2.710	0.183	0.067	0.49	3	944.2
117	94.01	2.707	0.047	0.017	0.10	2	1205.8
118	100.00	2.706	0.063	0.023	0.00	1	1166.3

Appendix G Continued.

119	91.96	2.709	0.153	0.057	0.04	2	885.1
120	82.13	2.709	0.085	0.031	0.22	3	976.4
121	96.21	2.708	0.080	0.029	0.02	2	1167.9
122	58.43	2.711	0.283	0.104	0.65	3	Reserved
123	60.07	2.710	0.325	0.120	0.47	3	834.4
124	43.53	2.711	0.240	0.089	1.13	3	990.2
125	65.88	2.708	0.180	0.066	0.70	3	Reserved
126	49.17	2.713	0.359	0.133	0.78	3	785.9
127	40.98	2.713	0.488	0.180	0.97	3	872.2
128	53.12	2.709	0.170	0.063	1.26	3	977.8
129	62.18	2.711	0.219	0.081	0.27	3	Reserved
130	40.49	2.713	0.296	0.109	1.74	3	718.2
131*	56.72	2.711	0.241	0.089	0.46	3	395.3
132	57.06	2.713	0.526	0.194	1.64	3	961.9
133	61.61	2.709	0.209	0.077	0.15	3	Reserved
134	63.90	2.711	0.290	0.107	0.80	3	890.3
135	49.32	2.712	0.336	0.124	1.14	3	Reserved
136	61.35	2.708	0.233	0.086	0.50	3	822.5
137	100.00	2.703	0.046	0.017	0.00	1	1398.6
138	100.00	2.703	0.035	0.013	0.00	1	1201.0
139	100.00	2.703	0.039	0.014	0.00	1	1202.3
140	100.00	2.704	0.037	0.014	0.00	1	1349.2
141	100.00	2.704	0.031	0.011	0.00	1	1441.3
142	100.00	2.703	0.037	0.014	0.00	1	1488.7
143*	100.00	2.707	0.012	0.004	0.00	1	1728.1
144	100.00	2.702	0.009	0.003	0.00	1	1397.6
145	100.00	2.701	0.034	0.013	0.00	1	1441.7
146	100.00	2.703	0.026	0.010	0.00	1	1490.1
147	100.00	2.703	0.017	0.006	0.00	1	Reserved
148	100.00	2.706	0.054	0.020	0.00	1	1287.8
149	100.00	2.704	0.020	0.008	0.00	1	1220.1

Appendix G Continued.

150	100.00	2.704	0.014	0.005	0.00	1	1383.3
151	100.00	2.703	0.023	0.009	0.00	1	Reserved
152	100.00	2.704	0.023	0.009	0.00	1	1445.6
153	100.00	2.704	0.015	0.005	0.00	1	1461.7
154	100.00	2.704	0.003	0.001	0.02	1	1512.5
155	100.00	2.702	0.023	0.009	0.00	1	Reserved
156	100.00	2.706	0.092	0.034	0.00	1	1333.8
157*	100.00	2.704	0.063	0.023	0.00	1	1545.4
158	100.00	2.705	0.006	0.002	0.00	1	1167.2
159	31.66	2.713	1.060	0.391	1.86	4	656.3
160	1.75	2.713	0.816	0.301	4.63	4	750.3
161	42.90	2.709	0.425	0.157	0.72	4	684.1
162	12.41	2.709	0.634	0.234	2.65	4	760.6
163	7.06	2.710	0.772	0.285	3.18	4	666.3
164	5.90	2.712	1.040	0.384	2.76	4	696.0
165	19.34	2.710	0.587	0.216	2.60	4	625.3
166*	11.13	2.710	0.857	0.316	1.69	4	896.9
167	0.00	2.713	1.209	0.446	0.00	4	453.5
168	0.60	2.710	0.987	0.364	3.58	4	596.1
169	14.83	2.715	1.090	0.401	1.54	4	389.1
170	5.11	2.709	0.758	0.280	1.00	4	731.1
171	32.02	2.712	0.575	0.212	3.20	4	634.5
172	10.02	2.712	0.988	0.364	0.51	4	577.4
173	4.85	2.711	1.363	0.503	0.87	4	511.9
174	17.50	2.708	0.864	0.319	2.20	4	555.9
175	2.71	2.710	1.098	0.405	1.04	4	493.5
176	18.91	2.710	0.840	0.310	1.78	4	664.4
177	21.12	2.710	0.757	0.279	3.55	4	463.3
178	0.67	2.716	0.947	0.349	3.95	4	412.3
179	56.95	2.710	0.334	0.123	1.21	4	574.3
180	3.15	2.711	1.128	0.416	2.23	4	Reserved

Appendix G Continued.

181	14.59	2.717	1.485	0.547	1.64	4	676.5
182	56.39	2.710	0.338	0.125	0.79	4	632.7
183	6.02	2.712	1.000	0.369	3.11	4	693.7
184	6.45	2.709	0.914	0.337	1.55	4	545.1
185	2.65	2.708	0.548	0.202	4.22	4	Reserved
186	7.92	2.711	1.328	0.490	2.53	4	Reserved
187	16.53	2.710	0.757	0.279	2.88	4	595.5
188	47.26	2.712	0.657	0.242	1.53	4	604.2
189	0.00	2.709	0.732	0.270	0.00	4	762.5
190	0.76	2.712	1.078	0.397	3.60	4	617.9
191*	27.16	2.712	0.684	0.252	0.70	4	738.4
192	5.68	2.712	1.223	0.451	2.64	4	707.2
193	0.00	2.711	0.838	0.309	0.00	4	534.4

*) Specimens have not been used in multiple regression and neural network analysis.

APPENDIX H- F-Table

95% POINTS FOR THE F DISTRIBUTION

Denominator Degrees of Freedom	Numerator Degrees of Freedom										
*	1	2	3	4	5	6	7	8	9	10	*
1	161	199	216	225	230	234	237	239	241	242	1
2	18.5	19.0	19.2	19.2	19.3	19.3	19.4	19.4	19.4	19.4	2
3	10.1	9.55	9.28	9.12	9.01	8.94	8.89	8.85	8.81	8.79	3
4	7.71	6.94	6.59	6.39	6.26	6.16	6.09	6.04	6.00	5.96	4
5	6.61	5.79	5.41	5.19	5.05	4.95	4.88	4.82	4.77	4.74	5
6	5.99	5.14	4.76	4.53	4.39	4.28	4.21	4.15	4.10	4.06	6
7	5.59	4.74	4.35	4.12	3.97	3.87	3.79	3.73	3.68	3.64	7
8	5.32	4.46	4.07	3.84	3.69	3.58	3.50	3.44	3.39	3.35	8
9	5.12	4.26	3.86	3.63	3.48	3.37	3.29	3.23	3.18	3.14	9
10	4.96	4.10	3.71	3.48	3.33	3.22	3.14	3.07	3.02	2.98	10
11	4.84	3.98	3.59	3.36	3.20	3.09	3.01	2.95	2.90	2.85	11
12	4.75	3.89	3.49	3.26	3.11	3.00	2.91	2.85	2.80	2.75	12
13	4.67	3.81	3.41	3.18	3.03	2.92	2.83	2.77	2.71	2.67	13
14	4.60	3.74	3.34	3.11	2.96	2.85	2.76	2.70	2.65	2.60	14
15	4.54	3.68	3.29	3.06	2.90	2.79	2.71	2.64	2.59	2.54	15
16	4.49	3.63	3.24	3.01	2.85	2.74	2.66	2.59	2.54	2.49	16
17	4.45	3.59	3.20	2.96	2.81	2.70	2.61	2.55	2.49	2.45	17
18	4.41	3.55	3.16	2.93	2.77	2.66	2.58	2.51	2.46	2.41	18
19	4.38	3.52	3.13	2.90	2.74	2.63	2.54	2.48	2.42	2.38	19
20	4.35	3.49	3.10	2.87	2.71	2.60	2.51	2.45	2.39	2.35	20
21	4.32	3.47	3.07	2.84	2.68	2.57	2.49	2.42	2.37	2.32	21
22	4.30	3.44	3.05	2.82	2.66	2.55	2.46	2.40	2.34	2.30	22
23	4.28	3.42	3.03	2.80	2.64	2.53	2.44	2.37	2.32	2.27	23
24	4.26	3.40	3.01	2.78	2.62	2.51	2.42	2.36	2.30	2.25	24
25	4.24	3.39	2.99	2.76	2.60	2.49	2.40	2.34	2.28	2.24	25
26	4.23	3.37	2.98	2.74	2.59	2.47	2.39	2.32	2.27	2.22	26
27	4.21	3.35	2.96	2.73	2.57	2.46	2.37	2.31	2.25	2.20	27
28	4.20	3.34	2.95	2.71	2.56	2.45	2.36	2.29	2.24	2.19	28
29	4.18	3.33	2.93	2.70	2.55	2.43	2.35	2.28	2.22	2.18	29
30	4.17	3.32	2.92	2.69	2.53	2.42	2.33	2.27	2.21	2.16	30
35	4.12	3.27	2.87	2.64	2.49	2.37	2.29	2.22	2.16	2.11	35
40	4.08	3.23	2.84	2.61	2.45	2.34	2.25	2.18	2.12	2.08	40
50	4.03	3.18	2.79	2.56	2.40	2.29	2.20	2.13	2.07	2.03	50
60	4.00	3.15	2.76	2.53	2.37	2.25	2.17	2.10	2.04	1.99	60
70	3.98	3.13	2.74	2.50	2.35	2.23	2.14	2.07	2.02	1.97	70
80	3.96	3.11	2.72	2.49	2.33	2.21	2.13	2.06	2.00	1.95	80
100	3.94	3.09	2.70	2.46	2.31	2.19	2.10	2.03	1.97	1.93	100
150	3.90	3.06	2.66	2.43	2.27	2.16	2.07	2.00	1.94	1.89	150
300	3.87	3.03	2.63	2.40	2.24	2.13	2.04	1.97	1.91	1.86	300
1000	3.85	3.00	2.61	2.38	2.22	2.11	2.02	1.95	1.89	1.84	1000
*	1	2	3	4	5	6	7	8	9	10	*

APPENDIX I- t-Table

PERCENTAGE POINTS OF THE T DISTRIBUTION

Tail Probabilities								
One Tail		0.10	0.05	0.025	0.01	0.005	0.001	0.0005
Two Tails		0.20	0.10	0.05	0.02	0.01	0.002	0.001
D	1	3.078	6.314	12.71	31.82	63.66	318.3	637
E	2	1.886	2.920	4.303	6.965	9.925	22.330	31.6
G	3	1.638	2.353	3.182	4.541	5.841	10.210	12.92
R	4	1.533	2.132	2.776	3.747	4.604	7.173	8.610
E	5	1.476	2.015	2.571	3.365	4.032	5.893	6.869
E	6	1.440	1.943	2.447	3.143	3.707	5.208	5.959
S	7	1.415	1.895	2.365	2.998	3.499	4.785	5.408
	8	1.397	1.860	2.306	2.896	3.355	4.501	5.041
O	9	1.383	1.833	2.262	2.821	3.250	4.297	4.781
F	10	1.372	1.812	2.228	2.764	3.169	4.144	4.587
	11	1.363	1.796	2.201	2.718	3.106	4.025	4.437
F	12	1.356	1.782	2.179	2.681	3.055	3.930	4.318
R	13	1.350	1.771	2.160	2.650	3.012	3.852	4.221
E	14	1.345	1.761	2.145	2.624	2.977	3.787	4.140
E	15	1.341	1.753	2.131	2.602	2.947	3.733	4.073
D	16	1.337	1.746	2.120	2.583	2.921	3.686	4.015
O	17	1.333	1.740	2.110	2.567	2.898	3.646	3.965
M	18	1.330	1.734	2.101	2.552	2.878	3.610	3.922
	19	1.328	1.729	2.093	2.539	2.861	3.579	3.883
	20	1.325	1.725	2.086	2.528	2.845	3.552	3.850
	21	1.323	1.721	2.080	2.518	2.831	3.527	3.819
	22	1.321	1.717	2.074	2.508	2.819	3.505	3.792
	23	1.319	1.714	2.069	2.500	2.807	3.485	3.768
	24	1.318	1.711	2.064	2.492	2.797	3.467	3.745
	25	1.316	1.708	2.060	2.485	2.787	3.450	3.725
	26	1.315	1.706	2.056	2.479	2.779	3.435	3.707
	27	1.314	1.703	2.052	2.473	2.771	3.421	3.690
	28	1.313	1.701	2.048	2.467	2.763	3.408	3.674
	29	1.311	1.699	2.045	2.462	2.756	3.396	3.659
	30	1.310	1.697	2.042	2.457	2.750	3.385	3.646
	32	1.309	1.694	2.037	2.449	2.738	3.365	3.622
	34	1.307	1.691	2.032	2.441	2.728	3.348	3.601
	36	1.306	1.688	2.028	2.434	2.719	3.333	3.582
	38	1.304	1.686	2.024	2.429	2.712	3.319	3.566
	40	1.303	1.684	2.021	2.423	2.704	3.307	3.551
	42	1.302	1.682	2.018	2.418	2.698	3.296	3.538
	44	1.301	1.680	2.015	2.414	2.692	3.286	3.526
	46	1.300	1.679	2.013	2.410	2.687	3.277	3.515
	48	1.299	1.677	2.011	2.407	2.682	3.269	3.505
	50	1.299	1.676	2.009	2.403	2.678	3.261	3.496
	55	1.297	1.673	2.004	2.396	2.668	3.245	3.476
	60	1.296	1.671	2.000	2.390	2.660	3.232	3.460
	65	1.295	1.669	1.997	2.385	2.654	3.220	3.447
	70	1.294	1.667	1.994	2.381	2.648	3.211	3.435
	80	1.292	1.664	1.990	2.374	2.639	3.195	3.416
	100	1.290	1.660	1.984	2.364	2.626	3.174	3.390
	150	1.287	1.655	1.976	2.351	2.609	3.145	3.357
	200	1.286	1.653	1.972	2.345	2.601	3.131	3.340
Two Tails		0.20	0.10	0.05	0.02	0.01	0.002	0.001
One Tail		0.10	0.05	0.025	0.01	0.005	0.001	0.0005
Tail Probabilities								

APPENDIX J- XRD Graphs of Breccia Rock Constituents

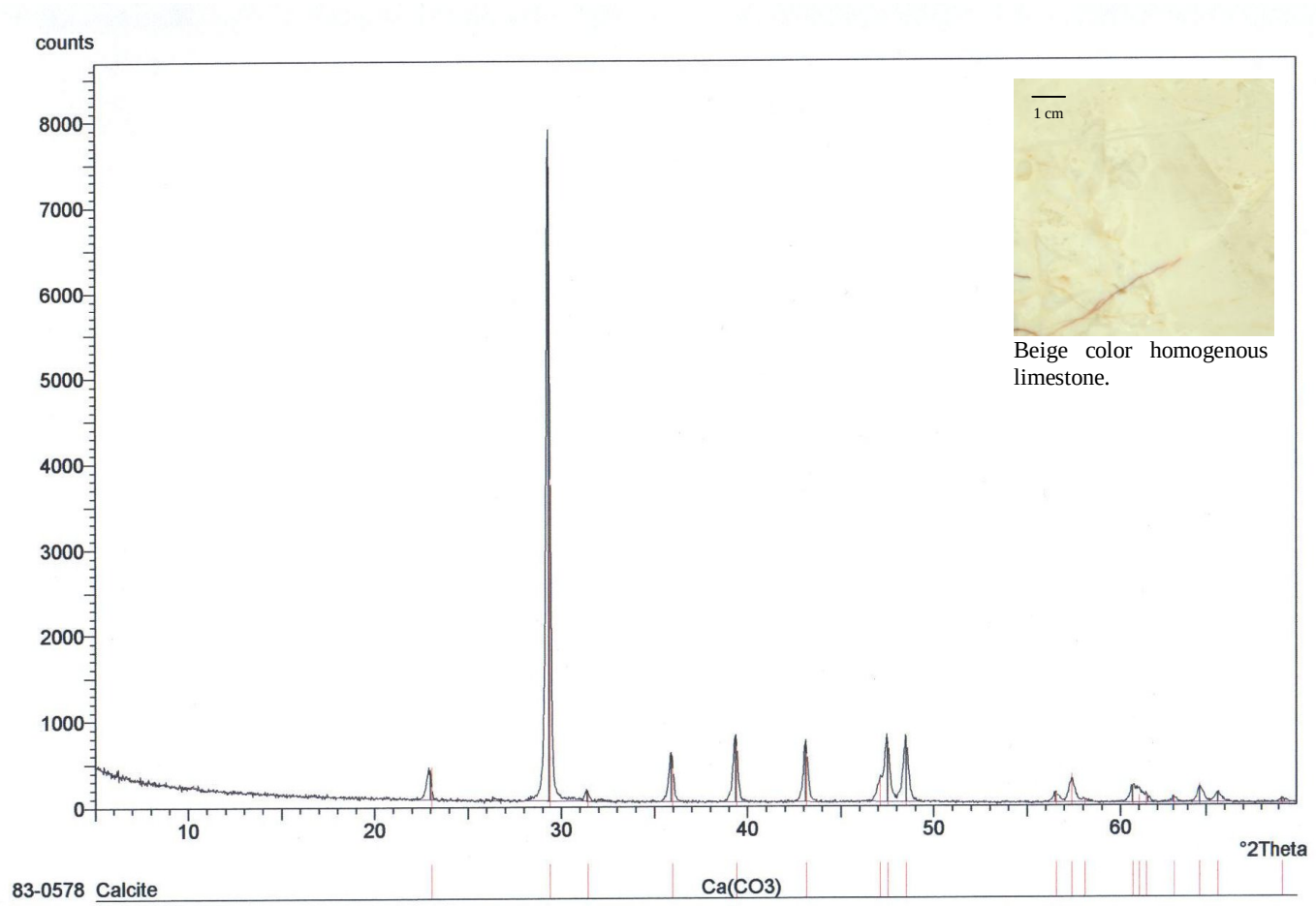

Beige color homogenous limestone.

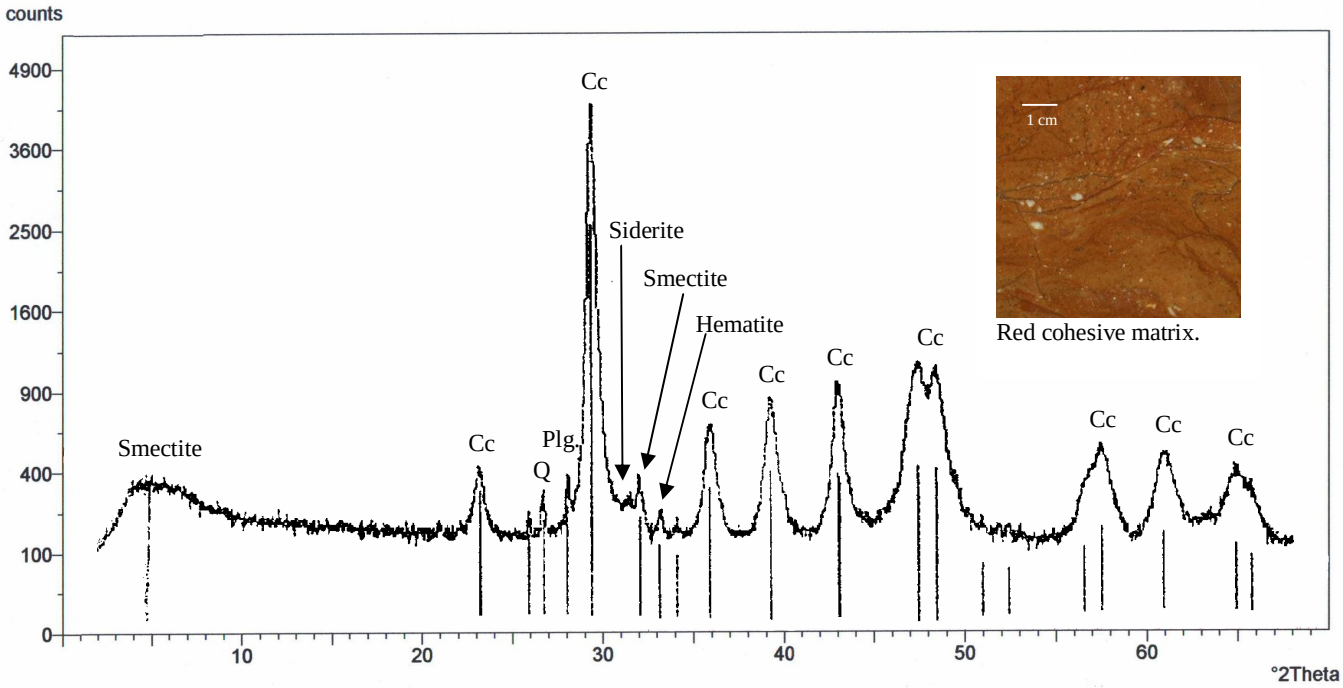
counts
4900
3600
2500
1600
900
400
100
0
10
20
30
40
50
60
°2Theta
Smectite
Cc
Plg.
Q
Cc
Siderite
Smectite
Hematite
Cc
Cc
Cc
Cc
Cc
Cc
Cc
1 cm
Red cohesive matrix.

LIST OF TABLES

Pages

LIST OF FIGURES

Pages

LIST OF SYMBOLS

u : The distance of an object point from the plane of the lens

v : The distance of the focused image from the plane of the lens

f : The focal length of the lens

M: Number of cell column on the image plane

N: Number of cell row on the image plane

m: Number of cell column on the CCD plane

n: Number of cell row on the CCD plane

x_{im} : X coordinate of the point in the pixel plane (pixel)

y_{im} : Y coordinate of the point in the pixel plane (pixel)

x : X coordinates of the points in the CCD plane (mm)

y : Y coordinates of the points in the CCD plane (mm)

f(x,y): Definition of an image in matrix form

R: Response of the spatial filter

g(x,y):Value of the segmented image

T: Threshold value

$\%Passing_g$: Percent passing values for the g^{th} grain (%)

e_v: Volumetric shrinkage strain (%)

V_i: Initial volume of the specimen (cm^3)

V_f: Final volume of the specimen (cm^3)

D: Diameter of the test specimen (mm)

a : The angle between the central and the tangent lines

a: The distance between the central and tangent lines on the background plane (mm)

b: The distance between the center of the specimen and the background (mm)

T_{p1}: First tangent point

T_{p2}: Second tangent point

r : Radius of the specimen (mm)

R : Roundness parameter

e : Eccentricity parameter

a : Semi major axis of the ellipse (pixel)

b : Semi minor axis of the ellipse (pixel)

c_i : Coefficient of inclusion

c_e : Coefficient of exclusion

d_p: Normalized digital signature value

N_p: Number of pixel along the perimeter

d_p: The distance from the border of the shape to the center of the equivalent circle (pixel)

r_e: The radius of the equivalent circle (pixel)

$W_{saturated}$: Weight of rock specimens in saturated condition (g)

W_{dry}: Weight of rock specimens in dry condition (g)

V_{voids}: Volume of voids (cm^3)

$V_{specimens}$: Volume of specimens (cm^3)

n: Effective porosity (%)

$W_{in\ air}$: Weight of specimen in air (g)

$W_{in\ water}$: Weight of specimen in water (g)

γ: Density of the water (g/cm^3)

c_x: Centroidal x coordinate of the breccias in the specimen surfaces (pixel)

c_y: Centroidal y coordinate of the breccias in the specimen surfaces (pixel)

C_x:Center of gravity for breccia grains for x axis (pixel)

C_y: Center of gravity for breccia grains for y axis (pixel)

C_z: Center of gravity for breccia grains for z axis (pixel)

e: Three dimensional centroidal coordinates of the breccia grains (pixel)

R^2: Coefficient of determination

F: F ratio

Y: Predicted unconfined compressive strength (kg/cm^2)

b_k:Beta weights of the k^{th} independent variable

e_i: Independent normally distributed random variables

RSS: Residual sum of squares

u_k: Linear combiner output due to the input signals

w_{kj}: Snaptic weights of neurons

y_k: Output signal of neuron

b_k : Bias

j (.): Activation function